Low-Temperature Synthesis and Magnetism of Novel Frameworks

Patricia Leyva-Bailen

A Thesis Submitted for the Degree
of
Doctor of Philosophy

Heriot-Watt University
Department of Chemistry
June 2009

Abstract

Solvothermal and ionothermal syntheses have been used in this work for the generation of novel frameworks containing oxy-anions in the presence of organic amines and ionic liquids. The new phases have been characterised using X-ray diffraction techniques, elemental analysis, thermogravimetric analysis, spectroscopic methods and SQUID magnetometry.

The role of the 1-ethyl-3-methylimidazolium bromide ([EMIM] Br) ionic liquid has been investigated, resulting in the formation of the $(NH_4)_2M_2(SO_4)_3$ (M=Mn, Fe) langbeinite-type phases through an unusual redox process in which sulphur is oxidised to sulphate under vacuum conditions. Both materials exhibit paramagnetic behaviour. The use of the [EMIM] Br ionic liquid has also afforded the determination of the crystal structure of the mixed-anion barium carbonate chloride $Ba_3Cl_4CO_3$, previously only obtainable in polycrystalline form. It consists of a complex three-dimensional network, in which the barium and carbonate ions define chains which are cross-linked *via* chloride ions.

Solvothermal synthesis has been employed for the investigation of the system MSO_4:amine:H_2SO_4:H_2O (amine= ethylenediamine (en) and triethylenetetramine (trien)) yielding the formation of novel transition metal sulphates. A common building block M_4O_{20} has been identified and effectively incorporated in the structure of $[Mn_4(SO_4)_8(OH)_2(H_2O)_2](enH_2)_5$, $[Fe_3(SO_4)_3(OH)_2(H_2O)_2](NH_4)_2$ and the hybrid $[Mn_3(SO_4)_3(OH)_2(trienH_2)]$, in which $trienH_2^{2+}$ cations serve to link $[Mn_3(SO_4)_3(OH)_2]^{2-}$ layers into a three-dimensional structure. Both the manganese hybrid and the iron sulphate constitute examples of frustrated systems. The iron phase exhibits a complex magnetic behaviour and is magnetically ordered at room temperature. En and trien have been successfully linked to the metal centre in $[M(SO_4)(trien)]$ and $[Mn(SO_4)(en)]$, generating two- and three-dimensional hybrid structures, respectively. The layered sulphates $[Co_3(SO_4)_3(OH)_2](enH_2)$ and $[Mn(SO_4)_2](enH_2)$, in which layers are charge balanced by enH_2^{2+} cations, have also been prepared. The former constitutes a rare example of Kagome layer structure with a unique connectivity, whose magnetic properties showed the presence of geometrical magnetic frustration.

The successful addition of rare-earths into the reactions has resulted in the formation of new rare-earth sulphates with different dimensionalities. Using

ethylenediamine the formation of layered structures was favoured and $[Ln_2(SO_4)_6(H_2O)_2](enH_2)_3$, $[Dy(SO_4)_2](enH_2)_{0.5}$ and the hybrid $[Ln_2(SO_4)_6(enH)_2](enH_2)_2$, in which the metal centre is directly connected to the organic amine through Ln-N bond, were obtained together with the one-dimensional $[La(SO_4)_3](enH_2)_{1.5}$. The ribbon-like $[Dy_2(SO_4)_6(H_2O)](trienH_4)_{1.5}$ and $[Sm_4(SO_4)_{10}(H_2O)_4](pipH_2)_4$, built up from three-dimensional motifs in which channels of eight- and twelve-membered rings are generated, have also been prepared employing triethylenetetramine and piperazine, respectively. The rare-earth ions exhibit paramagnetic behaviour with the exception of the samarium sulphate, which is magnetically ordered at room temperature.

A mis padres,

Por acompañarme siempre en el camino

ACKNOWLEDGEMENTS

I wish to thank my supervisors Prof Anthony V. Powell and Dr Paz Vaqueiro for their unconditional help and support and their valuable advice.

I would also like to thank Christina Graham for performing elemental analysis, Dr Georgina Rosair for assistance with single crystal X-ray diffraction data and Dr Javier Sanchez Benitez from Edinburgh University for his kind help with SQUID measurements and for making those long days seem shorter.

Thank you to my colleagues and friends in the Solid State Chemistry group for all the moments we have shared together.

I would like to express my gratitude to my friends Lucia, Gerard, Iwona, Isaela, Victor and Santi for their friendship, their support and for making me laugh when I needed it the most. I could not imagine these years without them.

A special acknowledge to my parents, my sister and my boyfriend for their encouragement and for always believing in me.

Declaration Statement

Table of contents

Chapter 1: INTRODUCTION

1.1 Chemistry of Materials

1.1.1 Background

Solid-state chemistry focuses on the optimisation of novel materials for specific applications, using high temperatures as a traditional route. Products of such reactions are generally limited to thermodynamically stable phases, with relatively simple crystal structures with high density. The recent increased interest in soft-chemistry techniques is motivated by their potential to provide access to metastable phases which may have different structural and physical properties from those materials obtained using conventional synthetic techniques. Most research efforts are concerned with the design and prediction of new structures and materials [1-3]. There is a wide range of synthetic methods for solid-state chemistry which have yielded numerous discoveries. Among them, direct-combination high-temperature approaches [4-6], synthesis of fluxes and melts [7, 8], synthesis from solutions [9, 10] and hydrothermal synthesis [11-13], which have allowed the synthesis of *e.g.* alloys from suspensions, the synthesis of extended frameworks or the low-temperature synthesis of chalcogenides, can be cited.

Solvothermal and hydrothermal reactions, in which water or any other solvent such as organic solvents are used respectively, offer a way for the synthesis of novel materials. Inorganic-organic hybrid metal chalcogenides have been successfully prepared under these conditions and their properties have been studied for their applications in hydrogen production and ionic conductivity [14-16]. Solvothermal and hydrothermal reactions constitute the preferred synthetic approach for the synthesis of hybrid inorganic-organic materials assembled from molecular building blocks, materials which provide potential for a variety of applications and chemical properties due to the possibility of combining both the inorganic and the organic functionalities. Some possible combination of properties would be those associated to the inorganic layer, such as conducting, semiconducting, magnetic and luminescent behaviour, with those of the organic moieties, such as mesomorphic, ferroelastic, hyperpolarizable and polymerizable behaviour. Zeolites, silicates, metal carbonates, phosphates and carboxylates are generally synthesised under solvothermal/hydrothermal conditions [1, 17-21].

Very recently, ionic liquids (ILs) have been proven to be good solvents for the synthesis of framework compounds due to their ability to dissolve organic and inorganic compounds, which has allowed the synthesis of hybrid materials. This synthetic method is known as ionothermal synthesis, and has been used for the preparation of aluminophosphates [22], cobalt aluminophosphates [23] and organic-inorganic hybrid materials [24].

In this work, solvothermal and ionothermal methods have been used for the preparation of novel inorganic materials containing oxy-anions. Transition metal and rare-earth sulphates frameworks exhibiting interesting magnetic behaviour were obtained by solvothermal synthesis in the presence of organic amines and langbeinite-type structures and barium carbonate chloride by ionothermal synthesis, demonstrating the potential of these two synthetic approaches for the preparation of novel materials.

1.1.2 Synthesis

The synthesis of open-framework compounds has been reviewed by Davis and Lobo [25] and by Morris and Weigel [26]. Synthetic zeolites have been known since the pioneering works of Barrer [27] and Milton [28], in which materials were prepared in the presence of organic alkyl ammonium cations. It was later observed that organic amines could be employed for the synthesis of zeolites which resulted in a wide variety of structures [29]. The organic amines play different roles: as templates (which refer to the formation of a distinctive structure which reflects the geometrical and electronic nature of the template); as structure-directing agents (in which the organic amine leads to the formation of a specific zeolite structure); and as space fillers (in which the organic amines exclude solvent molecules, enhancing the van der Waals interactions between the organic components and the framework species providing the enthalpic driving force for the reaction). More recently, ionic liquids have been employed in what is been called ionothermal synthesis, which is an alternative low-temperature method, analogous to hydrothermal and solvothermal reactions. However, some differences can be introduced in the synthetic process due to their unusual properties, such as their low vapour pressures that allow reactions to be conducted at ambient pressures. Similar to amines, ionic liquids have been proven to have different roles in the synthesis of new materials: they can act as solvents, they can be viewed as solvent-reactants and there have been few examples of ionic liquids acting as solvent-template-reactants [30, 31].

1.2 Open-framework architectures

1.2.1 Introduction

The study of inorganic open-framework materials has become a very challenging area over the last years. One of the objectives of the study of open-framework architectures is to search for materials with porous structures which may provide catalytic and sorption properties. The discovery of fascinating structures of different dimensionalities offering new properties and applications has been equally important.

The discovery of the aluminophosphate structure, the first zeolite-analogue $AlPO_4$, by Flaningen *et al*. in 1982 [32] represented a breakthrough in the synthesis of porous solids, which had previously focused on aluminosilicates zeolites, stimulating the synthesis of novel inorganic porous materials [19] and other structures with different dimensionalities [33]. Most of these compounds are based upon oxygen-containing inorganic materials exhibiting one-, two- and three-dimensional structures, in which the open-framework is built up using a variety of building units. The concept of a secondary building unit was first employed to describe the framework structures of aluminosilicates [34] and is now applied to octahedral-tetrahedral systems (Table 1.1). The simplest secondary building unit is that generated from two metal-centered tetrahedra or octahedra generally linked by sharing vertices (SBU-2) and it generally acts as a linker between other secondary building units. In addition to oxide containing phases, the synthesis of open-frameworks of other anions, such as nitrides [35], halides [36] or sulfides [37], has been demonstrated. Reviews on metal carboxylates [20] and organically-templated metal sulphates, selenites and selenates [38] have been published and more recently the synthesis of open-framework structures of compounds of the transition metals has been reviewed [21].

Currently, research focuses on the design of novel structures involving the introduction of organic molecules as constituents of the structure. Such hybrid structures, in which the organic ligands connect inorganic frameworks to generate void volumes into the structure, have attracted much interest due to the possibility of taking advantage of metal coordination and the functionality of the organic component.

Although applications of such materials are dominated by the aluminosilicates zeolites, there have been efforts in the design of a new generation of multifunctional porous materials that combine the classical applications of zeolites with the discovery of novel materials and the development of their physical properties, such as optical, magnetic and

conductive properties. Encouraging reports of the ability of metal-ion porous materials in the sorption of methane [39] and hydrogen [40] as well as improvements in the use of these materials in the ion-exchange [41-43], catalysis [44, 45] and separation processes [46], have been published. A general overview of multifunctional porous materials describing their properties has recently been reported [47]. Among them, magnetic materials are the most abundant and a wide number of inorganic and hybrid inorganic-organic materials with interesting magnetic properties, in which transition metals form part of the structure, have been synthesised.

Table 1.1. Secondary building units (SBUs) of open-framework structures [21].

SBU	Geometry	SBU	Geometry
SBU-2	metal polyhedron (MO_4, MO_5 or MO_6) + tetrahedron (TO_4)	SBU-8	4 metal polyhedra (MX_5 or MX_6) + 4 tetrahedra (TO_4)
SBU-4	2 metal polyhedra (MO_5 or MO_6)+ 2 tetrahedra (TO_4) (most common)	SBU-9	4 metal octahedra (MX_6 or MO_6) + 5 tetrahedra (TO_4)
SBU-5	2 metal octahedra (MO_6) + 3 tetrahedra (TO_4)	SBU-10	4 metal octahedra (MO_6) + 6 tetrahedra (TO_4)
SBU-6	3 metal polyhedra (MX_5 or MX_6) + 3 tetrahedra (TO_4)	SBU-11	5 metal octahedra (MX_6) + 6 tetrahedra (TO_4)
SBU-7	3 metal polyhedra (MX_5 or MX_6) + 4 tetrahedra (TO_4)	SBU-12	4 metal octahedra (MO_4X_2) + 8 tetrahedra (TO_4)

*(M, metal; O, oxygen; X, halogen or any anion; T, tetrahedral centre: S, O, P, As, Se, etc.)

In the following sections, the structures of the most relevant silicates, phosphates, carboxylates and other related compounds will be described. This is followed by a more exhaustive survey of organically-templated metal sulphate architectures and their properties as well as the use of ionic liquids as potential solvents for the generation of open-framework structures.

1.2.2 Overview of interesting background materials

1.2.2.1 Silicates

The aluminosilicate zeolites of general formula $A_{x/n}$ $[Si_{1-x}Al_xO_2]$ mH_2O were the first class of nanoporous materials to be recognised, and as many as 100 different architectures based upon vertex-sharing $[SiO_4]$ and $[AlO_4]$ tetrahedra are known [48]. They are very interesting materials due to their exciting catalytic, adsorption and ion-exchange

properties. Besides the aluminosilicate zeolites, some synthetic analogues have been explored [49-51]. Most silicate structures are formed in the presence of alkali or alkali earth metals. Silicates containing transition metals have attracted interest for their properties and they have been reviewed by Rocha and co-workers [34]. Most of the synthetic and natural silicates present a three-dimensional structure. Among them, the best known transition metal silicate is ETS-10, $[Na,K]_2$-$[TiSi_5O_{13}]$□·xH_2O (Figure 1.1), built up from infinite chains of TiO_6 octahedra that link together sharing vertices. These chains are connected by SiO_4 tetrahedra forming a layer. Layers are interconnected by SiO_4 tetrahedra forming a three-dimensional network with channels of twelve-membered rings, in which Na^+/K^+ ions occupy the channels within this network [51, 52]. This material has been found to be suitable for supporting metals and for ion-exchange applications.

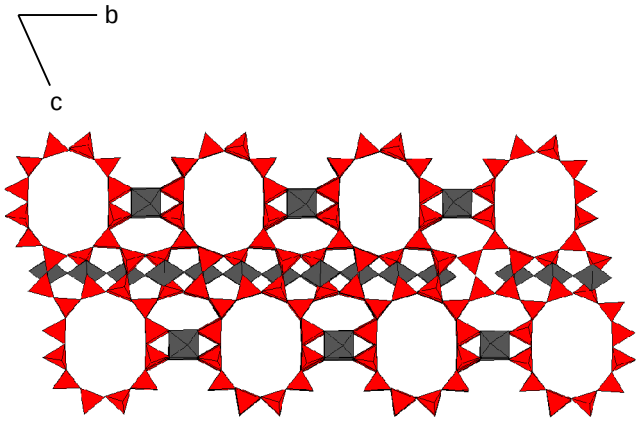

Figure 1.1. One layer of ETS-10 (SiO_4 tetrahedra, red; TiO_6 octahedra, grey)

Zirconosilicates, such as $[Na]_2[Zr_5Si_2O_{15}]\cdot nH_2O$ [53], obtained by mild hydrothermal conditions, as well as niobosilicates such as $[C_4N_2H_{11}]$ $[Nb_3SiO_{10}]$, which also exhibits ion-exchange properties [54], prepared in the presence of organic amines, have been reported.

One family of compounds that approaches the stability of the silicates is the aluminium phosphates, which are very close to the silicates in terms of structure and isoelectric nature of $[Al_{0.5}P_{0.5}O_4]^{4-}$ compared with $[SiO_4]^{4-}$.

1.2.2.2 Phosphates

Flanigen and co-workers discovered the microporous aluminophosphate $AlPO_4$-*n* (n refers to a structural type) at the beginning of the 1980s [32]. There have been attempts to prepare other phosphates, such as gallophosphates [55-58] but special attention has been

paid to the study of those containing transition metals due to their different valence states, their coordination numbers, their tendency to form metal-oxygen-metal bonds and their potential catalytic, electrical, optical and magnetic properties [59-62]. The formation of open-framework structures of iron phosphates was reported in 1986 [63]. Since then, the interest in this type of materials has risen and several reports of metal phosphates have been published. Although most of the metallophosphates are iron-based [64, 65], there are interesting examples of cobalt [66, 67], manganese [68, 69], vanadium [70] and nickel [71, 72] phosphates. Among them, cobalt is of particular interest owing to its ability to adopt tetrahedral coordination identical to that exhibited for silicon and aluminium in the formation of zeolites. This provides structural conditions for porosity with potential catalytic and magnetic properties. The molecular cobaltophosphate, $[C_6N_4H_{21}][Co(H_2PO_4)(HPO_4)_2]$ [73], which was prepared hydrothermally in the presence of tris(2-aminoethyl)amine, exhibits a structure built up from CoO_4 and H_2PO_4 tetrahedra linked by vertex-sharing to form a four-membered unit (Figure 1.2). The structure is stabilized by hydrogen bonding involving phosphate groups and protonated amine molecules. Magnetic measurements showed weak antiferromagnetic character.

One-dimensional phosphates are generally formed by MO_4 or MO_6 polyhedra connected to PO_4 tetrahedra to form chains. Magnetic measurements have shown antiferromagnetic behaviour for most of them. The simplest one-dimensional structure, that has been observed for only a few transition metal phosphates (V [74], Co [75], Cu [76] and Nb [77]), is formed by four-membered rings of metal-centered octahedra and PO_4 tetrahedra linked together to form one chain. The most common one-dimensional structure is that of the mineral tancoite, $[LiNa_2H][Al(PO_4)_2(OH)]$ [78], that has been found in phosphates of vanadium [79], iron [80] and titanium [81]. Its structure consists of chiral one-dimensional chains built up from corner-sharing TiO_6 octahedra bridged by PO_4^{2-} tetrahedra (Figure 1.3(a)).

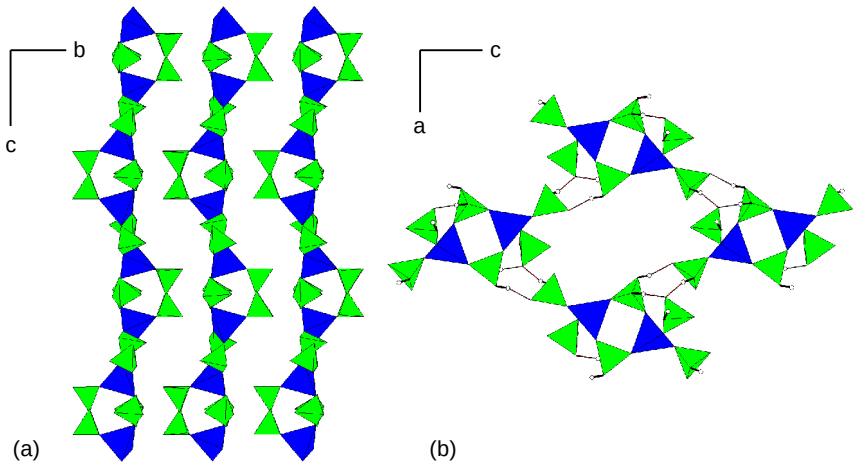

Figure 1.2. (a) Structure of $[C_6N_4H_{21}][Co(H_2PO_4)(HPO_4)_2]$ parallel to the [010] plane; (b) Four-membered unit built up from CoO_4 and H_2PO_4 tetrahedra (H_2PO_4 tetrahedra, green; CoO_4 tetrahedra, blue, hydrogen, white).

More structural diversity is found when two-dimensional structures are considered. This overview will focus on materials which exhibit magnetic interactions at low temperature. The layered ferrophosphate $[C_6N_4H_{21}][Fe^{III}_{3-x}Fe^{II}_xF_2(PO_4)(HPO_4)_2]_2$ (x≈1.5) displays an unusual structure [82] that consists of layers, formed by FeO_4F_2 octahedra and PO_4 tetrahedra linked through their vertices, separated by protonated amine molecules. In this structure, the Fe^{II} ions form the SBU-4s (secondary building unit constructed from two metal-centered octahedra and two tetrahedra). A remarkable feature of this structure is the presence of chains of Fe^{II}-O-Fe^{II} that are connected by Fe^{III} octahedra forming infinite two-dimensional sheets of Fe-O/F-Fe (Figure 1.3(b)). Magnetic studies indicate antiferromagnetic interactions. Layered cobaltophosphates, such as $[NH_3(CH_2)_2NH_3][Co(PO_4)]\cdot 0.5H_2O$ [67], in which the connection of CoO_4 tetrahedra defines chains which are connected into layers by PO_4 units, and manganophosphates, such as $[C_2H_{10}N_2][Mn_2(HPO_4)_3]\cdot H_2O$ [83], consisting of Mn-O-Mn infinite chains connected by phosphate units, have been reported. Both compounds show antiferromagnetic interactions.

The variety of three-dimensional phosphate structures has been reviewed by Cheetham and co-workers [19]. Three-dimensional structures constitute the dominant phosphate structural class and their three-dimensional structures are generally described making use of secondary building units (SBUs). Three-dimensional ferrophosphates, which constitute a very extensive and important family of compounds, have been reviewed by

Moore *et al*. [84, 85] Among them, $[AlFe_{24}(OH)_{12}(PO_4)_{17}(H_2O)_{24}]\cdot 51H_2O$, which contains twenty-four-membered ring channels, might be highlighted for its catalytic applications.

A variety of compounds involving mixed-metal phosphates with manganese have been reported since the manganese gallophosphate MnGPO-1 was first prepared [86]. The structure of a three-dimensional manganese phosphate is displayed in Figure 1.4(a), and consists of an infinite Mn-O-Mn framework that contains ammonium cations in the cavities [76]. Magnetic susceptibility measurements point to ferrimagnetic ordering. Another example is that of the manganese gallium phosphate of formula $Mn_3(H_2O)_6Ga_4(PO_4)_6$, which was synthesized under hydrothermal conditions. The crystal structure consists of a central $Mn(H_2O)_4O_2$ octahedron which links to two $Mn(H_2O)_2O_4$ octahedra at trans edges. These clusters reside in tunnels formed by GaO_5 trigonal pyramids and PO_4 tetrahedra (Figure 1.4(b)).

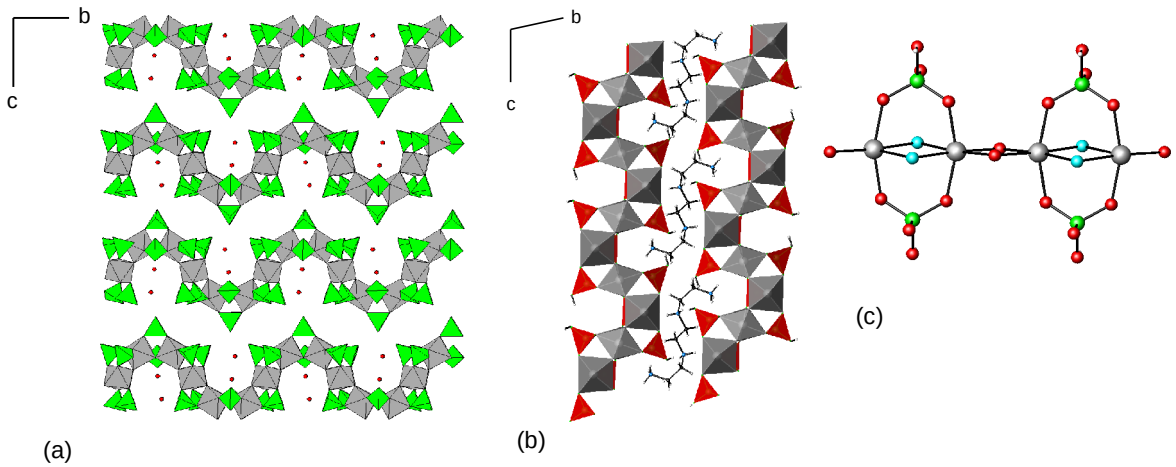

Figure 1.3. (a) Spirals of TiO_6 octahedra linked through PO_4 tetrahedra along [010] direction (TiO_6 octahedra, grey; PO_4 tetrahedra, green; O atoms, red); (b) Layered structure of $[C_6N_4H_{21}][Fe^{III}_{3-x}Fe^{II}_xF_2(PO_4)(HPO_4)_2]_2$ (x≈1.5) (FeO_4F_2 octahedra, grey; PO_4 tetrahedra, red; C, black; N, blue; H, white) (c) Connectivity between two building units (SBU-4s) (Fe, grey; P, green; O, red; F, blue).

The three-dimensional structures of nickel phosphates [87, 88], vanadium phosphates [89, 90] and cobalt phosphates [91-93] have also been reported. Very recently, the structure of the first four organically templated tetravalent uranium phosphates was reported [94]. All four materials display unique dimer-structured topologies with various

dimensionalities, in which U^{4+} ions are located in the center of bicapped trigonal prisms that link by their edges to form dimeric units.

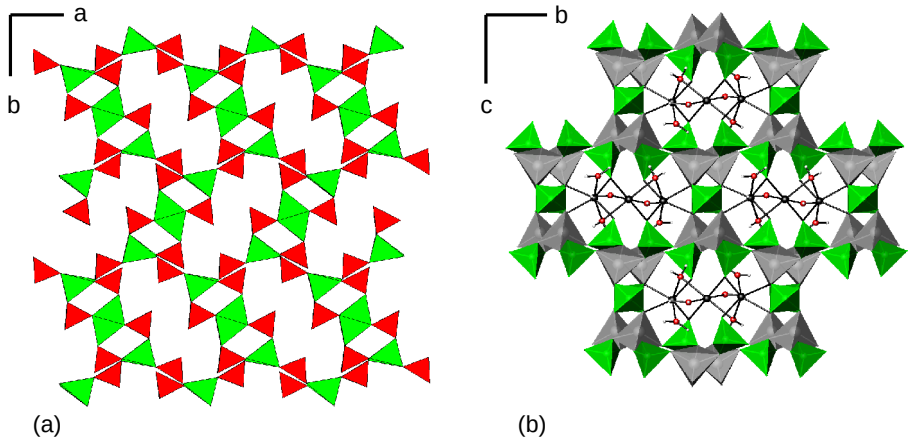

Figure 1.4. (a) Polyhedral representation of $(NH_4)[Mn_4(PO_4)_3]$ showing edge-shared MnO_5 polyhedra forming Mn-O chains, that linked through PO_4 tetrahedra to form a layer (MnO_5 polyhedra, green; PO_4 tetrahedra, red) (b) Polyhedral representation of $Mn_3(H_2O)_6Ga_4(PO_4)_6$, in which Mn centers reside in the tunnels built of GaO_5 trigonal pyramids and PO_4 tetrahedra (Mn, black; O, red; GaO_5 trigonal pyramids, grey; PO_4 tetrahedra, green).

1.2.2.3 Metal carboxylates

Metal carboxylates, which include mono- and dicarboxylates, oxalates and hybrid structures, have become an important family in the last years not only because they form open-framework structures resulting from the presence of the carboxylate function itself, but also because the carboxylate group acts as a linker between inorganic moieties [20]. Some of the carboxylates exhibit novel adsorption and magnetic properties [95, 96]. Recently a review on the structure and properties of various families of metal carboxylates has been published [20].

Reports of open-framework monocarboxylates structures are limited. An interesting layered coordination polymer, $[(Cu_2(OOCCH_3)_4)_3(tpt)_2]\cdot 2MeOH$ (tpt=tris(3-aminopropyl amine) [97], in which copper acetate dimers are bridged by tpt groups exhibiting a large-pore structure, has been reported. A three-dimensional framework, $[Ba_9(MeCOO_2)_{14}](ClO_4)_4$, has also been synthesised [98]. The structure is based on Ba_9 clusters that are connected by acetate and perchlorate bridges. Reports on the synthesis and

crystal structure of microporous metal hydroxyacetates [99, 100] as well as heteronuclear rare-earth trichloroacetates [101, 102] have been published.

Dicarboxylates have also been used for the synthesis of novel frameworks with zero-, one-, two- and three-dimensionalities [103, 104]. Preparation of three-dimensional carboxylates based on metals has become an interesting area of study due to their potential applications. Ferey and co-workers have extensively studied these systems. Preparation of metal-organic frameworks (MOFs) has been achieved by copolymerization of molecular building blocks with organic linkers in a polar solvent under mild conditions to form stable porous structures [105, 106].

Recently, a three-dimensional nickel fumarate with a three-dimensional open-framework, $[Ni_3(OH)_2(OOC\text{-}C_2H_2\text{-}COO)(H_2O)_4]\cdot 2H_2O$, has been synthesized [107]. The structure consists of chains of nickel octahedra connected by fumarate ions to form a three-dimensional network, in which water molecules reside in cavities (Figure 1.5(a)). Also the synthesis of cobalt dicarboxylates with interesting magnetic properties has been reported. For instance, the synthesis of $Co_5(OH)_2(C_4H_4O_4)_4$ which exhibits ferromagnetic behaviour, has been published [108]. The three-dimensional structure is formed from layers of edge-sharing CoO_6 octahedra pillared by succinate ions (Figure 1.5(c)). The first series of hydrothermally prepared rare-earth carboxylates with three-dimensional open-framework structures was reported in 1998 [109]. The structure of $[Ln(H_2O)]_2[OOC(CH_2)_3COO]_3\cdot 4H_2O$ (Ln=Nd, Pr, Sm, Eu, Gd, Dy, Ho, Y) consists of chains of edge-sharing NdO_9 polyhedra, linked together by $(OOC(CH_2)_3COO)$ chains forming channels parallel to the rare-earth chains (Figure 1.5(b)).

Many metal oxalate structures, where the oxalate ions act as a rigid bidentate ligand facilitating the formation of extended structures, have been reported. Transition metal oxalates constitute interesting materials because they can incorporate magnetic centers into the structure. Some examples of these structures are shown in Figure 1.6. The first of these three structures to be described, (Figure 1.6(a)) consists of a two-dimensional copper network of formula $[Cu_2(bpym)(ox)Cl_2]_n$ (bpym=2,2-bipyrimidine) built up from alternating bpym and oxo-bridged copper chains connected through chloride ligands. Magnetic measurements showed antiferromagnetic interactions [110]. The crystal structure of the iron compound $[Fe(C_2O_4)(C_{10}H_8N_2)]_n$ is depicted in Figure 1.6(b). It consists of infinite zig-zag chains built up from $[Fe(C_2O_4)(bipy)]$ units linked by C_2O_4 ligands [111]. The manganese analogue is isostructural [112]. In $(3\text{-}MePyH)_{2n}[Mo_2O_4(C_2O_4)Cl_2]_n$ (Figure

1.6(c)), the bisbidentate oxalate anion acts as a bridge between two dinuclear $[Mo_2O_4]^{2+}$ subunits which link together to form a chain [113].

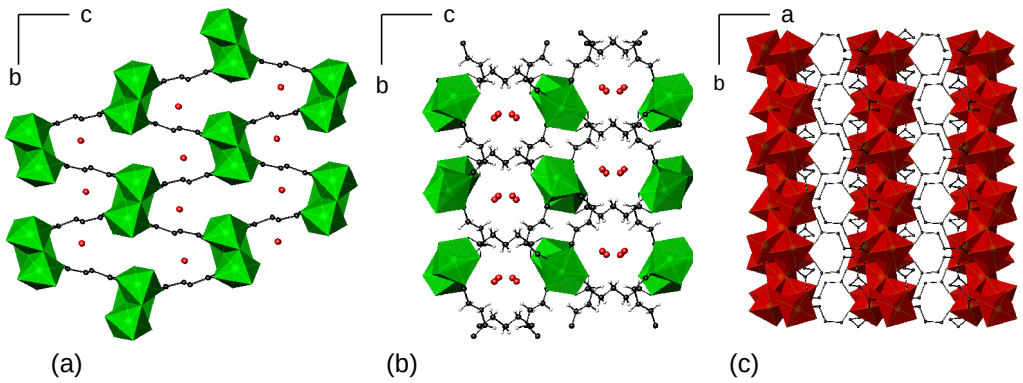

Figure 1.5. (a) NiO_6 chains of $[Ni_3(OH)_2(OOC\text{-}C_2H_2\text{-}COO)(H_2O)_4]\cdot 2H_2O$ along [100] (NiO_6 octahedra, green; O, red; fumarate anion, black); (b) Structure of $[Ln(H_2O)]_2[OOC(CH_2)_3COO]_3\ 4H_2O$ (Ln=Nd, Pr, Sm, Eu, Gd, Dy, Ho, Y) showing the channels parallel to [100] (NdO_9 polyhedra, green; O, red; C chains, black); (c) Layers of CoO_6 octahedra running parallel to [100] in $Co_5(OH)_2(C_4H_4O_4)_4$ (CoO_6 octahedra, red; succinate chains, black).

Two dimensional mixed-metal oxalates with chromium centers which exhibit ferromagnetically-ordered spins were reported by Tamaki *et al* [114]. Mixed-valence oxalates with general formula $A[M^{II}M^{III}(ox)_3]$ (A=monocation; M^{II}=Co, Ni, Fe, Cu, Zn, Mn; M^{III}=Co, Cr, Fe) (Figure 1.7(a)) also exhibit magnetic interactions at low temperature [115, 116].

There is an increasing interest in lanthanide carboxylates for their ability to form porous materials. Some hydrated lanthanide oxalates [117, 118] as well as rare-earth oxalates [119, 120] possessing cavities and channels [121, 122] have been prepared and characterized. The use of the oxalate ligand has provided interesting materials with two- and three-dimensional structures [123, 124]. The two structures represented in Figure 1.7 constitute examples of mixed-metal rare-earth metal oxalates with zeolite-like properties. $La(H_2O)_2M(C_2O_4)_2\cdot H_2O$ (M=K, NH_4) (Figure 1.7(a)) displays a layered structure, in which layers are formed by four-membered rings $[La(C_2O_4)]_4$ [125]. The crystal structure of $Y(H_2O)Cs(C_2O_4)_2$ (Figure 1.7(b)) consists of layers of corrugated planes of yttrium atoms linked by the oxalate groups, with the caesium ions intercalated between them [126].

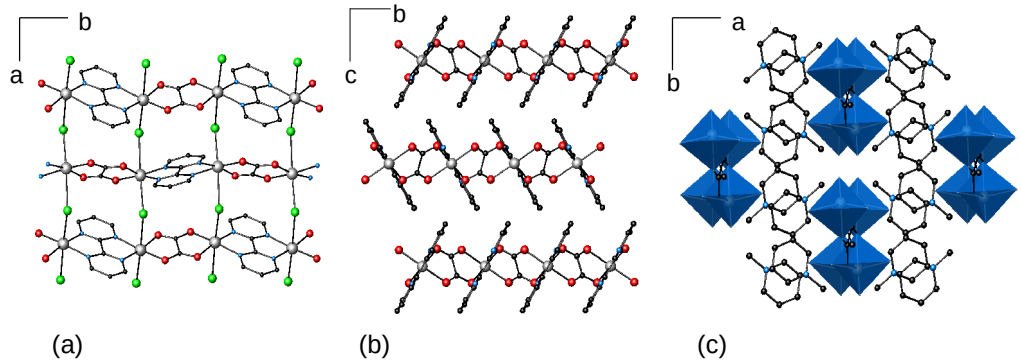

Figure 1.6. (a) One layer of $[Cu_2(bpym)(ox)Cl_2]_n$ along the *c*-axis (Cu centers, grey; Cl, green; O, red; C, black; N, blue); (b) Chains of $[Fe(C_2O_4)(C_{10}H_8N_2)]_n$ along *b*-axis (Fe, grey; O, red; C, black; N, blue); (c) Structure of $(3\text{-}MePyH)_{2n}[Mo_2O_4(C_2O_4)Cl_2]_n$ (MoO_6 octahedra, blue; C, black; N, blue).

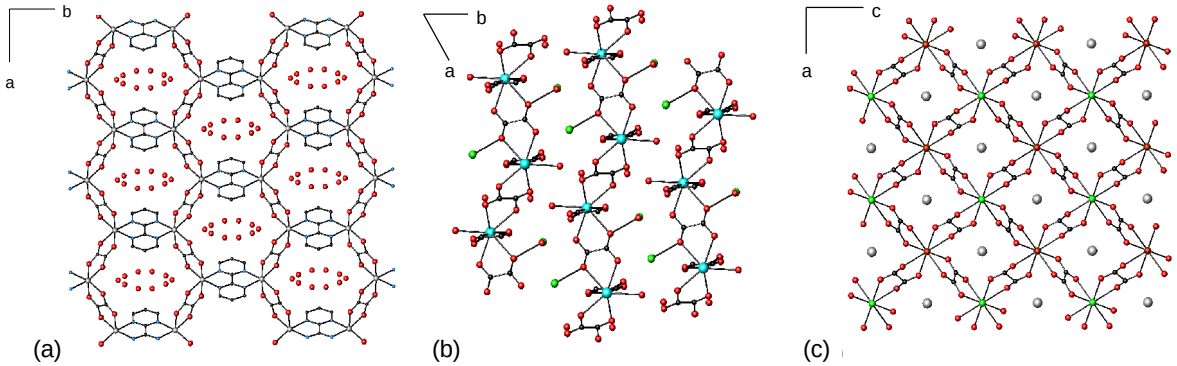

Figure 1.7. (a) View of a 2D layer in $[Cp_2Z]$ $[M^{II}M^{III}(ox)_3]$ (Z=Co, Fe, Mn; M^{II}=Fe, Mn, Co, Cu, Ni; M^{III}=Cr, Fe) (M^{II}-M^{III}, grey; O, red; C, black; N, blue); (b) Layered structure of $La(H_2O)_2M(C_2O_4)_2{\cdot}H_2O$ (M=K, NH_4) along the *c*-axis (C, black; M, green; La, blue; O, red) (c) One layer of $Y(H_2O)Cs(C_2O_4)_2$ along *b*-axis (Y, green; C, black; O, red; Cs, grey).

Organoammonium ions have been used for the synthesis of uranyl oxalates [127] and rare-earth oxalates with open-framework architectures possessing layers with honeycomb-like apertures [128, 129].

1.2.2.3.1 Hybrid Phosphato- and Arsenato-oxalates

A large number of hybrid oxalates formed by introducing anionic building units into the structure, such as phosphate or arsenate, have been synthesised and their structure reported. Two illustrative examples will be described as those materials have recently been reviewed [20]. $[NH_3(CH_2)_3NH_3][Mn_2(HPO_4)_2(ox)(H_2O)_2]$ [130] displays a three-

dimensional structure formed by hybrid layers, in which the oxalate is part of the layer. The protonated amine molecules reside in the channels of twelve-membered rings (Figure 1.8(a)). In contrast, in $[Fe_2(HPO_4)_2(ox)(H_2O)_2]\cdot H_2O$ [131], metal-phosphate layers are pillared with the oxalate ions (Figure 1.8(b).

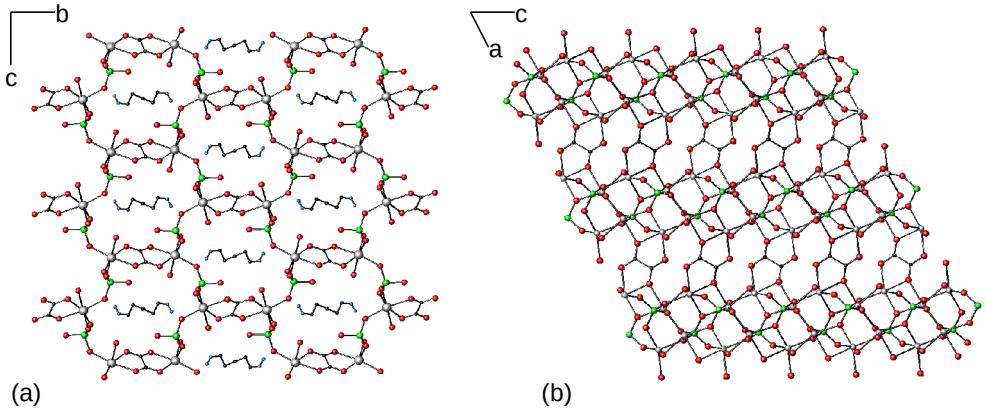

Figure 1.8. (a) Structure of $[NH_3(CH_2)_3NH_3][Mn_2(HPO_4)_2(ox)(H_2O)_2]$ showing the 12-membered apertures (Mn, grey; P, green; O, red; C, black; N, blue); (b) Structure of $[Fe_2(HPO_4)_2(ox)(H_2O)_2]\cdot H_2O$ (Fe, grey; P, green; O, red; C, black).

1.2.2.4 Other related structures containing oxy-anions

In comparison with the huge effort that has been spent on silicates and phosphates, germanates and borates remain relatively unexplored. One interesting family that has been reported is that of the boron sodalite, $Zn_4O(BO_2)_6$ [132], whose structure is built up from BO_4 tetrahedra.

Germanates of composition $M_{4-x}H_xGe_7O_{16}\cdot nH_2O$ have been known for years [133]. The structure consists of edge- and face-sharing GeO_6 octahedra connected to each other *via* GeO_4 tetrahedra. Few transition metal germanates have been synthesised in the presence of an organic amine. Germanates containing niobium [134, 135] and zirconium [136] represent some of the few examples. For instance, the structure of $[C_6N_2H_{18}][Ge_{2.2}Nb_{0.8}O_{6.8}F_{1.2}]$ [134] consists of a three-dimensional framework containing two types of channels defined by ten-membered rings and one channel by eight-membered rings of NbO_5F octahedra and GeO_4 tetrahedra. The protonated amine is located at the centre of the channels of ten-membered rings (Figure 1.9(a)).

Open-framework arsenates have also been studied as analogues of the lighter phosphate congener but precautions are required when handling it due to its toxicity. Arsenates are typically obtained under hydrothermal conditions from arsenic acid, a metal source and inorganic cations or organic amines. In terms of their magnetic properties, $[Fe(AsO_4)F]\cdot NH_4$ constitutes an interesting example of this family of compounds, which exhibits a transformation from a two-dimensional structure into a porous three-dimensional network with channels of six-membered rings of formula $[Fe(AsO_4)]$ after heating up to 798 K [137, 138]. This structure shows strong antiferromagnetic interactions.

A small number of amine-templated metal selenites and selenates have also been reported. Since the synthesis of the organically-templated selenite $[CN_3H_6]_4[Zn_3(SeO_3)_5]$ [139], which possesses a layered structure formed by the linking of $Zn_3Se_2O_{12}$, and the three-dimensional iron and zinc ones [140, 141], a range of amine-templated selenites with one- [142], two- [143, 144] and three-dimensional [145] structure have also been published.

Only recently it has been possible to obtain open-framework metal selenates which were not accessible before due to the instability of the Se(VI) in a basic medium. One-dimensional selenates, such as the zinc selenate $[Zn(SeO_4)(phen)(H_2O)]$ [146], two-dimensional structures, such as the one displayed by $[C_4N_2H_{14}][La_2(SeO_4)_4]\cdot H_2O$ [147], and three-dimensional selenates, such as $[C_2N_2H_{10}][La_2(SeO_4)_4(H_2O)_3]\cdot H_2O$ [148] have been prepared in an acid medium under hydrothermal conditions. The selenite system is of particular interest because of the possibility of forming mixed-anion compounds containing both SeO_3^{2-} and SeO_4^{2-}. One example belonging to this system is $Th(SeO_3)(SeO_4)$ [149], which adopts a three-dimensional structure formed from ThO_9 tricapped trigonal prisms, trigonal pyramidal selenite, SeO_3^{2-}, and tetrahedral selenate, SeO_4^{2-}(Figure 1.9(b)).

1.3 Organically-templated metal sulphates

1.3.1 Oxy-anion of sulphur as a building-unit

In recent years, there has been a growing interest in the study of the oxy-anion of sulphur as a building unit in the synthesis of open-framework structures with metal-oxygen polyhedra. Sulphates form stable structures with relatively low valence metal ions, although the S-O bonds are less covalent than the corresponding Si and P ones, and therefore polysulphates units are less likely to be formed. A wide variety of open-framework sulphate structures with different dimensionalities has been synthesised. The majority of these

materials have been prepared under hydrothermal conditions in the presence of organic amines, employing fluoride ions. Rao and co-workers recently reviewed organically-templated metal sulphates. In the following section, the structure and magnetic properties of one-, two- and three-dimensional sulphates will be discussed.

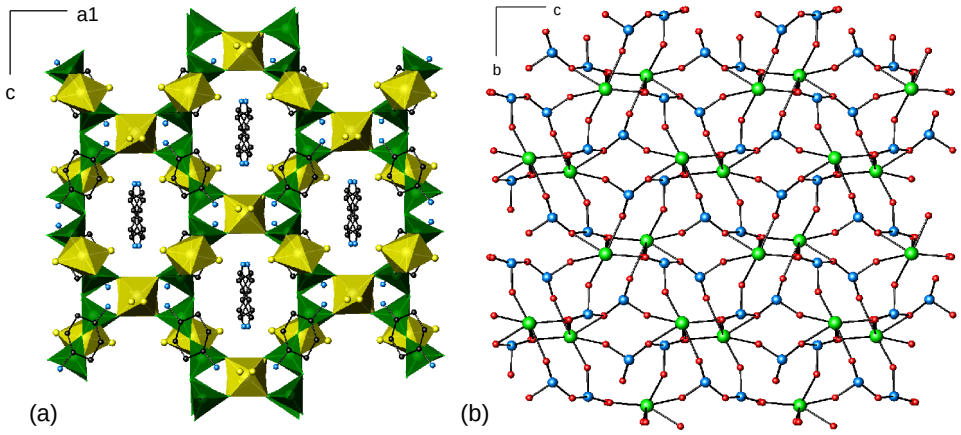

Figure 1.9. (a) Polyhedral representation of the framework structure of $[C_6N_2H_{18}][Ge_{2.2}Nb_{0.8}O_{6.8}F_{1.2}]$ (NbO_5F octahedral, yellow; GeO_4 tetrahedra, green); (b) Extended structure of $Th(SeO_3)(SeO_4)$ (Th, green; Se, blue; O, red).

1.3.2 One Dimensional Sulphates

Since the works of Rao and co-workers [150] in the synthesis of a family of organically-templated metal sulphates a large variety of sulphates possessing one-dimensional structures have been described and a wide diversity of chain topologies have been observed, many of which are similar to the phosphate structures.

The first members of this family are four linear cadmium sulphates with the linarite-like chain structure [150, 151]. The structure of these compounds is built up of infinite chains of $[CdX_2SO_4]^{2-}$ (X=Cl, Br) along [010], which are analogous of those found in the mineral linarite [152], in which CdX_4O_2 octahedra share edges in a *trans* fashion through their X ions, with the sulphate tetrahedra linked to the chains as a symmetrical bridge (Figure 1.10(a)). One-dimensional chains are arranged parallel to one another to form a layer-like arrangement, with the protonated amine molecules placed between the layers, which held them together in a hydrogen-bonded system. The same type of chain has been identified in the iron sulphate $[Fe_2O(OH)(SO_4)][C_5H_4NCO_2]$ [153].

The simplest chain structure is a single-stranded chain that was found in $[Zn(SO_4)(H_2O)_2(C_{10}N_2H_8)]$ [154], that is anologous to the mineral chalcanthite [155]. In the zinc sulphate compound the chains are built up of $[ZnO_4N_2]$ octahedra and SO_4 tetrahedra that link together sharing vertices (Figure 1.10(b)). Chains are Zn-O-S-O-Zn like, in which one sulphate tetrahedron serves to connect adjacent Zn centres. The two nitrogen atoms of the coordination sphere of Zn are provided by the 2,2'-bypiridine ligand. A similar chain structure has been found in a vanadium sulphate, $[NH_2(CH_2)_4NH_2][(VO)(H_2O)(SO_4)_2]$, consisted of alternating $VO_5(H_2O)$ octahedra bridged by SO_4 tetrahedra in a *trans* fashion to form a simple one-dimensional chain along the *a*-axis (Figure 1.10(c)) [156]. Magnetic measurements reveal weak antiferromagnetic interactions.

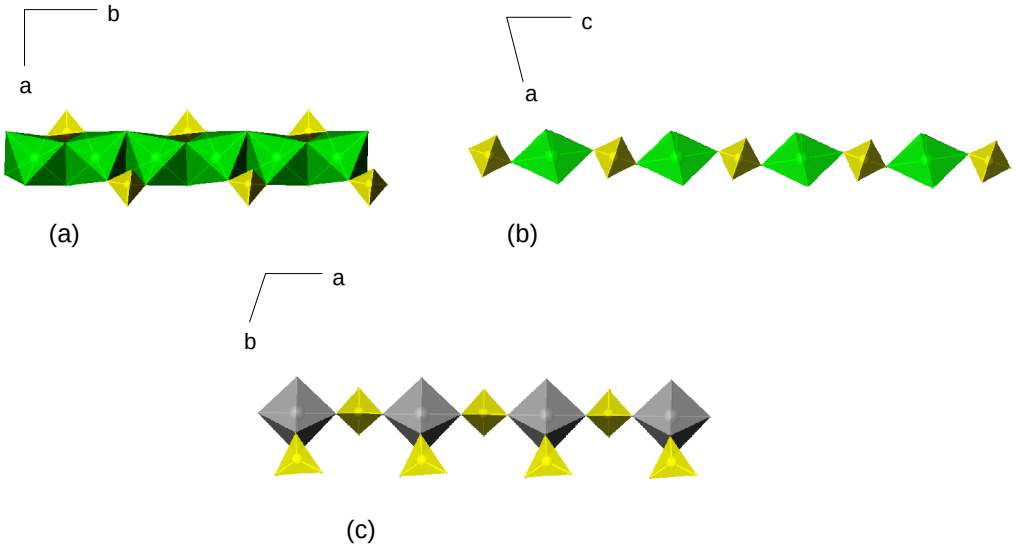

Figure 1.10. (a) Linarite-type chain in which CdX_4O_2 octahedra link together sharing edges (CdX_2O_4 octahedra, green; SO_4 tetrahedra, yellow); (b) Single-stranded chain for $[Zn(SO_4)(H_2O)_2(C_{10}N_2H_8)]$ (ZnN_4O_2 octahedra, green; SO_4 tetrahedra, yellow); (c) Stranded chain of alternating $VO_5(H_2O)$ octahedra and SO_4 tetrahedra ($VO_5(H_2O)$, green; SO_4 tetrahedra, yellow).

A number of vanadium sulphates with different chain topologies have been published [156, 157]. $[NH(CH_2)_6NH][(VO)_2(OH)_2(SO_4)_2]\cdot H_2O$ [156] exhibits the Kröhnkite-type chain [155], which has also been observed in open-framework phosphates [158, 159] and selenates [160]. The structure of this compound consists of linear chains of V_2O_8 dimers of square-pyramids connected by corner-sharing SO_4 tetrahedra, forming four-membered rings along [100] (Figure 1.11(a)). The study of its magnetic properties shows

weak antiferromagnetic interactions. A similar structure has been found in the iron sulphate $[C_6N_2H_{18}]_{0.5}[Fe(SO_4)_2(H_2O)_2]$, in which two SO_4 tetrahedra share corners with adjacent FeO_6 octahedra, resulting in an infinite chain containing four-membered rings [161]. The tancoite chain structure [162] has been found in the vanadium sulphate $[NH_3(CH_2)_2NH_3][(V(HO)(SO_4)_2]\cdot H_2O$ [156] (Figure 1.11(c)) and in the gallium vanadium sulphate $[C_2H_{10}N_2]_4[GaV_3(SO_4)_8(OH)_4]\cdot 4H_2O$ [157]. Linear chains are built from MO_6 octahedra which link together sharing vertices forming a zig-zag chain, and bridging OH and SO_4 tetrahedra (Figure 1.11(b)). Two iron sulphate compounds of composition $[C_2N_2H_{10}][Fe(SO_4)_2(OH)]\cdot H_2O$ [161] and $[C(NH_2)_3]_2[FeF(SO_4)_2]$ [163] have also been found to possess the tancoite-type chain. $[C(NH_2)_3]_2[FeF(SO_4)_2]$ exhibits antiferromagnetic interactions. $[C_4N_2H_{12}][Fe_2(SO_4)_3(OH)_2(H_2O)_3]\cdot H_2O$ displays a structure containing chains in which SO_4 groups have been partially substituted by two water molecules that can be considered as a derivative of the tancoite-type [161]. $[NH_2(CH_2)_4NH_2][FeF_3SO_4]$ [163] contains the $[FeF_3SO_4]^{2-}$ chain which is the basic structural motif of butlerite [164] and comprises FeF_4O_2 octahedra sharing vertices with their neighbours through fluorine with bridging SO_4 tetrahedra. The individual chains are held together by hydrogen-bond interactions involving protonated amine molecules (Figure 1.12).

Ferrinatrite-type chains [165], which have been previously observed in iron [166] and vanadium [167] arsenates, were identified in the iron sulphate $[C_2N_2H_{10}]_{1.5}[Fe(SO_4)_3]\cdot 2H_2O$ [161]. Three SO_4 tetrahedra share corners with the adjacent FeO_6 octahedra resulting in an infinite chain along [001] (Figure 1.13(a)). $[C_6N_2H_{18}]_{0.5}[Fe_2(SO_4)_3(H_2O)_4(OH)]\cdot H_2O$ [161] shows the same connectivity between the metal centered octahedra as that in the tancoite chain, but pairs of linked octahedra are separated by a bridging SO_4 tetrahedron *via* vertex-sharing (Figure 1.13(b)). This structure has also been observed in copiapite [168].

The preparation of organically-templated metal sulphates has been extended to the synthesis of a one-dimensional sulfated α-molybdena $[C_5H_{14}N_2][(MoO_3)_3(SO_4)]\cdot H_2O$ under hydrothermal conditions [169]. The structure consists of chains of $[(MoO_3)_3(SO_4)]_n^{2n-}$, with a structure analogous to that of α-molybdena, in which MoO_6 octahedra are connected by shared edges in a zig-zag fashion (Figure 1.14).

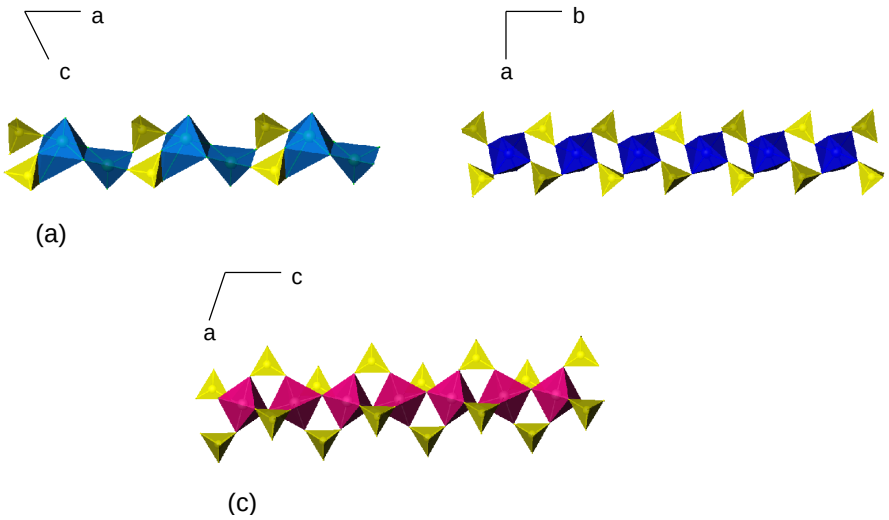

Figure 1.11. (a) Kröhnkite-type chain in $[NH(CH_2)_6NH][(VO)_2(OH)_2(SO_4)_2]\cdot H_2O$ (VO_5 square-pyramids, blue; SO_4 tetrahedra, yellow); Chain in $[C_4N_2H_{12}][Fe_2(SO_4)_3(OH)_2(H_2O)_3]\cdot H_2O$ derivated from the tancoite-type chains (FeO_6 octahedra, blue; SO_4 tetrahedra, yellow); (c) Tancoite-type chain for $[NH_3(CH_2)_2NH_3][(V(HO)(SO_4)_2]\cdot H_2O$ (VO_6 octahedra, pink; SO_4 tetrahedra, yellow).

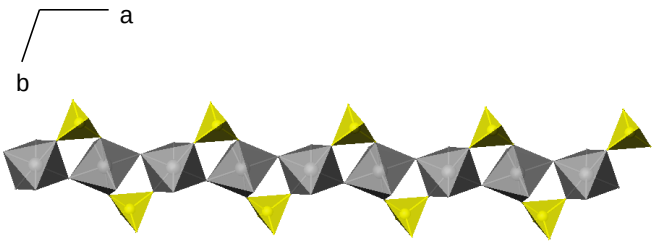

Figure 1.12. Butlerite-type chain for $[NH_2(CH_2)_4NH_2][FeF_3SO_4]$ in which $[FeF_4O_2]$ octahedra share vertices to form an individual chain with SO_4 tetrahedra acting as a bridge (FeF_4O_2 octahedra, grey; SO_4 tetrahedra, yellow).

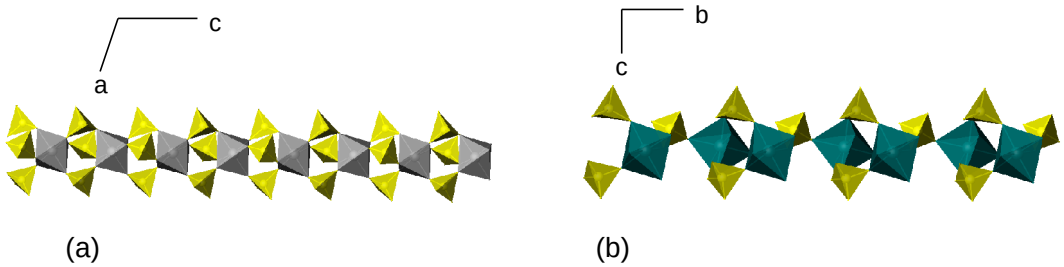

Figure 1.13. (a) Linear chain for $[C_2N_2H_{10}]_{1.5}[Fe(SO_4)_3]2H_2O$ (FeO_6 octahedra, grey; SO_4 tetrahedra, yellow); (b) Copiapite-type chain for $[C_6N_2H_{18}]_{0.5}[Fe_2(SO_4)_3(H_2O)_4(OH)]\cdot H_2O$ (FeO_6 octahedra, green; SO_4 tetrahedra, yellow).

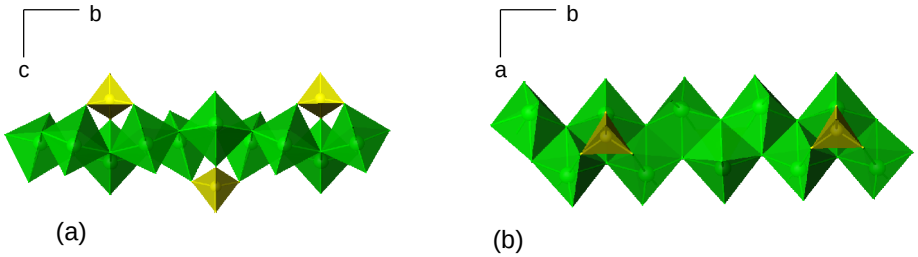

Figure 1.14. Chain in $[C_5H_{14}N_2]](MoO_3)_3(SO_4)]\cdot H_2O$ viewed along (a) [100] direction; (b) along [-101] direction (MoO_6 octahedra, green; SO_4 tetrahedra, yellow).

It is possible to obtain double-stranded chains as it has been found in an iron sulphate of formula $[NH_3(CH_2)_2NH_3][FeF_3(SO_4)]$ [163]. The structure comprises alternating FeF_3O_3 octahedra and SO_4 tetrahedra, forming a ladder with four-membered rings running along the crystallographic *a*-axis, in which each octahedron shares vertices with three bridging ligands (Figure 1.15). The formation of this type of ladders in the metal sulphate family is quite unusual and, to date, there are not many reports in the literature [170]. As it has been observed for zinc phosphates, these chains could give rise to higher dimensional structures [171]. Magnetic measurements demonstrate weak antiferromagnetic interactions at low temperature.

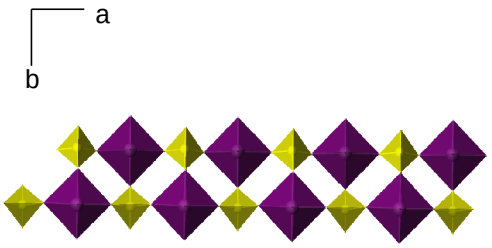

Figure 1.15. Double-stranded chain in $[NH_3(CH_2)_2NH_3][FeF_3(SO_4)]$ to form ladders (FeF_3O_3 octahedra, purple; SO_4 tetrahedra, yellow).

One-dimensional chains have been found in several uranium sulphates, in which a common chain topology has been identified. These include the uranium sulphates USO-1 [172], USO-3 [173], USO-9 [174], USO-11 [175], USO-18 [176], USO-22 [177] and USO-26 [178] (USO = $[UO_2(SO_4)_2]$ or $[UO_2(H_2O)(SO_4)_2]$) as well as $[Mn(UO_2)(SO_4)_2(H_2O)]\cdot 4H_2O$ [179] and $[(UO_2)(H_2PO_4)_2(H_2O)](H_2O)_2$ [180]. The structure is built up of anionic chains $[UO_2(H_2O)(SO_4)_2]^{2-}$, in which each UO_7 polyhedron shares vertices with four sulphate tetrahedra as shown in Figure 1.16(a). The uranium sulphates

$[N_2C_{10}H_{10}][UO_2(SO_4)_2]\cdot H_2O$ (USO-6) and $[N_2C_6H_{18}][(UO_2)_2(H_2O)_3(SO_4)_3]$ (USO-7) contain chains based upon a $[UO_2(SO_4)_{3/3}]$ backbone [174]. USO-6 one-dimensional structure consists of double-chains of UO_7 polyhedra connected through bridging SO_4 tetrahedra forming four-membered rings in which each polyhedron shares an edge with a terminal SO_4 tetrahedra (Figure 1.16(b)). Each chain in USO-7 exhibits the same basic topology as USO-6, but terminal SO_4 tetrahedra are linked to UO_7 polyhedra sharing one vertex (Figure 1.16(c)).

USFO-2 (USFO = $[UO_2F_x(SO_4)_2$ or $UO_2F(H_2O)(SO_4)_2]$) displays a chain structure unprecedented in uranium chemistry in which bridging fluorides connect adjacent uranium polyhedra through a shared edge to form dimers, which are in turn connected *via* sulphate groups (Figure 1.17(a)) [181]. Each of the uranium centres shows pentagonal bypiramidal coordination geometry. $[UO_2F_2(SO_4)_2]^{2-}$ chains stack along the [100] and [001] directions, with protonated amine cations located between them.

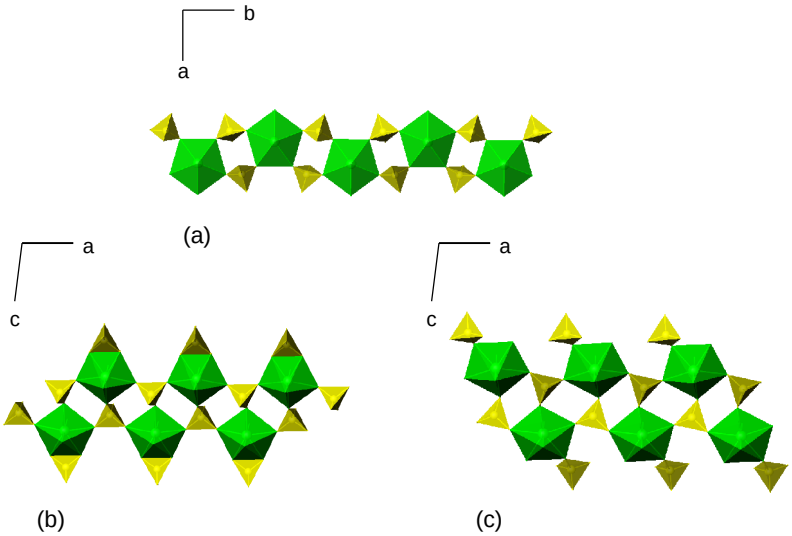

Figure 1.16. (a) One-dimensional $[UO_2(H_2O)(SO_4)_2]^{2-}$ chains; (b) One-dimensional $[UO_2(SO_4)_2]^{2-}$ chains in USO-6; (c) One-dimensional $[UO_2(H_2O)(SO_4)_2]^{2-}$ in USO-7.

The first organically-templated one-dimensional lanthanum sulphate $[C_4N_3H_{16}][La(SO_4)_3]\cdot H_2O$ was prepared under hydrothermal conditions by Xing and co-workers [182]. The structure consists of infinite-linear $[La(SO_4)_3]_n^{3-}$ chains of LaO_{12} polyhedra which share faces and SO_4 tetrahedra connected to the chains by sharing both corners and edges (Figure 1.17(b)).

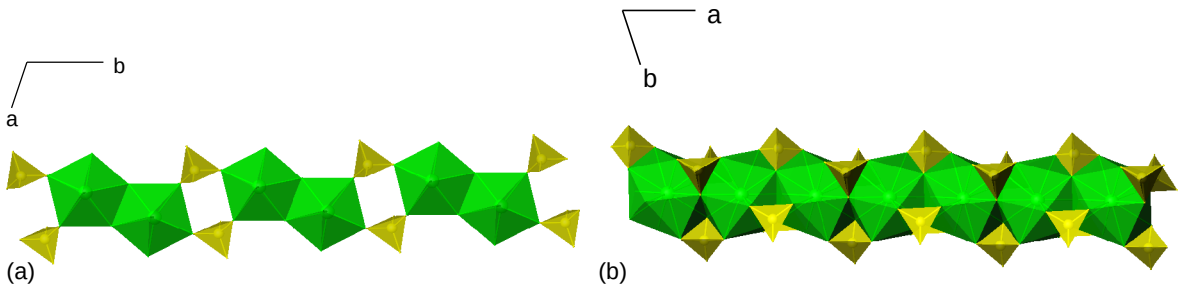

Figure 1.17. (a) $[UO_2F_{2/2}F_{1/1}(SO_4)_{2/2}]^{2-}$ chains in USFO-2 (UO_7 polyhedra, green; SO_4 tetrahedra, yellow); (b) $[La(SO_4)_3]_n^{3-}$ chains in $[C_4N_3H_{16}][La(SO_4)_3]\cdot H_2O$ (LaO_{12} octahedra, green; SO_4 tetrahedra, yellow).

The synthesis of two mixed transition metal/rare-earth sulphates with general formula $YM(OH)_3(SO_4)$ (M=Ni, Cu) has been described by Jacobson *et al.* [183] under hydrothermal conditions. These compounds are of interest because conductivity has been observed in some yttrium copper oxides containing sulphates [184]. The structure consists of MO_6 octahedra and SO_4 tetrahedra linked together to form complex chains $[M(OH)_3(SO_4)]$ and YO_8 polyhedra that are connected to MO_6 octahedra.

1.3.3 Two-Dimensional Sulphates

Organically-templated layered metal sulphates are not that abundant in comparison to one-dimensional sulphates, with the exception of the Kagome layers which are the dominant class among the two-dimensional sulphates and that will be discussed later on in this section.

Rao and co-workers obtained the layered organically-templated metal sulphate $[C_4N_2H_{12}][Cd_3Cl_{10}(SO_4)_2(H_2O)]\cdot 3H_2O$ by the reaction of piperazinium sulphate with cadmium chloride [150]. Its structure consists of two parallel chains built up of $CdCl_3O_3$, $CdCl_3O_2$ and SO_4 units connected *via* $CdCl_6$ octahedra to form an anionic strip-like quasi layer with apertures of eight-membered rings, in which the strips are held together by hydrogen-bond interactions (Figure 1.18(a)). This unusual structure was previously found in an open-framework cobalt phosphate [185].

There are few examples of layered iron sulphates obtained under hydrothermal conditions. Among them, the layered $[NH_3(CH_2)_2NH_2(CH_2)_2NH_3][Fe_2F_2(SO_4)_2(H_2O)_2]$ [163] can be considered to be formed from butlerite-type chains and it displays a structure

similar to that of the layered fluorophosphates ULM-10 [186]. The structure is constructed from FeF_2O_4 and $FeF_2O_2(H_2O)_2$ octahedra connected by sharing vertices to form infinite chains that link to one another *via* SO_4 tetrahedra to produce a porous layer containing an eight-ring window (Figure 1.18(b)). The diprotonated ethylenediamine cations occupy the interlayer sites and interact with the inorganic sheets through hydrogen-bonds. Magnetic susceptibility measurements reveal a complex behaviour which suggests the presence of metamagnetism. In the mixed metal valence sulphate $[NH_2(CH_2)_4NH_2][Fe_2^{III}Fe_3^{II}F_{12}(SO_4)_2(H_2O)_2]$, iron octahedra share corners to form infinite chains which are linked by a trimer of edge-sharing octahedra to form a layer with apertures of ten-membered rings [187]. Magnetic measurements reveal a ferrimagnetic transition and a transition to a canted antiferromagnetic state at low temperature.

The organically-templated layered nickel sulphate, $[C_4N_2H_{12}][Ni_3F_2(SO_4)_3(H_2O)_2]$, synthesised using piperazine as structure-directing agent [188], displays a structure constructed from inorganic layers of $[Ni_3F_2(SO_4)_3(H_2O)_2]^{2-}$ held together by H-bond interactions with the piperazine cations in the interlayer space. Layers consist of edge-sharing NiF_2O_4 octahedra and bridging SO_4 tetrahedra that are linked to Ni octahedra sharing vertices (Figure 1.18(c)). The structure of this material can be compared to that of the mineral sulfoborite which is built up of sheets of MgO_6 and SO_4 tetrahedra [189]. This material is ferrimagnetic with hysteresis at low temperatures.

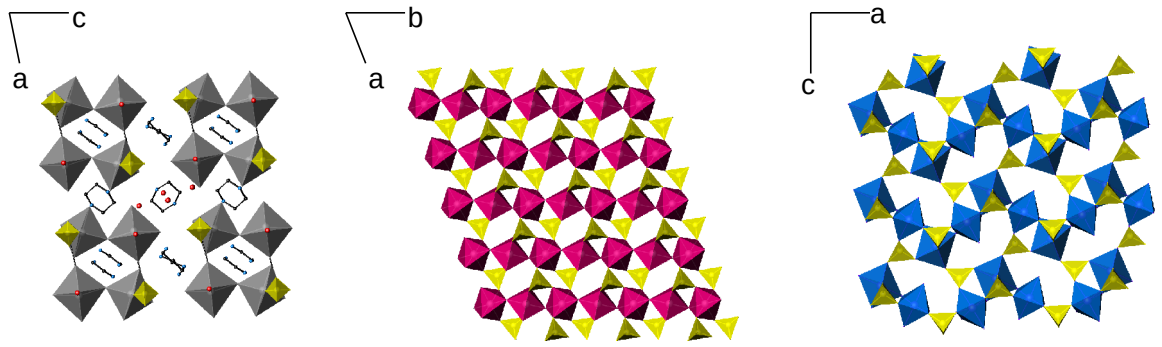

Figure 1.18. (a) Strip-like quasi-layer of $[C_4N_2H_{12}][Cd_3Cl_{10}(SO_4)_2(H_2O)]\cdot 3H_2O$ with the amine molecules in the cavities within the 8-membered apertures (CdO_6 octahedra, grey; SO_4 tetrahedra, yellow; C, black; N, blue; O, red); (b) Butlerite-type chains fused together to form one layer in $[NH_3(CH_2)_2NH_2(CH_2)_2NH_3][Fe_2F_2(SO_4)_2(H_2O)_2]$ (FeF_2O_4 octahedra, pink; SO_4 tetrahedra, yellow); (c) Inorganic layer in $[C_4N_2H_{12}][Ni_3F_2(SO_4)_3(H_2O)_2]$ (NiF_2O_4 octahedra, blue; SO_4 tetrahedra, yellow).

Several new layered rare-earth sulphates templated with amines have been prepared recently. A review of lanthanide compounds was published by Wickleder [190]. A layered compound of formula $[La_2(SO_4)_4][C_3N_2H_{12}]$ in which layers are formed by fusion of edge-sharing four-membered ring ladders has been prepared and characterised (Figure 1.19(a)) [191]. A family of rare-earth sulphates with general formula $[Ln_2(SO_4)_4][C_2N_2H_{10}]$ (Ln=La, Nd), in which Ln is nine-coordinated by sulphate oxygens, has also been synthesised [191]. Metal polyhedra are connected sharing vertexes and SO_4 tetrahedra act as a bridge between polyhedra through sharing corners and edges, resulting in four-membered rings, which in turn join together forming layers (Figure 1.19(b)). In the family $[Ln_2(SO_4)_4(H_2O)_4][C_6N_2H_{14}]_2[C_2N_2H_8][SO_4][H_2O]_3$ (Ln=La, Pr, Nd), Ln atoms are also nine-coordinated and possess a two-dimensional structure in which corrugated layers are built up from vertex- and edge-sharing LnO_9 polyhedra and SO_4 tetrahedra (Figure 1.19(c)) [191].

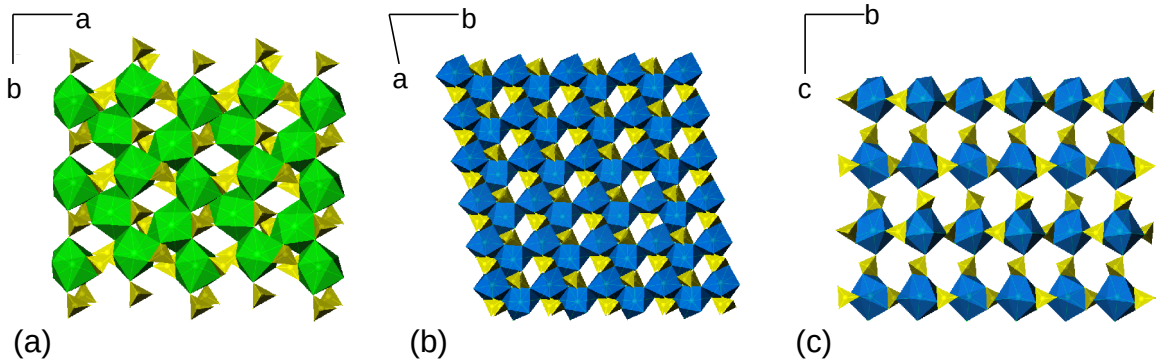

Figure 1.19. (a) Layer formed by joining ladders in $[La_2(SO_4)_4][C_3N_2H_{12}]$ (LaO_9 polyhedra, green; SO_4 tetrahedra, yellow); (b) Polyhedral representation of a layer in $[Nd_2(SO_4)_4][C_2N_2H_{10}]$ (NdO_9 polyhedra, blue; SO_4 tetrahedra, yellow); (c) Layer formed by NdO_9 polyhedra and SO_4 tetrahedra in $[Ln_2(SO_4)_4(H_2O)_4][C_6N_2H_{14}]_2[C_2N_2H_8][SO_4][H_2O]_3$ (NdO_9 polyhedra, blue; SO_4 tetrahedra, yellow).

The majority of two-dimensional lanthanum sulphates adopts a corrugated layer as it was observed in the lanthanum sulphate previously described and in the layered structures of $[C_2N_2H_{10}][La_2(H_2O)_4(SO_4)_4]\cdot 2H_2O$ [192] and $[La_2(H_2O)_2(SO_4)_6][C_2H_{10}N_2]_3$ [193]. The former comprises a network of LaO_{10}, LaO_8 polyhedra and SO_4 tetrahedra that link together sharing vertices and edges forming zig-zag layers that can be viewed as being made up of ladder-like chains connected through bridging SO_4 tetrahedra (Figure 1.20(a)). These corrugated layered structures can be compared to that of the neodymium sulphate

$[N_2H_5][Nd(H_2O)(SO_4)_2]$, with the difference that in the latter $(N_2H_5)^+$ cations are connected to the metal centre (Figure 1.20(b)) [194]. The mixed layered cerium phospho-sulphate was synthesised and characterised by Yu *et al.* [195] Its structure consists of a network of CeO_9 polyhedra, PO_4 and SO_4 tetrahedra, in which CeO_9 polyhedra form corrugated chains that connect *via* PO_4 and SO_4 tetrahedra to create two-dimensional layers (Figure 1.20(c)). More recently the structure of a piperazine templated two-dimensional cerium sulphate of formula $[C_4N_2H_{12}][Ce_2(SO_4)_6H_2O)_2]\cdot H_2O$, constructed from corrugated sheets, has been published [196] as well as that of a mixed-valence chromium(III)-cerium (III)/(IV) sulphate with a layered structure that differs from all the known mixed-valence cerium compounds which adopt three-dimensional framework structures [197]. The structure is constructed of layers of cerium atoms interlinked by sulphate groups, forming channels that host $[Cr(H_2O)_6]^{3+}$ and $[Ce(SO_4)_3(H_2O)_6]^{3-}$ units.

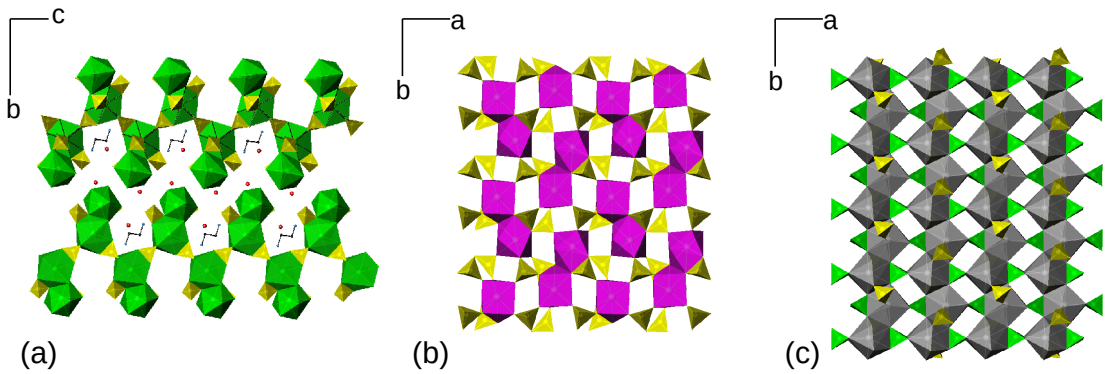

Figure 1.20. (a) Inorganic zig-zag layer in $[C_2N_2H_{10}][La_2(H_2O)_4(SO_4)_4]\cdot 2H_2O$ (LaO_n polyhedra, green; SO_4 tetrahedra, yellow; O, red; C, black; N, blue); (b) Layered structure of the neodymium sulphate $[N_2H_5][Nd(H_2O)(SO_4)_2]$ (NdO_9 polyhedra, pink; SO_4 tetrahedra, yellow); (c) Layered structure of $[enH_2][Ce(PO_4)(HSO_4)(H_2O)]$ (CeO_9 polyhedra, grey; PO_4 tetrahedra, green; SO_4 tetrahedra, yellow).

Uranium sulphates are commonly built up of four-membered rings linked by SO_4 tetrahedra giving rise to a wide variety of layered topologies. In USO-8, whose structure is displayed in Figure 1.21, layers consist entirely of four-membered rings [174].

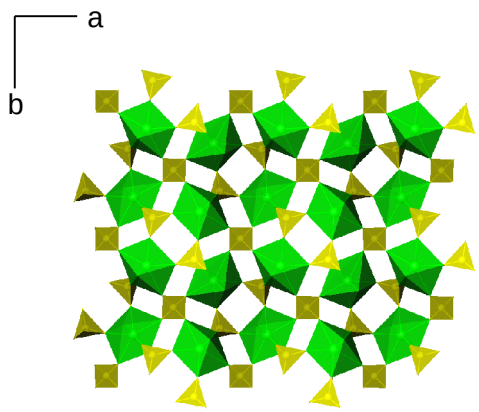

Figure 1.21. Two-dimensional layer in USO-8 (UO_7 polyhedra, green; SO_4 tetrahedra, yellow).

Depending on the mode of connectivity, other layered structures have been obtained. $[C_6N_2H_{14}][UO_2(H_2O)(SO_4)_2]$ [178] (Figure 1.22(a)) comprises twelve-membered rings along with four-membered rings whereas $[C_3N_2H_{12}][(UO_2)_2(H_2O)(SO_4)_3]$ [172] (Figure 1.22(b)) contains six-membered rings along with four-membered rings. Uranium sulphates with structures similar to those found in rare-earth sulphates with apertures of eight-membered rings have also been prepared [198]. In USO-28, $[N_4C_6H_{22}][UO_2(SO_4)_2]_2$, layers are formed by the connection of UO_7 pentagonal pyramids and SO_4 tetrahedra sharing edges and vertices as shown in Figure 1.22(c), in which $[trienH_4]^{4+}$ (trien=triethylenetetramine) cations reside in the interlayer space. However, in USO-29, $[N_5C_8H_{28}]_2[(UO_2)_5(H_2O)_5(SO_4)_{10}]\cdot H_2O$, UO_7 polyhedra connect to SO_4 tetrahedra *via* vertex-sharing to form $[(UO_2)_5(H_2O)_5(SO_4)_{20/2}]_n^{10n-}$ layers resulting in a wave-like structure (Figure 1.22(d)).

Organically-templated uranium sulphates have also been synthesised in the presence of hydrofluoric acid as a mineraliser. The structures of five novel uranium sulphate fluorides prepared by O'Hare and co-workers [181] are depicted in Figure 1.23. USFO-4 (Figure 1.23(b)), USFO-5 (Figure 1.23(c)) and USFO-7 (Figure 1.23(e)), contain infinite $(U\text{-}F\text{-}U)_n$ chains which link together to form layers. However, USFO-3 (Figure 1.23(a)) and USFO-6 (Figure 1.23(d)) contain terminal fluoride ligands that prevent the formation of the previously mentioned infinite chains. In USFO-3 and USFO-6, dimers and tetramers are formed respectively, and they are joined together through bridging SO_4 tetrahedra by corner linking (Figure 1.23).

Amine-templated thorium sulphates of formula $[NH(CH_2)_6NH]_2[Th_2(SO_4)_6(H_2O)_2]\cdot 2H_2O$, whose structure consists of cages, and $[NH_2(CH_2)_4NH_2][Th_3(SO_4)_7(H_2O)_4]\cdot 5H_2O$, whose structure contains layers derived from the connectivity of layers, have also been obtained under hydrothermal conditions [199]. They constitute the second family of actinide sulphates after the uranium sulphate family described previously.

The first indium sulphate coordination complex, [2,2-bipy] $[In_2(OH)_2(H_2O)][SO_4]_2$, in which layers are built up from butlerite-type chains and four-rings units, has also been lately prepared under hydrothermal conditions [200].

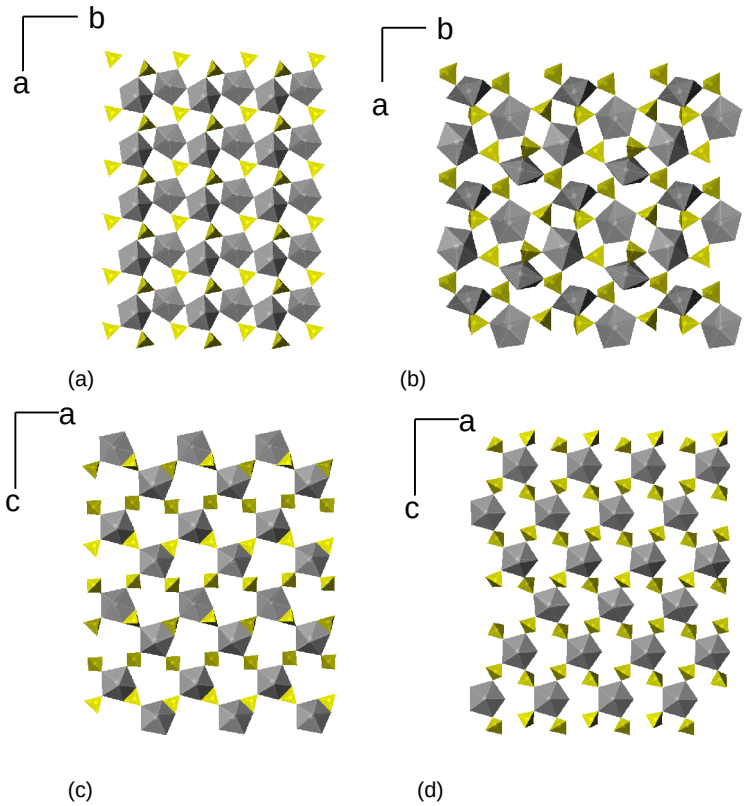

Figure 1.22. (a) Layered structure of USO-5; (b) layered structure of USO-2; (c) Layers in USO-28; (d) 2D structure of USO-29 (UO_7 polyhedra, grey; SO_4 tetrahedra, yellow).

1.3.4 Kagome Lattice in Two Dimensional Sulphates

1.3.4.1 Magnetism of the Kagome Lattice

One of the main reasons to study compounds of the transition metals is to investigate their magnetic behaviour, as they possess unpaired electrons. The magnetic properties of a solid depend on the number of unpaired electrons in the ground state as well

as in the site symmetry of the magnetic ion. In framework compounds magnetic interactions between the metal centres generally occur by super exchange through the connecting ligand, M-O/M-F. According to Goodenough [201, 202] and Kanamori [203], the character of this interaction is dependent on the angle M-O/F-O and the electronic occupancy. When atoms are connected in a linear array such as M-O-M (case of MO_6 octahedra sharing vertices) usually have oppositely aligned spins and therefore, antiferromagnetic coupling between the spins of the bridged ligands occurs. The strength of the exchange coupling *via* a bridging ligand is dependent on the M-O-M angle and it is weakened when it is reduced towards 90°. Under these circumstances ferromagnetic interactions become dominant.

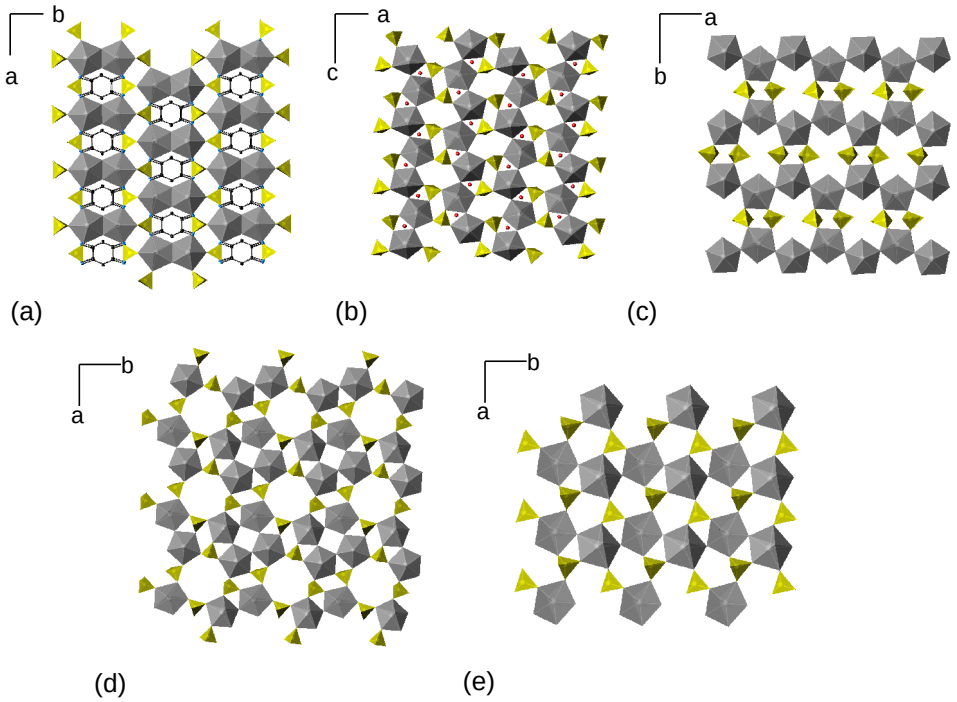

Figure 1.23. Layered structure of (a) USFO-3; (b) USFO-4; (c) USFO-5; (d) USFO-6; (e) USFO-7 ($UO_{7-n}F_n$ polyhedra, grey; SO_4 tetrahedra, yellow)

The Kagome lattice is a special case of magnetism and materials possessing this type of lattice have generated a tremendous interest due to the variety of magnetic ground state structures, which offer unique low-energy and low-temperature characteristics in the magnetic properties [201, 202, 204, 205]. The Kagome lattice has emerged to be an

important tool for the understanding of geometrical magnetic frustration in compounds of the transition metals.

Frustrated materials can be grouped into two categories: spin-glasses in which frustration is due to disorder in structure and frustration in spin; and geometrically frustrated systems in which frustration arises from the topological arrangement of the magnetic ions in the lattice [206]. The word frustration was introduced to describe a situation in which a system cannot simultaneously minimise the interaction energies between its components [207]. One simple example is shown in Figure 1.24. Let's suppose three magnetic ions reside on the corner of a triangle with antiferromagnetic interactions between them. Once the first two spins align anti-parallel, the third one is frustrated because its two orientations (up or down) give the same energy - the third spin cannot simultaneously minimise the antiferromagnetic interactions with both of the other two. Thus the ground state is two-degenerate [208]. The triangular array is just one manifestation of a frustrated system. It has also been found in compounds based on tetrahedra which share corners, edges or faces.

This phenomenon is observed in materials possessing the Kagome lattice. Among these systems $Rb_2M_3S_4$ (M=Ni, Co, Mn) [209, 210], $NaFe_3(SeO_4)_2(OH)_6$ [211], $SrCr_xGa_{12-x}O_{19}$ [212], $M_3V_2O_8$ [213], (being M a magnetic ion), Keplerates [214] and jarosites [215, 216] can be cited. The structure of the Kagome layer consists of hexagonal tungsten bronze sheets in which one magnetic ion is shared by two adjacent triangles. This structure is obtained by representing only the metal centres within the layers (Figure 1.25).

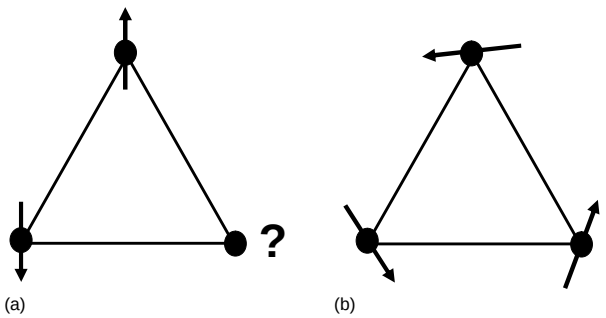

Figure 1.24. Triangular arrangement of spins with antiferromagnetic interactions between them (a) antiparallel alignment of the first two spins; (b) Two-degenerate ground state of the antiferromagnetically couple arrangement.

The structure and magnetic properties of a wide number of compounds of the transition metals which exhibit the Kagome lattice have recently been reviewed by Rao and co-workers [217].

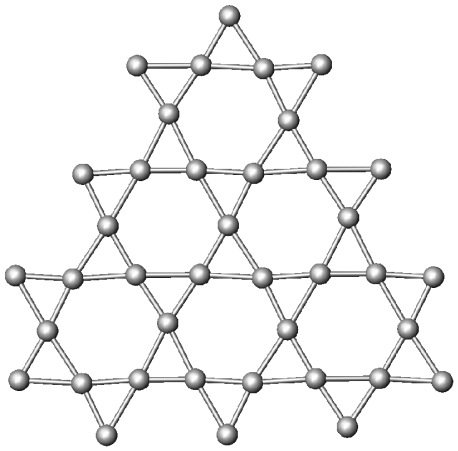

Figure 1.25. Layer Kagome hexagonal sheet obtained by representing metal centers.

1.3.4.2 Examples of 2D Transition-Metal sulphates with the Kagome lattice

Most of the transition metal sulphates which exhibit the Kagome Lattice belong to the jarosite family, ($K_2[Fe_6^{III}(SO_4)_4(OH)_{12}]$ (Figure 1.26), in which spin-magnetic frustration has been observed [218]. Studies of their magnetic properties show magnetic frustration or low-temperature antiferrimagnetism [219]. Recently, efforts have focused on the preparation of other transition metal sulphates with the Kagome lattice through hydrothermal processes.

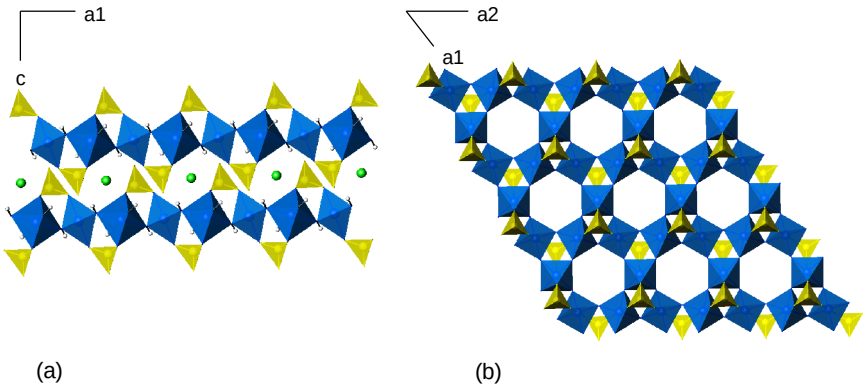

Figure 1.26. (a) Layers of $[Fe_6^{III}(SO_4)_4(OH)_{12}]$ alternating with K^+ cations in the jarosite structure along the *c*-axis; (b) One hexagonal layer of $K_2[Fe_6^{III}(SO_4)_4(OH)_{12}]$ showing the one-dimensional six-membered ring channels (FeO_6 polyhedra, blue; SO_4 tetrahedra, yellow; K^+ cations, green).

To date, in the majority of the resulting compounds the metal centres are connected by F bridges to form layers with the Kagome lattice. These studies have focussed on the synthesis of amine-templated iron sulphates. The iron sulphate compounds $[HN(CH_2)_6NH][Fe^{III}Fe_2{}^{II}F_6(SO_4)_2][H_3O]$ and $[NH_3(CH_2)_2NH_2(CH_2)_2NH_2(CH_2)_2NH_3][Fe^{III}Fe_2{}^{II}F_6(SO_4)_2]$ (Figure 1.27(a)) constitute an example of a Kagome lattice involving mixed-valence iron, synthesised by Rao and co-workers [220, 221]. The former consists of layers of corner-sharing $Fe^{III}F_4O_2$ and $Fe^{II}F_4O_2$ octahedra and SO_4 tetrahedra linked together through bridging Fe-F and Fe-O-S bonds, whilst in the latter three edge-sharing $Fe^{II}F_4O_2$ octahedra are present. Both compounds present similar magnetic behaviour. They show a divergence between the field-cooled (FC) and the zero-field cooled (ZFC) measurements which is characteristic of a magnetically-frustrated ground state and that suggests spin-glass behaviour [222, 223]. Similar behaviour had been found in other iron compounds with the Kagome lattice [215, 218, 224]. However, at low temperature magnetic hysteresis is observed which is characteristic of ferrimagnetism (Figure 1.27(b)).

Consequent studies on this system lead to the synthesis of $[NH_3(CH_2)_6NH_3][Fe^{II}_{1.5}F_3(SO_4)]\cdot 0.5H_2O$ [216], which exhibits the same Kagome lattice topology observed in jarosite but contains only Fe^{2+} instead of Fe^{3+}. However, its magnetic properties differ from those of the jarosite due to the presence of iron in +2 oxidation state. It is ferrimagnetic below 19 K undergoing a possible change in magnetic structure below 15 K, suggested by the presence of a significant antiferromagnetic component, in contrast with the Fe (III) Kagome compounds whose magnetic properties are characterised by magnetic frustration.

Recently, an organically-templated iron(II) sulphate of composition $[NH_3(CH_2)_2NH_2(CH_2)_2NH_3]_4[Fe^{II}_9F_{18}(SO_4)_6]\cdot 9H_2O$ [225] has been synthesised. It exhibits a distorted Kagome structure as a result of two types of Fe octahedra: one in which four F atoms are in equatorial positions and two O in axial positions, as occurs in the jarosite structure (perfect Kagome lattice); and another in which three F and one O are in equatorial position and one F and one O are located in axial positions. Magnetic measurements showed canted antiferromagnetism at low temperatures. Also a nickel Kagome compound $[C_6N_2H_8][Ni_3F_6(SO_4)_2]$ [226], which consists of anionic layers of vertex-sharing NiF_4O_2 octahedra and SO_4 tetrahedra, has been found to be a canted antiferromagnet.

The cobalt (II) sulphate $[NH_2(CH_2)_2NH_2][NH_4]_2[Co_3F_6(SO_4)_2]$, recently reported by Rao *et al*., also exhibits a Kagome lattice [227]. Its magnetic properties are comparable with those of the analogous Fe (III) compounds, involving weak antiferromagnetic interactions.

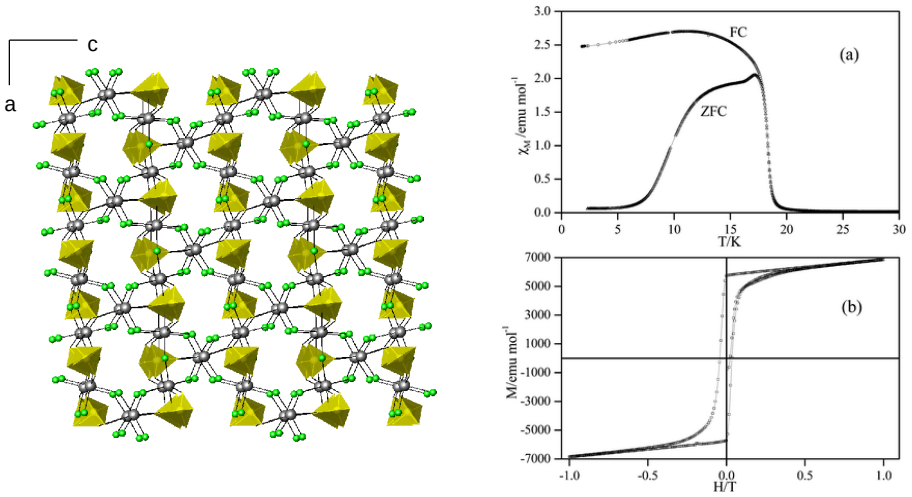

(a) (b)

Figure 1.27. (a) Representation of one layer with 6-membered ring channels of $[N_4C_6H_{32}][Fe^{III}Fe_2{}^{II}F_6(SO_4)_2]$ (Fe centres, grey; F, green; SO_4 tetrahedra, yellow) (b) Magnetic measurements of $[N_4C_6H_{32}][Fe^{III}Fe_2{}^{II}F_6(SO_4)_2]$ (top figure) Divergence between the ZFC and FC susceptibility curves (bottom figure) Hysteresis loop characteristic of antiferrimagnetism [220].

Attempts to obtain Kagome compounds with manganese produced $[C_4N_2H_{12}][NH_4]_2[Mn_3F_6(SO_4)_2]$ [228], whose structure is built up of corner sharing MnF_4O_2 octahedra and SO_4 tetrahedra that link together *via* Mn-F-Mn and Mn-O-S bonds to form the Kagome layer. The magnetic properties of this manganese sulphate differ from those of the Fe (III) Kagome compounds; neither magnetic frustration nor long-range antiferromagnetic ordering was observed. Instead, magnetic susceptibility data showed that the material is essentially paramagnetic with antiferromagnetic interaction, exhibiting only short-range order.

1.3.5 Three-Dimensional Sulphates

A three-dimensional nickel sulphate with formula $[C_4N_2H_{12}][Ni_2F_4(SO_4)H_2O]$ was obtained under hydrothermal conditions in the presence of piperazine [188]. Its structure is

built up of NiO_2F_4 octahedra that share edges through fluorine to form dimeric units $Ni_2F_6O_4$. These are linked by sharing edges to form sinusoidal chains that are interlinked by corner-sharing SO_4 tetrahedra to form layers with channels of eleven-membered rings (Figure 1.28(a)). These layers are cross-linked by SO_4 tetrahedra to form a three-dimensional structure containing elliptical channels (Figure 1.28(b)). The channels are occupied by diprotonated piperazine cations that interact with the framework through hydrogen bonds. Magnetic measurements reveal weak antiferromagnetic interactions.

A wide range of cobaltosulphate layers pillared by a variety of linear diamines has been prepared [229-231]. Among them, it is worthwhile to mention the cobalt sulphate templated by ethylenediamine $[(NH_2(CH_2)_2NH_2]_{0.5}[Co_4(SO_4)(OH)_6]\cdot 3H_2O$, which shows metamagnetism [231]. Three-dimensional hydroxy-sulphates containing nickel, manganese and cobalt with attractive magnetic properties have also been synthesised under hydrothermal conditions. The isostructural compounds of formula $M_3(OH)_2(SO_4)_2(H_2O)_2$ (M=Mn, Ni, Co) display a three-dimensional structure consisting of corrugated metal-hydroxide layers which are connected to one another *via* bridging SO_4 tetrahedra to form a three-dimensional network. These metal hydroxide sulphates have been found to be canted antiferromagnets [232-234]. More recently, a pillared-layered coordination polymer, $[Co(SO_4)][NH_2(CH_2)_2NH_2]$, with a three-dimensional structure consisting of cobalt sulphate sheets built up of alternating CoO_4N_2 octahedra and SO_4 tetrahedra, with the ethylenediamine molecules connecting the metal centres, has been obtained [235]. It exhibits paramagnetic behaviour at room temperature. This structure constitutes an example of a three dimensional inorganic-organic hybrid material.

Solvothermal synthesis has allowed the preparation of other three dimensional hybrid compounds such as the three-dimensional mixed-valence Cu^ICu^{II} coordination polymer $[Cu^ICu^{II}(mal)(SO_4)(bpy)_2(H_2O)]_n$, (mal=malate and bpy=4,4-bipyridine), in which a Cu^{2+} dimer containing Cu centres brigded by malate and SO_4 tetrahedra can be identified. SO_4 tetrahedra also connect the dimers with the Cu^+ centres. Double chains are built up from linkage between these building units with 4,4-bipyridine molecules. The three-dimensional structure is formed by interconnected double chains through bridging SO_4 tetrahedra [236].

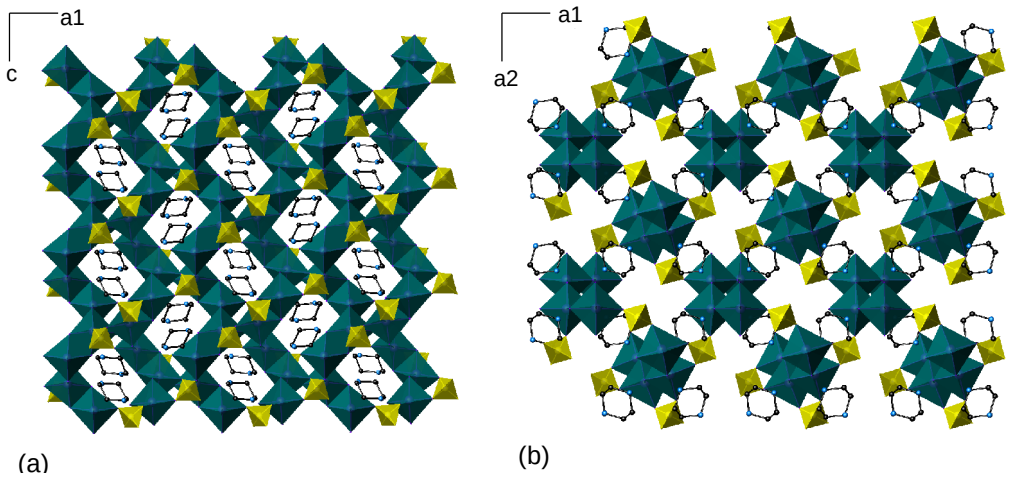

Figure 1.28. (a) Sinusoidal chains formed by edge-sharing NiO_6 octahedra in which the eleven-membered channels are filled up by organic molecules; (b) Cross-linking between layers to form the three-dimensional structure of $[C_4N_2H_{12}][Ni_2F_4(SO_4)H_2O]$ (NiO_6 octahedra, green; SO_4 tetrahedra, yellow; C, black; N,blue)

A novel cadmium sulphate network of general formula $[Cd(BIMB)_{0.5}(SO_4)(H_2O)]_n \cdot nH_2O$ has also been prepared by solvothermal synthesis using 1,4-bis(imidazol-1-methyl)benzene (BIMB) as solvent [237]. The structure comprises CdO_6 octahedra and SO_4 tetrahedra connected to form layers (Figure 1.29(a)). Layers are coordinated by BIMB forming the three-dimensional structure, whose cavities contain water molecules (Figure 1.29(b)).

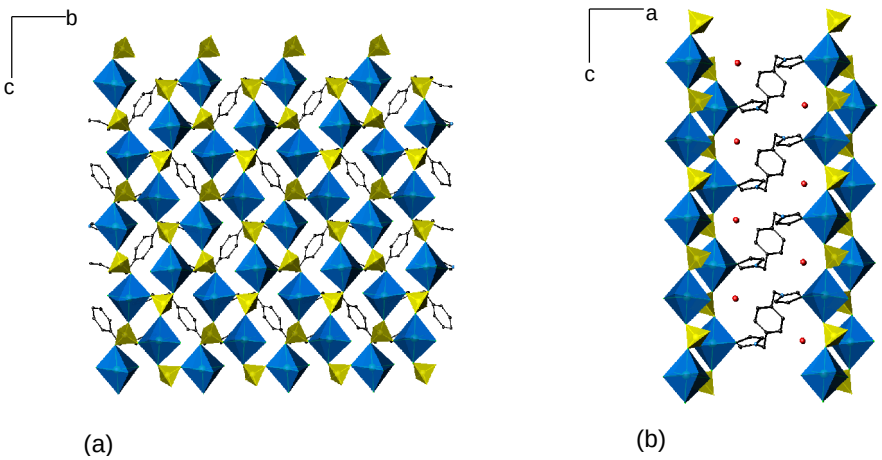

Figure 1.29. (a) One layer in $[Cd(BIMB)_{0.5}(SO_4)(H_2O)]_n \cdot nH_2O$ formed by alternating CdO_6 octahedra and SO_4 tetrahedra; (b) Linkage between the inorganic sheets and the organic molecules into a three-dimensional network (CdO_6 octahedra, blue; SO_4 tetrahedra, yellow; C, black; N, blue; O, red).

The first hydrothermally prepared scandium sulphate was obtained by Morris *et al.* [238] $Sc_7(S/P,O_4)_{12}$ displays a three-dimensional structure in which ScO_6 octahedra share corners with $(S/P)O_4$ tetrahedra, to give a structure with supercages of a free diameter of 13 Å, connected *via* smaller cages (Figure 1.30(a)).

In contrast to the large number of two-dimensional rare-earth sulphates, only a small number of three-dimensional networks are known. A common characteristic found in the majority of lanthanum sulphates is the presence of eight-membered rings units. The crystal structures of some illustrative examples of rare-earth sulphates containing eight-membered rings units will be described. The three-dimensional structure of $[La_2(H_2O)_2(SO_4)_4](C_4H_{12}N_2)_2$ [193] consists of lanthanum atoms and sulphate groups connected together forming apertures of eight-membered rings in which protonated piperazinium cations are located (Figure 1.30(b)). Rao and co-workers obtained the three-dimensional rare-earth sulphates of formula $[Ln_2(H_2O)_2(SO_4)_5][C_2N_2H_{10}]_2$ with Ln=La, Pr, Nd. Their structure contains channels of eight-membered rings surrounded by four apertures of sixteen-membered rings (Figure 1.31(a)). The three-dimensional structure of the neodymium sulphate $[Nd_2(SO_4)_4(H_2O)_2][C_4N_2H_{12}]$ contains four apertures of twelve-membered rings around each aperture of eight-membered rings (Figure 1.31(b)) [191].

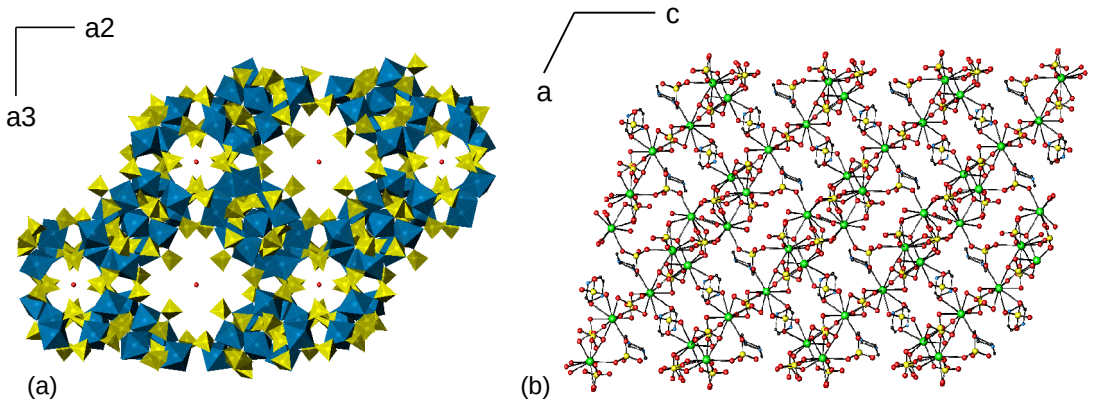

Figure 1.30. (a) Framework structure of $Sc_7(S/P,O_4)_{12}$ (ScO_6 octahedra, green; SO_4 tetrahedra, yellow); (b) Crystal structure of $[La_2(H_2O)_2(SO_4)_4](C_4H_{12}N_2)_2$ showing its three-dimensional structure (La, green; S, yellow; O, red; C, black; N, blue).

Three-dimensional cerium and europium sulphates have been recently synthesised under hydrothermal conditions [239, 240]. The cerium sulphates $[C_4H_{12}N_2]_4[Ce_8(SO_4)_{16}(H_2O)_8]$, which exhibits a three-dimensional anionic open-framework structure compensated by piperazine cations residing in the zigzag channels within the network, and

$[C_2H_{10}N_2]_2[Ce_2(SO_4)_5(H_2O)_2]$, which displays the characteristic apertures of eight-membered rings as well as sixteen-membered rings in which protonated ethylenediamine cations reside, constitute the first examples of three-dimensional open-framework cerium sulphates [239]. The europium sulphate $[NaEu(H_2O)(SO_4)_2]$, whose structure is built up from helical chains connected together through corner-sharing polyhedra to form a three-dimensional network, exhibits photoluminescent properties [240].

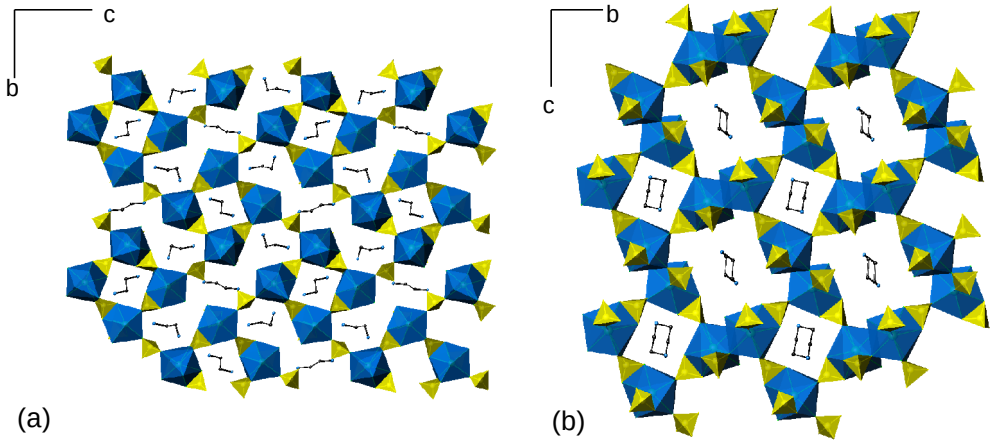

Figure 1.31. (a) A layer in $[Ln_2(H_2O)_2(SO_4)_5][C_2N_2H_{10}]_2$ comprising LnO_9 and SO_4 tetrahedra that are connected by sharing edges and vertices forming eight- and sixteen-membered rings; (b) A layer of the three-dimensional compound $[Nd_2(SO_4)_4(H_2O)_2][C_4N_2H_{12}]$, in which channels of eight- and twelve-membered rings are appreciated (LnO_9 and NdO_9 polyhedra, blue; SO_4 tetrahedra, yellow; C, black; N, blue).

A family of three-dimensional coordination polymers of general formula $[Ln(INO)(H_2O)(SO_4)]_n$ (Ln=La, Ce, Pr, Nd, Sm, Eu, Gd, Tb, Dy, Ho, Er, Tm, Yb, Lu) has also been synthesised. These structures are formed by connection of layers, chains or dimers of Ln-SO_4 by INO (INO=isonicotinate-N-oxide) [241]. According to the size of the rare-earth ion, three different structures type were observed: type I for large ions (La, Ce, Pr), type II form medium size ions (Nd, Sm, Eu, Gd, Tb) and type III for small ions (Dy, Ho, Er, Tm, Yb, Lu). The structure of Type I compounds comprises two dimensional Ln-sulphate layers pillared by INO into a three-dimensional network. Type II consists of a three dimensional structure generated by the connection of Ln-SO_4-H_2O chains *via* INO ligands. Type III is constructed from dimers bridged by SO_4 tetrahedra which are connected by INO bridges. Weak ferromagnetism was observed in the gadolinium compound. Luminescense studies reveal that the europium-containing material exhibits very strong red

luminiscense due to the $^5D_0 \rightarrow {}^7F_1$ transition, whereas the terbium compound emitted green light, emission that can be assigned to a $^5D_4 \rightarrow {}^7F_J$ (J=6,5,4,3) transition.

A three-dimensional lanthanum sulphate squarate, $La_2(H_2O)_4(SO_4)_2(C_2O_4)$, that constitutes the first member of a family of hybrid materials, has been hydrothermally synthesised [242]. Moreover, very recently two series of novel three-dimensional hybrid organic-inorganic frameworks, in which two-dimensional hybrid layers are constructed from lanthanide sulphate chains and oxalates that are pillared with 1,4-piperazine diacetic acid molecules, have been prepared [243].

The first organically-templated 3*d*-4*f* mixed metal sulphates $[enH_2][La_2M(SO_4)_6(H_2O)_2]$ (M=Ni, Co) (Figure 1.32) were synthesised and characterised by Clearfield *et al.* [244] The structure consists of a three-dimensional anionic network made up from MO_6 octahedra and LaO_{10} polyhedra that are interconnected through bridging SO_4 tetrahedra, resulting in apertures of eight-membered rings in which diprotonated ethylenediamine cations are located.

The synthesis and crystal structure of the first actinide sulphate with a three-dimensional structure was reported by O'Hare and co-workers [245]. The structure of $[NC_4H_{12}][(UO_2)_6(H_2O)_2(SO_4)_7]$ (MUS-1) (Figure 1.33) is formed from vertex linkage of UO_7 polyhedra to four adjacent SO_4 tetrahedra. This results in channels directed along [001] that are occupied by tetramethylammonium cations.

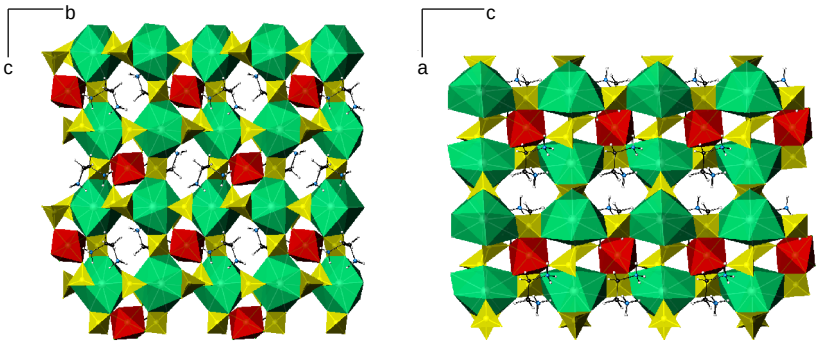

Figure 1.32. Polyhedral representation of the three-dimensional structure of $[enH_2][La_2M(SO_4)_6(H_2O)_2]$ (a) along *a*-axis and (b) along *b*-axis (LaO_{10} polyhedra, green; NO_6 octahedra, red; SO_4 tetrahedra, yellow; C, black; N, blue).

Whilst hydrothermal synthesis was not used for the preparation of a thorium sulphate of formula $[Th_3(SO_4)_6(H_2O)_6]\cdot H_2O$ [246] belonging to the family of actinide

sulphates, it is worth mentioning that this compound displays a very interesting feature that might be important for future applications. It contains large open-framework voids of 11.5 Å, that are comparable to the largest of the microporous and open-framework actinide materials reported to date by O'Hare and co-workers [247, 248].

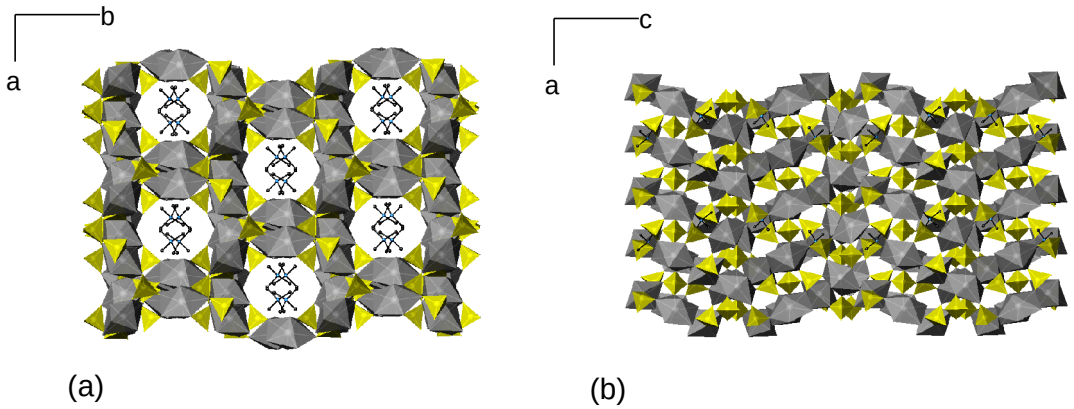

Figure 1.33. (a) Structure of MUS-1 along *c*-axis; (b) Zig-zag structure in MUS-1 along *b*-axis (UO_7 polyhedra, grey; SO_4 tetrahedra, yellow, C, black, N, blue).

1.4 Open-frameworks from Ionic Liquids (ILs)

1.4.1 Definition, preparation and properties

Ionic liquids are generally defined as organic salts that melt at or below 100ºC to afford liquids composed solely of cations and anions. The most common salts in use are those of N,N´-dialkylimidazolium or N-alkylpyridinium cations, although alkylammonium or alkylphosphonium salts can also be used. Regardless they are well-known solvents, they have attracted a lot of interest in recent years, in particular as solvents for organic chemistry synthesis. The first ionic liquid, $[Et_4N][NO_3]$ with a melting point of 12°C, was reported by Walden back in 1914 [249], but it was not until 1948 that the first room temperature ionic liquid was developed from [EMIM]Cl-$AlCl_3$ ([EMIM]=1-ethyl-3-methylimidazolium) [250]. Ionic liquids have been used in many areas of chemistry and industry due to their potential as green alternatives to traditional organic solvent [251-253]. They also constitute potential solvents for materials' synthesis. Besides their electrochemical properties that have been demonstrated by their widely use in electrosynthesis of metallic nanoparticles, such as palladium [254], iridium [255] and semiconductor nanoparticles, such as Ge nanoclusters [256], other advantages of using ionic liquids that can be cited [257] are: they

can have low interface tensions and low viscosity; they are highly polar solvents and present high ionic conductivity; they exhibit high thermal stability, therefore reactions can be conducted at temperatures beyond 100°C in non-pressurized vessels; ionic liquids facilitate inorganic synthesis from very polar starting materials under ambient conditions and under anhydrous or water poor conditions; and the last advantage of ionic liquids is that they form extended hydrogen bond systems in the liquid state and are therefore highly structured [258, 259]. Their solvent properties are determined by the ability of the salt to act as a hydrogen-bond donor and/or acceptor and the degree of localization of the charge on the anion.

There are two principal methods for the preparation of ionic liquids [250]: (a) metathesis of a halide salt with silver, a metal from group I, or ammonium salt of the desired anion and acid-base neutralization reactions; (b) combination of a halide salt with metal halide. Recently, it has been found that is possible to form ionic compounds (eutectic mixtures) which are liquids at temperatures of 100°C or below, by reacting a quaternary amine salt with an organic material which is solid at 20°C and capable of forming a hydrogen bond with the anion of the ammonium salt. Examples include amides (e.g. urea, thiourea), carboxylic acids (e.g. oxalic acid, benzoic acid)), alcohols (e.g. benzyl alcohol) and phenols. The liquid form of the compound is stabilised by the charge delocalization created by the hydrogen bonding of the organic compound with the anion of the ammonium salt [260]. These compounds can also be used as electrolytes in electrochemical devices or in photovoltaic devices, for dissolution of ionic species, as catalysts or as chemical reagents [261].

1.4.2 Ionothermal synthesis as a route for the preparation of inorganic materials

Since in 2004 Cooper et *al*. [22] first reported the synthesis of a zeolite in an ionic liquid, this synthetic methodology has been termed ionothermal synthesis to distinguish it from solvothermal and hydrothermal methods. Due to its unique ability to act both as solvent and template, the addition of other solvent is not needed. This represents an advantage compared to hydrothermal synthesis because it eliminates competition between template-framework and solvent-framework interactions. However, it has been established that the addition of water or fluoride plays an important role in ionothermal synthesis because it allows a level of control in the process that is absent in other methods. In

addition, the low vapour pressure of most ionic liquids allows the synthesis to take place at ambient pressures. With these properties, the formation of attractive materials with exciting properties would be expected. In fact, several new morphologies and new compounds have been obtained under these conditions. Initially, conventional heating was used for the synthesis, but Xu et *al*. [262] introduced microwave heating, as ionic liquids are good microwave absorbers, with the important advantage of reducing the reaction time.

1.4.2.1 Zeotype Materials: Phosphates and silicates

The first new zeotype material reported using the ionothermal method was SIZ-1 (St Andrews Ionothermal Zeolite-1), synthesised in the ionic liquid 1-ethyl-3-methyl-imidazolium bromide ([EMIM] Br). It displays a structure with hanging P-O bonds and contains aluminium in two different coordination environments (4- and 5-coordinated) (Figure 1.34(a)) [22]. Similar characteristics are found in the layered SIZ-6, in which in addition to 4- and 5-coordinate aluminium ions, 6-coordinate species are also present (Figure 1.34(b)). Both SIZ-1 and SIZ-6 are new zeotype structures. Other SIZ-*n* type materials have been synthesised both with known or new topologies. SIZ-3 and SIZ-4 were produced by adding fluoride to the reaction mixture to form fully condensed frameworks, without hanging P-O bonds, demonstrating that the addition of a mineraliser increases the solvating power (Figure 1.34(c and d)) [22]. The ionothermal synthesis of open-framework materials has been reviewed by Morris *et al*. [263]

Until recently, the bulk of the work in ionothermal synthesis concentrated on the use of [EMIM] Br as solvent. However the synthesis of a novel chain structure $Al(H_2PO_4)_2F$ using $EMITf_2N$ (1-ethyl-3-methyl-imidazolium bis((trifluoromethyl) sulfonyl)amide) has recently been described. This overcomes disadvantages of [EMIM] Br, which include its hygroscopic nature and its thermal stability (Figure 1.35(a)) [264]. Also the effect of the alkyl chain length of imidazolium-based ionic liquids has been studied and as a result SIZ-4, SIZ-6, SIZ-10 (Figure 1.35(b)) and SIZ-11 were synthesised, indicating that in this synthesis the ionic liquid is acting more as space filler rather than as a structure directing agent [265].

The cobalt aluminophosphates SIZ-7, SIZ-8 and SIZ-9 were synthesised using [EMIM] Br both as solvent and template, confirming that the ionothermal method is suitable for the preparation of transition metal frameworks with potential applications such

as in catalysis or sorption processes [23]. The three zeotype structures SIZ-7, SIZ-8 and SIZ-9 have different topologies from the aluminophosphates. Particularly, SIZ-7 shows a novel framework structure consisting of double-crankshaft chains parallel to the crystallographic *a*-axis. These chains are connected into a one-dimensional zeolite structure with eight-ring windows (Figure 1.36).

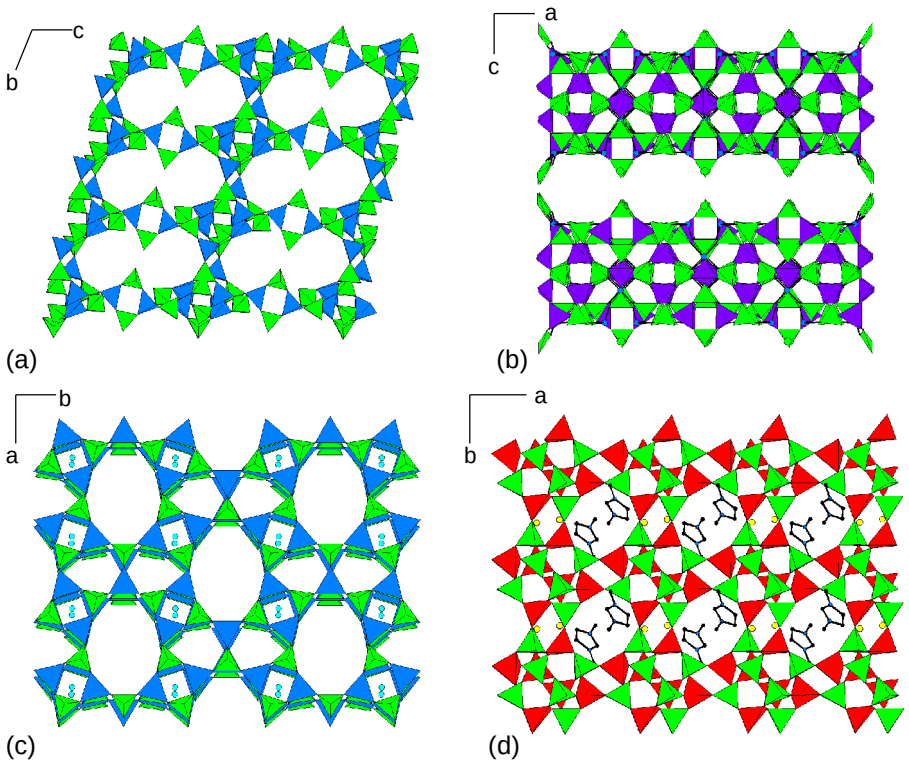

Figure 1.34. (a) SIZ-1(PO_4, green; AlO_n (n=4,5), blue) ; (b) SIZ-6 (PO_4 tetrahedra, green; AlO_n (n=4,5,6), magenta) ; (c) SIZ-3 (PO_4 tetrahedra, green, AlO_4 tetrahedra, blue, F atoms, light blue) ; (d) SIZ-4 (PO_4, green, AlO_4, red, F atoms, yellow, C, black, N, blue).

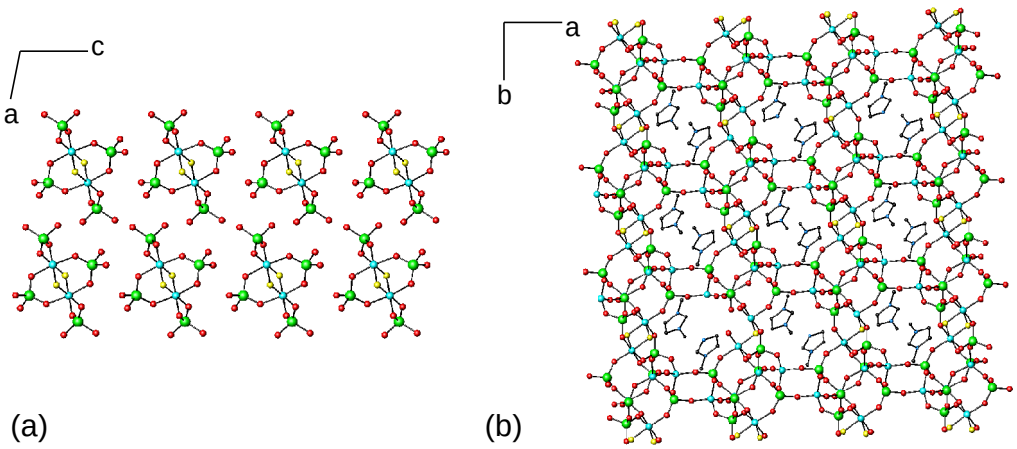

Figure 1.35. (a) Structure of $Al(H_2PO_4)_2F$ (P, green; O, red; Al, blue; F, yellow); (b) Structure of SIZ-10 (P, green; O, red; Al, blue; F, yellow; C, black; N, dark blue).

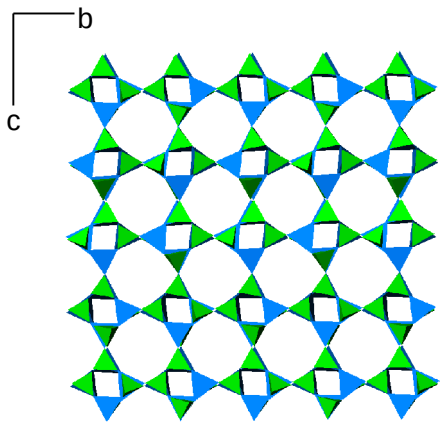

Figure 1.36. SIZ-7 (CoO_4 tetrahedra; blue; PO_4 tetrahedra, green)

Given that it is possible to obtain aluminophosphates and cobalt aluminophosphates using ionothermal techniques, it is logical to think that silicon-based zeolites may be produced under these conditions. Indeed, SIZ-12, a pure silicate obtained ionothermally, is built up from layers of distorted double-crankshaft chains which are linked into a three-dimensional network [266].

Eutectic mixtures have been also tried as solvents in ionothermal synthesis as alternatives to ionic liquids. However, there are only few examples of zeotype materials obtained using eutectic mixtures [267, 268]. The use of deep eutectic solvents permits the synthesis of several aluminophosphates highlighting the versatility of this technique as well as its potential to prepare materials that are difficult to be obtained under hydrothermal conditions, as evidenced by the synthesis of the first non-fluoride gallium phosphate adopting the Zeolite-A structure [269]. Recently an unusual choline-templated cobalt aluminophosphate with a zeolite-related layered structure (SIZ-13) has been reported together with two other cobalt aluminophosphate zeolite analogues (SIZ-14 and SIZ-15) with a known topology [270]. SIZ-13, unlike many other zeolite-type materials, contains cobalt ions ordered in one crystallographic site at the corner of the building unit, coordinated to three oxygen atoms and one chlorine, forming terminal Co-Cl bonds, instead of the common four oxygen atoms (Figure 1.37). These Co-Cl units are generally not accessible using traditional routes due to their sensitivity to hydrolysis, thus illustrating how these new approaches open new possibilities in materials chemistry. This versatility has also been evidenced by the ionothermal synthesis of a new open-framework aluminophosphate with unique Al/P ratio of 6/7 [271].

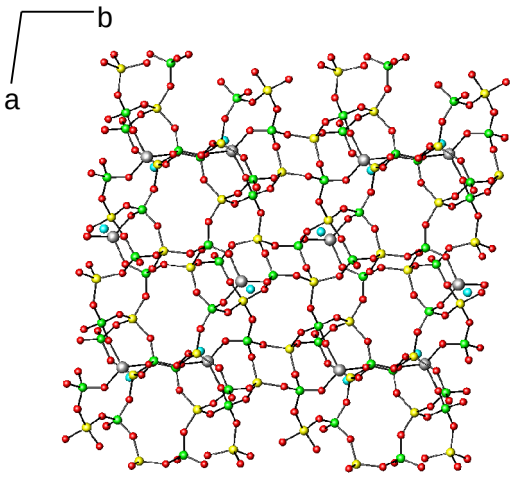

Figure 1.37. Layered structure of SIZ-13 of formula $[Al_3CoClP_4O_{16}][C_5H_{13}NOH]_2$ (Co, grey; Cl, blue; O, red; Al, yellow; P, green).

1.4.2.2 Ionothermal synthesis of metal-organic frameworks

The first organic-inorganic hybrid material obtained under ionothermal conditions using the ionic liquid [BMIM] BF_4 solvent is [Cu(bpp)] BF_4 (bpp=1,3-bis(pyridyl)propane) built up of a wave-like Cu-bpp chain that is extended into a two-dimensional network *via* Cu-Cu interactions (Figure 1.38(a)) [272]. The synthesis of $Cu_3(tpt)_4(BF_4)(tpt)_{2/3}.5H_2O$ (tpt=2,4,6-tris(4-pyridyl)-1,3,5-triazine) carried out using the same ionic liquid, constitutes the first example of a three-dimensional metal-organic framework with an unprecedent 2-fold interpenetrating (3,4)-connected net with large channels [273]. This is not the only example of an interprenetrating network. A few months ago, an organic Zn complex with a novel six-connected net that had never been observed previously, was obtained [274].

In the last few years, microwave-assisted synthesis has been employed for ionothermal synthesis. An anionic cadmium organic framework, $[C_6H_{11}N_2][Cd(C_9H_3O_6)]$, with a three-dimensional structure formed by CdO_6 octahedra bridged together through the organic molecule in whose cavities the ionic liquid resides, has been prepared (Figure 1.38(b)) [275]. Similarly, a nickel coordination polymer $[EMIM]_2[Ni_3(TMA)_2(OAc)_2]$ ([EMIM]=1-ethyl-3-methylimidazolium) with a novel anionic three-dimensional structure was obtained by Morris *et al*. [276] The structure consists of octahedral $[Ni_3(COO)_8]_6$ building units, which are linked into layers, and neutral TMA (trimethylamine) connecting them together to form the three-dimensional network (Figure 1.38(c)).

Using 1-alkyl-3-methylimidazolium bromide, Xu and co-workers have obtained six three-dimensional zinc-containing metal-organic frameworks with different crystal structures, three of which are shown in Figure 1.39 [277].

Eutectic mixtures have also been employed for the generation of metal-organic frameworks. A novel coordination polymer $[Zn(O_3PCH_2CO_2)]\cdot NH_4$ [278] was synthesised using the choline chloride/urea eutectic mixture (Figure 1.40(a)). Iron, manganese and gallium oxalatophosphonates with three-dimensional networks have also been prepared *via* ionothermal synthesis using an eutectic mixture [279-281]. The structure of $Cs_2Fe(C_2O_4)_{0.5}(HPO_4)_2$ is depicted in Figure 1.40(b). It comprises FeO_6 octahedra connected through HPO_4^{2-} and oxalate ions to form a three-dimensional network containing channels of twelve-membered rings occupied by Cs^+ ions [280].

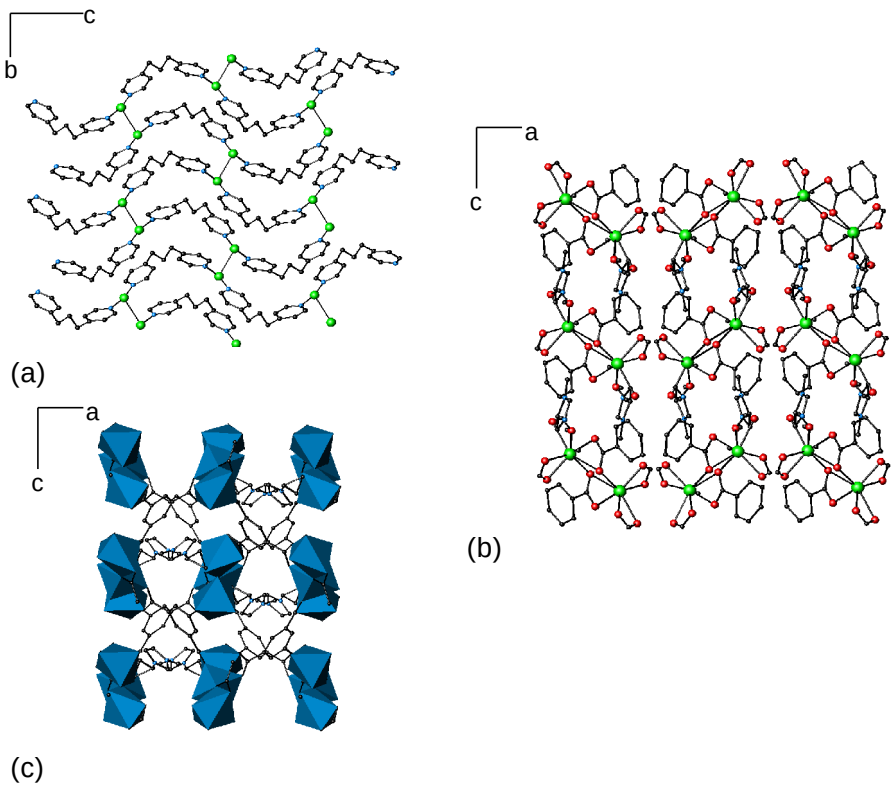

Figure 1.38. (a) Wave-like chains in $[Cu(bpp)]BF_4$ (Cu centres, green; C, black; N, blue); (b) Three-dimensional structure of $[C_6H_{11}N_2][Cd(C_9H_3O_6]$ showing 1-ethyl-3-methylimidazolium cations in the void space (Cd centres, green; O, red; C, black, N, blue); (c) View along the *b*-axis of the three-dimensional network composed of $Ni_3(COO)_8$ (NiO_6 octahedra, blue; C, black; N, blue).

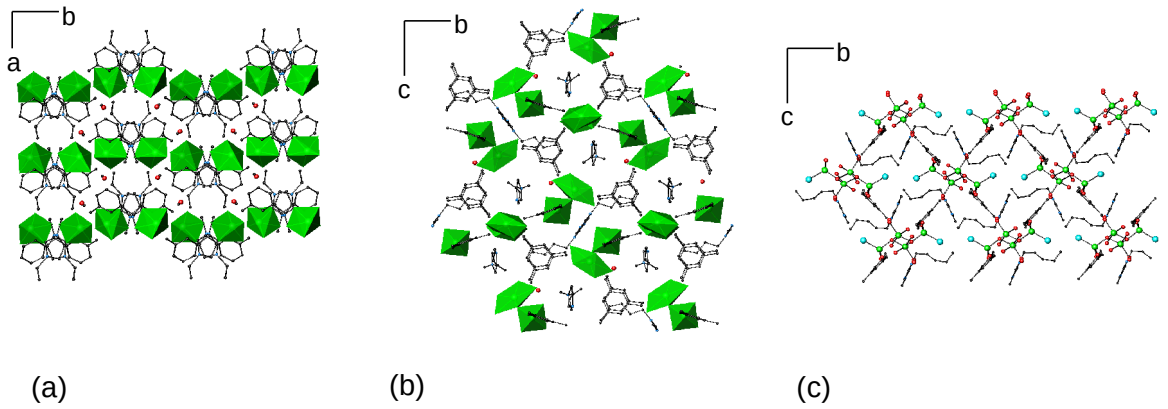

Figure 1.39. (a) Structure of $[Zn_3(BTC)_2(H_2O)_2]2H_2O$ (ZnO_5 polyhedra, green; C, black; N, blue; O, red); (b) Structure of [PMI][Zn(BTC)] (ZnO_6 octahedra, green; O, red; N, blue; C, black); (c) Structure of (AMI)[Zn_2(BTC)(OH)Br] (Zn, green; Br, blue; O, red; C, black; N, dark blue).

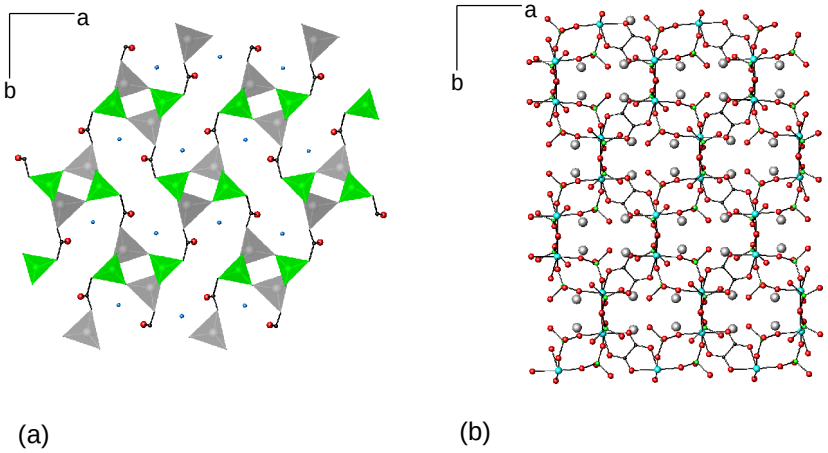

Figure 1.40. (a) Structure of $[Zn(O_3PCH_2CO_2)]\cdot NH_4$ in which NH_4^+ cations are located inside the channels (N, blue; ZnO_3C tetrahedra, grey; PO_3C tetrahedra, green; O, red); (b) Structure of $Cs_2Fe(C_2O_4)_{0.5}(HPO_4)_2$ (Cs, grey; Fe, blue; P, green; O, red).

1.5 Aims of this work

The aim of this work is to use solvothermal, hydrothermal and ionothermal methods for the preparation of novel materials containing oxy-anions and study their magnetic properties. As already described in this chapter, open-framework inorganic and inorganic-organic hybrid materials constitute an important area of study in materials chemistry due to their potential applications in areas such as sorption and catalysis. Besides the aluminosilicate zeolites, a wide range of phosphates and carboxylates containing transition

metals have been prepared. Since the works of Rao and co-workers in the synthesis of a family of organically-templated cadmium sulphates, there has been a growing interest in the study of the oxy-anions of sulphur for the generation of compounds of the transition metals. The major research interest for the study of compounds of the transition metals lies in their magnetic behaviour. Therefore, the use of the sulphate tetrahedra as a building unit for the generation of transition metal frameworks will be explored making use of a wide variety of amines, and their magnetic properties will be intensely investigated. Furthermore, rare-earth elements display interesting coordination chemistry that can provide access to novel framework architectures and they have been under intense study due to their potential applications in ion exchange, fluorescence, luminescence, separation of lanthanide elements and ion conduction. To date, structural information and measurements of physical properties of organically-templated rare-earth sulphates are very limited. In this work, solvothermal synthesis will be employed as a route for the preparation of novel rare-earth sulphates, which may exhibit interesting topologies, and their magnetic properties will be studied. The final aim of this research project is to investigate the ionothermal method for the synthesis and characterisation of inorganic materials containing oxy-anions.

Chapter 2: Preparation and Characterisation

2.1 Synthesis

2.1.1 Introduction

Solvothermal reactions are defined as chemical reactions between precursor(s) dispersed in a solvent at a temperature higher that the boiling temperature of the solvent and under high pressure conditions, usually carried out in sealed autoclaves. The method has proved to be extremely efficient both in the search for new compounds with specific physical properties and in the systematic physicochemical investigation of intricate multicomponent systems at elevated temperatures and pressures. The most common solvent used in these reactions is water, giving rise to what has been named hydrothermal reactions, but also other solvents, such as organic solvents or ionic liquids (ionothermal synthesis) have been tried. Typical reactions involve mixing solid reagents in a Teflon liner (Figure 2.1), with an inner volume of 23 mL when carrying out a laboratory-scale synthesis, which is closed and placed inside a stainless steel autoclave. Then, the autoclave is heated up inside an oven to maximum 473 K (because above this temperature the Teflon will warp). While these are the most frequently used containers, other containers, such as sealed tubes, can be employed.

Chemical factors, such as the nature of the solvent, the metal-salt type and the reagent ratio, thermodynamical factors, such as the temperature and the pressure, and other variables such as the reaction time, play an important role in these reactions. In order to be able to screen that many possible combinations, parallel and combinatorial synthetic approaches have been developed, allowing the performance of up to 1000 reactions simultaneously [282]. This high-throughput synthesis has been used in the preparation of zeolites [282] and phosphates [283] under hydrothermal conditions.

2.1.2 Synthetic Methods

2.1.2.1 The Ionothermal Synthesis

The Ionothermal method was used for the synthesis of the barium carbonate chloride and langbeinite-type phases. For this purpose, the ionic liquid was placed in a pyrex tube with the other reactants. The tube was connected to a vacuum line, and the contents were frozen using liquid N_2. Before sealing with a blow torch, the tube was

evacuated for at least 10 minutes down to 1 torr. The tube was placed in a Teflon holder inside an oven in which it was heated up to the desired temperature, normally between 423 K and 443 K. The products were then cooled down slowly over 12 hours to room temperature and the tubes were opened in the fume cupboard. The products were filtered and washed with methanol and acetone and dried in air at room temperature.

2.1.2.2 The Hydrothermal/Solvothermal Synthesis

The Solvothermal method was applied for the synthesis of transition metal and rare-earth sulphates. The reagents were loaded into a 23 mL Teflon-lined stainless steel autoclave. After stirring the mixture, the container was closed, heated at 423-443 K for up to six days typically and then cooled down to room temperature at a cooling rate of 1 K min^{-1}. The products were filtered, washed with deionized water, methanol and acetone and dried in air at room temperature.

All crystalline products obtained using both methods were primarily analysed using single-crystal X-ray diffraction and powdered products by powder X-ray diffraction.

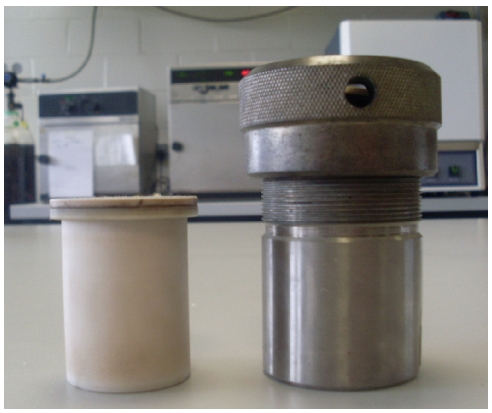

Figure 2.1. Teflon liner and solvothermal stainless steel autoclave.

2.2 Structural Determination Methods

2.2.1 Powder X-ray diffraction

The bulk reaction products were characterised by powder X-ray diffraction using three different instruments due to the installation of two new pieces of equipment during the course of this research project. A description of the three instruments will be shown in the next sections.

2.2.1.1 Philips PA2000 Powder Diffractometer

At the first stages of this project, a Philips PA2000 powder diffractometer, with nickel filtered CuK_α radiation (λ=1.5418 Å) was used. The samples were finely ground and located in flat plate aluminium holders. For small samples, a ground portion of it was mixed with vacuum grease and mounted on a microscope slide that was used as a holder. Data for routine identification were collected at a counting time of 1 s at 0.05° increments in 2θ over the angular range of $5 \leq 2\theta\ /° \leq 80$. When higher resolution data were required, the counting time was increased to 5 s per step and the step size reduced to 0.02°, while the angular range was kept unchanged. The powder X-ray diffraction pattern of the new crystalline phase was simulated using Powder cell (version 2.4) [284] and compared to the one obtained experimentally. Unassigned peaks due to crystalline impurities were compared to the powder X-ray diffraction patterns of known transition metal sulphates and barium carbonates, which are available from the Inorganic Crystal Structure (ICSD) and Cambridge Structural Database (CSD) [285].

2.2.1.2 D8 Discover Bruker Diffractometer

A D8 Discover Bruker diffractometer with nickel filtered CuK_α radiation (λ=1.5418 Å) equipped with a Goebel-mirror to focus the X-ray beam which operates in transmission has also been used (Figure 2.2). Routine scans on the samples obtained from each batch of reactions were performed using the D8 Discover diffractometer over the angular range $4 \leq 2\theta\ /° \leq 50$ at a counting time of 0.02 s per step in 0.25 increments. A ground portion of each of these samples was located in one of the 96 holes that formed each holder.

2.2.1.3 D8 Advance Bruker Diffractometer

A D8 Advance Bruker diffractometer fitted with Bruker LynxExe linear detector and operating with germanium-monochromated $CuK_{\alpha1}$ radiation (λ=1.54056 Å) in Bragg-Bentano geometry was used when high resolution data were required over the angular range $5 \leq 2\theta\ /° \leq 85$ in 0.01 increments, counting for 0.4 s at each step. Zero-background holders were used instead of the standard powder holders due to the small quantities of sample available. These are holders made of single-crystal silicon of 24.5 mm in which the diffraction peak that may be produced is in a position in the diffraction pattern that does not interfere with interpretation of the results (2θ=69°). Samples were ground to a fine powder

and loaded into the zero-background holders by smearing a trace of vaseline onto the surface of the holder and sprinkling the powder sample into this.

The EVA program [286] was used for the initial examination and evaluation of powder X-ray diffraction data collected using both D8 Bruker diffractometers. The powder X-ray diffraction pattern of any new crystalline phase was simulated using Powder cell (version 2.4) [284] and compared to that obtained experimentally. Unassigned peaks due to crystalline impurities were compared to the powder X-ray diffraction patterns of known transition metal and lanthanide sulphates and barium carbonates by searching the Powder Diffraction File (PDF) Database [287]. Refinement of lattice parameters for a given set of diffraction data was done with the TOPAS program [288].

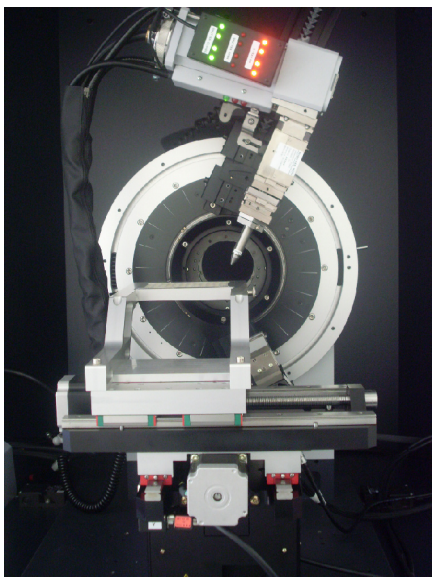

Figure 2.2. D8 Discover Bruker diffractometer

2.2.2 Single-crystal X-ray diffraction

Crystalline products were analysed by single- crystal X-ray diffraction using a Bruker X8 APEX 2 diffractometer with graphite monochromated MoK_{α} radiation (λ=0.71073 Å). X-ray data were collected at 293 K.

A selected crystal, of typical dimensions 0.3 x 0.2 x 0.2 mm, which was mounted on a glass fibre using cyanoacrylate adhesive under optical microscope, was supported on a goniometer head and centred within the X-ray beam. The unit cell was determined by collecting 12 frames, at exposure time of 10 seconds, for 6° Ω sweeps at 0, 120 and 240° Φ angles and constant 2θ and χ angles. The 36 diffraction patterns produced were analysed

using Apex-2 software [289] from which the unit cell geometry was determined, and refined. The initial examination of the crystal also showed the quality of the crystal. If less than 75% of the diffraction spots were fitted by the assigned unit cell and the RMS (Root Mean Square) angle was greater than 0.3, a better crystal was selected before proceeding with the experiment. At this stage an initial assessment of the crystal system was carried out but it was found to be preferable to perform data collection assuming triclinic symmetry with a resolution of 0.7 Å and 10 seconds exposure time per frame collecting at least 99 % of the data, using Apex-2 software [289]. The crystal system and the space group were later determined on the basis of the complete data set.

A list of reflections was produced, with the *hkl* indices and the measured intensity. A data reduction process was then performed to apply corrections in which the intensities *I* were converted to observed structure amplitudes $|F_0|$ and the corresponding standard uncertainties σ(*I*) to σ(F_0) using the Apex-2 software [289]. Further corrections were done using the program SADABS [290] which corrects for changes in the incident X-ray beam intensity or scattering power of the crystal during the experiment, the X-ray absorption and the crystal decay. The result of this whole process is a list of reflections as *h*, *k*, *l*, $|F_0|$, σ(F_0). Once the intensities were corrected, the space group was determined using the Apex-2 software [289], which compared the intensities that were equivalent by symmetry, and considered which systematic absences, if any, were in the data.

Next step was the solution of the structure, in which atomic positions in the unit cell were obtained from the data. The electron density, $\rho(xyz)$, associated with the atoms is the reverse Fourier transform of the diffraction pattern.

$$\rho(xyz) = \frac{1}{V}\sum_{h,k,l} |F(hkl)|.\exp[i\Phi(hkl)].\exp[-2i\pi(hx+ky+lz)] \qquad (2.\ 1)$$

expression in which $|F(hkl)|$ refers to the corrected amplitudes, and exp[$i\Phi(hkl)$] and exp[$-2i\pi(hx+ky+lz)$] refer to the phases. The contribution of each reflection *hkl* to each position *xyz* were calculated from the measured amplitudes $|F(hkl)|$, but the phases of the reflections were unknown. To solve the structure and determine the phases, direct methods (SIR-92 [291]) were used, in which the most important reflections were selected working out the probable relationship among their phases and then trying different possible phases

to see how well the probability relationships were satisfied. The end result is an *E-map*, similar to an electron density map, from which atomic positions were determined.

Fourier calculations were carried out to locate possible lighter atoms such as O, C, N and H, using CRYSTALS program suite [292], which calculate the differences between the observed and the calculated structure factors $|F_0|$ - $|F_c|$ to construct a difference Fourier map, in which existing atoms of the current model would not appear. Instead it would show regions of low, positive electron density (peaks) associated with undetected light atoms or regions of negative electron density (holes), indicating that an atom has been wrongly placed at the position. Once most of the atoms have been located, least squares refinement procedures were used to improve the agreement between the observed and the calculated structure factors $|F_0|$ and $|F_c|$, and minimise *R*-factor, which is the residual factor, defined as

$$R = \frac{\Sigma\left||F_o| - |F_c|\right|}{\Sigma|F_o|} \tag{2.2}$$

which serves to express the completeness of the model by comparing the difference between the observed and the calculated structure factors $|F_0|$ and $|F_c|$. Typically *R* is around 0.02-0.07 for a complete model. Hydrogen atoms were placed geometrically on the O, C and N atoms after each cycle of refinement. A Chebychev polynomial weighting scheme was also added to provide empirical weights to the least-squares refinement [293]. In the final cycles of refinement, positional and anisotropic thermal parameters were refined until the goodness of fit was around 1.00 and *R* was as small as possible. Typically, a final map with no features outside the range ±1 eÅ^{-3} was accepted as evidence of a satisfactory structure determination.

2.3 Analytical methods

2.3.1 Thermal Analysis Techniques

2.3.1.1 Thermogravimetric Analysis

In thermogravimetric analysis the change in mass of a substance as a function of temperature or time is measured. Thermogravimetric measurements were performed using a DuPont Instruments 951 thermal analyser to determine the organic component of new crystalline phases. 5-10 mg of finely ground handpicked crystals were loaded into a quartz

crucible suspended from the balance arm by a platinum wire. The samples were heated under N_2 or O_2 gas which was passed through the sample at a flow rate of 60 mL min^{-1}. The temperature range and heating profile varied depending on the sample under study. Typical conditions for collecting data involved a starting isothermal segment for 60 minutes at 30°C, a ramp of 5°C min^{-1} to 1000°C and a final isothermal for 30 minutes at 1000°C before cooling.

2.3.1.2 Differential Scanning Calorimetry

In Differential Scanning calorimetry (DSC) the temperature of a sample is compared with that of an inert reference material during a programmed change of temperature. The sample and the reference are maintained at the same temperature until a thermal event, such as decomposition, melting or change in crystal structure, takes place. When that occurs, enthalpy changes are directly measured.

Approximately 5 mg of sample were pressed into a pellet and heated at a heating rate of 20 K min^{-1} on a TA Instruments DSC 2010 calorimeter fitted with a cryogenic unit, in which the sample compartment is purged with N_2.

2.3.2 Elemental Analysis

For CHN determination, an Exeter CE-440 Element Analyzer (Figure 2.3) was used. The sample is introduced in a capsule that is heated up in an oxygen environment, leading to the combustion of the sample to form CO_2, N_2, N_xO_y, H_2O and other products. The sample passes through a reduction tube that converts oxides of nitrogen in N_2, reaching a series of conductivity cells where the proportion of each gas is measured. From these readings, and the weight of sample used, the proportion of carbon, hydrogen and nitrogen are calculated. Measurements were performed by Mrs. C. Graham of the Chemistry Department in Heriot-Watt University on 2-3 mg of handpicked crystals.

2.3.3 Spectroscopic Methods

2.3.3.1 Fourier Transform Infrared (FTIR)

Fourier transform infrared spectroscopy is a technique for collecting infrared spectra in which instead of varying the frequency of the incident radiation in order to obtain the quantity of radiation absorbed or transmitted by the sample (IR), the IR beam that passes

through the sample is guided to an interferometer producing an interferogram. The resulting plot is obtained by applying a mathematical Fourier transform to the signal, in which the intensity of absorption as a function of frequency or wavelength is represented. This technique is especially useful for identifying specific functional groups, such as organic molecules.

A small amount of hand-picked crystals (*ca*. 5 mg) was pressed under vacuum in a CsI matrix at 10 tonnes for 3-5 minutes, until 13 mm diameter pellets, with 1-2 mm thickness, were obtained. Infrared spectroscopic data were recorded using a Perkin Elmer Spectrum RX FT-IR system in the range of 400-4000 cm^{-1}.

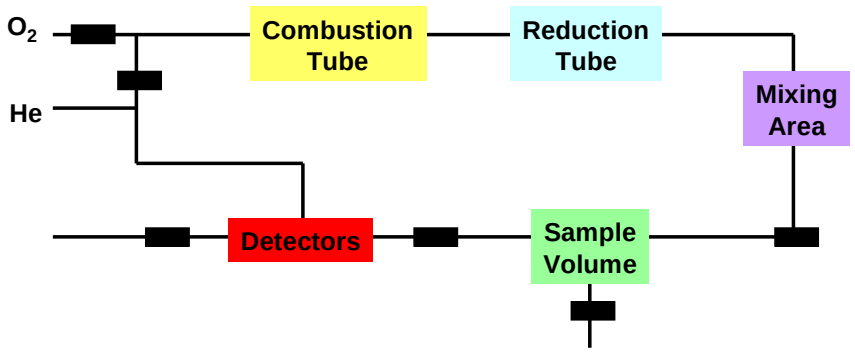

Figure 2.3. Schematic Diagram Exeter CE-440 Elemental Analyser [294]

2.3.3.2 Diffuse Reflectance

Finely-ground hand-picked single crystals (*ca*. 15 mg) diluted with $BaSO_4$ were deposited as a smooth thin layer over a diffuse reflectance holder. Diffuse Reflectance data were measured over the range 200-1100 nm (1.2-6.2 eV) in steps of 240 nm min^{-1} using a Perkin Elmer Lambda 35 UV-Vis Spectrometer. Absorption data and band gaps were analysed using the Kubelka-Munk function, which is defined as:

$$F(r_\infty) = \left({}^{1}\!/_{r_\infty} \right) \Big/ 2r_\infty = {}^{k}\!/_{s} \qquad (2.3)$$

The optical band gap is determined by reading the value of the y-axis where the absorption edge and the baseline cross.

2.3.3.3 Electron paramagnetic resonance (EPR)

Electron paramagnetic resonance is a spectroscopic technique, used for studying materials which possess one or more unpaired electrons, that detects changes in spin configuration. The EPR spectra are generated by varying the magnetic field at a constant frequency. The majority of EPR measurements are operated at microwave frequencies (9-10 GHz). An external magnetic field produces a splitting of the energy levels of a paramagnetic ion. By increasing the magnetic field, the separation between the lower and the upper energy states is widened until it matches the energy of the microwaves. At this state, an unpaired electron can move between the two energy levels. Since there normally are more electrons in the lower state, there is a net absorption of energy that is monitored and converted into a spectrum. That occurs at the resonance condition:

$$\Delta E = h\nu = g_e \mu_B B_0 \tag{2.4}$$

where g_e is the gyromagnetic ratio, μ_B is the Bohr magneton and B_0 is the applied magnetic field. EPR spectra are generally used to obtain information on the oxidation state, electronic configuration and coordination number of the paramagnetic ion as well as to determine the ground state *d* of orbital configuration and any structural distorsion of the ion.

Electron paramagnetic resonance (EPR) studies were performed by Dr Rodolfo Sánchez in the Centre of Science in Bariloche, Argentina.

2.4 Magnetic susceptibility measurements

2.4.1 Background

A magnetic field is created when charged particles are in motion. In an atom, the magnetic moment is a result of two types of motion of the electron: the spin magnetic moment due to the spinning of the electron on its axis, and the orbital magnetic moment due to the electron orbiting the nucleus. The total magnetic moment is a combination of the spin and orbital magnetic moments of the atoms of a material which give rise to the observed magnetic properties. Diamagnetism is a property of all materials. Its effect is very weak and opposes applied magnetic fields. In contrast, if in the presence of a magnetic field moments align themselves randomly causing an induced magnetisation parallel to it, paramagnetism takes place. The most common form of magnetic ordering is

antiferromagnetism, which involves antiparallel coupling of ions, giving zero overall magnetic moment. Ions may align parallel to each other, in which case the material exhibits ferromagnetic behaviour. A special case is that in which ions are partially anti-aligned, which results in a net magnetic moment. This behaviour is known as ferrimagnetism.

When a substance is subjected to a magnetic field, a magnetisation, **M**, defined as the magnetic dipole moment per unit volume, is acquired, which is proportional to the applied field **B** and can be expressed by

$$M = \mu_o^{-1} \chi_m B \tag{2.5}$$

where μ_o is the vacuum permeability and χ_m is the magnetic susceptibility, which is the magnetisation induced by unit applied magnetic field. The magnetic susceptibility per unit mass is defined as $\chi_\rho = \chi_m / \rho$ with units $kg^{-1}\ m^3$, but the molar susceptibility, defined as the susceptibility per mole of substance, is more useful in chemistry, and is given by

$$\chi_{mol} = \frac{\chi M_r}{10^3 \rho} \quad (m^3\ mol^{-1}) \tag{2.6}$$

where ρ and M_r are the density and the relative molecular mass, respectively.

Many paramagnetic substances obey the Curie law, especially at high temperature, which states that the magnetic susceptibility is inversely proportional to temperature:

$$\chi = \frac{C}{T} \tag{2.7}$$

in which C is the Curie constant. This equation applies when there is no spontaneous interaction between adjacent unpaired electrons. However, when this interaction occurs, which may develop into ferro- or antiferromagnetic ordering at low temperatures, a better fit to the high temperature behaviour in the paramagnetic region is provided by the Curie-Weiss law:

$$\chi_{mol} = \frac{C}{T - \theta} \tag{2.8}$$

where θ is the Weiss constant, which is positive for materials that show a tendency to ferromagnetic order and negative for those than instead display antiferromagnetic correlations.

Magnetic properties are often expressed in terms of the magnetic moment, μ, which is related to the molar susceptibility, χ_{mol}, by the following equation

$$\chi_{mol} = \frac{N_A \beta^2 \mu^2}{3kT} \tag{2.9}$$

which is the Langevin equation in which N_A is Avogadro's number (6.023×10^{23} mol^{-1}), β is the Bohr magneton (9.274×10^{-24} A m^2), k is the Boltzmann's constant (1.381×10^{-23} J K^{-1}) and T is the temperature (in K). With reference to equation (2.9), the Curie constant is therefore defined as:

$$C = \frac{N_A \beta^2 \mu^2}{3k} \tag{2.10}$$

When the excited state energies are larger than *kT*, the orbital and spin vectors, *L* and *S* respectively, interact strongly. In this situation, the total angular momentum (*J*) becomes dominant and *L* and *S* no longer dictate the macroscopic magnetic properties. In that situation equation (2.10) is obeyed. This relates the total angular momentum quantum number, *J*, to the total magnetic moment μ.

$$\mu = g\sqrt{J(J+1)} \tag{2.11}$$

g is known as the "Lande splitting factor" and is the ratio of magnetic moment to angular momentum, and can be expressed as

$$g = \tfrac{3}{2} + \frac{S(S+1) - L(L+1)}{2J(J+1)} \tag{2.12}$$

S is the total spin quantum number and L is the total orbital quantum number. For transition metal ions g=2, whereas for rare-earth ions $g_J < 1$ for $N < 7$ (less than half-filled subshell) and values $1 < g_J < 2$ when $N > 7$.

For the first row of transition metal complexes splitting of the d-orbitals by the ligand field often quenches the orbital moment so that L≈0. This means that J=S and equation reduces to the following spin-only equation,

$$\mu_{s.o.} = g\sqrt{S(S+1)} \tag{2.13}$$

When the moment differs from $\mu_{s.o.}$, it is possible that a finite value of *L*, i.e. an “orbital contribution” is contributing to the magnetic moment, or that the sample is not sufficiently dilute so that magnetic interactions between the open-shell ions are present.

For materials which show ferromagnetic ordering the saturated magnetic moment per ion can be determined. The saturation occurs when the Boltzman energy is much less than the magnetic energy, and the ground state level of the ion is solely occupied.

Measurements of the magnetisation as a function of field at low temperatures allow the calculation of the saturated magnetic moment.

The average magnetic moment of one molecule, $<\mu_z>$, summed over all the Zeeman levels is

$$\langle \mu_z \rangle = \frac{g\beta}{N_A} \sum_{m=-J}^{J} -nm \tag{2.14}$$

The component of the average magnetic moment in the field direction is expressed as:

$$\langle \mu_z \rangle = g\beta \frac{\sum_{m=-J}^{J} m \exp[-mx]}{\sum_{m=-J}^{J} \exp[-mx]} \tag{2.15}$$

where x is the ratio of magnetic energy $g\beta H_z$, which aligns the magnetic moments to the thermal energy kT that causes the system to orient randomly.

$$x = g\beta H_z / kT \tag{2.16}$$

Through mathematical manipulation, the average magnetic moment in the field is of the general form

$$\langle \mu_z \rangle = g\beta J B_J(x) \tag{2.17}$$

where the Brillouin function, $B_J(x)$, is defined as

$$B_J(x) = \frac{1}{J}\left[\left(J+\tfrac{1}{2}\right)\coth\left(J+\tfrac{1}{2}\right)x - \tfrac{1}{2}\coth x/2\right] \tag{2.18}$$

.

Hence, at high fields and low temperatures x>>1 and $B_J(x) \rightarrow 1$, and the average magnetic moment tends towards the saturated magnetic moment

$$\langle \mu_{sat} \rangle = g\beta J \tag{2.19}$$

. Therefore the saturated magnetic moment (in Bohr magnetons) approaches gJ as the field increases at low temperature. In the spin-only case, where g=2 and J=S, the spin-only magnetic moment approaches a maximum of 2S.

2.4.2 Measurement of magnetic properties

Magnetic properties were analysed using a **S**uperconducting **QU**antum **I**nterference **D**evice (SQUID) magnetometer. A SQUID magnetometer consists of a SQUID unit, which contains a superconducting loop separated by two Josephson junctions (for a DC SQUID),

a flux transformer including pick-up coils, a superconducting magnet and magnetic shielding, all of which are immersed in a liquid He-bath (Figure 2.4). To enhance the capabilities of the SQUID, the SQUID is not directly exposed to the magnetic field of interest, but inductively linked to the sample through a multiple-turn pickup coil. The SQUID is shielded from the ambient field by a superconducting niobium canister.

The magnetic field which is applied to the sample is produced by the superconducting magnet. When the sample is moved slowly through the pick-up coils, its magnetic moment induces a magnetic flux change in the pick-up coils, which is transferred via the flux-transformer to the SQUID unit. A change in the applied flux in the SQUID leads to a phase difference across the junctions, giving rise to a voltage across the loop that can be detected.

2.4.3 Experimental

SQUID magnetometry measurements were performed using a Quantum Design MPMS system and a XL MPMS system located at the University of Edinburgh. Samples of handpicked crystals (20-30 mg) were accurately weighed and loaded into gelatine capsules of known weight. The capsules were individually placed and secured in the middle of a plastic drinking straw and attached to the end of the sample stick. The sample is centred before being lowered into the cryostat. Measurements as a function of temperature were performed using zero-field-cooled/field-cooled (*zfc/fc*) mode. The *zfc* measurements were done by cooling the sample to 2-5 K when H=0. A magnetic field was then applied and the magnetisation measured as a function of temperature. The *fc* measurements were done by cooling the sample to 2-5 K in H=100G or 1000G, and the magnetisation was again measured as a function of temperature. Data were generally collected at 1 K steps at low temperature, increasing gradually to 10 K steps in the range of 150-300K. Measurements made as a function of field were performed at 5 K, after cooling the sample under zero-field. Data were collected in 500 G steps from 0 G to 10,000 G (1 T) in the MPMS system and to 70,000 (7 T) in the XL MPMS system.

The SQUID output is expressed as raw magnetisation, M_{raw} in electromagnetic units (emu), which was corrected for the diamagnetic contribution of the gelatine capsule, $M_{cap,}$ hence,

$$M_{corr} = M_{raw} - M_{cap} \qquad (2.20)$$

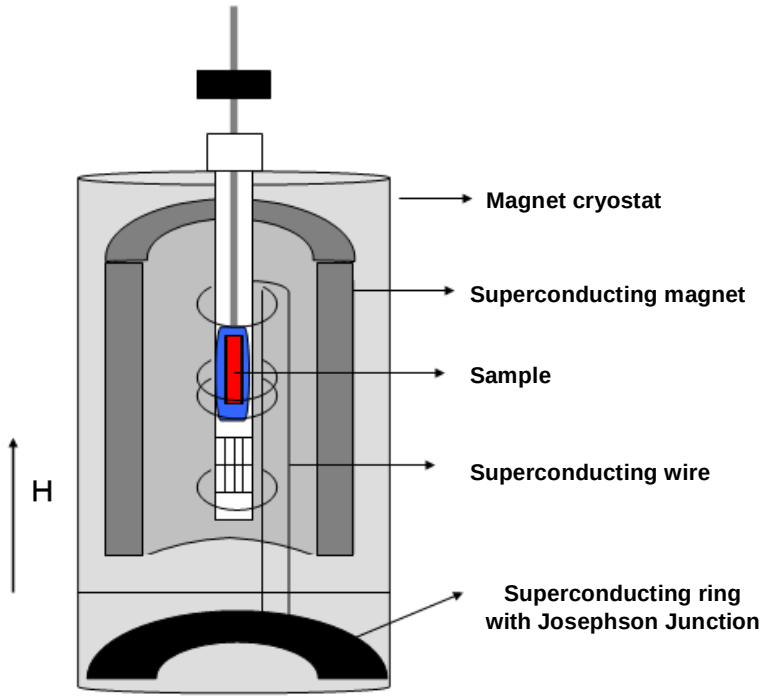

Figure 2.4. Schematic diagram of a SQUID magnetometer

The corrected magnetisation allows the determination of the molar susceptibility, χ_{mol}.

$$\chi_{mol} = \frac{M_{corr}}{nH} \tag{2.21}$$

where H is the external magnetic field and *n* is the number of moles in the sample. χ_{mol} was corrected for the diamagnetic contribution from the ions within the formula unit. For a material that exhibits Curie-Weiss behaviour, equation (2.22) can be expressed as

$$\frac{1}{\chi_{mol}} = \frac{T}{C} - \frac{\theta}{C} \tag{2.22}$$

A plot of $1/\chi_{mol}$ against T results in a straight line above the magnetic ordering temperature, with a gradient of 1/C and an intercept of -θ/C. The effective magnetic moment, μ_{eff}, can also be calculated using equation (2.23) simplified to

$$\mu_{eff} = \sqrt{\frac{8C}{m}} \tag{2.23}$$

in which *m* is the number of magnetic ions per formula unit.

The saturated magnetic moment was determined by plotting the moment per metal centre (μ_c) of a compound as a function of field. μ_c is calculated using the equation (2.24),

$$\mu_c = \frac{M_{corr}}{nmN_A} \tag{2.24}$$

in which M_{corr} is the corrected magnetisation in Bohr magnetons, n is the number of moles of sample, m is the magnetic centres per formula unit, and N_A is Avogadro's number.

The value to which the moment per metal centre tends is the saturated magnetic moment, μ_{sat}. This is the value of the magnetic moment in an infinite field.

$$\mu_{sat} = \sqrt{\frac{8\chi T}{n}} \tag{2.25}$$

Chapter 3: Ionothermal synthesis of materials containing oxy-anions

3.1 Introduction

In recent years, ionic liquids have increasingly been applied to the synthesis of inorganic particles, such as mesoporous $SrCO_3$ spheres and $CaCO_3$ hollow spheres [295]. Research into the ionothermal synthesis of microporous materials was stimulated by the report of the first synthesis of an aluminophosphate [22] and the syntheses of a layered aluminophosphate [264] and a cobalt aluminophosphate [23] in the presence of an ionic liquid. In these materials the ionic liquid acts both as solvent and structure directing agent.

The role of the ionic liquid in the low-temperature synthesis of inorganic materials has been investigated. With this purpose, a wide range of reactions was attempted employing a broad variety of reactants such as transition metals, transition metal sulphides and chlorides, transition metal salts (nitrates and carbonates) and sulphur, in the presence of 1-ethyl-3-methylimidazolium bromide ([EMIM] Br) ionic liquid (Figure 3.1) and the eutectic mixture urea/choline chloride. Using choline chloride/urea eutectic mixture, only few known simple salts, mainly binary sulphides, were synthesised. However, efforts directed to the synthesis of novel inorganic materials making use of 1-ethyl-3-methylimidazolium bromide ([EMIM] Br) ionic liquid were fruitful, demonstrating their potential for the generation of novel materials with promising properties.

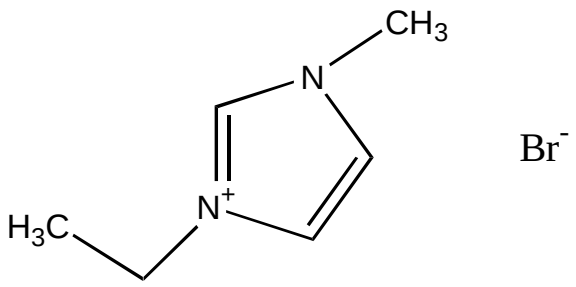

Figure 3.1. 1-Ethyl-3-methylimidazolium bromide ([EMIM] Br)

In this chapter, the ionothermal preparation and characterisation of the $(NH_4)_2M_2(SO_4)_3$ (M=Mn, Fe) **(1)-(2)** langbeinite-type phases and the barium carbonate chloride, $Ba_3Cl_4CO_3$ **(3)**, are reported, together with a study of the magnetic properties of

the former. Instead of the preferred synthetic approach in which Teflon-lined stainless steel autoclaves are used as reaction containers, sealed tubes were employed.

3.2 Langbeinite-type phases, $(NH_4)_2M_2(SO_4)_3$, M=Mn, Fe (1)-(2)

3.2.1 Synthesis

$(NH_4)_2Mn_2(SO_4)_3$ **(1)** was initially synthesised under ionothermal conditions in sealed tubes from the reaction of 0.1278 g of $In(NO_3)$, 0.021 g of S and 0.028 g of MnS in the presence of [EMIM] Br (0.5 g). The reagents were in the molar In:S:Mn:IL composition ratio 1:2:1:8. The mixture was placed in a Pyrex tube and the contents frozen with liquid nitrogen. The tube was connected to a vacuum line and evacuated to 1 Torr before sealing it with a glassblowing torch. The sealed tube was placed in an oven, heated at 170 °C for two days and then cooled to room temperature at a rate of 1 °C min^{-1}. The product was filtered, washed with methanol and acetone and dried in air at room temperature overnight. The product consisted of a mixture of crystals of **(1)**, which were identified by single-crystal X-ray diffraction, and a green powder identified as MnS by powder X-ray diffraction. Different reactions were attempted in order to optimise this synthesis and $(NH_4)_2Mn_2(SO_4)_3$ **(1)** was eventually obtained as a single phase consisting exclusively of the manganese langbeinite, using the same synthetic technique under the same conditions from reaction of 0.06 g of $Mn(NO_3)_2$ with 0.021 g of sulphur in the presence of 0.5 g of [EMIM] Br in the molar Mn:S:IL composition ratio 1:2:8. The product was filtered and washed with methanol and acetone. It consisted of crystals of $(NH_4)_2Mn_2(SO_4)_3$ **(1)** identified by single-crystal X-ray diffraction.

Following an analogous procedure, $(NH_4)_2Fe_2(SO_4)_3$ **(2)** was successfully synthesised from the reaction mixture $Fe(NO_3)_2{\cdot}9H_2O$ (0.264 g; 0.6 mmol), S (0.021g; 1.2 mmol) and [EMIM] Br (0.5 g; 2.4 mmol) in a composition ratio 1:2:4. The sealed tube was placed in an oven, heated at 170°C for two days and then cooled to room temperature at a rate of 1 °C min^{-1}. The product was filtered, washed with methanol and acetone and dried in air at room temperature overnight. The product consisted of crystals of $(NH_4)_2Fe_2(SO_4)_3$ **(2)** which were identified by single-crystal X-ray diffraction.

3.2.2 Single-crystal diffraction

Single-crystal X-ray diffraction data for $(NH_4)_2M_2(SO_4)_3$ (M= Mn, Fe) **(1)-(2)** were collected at 293 K using a Bruker Nonius X8 Apex diffractometer with Mo-Kα radiation (λ=0.71073 Å). Additional single-crystal X-ray diffraction data were collected at 100 K for $(NH_4)_2Mn_2(SO_4)_3$ **(1)**. Data were processed using the Apex-2 software [289]. The structures were solved using the direct methods program SIR92 [291], which located M (M=Mn, Fe), sulphur and most of oxygen atoms. Subsequent difference Fourier calculations, to locate the remaining O atoms and N atoms, and least-squares refinements were carried out using the CRYSTALS suite of programs [292]. Some hydrogen atoms were found in difference Fourier maps and the remaining introduced manually. In the final cycles of refinement, positional and anisotropic thermal parameters for all non-hydrogen atoms were refined. Crystallographic details are given in Table 3.1. Atoms coordinates for $(NH_4)_2M_2(SO_4)_3$ **(1)-(2)** at 293 K are given in Appendix B. Selected bond distances and angles at 293 K are summarised in Table 3.2. Atoms coordinates and selected bond distances and angles for $(NH_4)_2Mn_2(SO_4)_3$ **(1)** at 100 K are given in Appendix B and C, respectively.

3.2.3 Characterisation

Results of the CHN analysis for $(NH_4)_2Mn_2(SO_4)_3$ **(1)** gave H 1.83 % and N 6.44 %, which is in excellent agreement with the theoretical values (H 1.85 %; N 6.45 %). Elemental analysis for $(NH_4)_2Fe_2(SO_4)_3$ **(2)** gave H 2.1% and N 6.1 % which agrees with the value calculated from the crystallographically determined formula $(NH_4)_2Fe_2(SO_4)_3$ **(2)** (H 1.85%; N 6.43%).

Powder X-ray diffraction data were collected over the range $4 \leq 2\theta\ /° \leq 50$ on a ground portion of bulk sample. The diffraction patterns of the products indicate the presence of $(NH_4)_2M_2(SO_4)_3$ (M=Mn, Fe) **(1)-(2)** as the majority phases and the peaks can be indexed on basis of a cubic unit cell determined for $(NH_4)_2M_2(SO_4)_3$ (M=Mn, Fe) **(1)-(2)** from the single-crystal diffraction study (Appendix A). The extra peaks in the diffraction pattern of **(2)** were assigned to $(NH_4)_2(SO_4)$.

The mass losses observed during thermogravimetric analysis under oxygen for both $(NH_4)_2M_2(SO_4)_3$ (M=Mn, Fe) **(1)-(2)** phases are displayed on Figure 3.2. For both compounds, the weight loss takes place in two steps. For $(NH_4)_2Mn_2(SO_4)_3$ **(1)** (Figure 3.2(a)) the first step is consistent with the loss of the two moles of ammonia, one mole of

water and one mole of SO_2 (*ca.* 420 °C) with a total weight loss of *ca.* 30 % (calc: 26.75 %). The second step corresponds to the formation of Mn_3O_4 as the final product, which was confirmed by powder X-ray diffraction, with a total weight loss of 60.1 %, which is consistent with the calculated total weight loss (64.8 %). The thermogravimetrical analysis of $(NH_4)_2Fe_2(SO_4)_3$ **(2)** also displays a two-step decomposition process with a total weight loss of 60.4 %, in good agreement with the calculated value (63.4 %) (Figure 3.2(b)). The first step at 380°C of 8.4 % (calc: 7.91 %), is consistent with the removal of two moles of ammonia. The second step can be assigned to the removal of three moles SO_2, two moles of water and O_2 which corresponds to a weight loss of 52 % (calc: 55.56 %). The remaining product was identified as Fe_2O_3 by powder X-ray diffraction.

Table 3.1. Crystallographic data for $(NH_4)_2M_2(SO_4)_3$ (M=Mn, Fe) **(1)-(2)**.

$(NH_4)_2M_2(SO_4)_3$	**(1)**		**(2)**
Temperature / K	293	100	293
M_r	434.14	434.14	435.96
Crystal Size (mm)	0.46 X 0.46 X 0.46	0.46 X 0.46 X 0.46	0.16 X 0.22 X 0.33
Crystal Habit	Colourless tetrahedron	Colourless tetrahedron	Transparent cube
Crystal System	Cubic	Cubic	Cubic
Space Group	*P 2$_1$ 3*	*P 2$_1$ 3*	*P 2$_1$ 3*
***a*(Å)**	10.1818(2)	10.1718(9)	10.1575(10)
V (Å^3)	1055.54(4)	1052.43(16)	1047.998(18)
Z	4	4	4
μ (mm^{-1})	3.056	3.07	3.439
ρ_{calc} (g cm^{-3})	2.731	2.740	2.763
Residual electron density (min, max) (eÅ^{-3})	-0.63, 0.61	-0.47, 0.50	-0.71, 0.62
Measured data	30,543	28,456	30,463
Unique data	1076	1093	1029
Observed data *(I>3σ(I))*	996	974	969
R_{int}	0.015	0.031	0.016
R(F)	0.016	0.011	0.020
$_wR(F)$	0.017	0.012	0.052

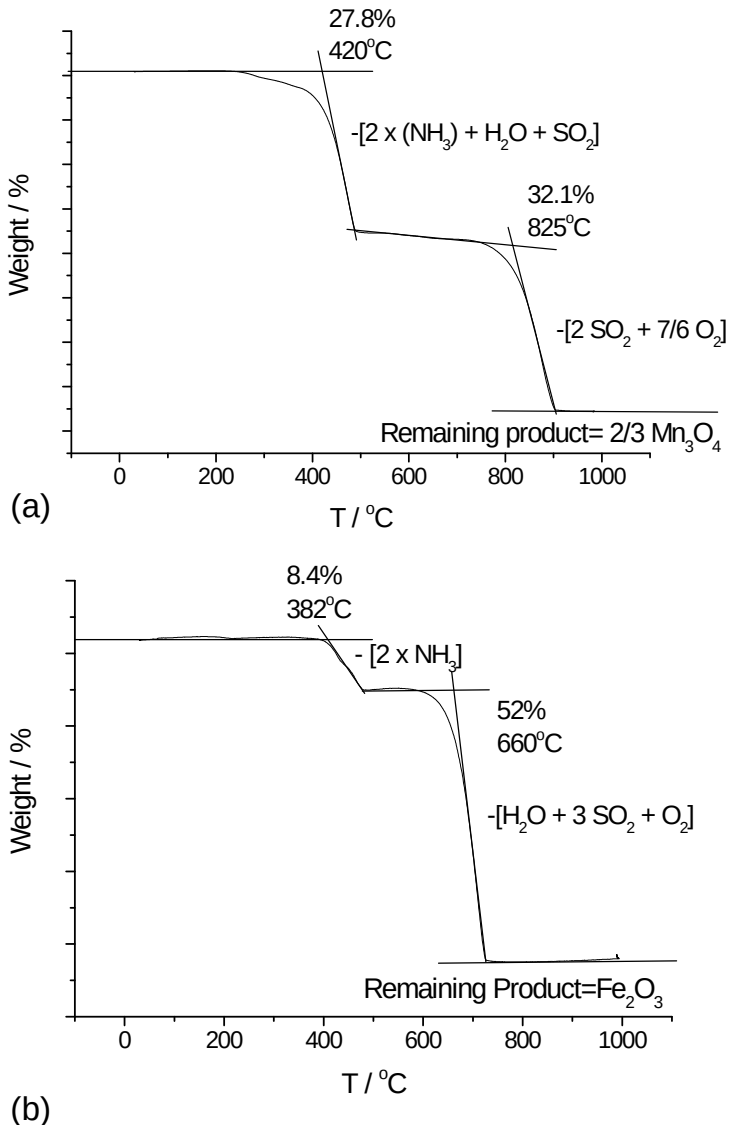

Figure 3.2. Thermogravimetric analysis data for (a) $(NH_4)_2Mn_2(SO_4)_3$ **(1)** and (b) $(NH_4)_2Fe_2(SO_4)_3$ **(2)**.

Infrared spectroscopic data is consistent with the formation of $(NH_4)_2Mn_2(SO_4)_3$ **(1)** and $(NH_4)_2Fe_2(SO_4)_3$ **(2)** (Figure 3.3). The vibrations appearing at 3390-3440, 1620 cm^{-1} and those at 1430-1440 cm^{-1} are due to the presence of NH_4^+ and can be assigned to the asymmetric stretching and the asymmetric and symmetric deformation, respectively. The vibrations at 1090-1120 cm^{-1} are attributed to the symmetric and asymmetric stretching of the SO_4^{2-} anion while those at 605-650 cm^{-1} correspond to the asymmetric deformation of the sulphate.

Differential scanning calorimetry measurements performed for $(NH_4)_2Mn_2(SO_4)_3$ **(1)** (Figure 3.4) in the range of temperatures -120 °C to 60 °C showed a variation in the

heat flow at around -47 °C (223 K), which can be associated with a possible transition taking place below this temperature. The large peak at -100 °C (173 K) is of instrumental origin. No anomaly in the heat flow was observed for $(NH_4)_2Fe_2(SO_4)_3$ **(2)**.

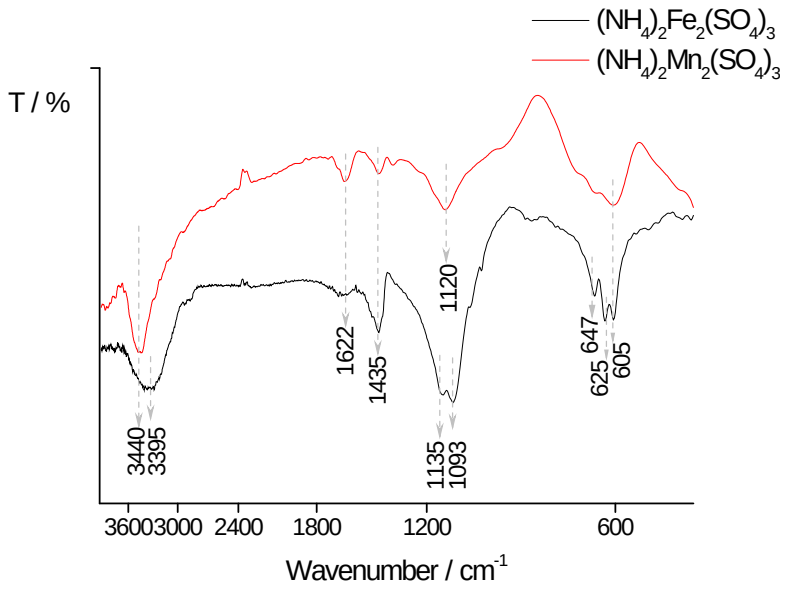

Figure 3.3. Infrared data for $(NH_4)_2Mn_2(SO_4)_3$ **(1)** (red line) and $(NH_4)_2Fe_2(SO_4)_3$ **(2)** (black line).

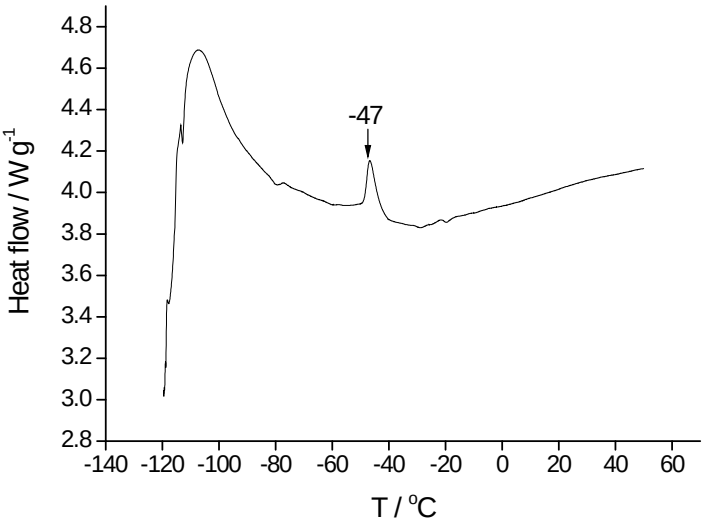

Figure 3.4. DSC measurements for $(NH_4)_2Mn_2(SO_4)_3$ **(1)**.

3.2.4 Crystal structure description

The crystal structure of $(NH_4)_2Mn_2(SO_4)_3$ **(1)** has been previously reported [296] and the two $(NH_4)_2M_2(SO_4)_3$ (M=Mn, Fe) **(1)-(2)** phases are isostructural. The local coordination scheme for both the manganese and the iron langbeinite-type compounds is

shown in Figure 3.5. In this structure each of the two crystallographically distinct metal centres is coordinated by six oxygen atoms. M-O distances range from 2.1580(12)-2.1710(13) Å for the manganese langbeinite **(1)** and from 2.1482(18)-2.168(2) Å for the iron langbeinite **(2)**, these distances being very similar for both crystallographically distinct metal centres.

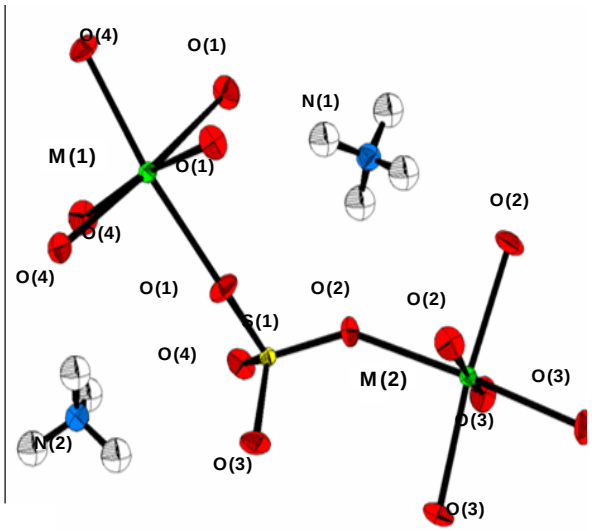

Figure 3.5. Local coordination scheme of $(NH_4)_2M_2(SO_4)_3$ (M=Mn, Fe) **(1)-(2)**. (O atoms, red; M atoms, green, N atoms, blue; S atoms, yellow)

Table 3.2. Selected bond distances (Å) and angles (°) for $(NH_4)_2M_2(SO_4)_3$ (M=Mn, Fe) **(1)-(2)** at 293 K.

Atoms (M=Mn)	**Bond distances/Å**	**Atoms (M=Fe)**	**Bond distances/Å**
Mn(1)-O(1)	3 x 2.1710(13)	Fe(1)-O(1)	3 x 2.1494(19)
Mn(1)-O(4)	3 x 2.1580(12)	Fe(2)-O(2)	3 x 2.168(2)
Mn(2)-O(2)	3 x 2.1587(12)	Fe(2)-O(3)	3 x 2.1483(18)
Mn(2)-O(3)	3 x 2.1664(12)	Fe(1)-O(4)	3 x 2.1569(19)
S(1)-O(2)	1.4695(12)	S(1)-O(1)	1.4708(18)
S(1)-O(3)	1.4609(12)	S(1)-O(2)	1.465(2)
S(1)-O(4)	1.4695(12)	S(1)-O(3)$^{(ii)}$	1.4727(18)
S(1)-O(1)	1.4691(13)	S(1)-O(4)	1.4619(19)
Atoms	**Bond angles/°**	**Atoms**	**Bond angles/°**
O(4)-Mn(1)-O(1)	3 x 90.74(6)	O(4)-Fe(1)-O(1)	3 x 88.96(8)

Atoms	Bond angles/°
O(4)-Mn(1)-O(1)	3 x 173.73(6)
O(4)-Mn(1)-O(1)	3 x 81.73(6)
O(1)-Mn(1)-O(1)	3 x 93.15(5)
O(4)-Mn(1)-O(4)	3 x 94.68(5)
O(2)-Mn(2)-O(3)	3 x 89.11(5)
O(2)-Mn(2)-O(3)	3 x 174.15(5)
O(2)-Mn(2)-O(3)	3 x 89.03(5)
O(2)-Mn(2)-O(2)	3 x 94.88(5)
O(3)-Mn(2)-O(3)	3 x 86.68(6)

Atoms	Bond angles/°
O(4)-Fe(1)-O(1)	3 x 89.05(8)
O(4)-Fe(1)-O(1)	3 x 174.38(8)
O(1)-Fe(1)-O(1)	3 x 86.92(8)
O(4)-Fe(1)-O(4)	3 x 94.79(7)
O(2)-Fe(2)-O(3)	3 x 94.61(8)
O(2)-Fe(2)-O(3)	3 x 90.67(8)
O(2)-Fe(2)-O(3)	3 x 81.73(8)
O(2)-Fe(2)-O(3)	3 x 173.81(8)
O(2)-Fe(2)-O(2)	3 x 93.28(7)

The average Mn-O distance *ca.* 2.164 Å is larger than the corresponding iron one (*ca*. 2.155 Å). Metal-oxygen distances are comparable with those reported for $MnSO_4$ [297] and $FeSO_4$ [298] with typical values reported to lie between 2.0992-2.2512 Å and 2.0243-2.2963 Å, respectively, and they are concurrent with the expected values for a covalent M-O bond (2.12 Å for a Mn-O bond and 1.98 Å for a Fe-O bond). S-O distances are also in agreement with the mean S-O distance of 1.473 Å usually found in other structures containing the sulphate oxy-anion.

Crystallographic data for $(NH_4)_2Mn_2(SO_4)_3$ **(1)** was collected at 100 K and it remains cubic with a contraction of the unit cell, with Mn-O distances ranging from 2.150(8)-2.1620(8) Å.

Each of the vertices of the MO_6 octahedron is shared with six sulphate tetrahedra forming a distorted octahedron, as shown in Figure 3.6, building a three-dimensional network in which the ammonia cations reside in the cavities within this network. Hydrogen bond distances are displayed in Appendix D. Cations and anions are held together in an extended hydrogen bond system.

3.2.5 Magnetic properties

Magnetic susceptibility data at 1000 G for $(NH_4)_2M_2(SO_4)_3$ (M=Mn, Fe) **(1)-(2)** are shown in Figure 3.7 and Figure 3.8. The reciprocal magnetic susceptibility as a function of temperature plot for $(NH_4)_2Mn_2(SO_4)_3$ **(1)** shows a discontinuity at *ca*. 45 K, the temperature at which the anomaly is observed in the magnetic susceptibility data. Above

this temperature, approximately 45 K, the reciprocal magnetic susceptibility can be fitted according to the Curie-Weiss law, with a negative value for the Weiss constant. The iron langbeinite phase **(2)** does not show the same anomaly and the reciprocal magnetic susceptibility data can be fitted to the Curie-Weiss law in the whole range of temperature. The Curie constants, magnetic moments and Weiss constants are summarized in Table 3.3. The effective magnetic moments for manganese and iron are close to the spin-only values. The Weiss constants are both negative with a higher value (-36.68(2) K) for the manganese langbeinite **(1)** constant compared to the corresponding iron containing phase **(2)**.

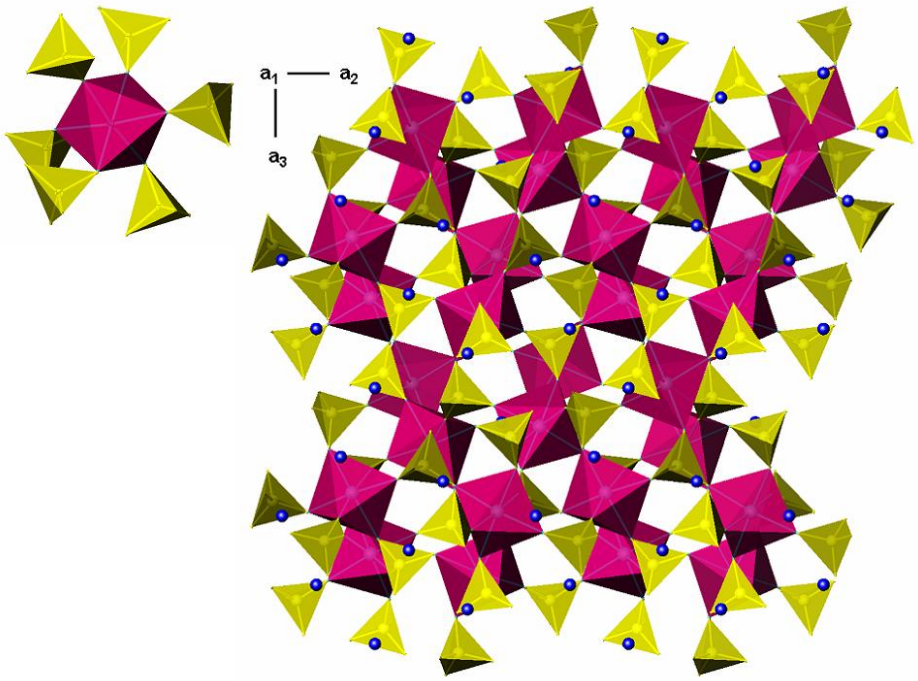

Figure 3.6. Three-dimensional structure of the langbeinite-type $(NH_4)_2M_2(SO_4)_3$ **(1)-(2)**. Inset: MO_6 octahedron surrounded by six SO_4 tetrahedra. Hydrogen atoms have been omitted for clarity (MO_6 octahedra, pink; SO_4 tetrahedra, yellow; N atoms, blue).

Table 3.3. Curie constants, magnetic moments and Weiss constants for $(NH_4)_2M_2(SO_4)_3$ (M=Mn, Fe) **(1)-(2)**.

M	C / cm^3 K mol^{-1}	μ_{eff} per M / μ_B	$\mu_{spin-only}$ / μ_B	θ / K
Mn	8.770(2)	6.22(1)	5.92	-32.75(2)
Fe	8.136(5)	5.705(4)	4.91	-20.93(2)

Both $(NH_4)_2Mn_2(SO_4)_3$ **(1)** and $(NH_4)_2Fe_2(SO_4)_3$ **(2)** display a decrease in the effective magnetic moment, as measured by the quantity $(8\chi T/n)^{1/2}$ in which n is the number of magnetic ions, on cooling from 310 K to 5 K (Figure 3.9). For $(NH_4)_2Mn_2(SO_4)_3$ **(1)** the magnetic moment decreases from 6.29(1) to 4.86(2) μ_B from 310 K to 45 K when it increases slightly to 5.07(1) μ_B from 45 K to 39 K. Below this temperature it decreases dramatically to 2.61(1) μ_B at 5 K. The effective magnetic moment for $(NH_4)_2Fe_2(SO_4)_3$ **(2)** decreases slowly from 310 K to 60 K from 5.7(1) to 4.95(2) μ_B, where the magnetic moment decreases rapidly to 2.45(1) μ_B at 5 K.

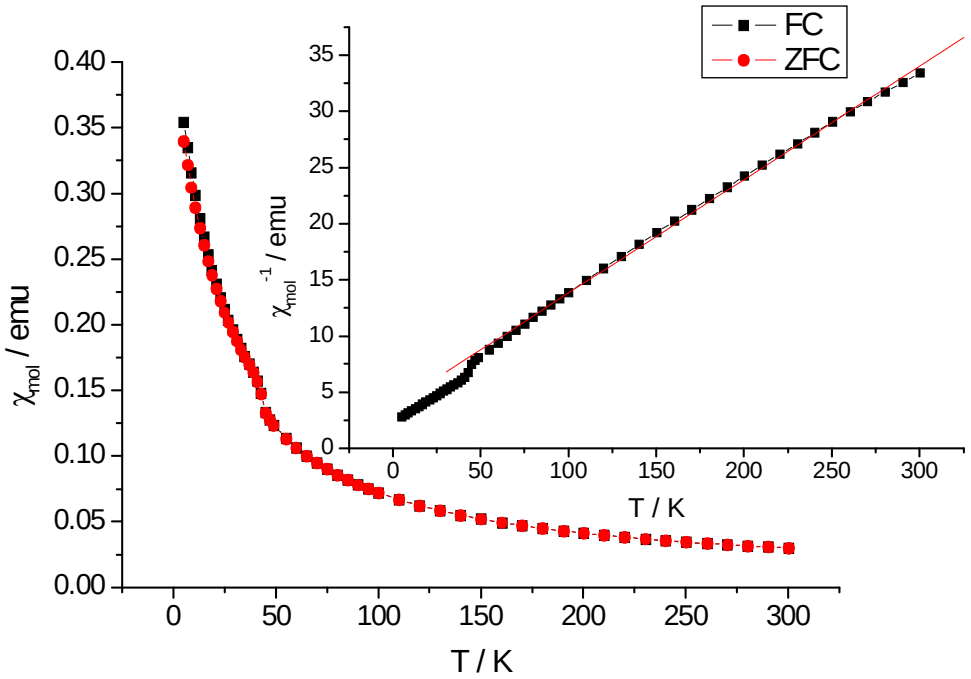

Figure 3.7. Zero field-cooled (Zfc)/ Field-cooled (Fc) susceptibility data and inverse susceptibility data (inset) for $(NH_4)_2Mn_2(SO_4)_3$ **(1)**. The red lines show the fit to the Curie-Weiss law.

The magnetisation as a function of field at 5 K was measured for $(NH_4)_2Mn_2(SO_4)_3$ **(1)** (Figure 3.11) and a linear increase in the magnetic moment per manganese ion with increasing field is observed, which means that there is no spontaneous magnetisation at 5 K.

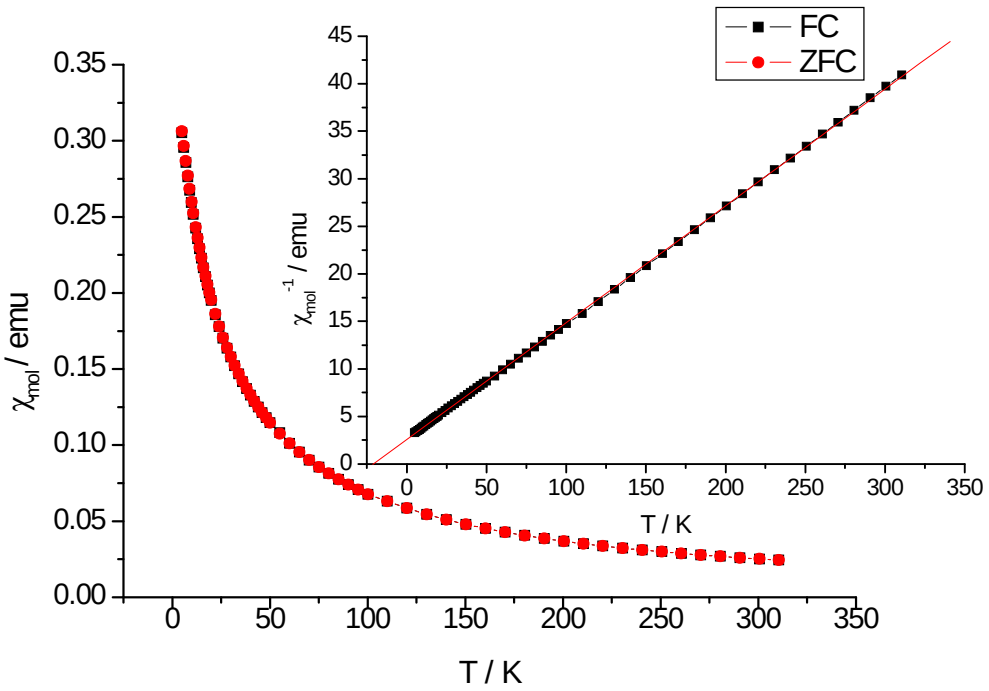

Figure 3.8. Zero field-cooled (Zfc)/ Field-cooled (Fc) susceptibility data and inverse susceptibility data (inset) for $(NH_4)_2Fe_2(SO_4)_3$ **(2)**. The red lines show the fit to the Curie-Weiss law.

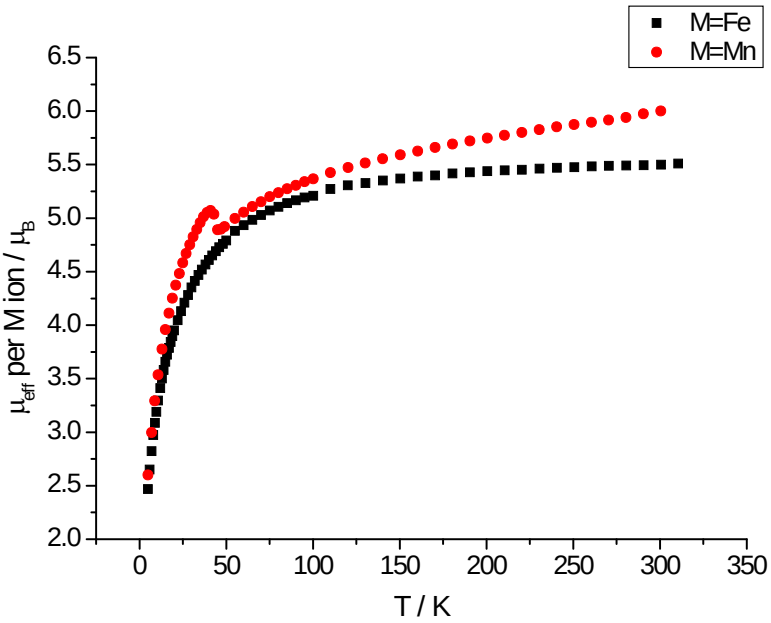

Figure 3.9. Effective magnetic moment per M(II) ion for $(NH_4)_2M_2(SO_4)_3$ (M=Mn, Fe) **(1)-(2)** as a function of temperature at 1000 G.

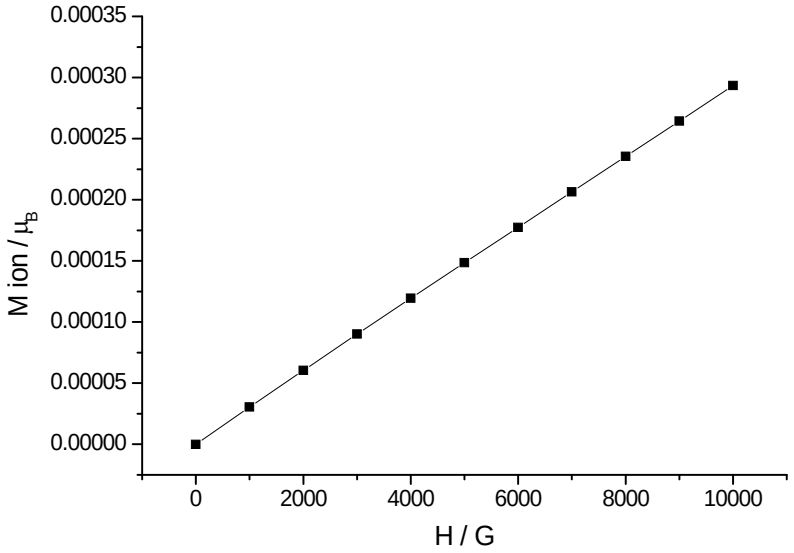

Figure 3.10. Magnetic moment per Mn(II) ion for $(NH_4)_2Mn_2(SO_4)_3$ **(1)** as a function of field at 5 K.

Further magnetic measurements were collected in Bariloche, Argentina at 100 G and 10,000 G. A hysteresis loop was measured from -12,000 G to 12,000 G (Figure 3.11). The dependency of the temperature at high field suggests that instead of an antiferromagnet, this material behaves as a weak ferromagnet. Magnetic susceptibility data were measured at 100 G and it is displayed in Figure 3.12. The zero field-cooled susceptibility plot shows a decrease in the magnetic susceptibility as the temperature is lowered, characteristic of antiferromagnetism. However, assuming Dzylohinski-Moriya behaviour, a decrease in the magnetic susceptibility at high field would have been expected. The effective magnetic moment for Mn^{2+} was calculated from the linear fitting of the Curie-Weiss law of the reciprocal magnetic susceptibility to be 7 μ_B which is higher than predicted (Figure 3.13).

3.2.6 EPR measurements

Electron paramagnetic resonance (EPR) studies were additionally carried out for $(NH_4)_2Mn_2(SO_4)_3$ **(1)** in the Centre of Science in Bariloche (Argentina) to identify paramagnetic centres and to further study the possibility of a phase transition at low temperature. The resonance field was measured as a function of temperature (Figure 3.14). Below the ordering temperature, the resonance field decreases as a result of an internal field.

The resonance linewidth as a function of temperature remains constant up to 40 K with a value of ΔH_{∞}=146 G, temperature after which it starts increasing. This is characteristic of systems that order (Figure 3.15).

The intensity of EPR was measured as a function of temperature and it is depicted in Figure 3.16. These data are in good agreement with what is expected from magnetic susceptibility measurements since the intensity of the EPR curve matches the susceptibility curve obtained at 100 and 2,000 G.

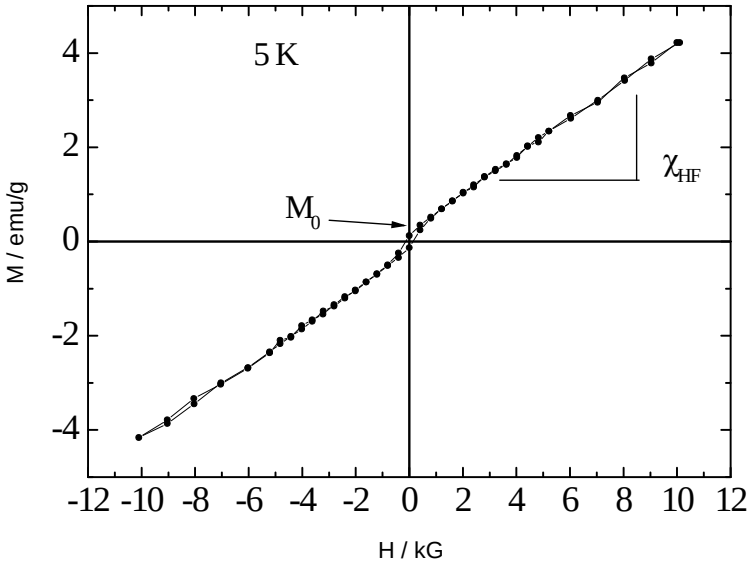

Figure 3.11. Magnetisation vs field for $(NH_4)_2Mn_2(SO_4)_3$ **(1)** from -12,000 to 12,000 G.

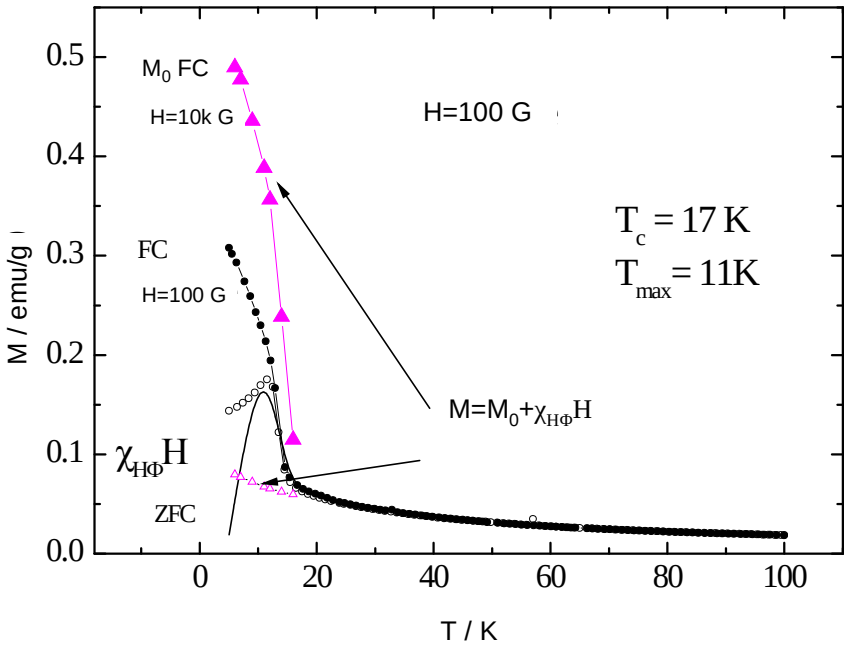

Figure 3.12. ZFC/FC magnetic susceptibility data for $(NH_4)_2Mn_2(SO_4)_3$ **(1)** at 100 G. Violet triangles represent the extrapolation of the data from M vs H plot at H=10,000 G.

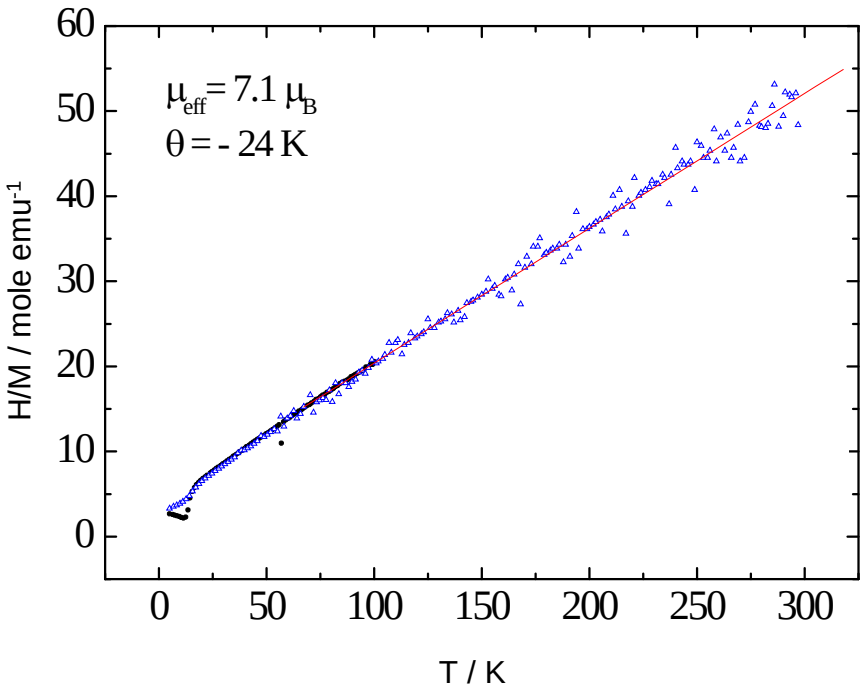

Figure 3.13. Reciprocal magnetic susceptibility at 100 G.

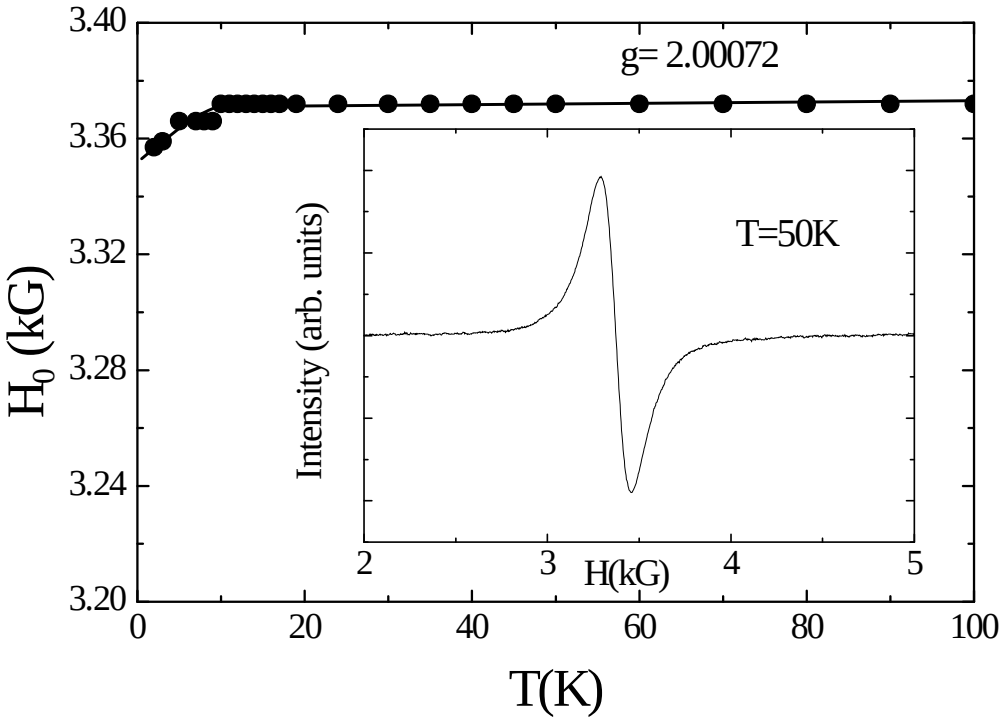

Figure 3.14. Resonance field vs temperature. Inset, intensity of signal at 50 K.

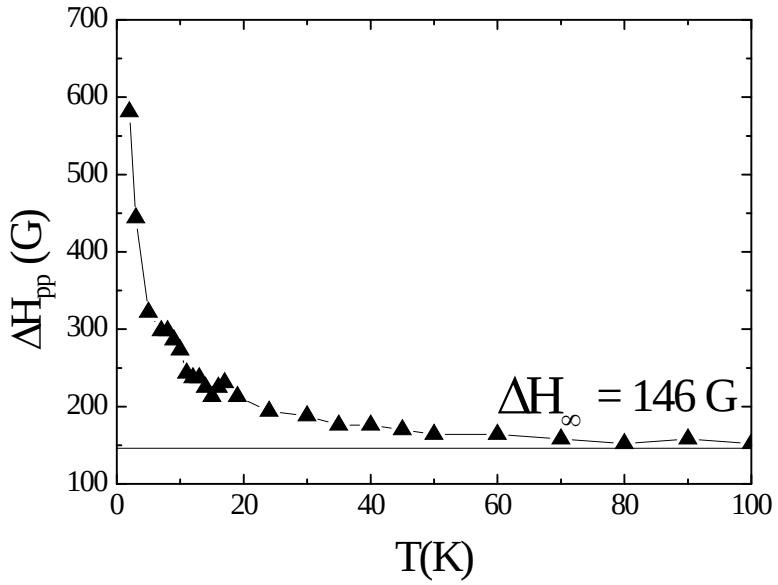

Figure 3.15. Resonance linewidth as a function of temperature for $(NH_4)_2Mn_2(SO_4)_3$ **(1)**.

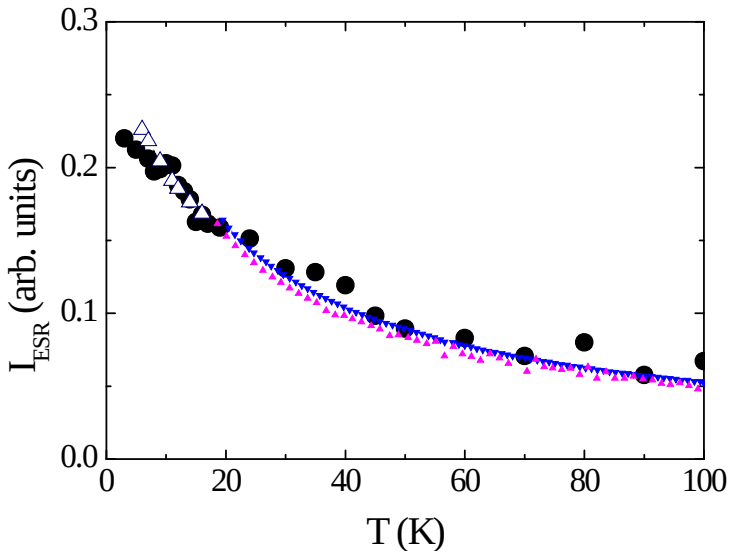

Figure 3.16. Intensity of EPR (full circles) as a function of temperature. (Violet triangles, magnetic susceptibility at 2,000 G; blue triangles, magnetic susceptibility at 100 G; Empty triangles, magnetic susceptibility at high field from the fitting of the magnetisation vs field measurement at high field).

3.2.7 Discussion

Two compounds belonging to the family of langbeinite-type phases, $(NH_4)_2Mn_2(SO_4)_3$ **(1)** and $(NH_4)_2Fe_2(SO_4)_3$ **(2)**, have been synthesised unexpectedly, using 1-ethyl-3-methylimidazolium bromide ([EMIM] Br) (Figure 3.1) through an unusual redox process. The synthesis of these two compounds was first published by Gatton *et al.* in 1958

[299]. Langbeinite-type crystals are sulphates and phosphates with the general formulae $M_2^+M_2^{2+}(SO_4)_3$ and $A_xM_2(PO_4)_3$ respectively, with $M^+=K^+$, Rb^+, Cs^+, NH_4^+, Tl^+; $M^{2+}=Mg^{2+}$, Ca^{2+}, Mn^{2+}, Co^{2+}, Ni^{2+}, Zn^{2+}, Cd^{2+}, Fe^{2+} and $A=Na^+$, K^+. These materials have attracted a lot of interest due to their properties such us their ferroelastic and ferroelectric behaviour, their magnetic properties and their structural phase transitions. On the basis of structural transitions, they can be classified into three different types, from type I, in which several phase transitions occur as the temperature is lowered, to type III, in which no phase transitions are observed. A classification of the langbeinite-type phases and some examples are included in Table 3.4.

Table 3.4. Classification of the langbeinite-type phases

Type	Phase transition	Example [300]
Type I	Cubic ($P2_13$) → Monoclinic ($P2_1$) → Triclinic ($P1$) → Orthorhombic ($P2_12_12_1$)	$Rb_2Cd_2(SO_4)_3$
Type II	Cubic ($P2_13$) → Orthorhombic ($P2_12_12_1$)	$K_2Cd_2(SO_4)_3$
Type III	Phase transitions do not take place	$Tl_2Mn_2(SO_4)_3$

At room temperature, with the exception of $K_2Cd_2(SO_4)_3$ and $K_2Ca_2(SO_4)_3$, both orthorhombic with space group $P2_12_12_1$ [301], most of the crystals of these langbeinite materials have a cubic structure with space group $P2_13$, a lattice parameter of approximately 10 Å, and four formula units per unit cell. They present a three-dimensional structure in which the building unit is a metal centered MO_6 octahedron surrounded by six SO_4 tetrahedra. Methods used traditionally for crystal growth involved slow evaporation of aqueous solutions containing a 1:2 molar ratio of $(M^+)_2$ SO_4 and $(M^{2+})SO_4$ [302] or growth at high temperature using the Czocharalski or Bridgman method [303, 304]. Lately, the synthesis of langbeinite-type compounds has been carried out by crystal growth at room temperature from saturated aqueous stochiometric solutions and subsequent recrystallization, such as the case of crystals of $K_2Mg_2(SO_4)_3$ and $K_2Mn_2(SO_4)_3$ [305, 306]. Nowadays, there are a number of reports in the synthesis and the study of the physical properties of the langbeinite-like compounds, such as luminescence and magnetic properties [307, 308]. Among them, the most interesting works on the basis of their magnetic properties are on langbeinites where the three-dimensional network is formed

from polyhedra of tri- (Ti, Fe, Cr, V, Y, rare-earth elements) or tetravalent (Ti, Zr) metals, while the interstitial cations are Na^{+}, K^{+}, Ba^{2+}.

In this project, the two $(NH_4)_2M_2(SO_4)_3$ (M=Mn, Fe) **(1)-(2)** langbeinite-type phases have been obtained following a straightforward low-temperature synthesis in the presence of an ionic liquid, in which crystals were obtained in a high yield (≈90 %). The manganese langbeinite **(1)** was initially synthesised in this project in the presence of indium nitrate. Subsequent reactions in order to obtain this material without using any metal nitrate source failed, suggesting that nitrate plays an essential role in this process. Eventually, $(NH_4)_2Mn_2(SO_4)_3$ **(1)** was successfully synthesised using manganese nitrate as a starting material, together with sulphur and the ionic liquid 1-ethyl-3-methylimidazolium bromide. It takes place *via* an unusual redox process in which a sulphate material is obtained from a reaction under vacuum conditions. The sulphur is acting as a reducing agent to be oxidised to sulphate. The nitrate, which is a very strong oxidizing agent, is needed for this reaction to work because it is reduced to ammonia in the process. It is probable that the ionic liquid remains un-reacted and is washed out in the filtering process. However, it provides the correct pH for initiating the redox reaction under aqueous conditions, since sulphur tends to be oxidised in neutral/basic media (E^0 SO_4^{2-}/S = -0.62 V; the electrode with the most negative electrode potential is oxidised). The redox half-equations involved in this process would be:

$$\text{Oxidation: } 4H_2O + S \rightarrow SO_4^{2-} + 8H^+ + 6e^- \quad E^0\, SO_4^{2-}/S = -0.62 \text{ V}$$

$$\text{Reduction: } 10H^+ + NO_3^- + 8e^- \rightarrow NH_4^+ + 3H_2O \quad E^0\, NO_3^-/NH_4^+ = 0.89 \text{ V}$$

$$\text{Final: } H_2O + 2H^+ + 4S + 3NO_3^- \rightarrow 4SO_4^{2-} + 3NH_4^+$$

The oxidation of sulphur to sulphate supplies the acidic media needed for the nitrate to be reduced to ammonium (E^0 NO_3^-/NH_4^+ = 0.89 V; the electrode with the most positive electrode potential is reduced). The synthesis was repeated under the same conditions using a different transition-metal nitrate source, obtaining the isostructural iron langbeinite, $(NH_4)_2Fe_2(SO_4)_3$ **(2)**. Analogous reactions were carried out using other nitrates of the transition metals from the first row in an attempt to expand the family of ammonium langbeinite-type phases without success.

$(NH_4)_2Fe_2(SO_4)_3$ **(2)** is isostructural with $(NH_4)_2Mn_2(SO_4)_3$ **(1)**, whose crystal structure has been previously discussed [296]. Both manganese and iron langbeinite-type

materials crystallise in the $K_2Mg_2(SO_4)_3$ structure type [309, 310]. They are isotypic with the langbeinites $(NH_4)_2M_2(SO_4)_3$ (M=Mg, Ca, Ni) [311] and $(NH_4)_2Cd_2(SO_4)_3$ [312]. These two ammonium transition metal sulphates constitute the first example of transition metal sulphates synthesised under ionothermal conditions.

In the so called type III, no phase transitions are observed. $Tl_2Cd_2(SO_4)_3$ is considered an example of type I [313], while many of the potassium langbeinites $K_2M_2(SO_4)_3$ appear to exhibit the second type [314]. Ammonium langbeinites have not been as well characterised as the potassium langbeinites. $(NH_4)_2Mn_2(SO_4)_3$ **(1)** was classified to be a type III by Hikita *et al.* [311] and further dielectric measurements on the effect of hydrostatic pressure did not show any transition down to -196 °C [300]. In this work, DSC measurements were performed down to -120°C (153 K) for both $(NH_4)_2M_2(SO_4)_3$ (M=Mn, Fe) **(1)-(2)** and a change in the heat flow was observed for the manganese langbeinite at 226 K (-47 °C) suggesting a transition of unknown origin. Moreover, the crystal structure solved at 100 K remains cubic, only a small contraction of the unit cell was observed as a consequence of decreasing the temperature. That indicates that the change in the heat flow observed for **(1)** is not due to a phase transition. Magnetic measurements were performed to study the possible magnetic nature of the anomaly observed in DSC measurements.

The magnetic data for $(NH_4)_2M_2(SO_4)_3$ (M=Mn, Fe) **(1)-(2)** show paramagnetic behaviour that can be fitted according to the Curie-Weiss law yielding negative Weiss constants, which suggests that dominant exchange interactions are antiferromagnetic.

$(NH_4)_2Fe_2(SO_4)_3$ **(2)** is paramagnetic over the whole range of temperatures measured (300-5 K). The plot of the magnetic moment as a function of temperature shows a downturn in the μ_{eff} due to the dependence of the effective magnetic moment with the temperature, as predicted by the Kotani theory. The effective magnetic moment for Fe^{2+} is slightly higher than the spin-only value for octahedral Fe^{2+}complexes, which usually lies between 5.0 and 5.6 μ_B in a high spin configuration. That fact may be due to orbital contribution, for which the Van Vleck formula can be applied, as the crystal field partly or fully quenches the orbital angular momentum, with a calculated effective magnetic moment of 5.5 μ_B.

In the $(NH_4)_2Mn_2(SO_4)_3$ **(1)** an anomaly is observed at 45 K in the reciprocal susceptibility plot vs. temperature. The magnetic moment decreases as a function of

temperature, before a sharp increase at 45 K after which temperature it starts decreasing again. This decrease in μ_{eff} could be due to antiferromagnetic interactions but the sharp upturn could not be explained. Measurement of the magnetic moment per formula unit as a function of field were attempted to investigate this phenomenon. It shows a linear behaviour between 0-10,000 G and the moment did not become saturated before 10,000 G. This suggests that no spontaneous magnetisation is present and that the material is paramagnetic with dominant antiferromagnetic exchange interactions at low temperature. From these data, the interaction at 45 K could not be assigned to a magnetic interaction. Further magnetic studies were attempted at 100 G and weak ferromagnetic behaviour was observed since the susceptibility is dependent on the temperature at high field. EPR measurements were performed to confirm the nature of these interactions. They are consistent with the magnetic measurements suggesting that there are clusters of Mn^{2+}, some of them exhibiting ordering whereas some others remain paramagnetic. These measurements might explain the interaction at 45 K that was initially observed. However, conclusive evidence can be obtained by collecting single-crystal X-ray diffraction data at 50 K on $(NH_4)_2Mn_2(SO_4)_3$ **(1)**. The anomaly showed by DSC measurements at 226 K is not due to any magnetic interaction since no anomaly was observed at this temperature. It has been reported that in langbeinite-type phases, the sulphate group can adopt many different orientations, tendency that is much prominent for the sulphate groups surrounding the divalent metal ions [315], exhibiting a multi-site disorder arrangement. Artman also suggested that the phase behaviour in ammonium langbeinites may arise from phenomena associated with motional dynamics of the ammonium ion [316]. This is supported by NMR and EPR studies which have reported that the NH_4 ion and SO_4 ion have dynamical disordered arrangements. Therefore, it is believed that the anomaly observed in the DSC measurements might be associated with an order-disorder transition occurring when lowering the temperature.

3.3 Barium carbonate chloride, $Ba_3Cl_4CO_3$

3.3.1 Synthesis

Using the analogous synthetic technique employed for the synthesis of the langbeinite phases, $Ba_3Cl_4CO_3$ **(3)** was prepared under ionothermal conditions from a mixture of 1-ethyl-3-methylimidazolium bromide ([EMIM] Br) ionic liquid, $BaCO_3$ and

$CoCl_2 \cdot 6H_2O$ with a molar composition $BaCO_3$:$CoCl_2.6H_2O$:[EMIM]Br of 1:2:8. The mixture was placed in a Pyrex tube and the contents frozen with liquid nitrogen. The tube was connected to a vacuum line and evacuated to 1 Torr before sealing it with a glassblowing torch. The sealed tube was placed in an oven, heated at 170°C overnight and then cooled to room temperature at a rate of 1°C min^{-1}. The product was filtered, washed with methanol and acetone and dried in an oven in air at 100 °C overnight. The solid product consisted of a mixture of colourless needles, identified by single crystal X-ray diffraction as $Ba_3Cl_4CO_3$ **(3)** and some white powder, identified as $BaCO_3$ by powder X-ray diffraction.

3.3.2 Single-crystal diffraction

Single-crystal X-ray diffraction data for $Ba_3Cl_4CO_3$ **(3)** were collected at 293 K using a Bruker Nonius X8 Apex diffractometer with Mo-Kα radiation (λ=0.71073 Å). Data were processed using the Apex-2 software [289]. The structure was solved using the direct methods program SIR92 [291], which located Cl, and Ba ions and some O atoms. Subsequent difference Fourier calculations, to locate the remaining O atoms and C atoms, and least-squares refinements were carried out using the CRYSTALS suite of programs [292]. In the final cycles of refinement, positional and anisotropic thermal parameters for all atoms were refined. Crystallographic details are given in Table 3.5. Atoms coordinates are given in Appendix B. Selected bond distances and angles are summarised in Table 3.6 and Table 3.7, respectively.

3.3.3 Characterisation

Powder X-ray diffraction data were collected and the diffraction pattern of the product indicates the presence of a mixture of phases, which were identified to be $BaCO_3$, $CoCl_2$ and 1-ethyl-3methylimidazolium bromide. The rest of the peaks can be indexed on basis of orthorhombic unit cell determined for $Ba_3Cl_4CO_3$ **(3)** from the single-crystal diffraction study. Comparison of the calculated and the observed powder X-ray diffraction patterns obtained using TOPAS program [288] and the refined lattice parameters are shown in Appendix A.

3.3.4 Crystal structure description

$Ba_3Cl_4CO_3$ **(3)** exhibits a complex three-dimensional structure in which barium and carbonate ions define a chain of anion-centered distorted octahedra that share common faces. The individual chains are cross-linked *via* $ClBa_x$ (x=4,5) polyhedra. The local coordination scheme for $Ba_3Cl_4CO_3$ **(3)** is shown in Figure 3.17.

There are two crystallographically distinct barium ions in the unit cell which are effectively nine-coordinated. Ba(1) has six chloride neighbours at *ca.* 3.15 Å, with a seventh at the longer distance of 3.467(2) Å. The coordination sphere of Ba(1) is completed by two carbonate ions, one acting as a monodentate ligand, the other as a bidentate ligand, at Ba-O distances of *ca*. 2.75 Å. The second barium ion, Ba(2), also has six neighbouring chloride ions, at distances ranging from 3.265(2) to 3.371(2) Å, together with three oxygen atoms belonging to two carbonate ions, one acting as a monodentate ligand and the other as a bidentate ligand, as occurs for Ba(1).

Table 3.5. Crystallographic data for $Ba_3Cl_4CO_3$ **(3)**

Formula	**$Ba_3Cl_4CO_3$ (3)**
M_r	613.84
Crystal size (mm)	0.18 X 0.18 X 0.20
Crystal habit	Colourless needle
Crystal system	Orthorhombic
Space group	*Pnma*
***a*(Å)**	8.4074(11)
***b*(Å)**	9.5886(12)
***c*(Å)**	12.4833(15)
V(Å^3)	1006.3(2)
Z	4
μ(mm^{-1})	12.628
ρ_{calc} (g cm^{-3})	4.051
Residual electron density (min, max) (eÅ^{-3})	-1.75, 4.68
Measured data	25333
Unique data	1540
Observed data (I>3σ(I))	934
R_{int}	0.0405
R(F)	0.0348
$_wR(F)$	0.0392

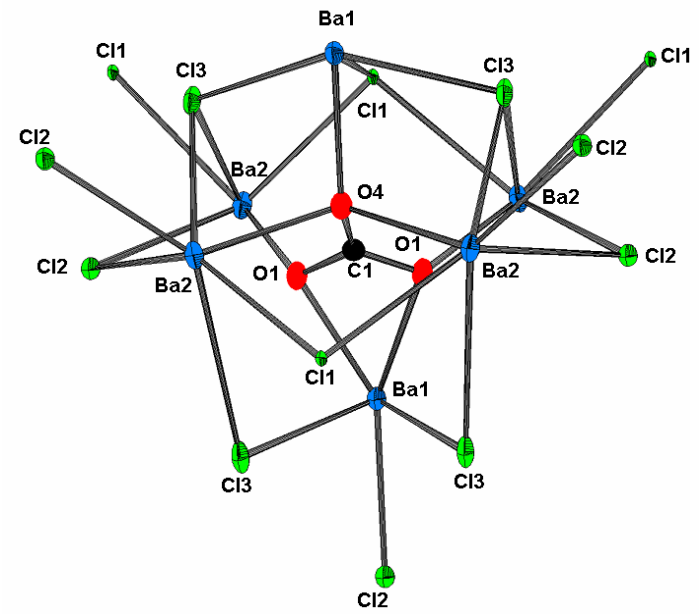

Figure 3.17. Local coordination of $Ba_3Cl_4CO_3$ **(3)** showing the atom labelling scheme and thermal ellipsoids at 50% probability.

Ba(2)-O distances are in the range 2.751(6)-2.800(6) Å. The Ba-Cl distances are comparable with those reported for $BaCl_2$ [317, 318], with the exception of the longer Ba(1)-Cl(1) distance of 3.467(2) Å, which lies outside the range of values for Ba-Cl distances reported for $BaCl_2$ (3.0618-3.3971 Å). This distance Ba(1)-Cl(1)=3.467(2) Å, is longer than the sum of the ionic radii for Ba and Cl (3.16 Å), with a contribution to the Ba(1) valence sum of only 0.122. Ba-O distances are also in agreement with those previously reported for $BaCO_3$ [319, 320]. Ba-O and Ba-Cl distances for $Ba_3Cl_4CO_3$ can be compared with those in the tetrabarium oxy-chloride, Ba_4OCl_6 [321], with longer Ba-O distances for $Ba_3Cl_4CO_3$ (*ca*. 2.75 Å) in comparison with those in Ba_4OCl_6 (*ca*. 2.51 Å), whereas Ba-Cl distances are in good agreement with the exception of the longer distance Ba(2)-Cl(2) of 3.809 Å for Ba_4OCl_6.

The barium and carbonate ions define a chain directed along [100], in which each oxygen atom of the carbonate ion exhibits μ_3 coordination to two Ba(1) and one Ba(2) ion (Figure 3.18(a)). The carbon atom of each of the carbonate ions resides at the centre of a distorted octahedron of barium ions and the chains can thus be considered to consist of carbon-centred CBa_6 octahedra that share common faces (Figure 3.18(b)). The CBa_3 chains of face-sharing CBa_6 octahedra are cross-linked by chloride ions. The local coordination of

each of the chloride ions and the bond distances to the barium ions are shown in Figure 3.19.

Table 3.6. Selected bond distances (Å) and bond valence sums for $Ba_3Cl_4CO_3$ **(3)**.

Atoms	Bond distances/Å	ν^a
Ba(1)-Cl(1)	3.467(2)	0.122
Ba(1)-Cl(2)	3.153(3)	0.286
Ba(1)-Cl(3)	2 x 3.176(2)	2 x 0.269
Ba(1)-Cl(3)'	2 x 3.118(2)	2 x 0.315
Ba(1)-O(1)	2.699(8)	0.332
Ba(1)-O(2)	2 x 2.770(5)	2 x 0.274
	Sum	2.456
Ba(2)-Cl(1)	3.367(1)	0.160
Ba(2)-Cl(1)'	3.329(1)	0.178
Ba(2)-Cl(2)	3.265(2)	0.211
Ba(2)-Cl(2)'	3.371(2)	0.159
Ba(2)-Cl(3)	3.269(2)	0.209
Ba(2)-Cl(3)'	3.278(2)	0.204
Ba(2)-O(1)	2.755(4)	0.284
Ba(2)-O(2)	2.800(6)	0.252
Ba(2)-O(2)'	2.751(6)	0.288
	Sum	1.945
C(1)-O(1)	1.276(14)	
C(1)-O(2)	2 x 1.294(7)	

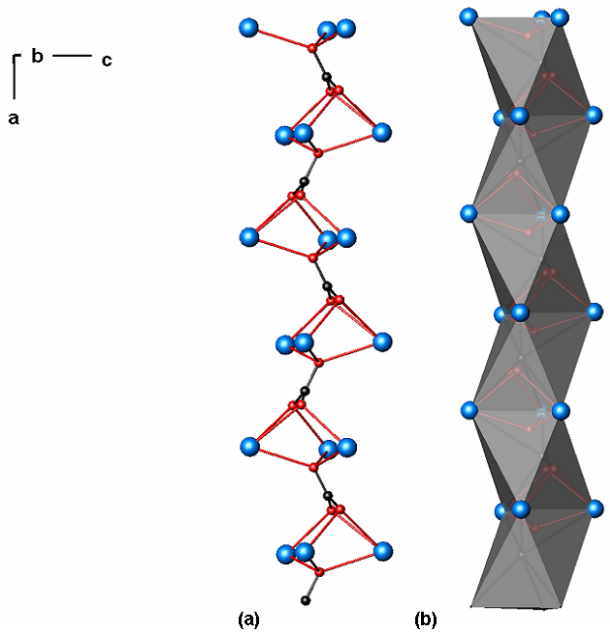

Figure 3.18. (a) A single chain of carbonate centered CBa_6 octahedra in ball and stick representation and **(b)** polyhedra representation. (O atoms, red; C atoms, black; Ba atoms, blue).

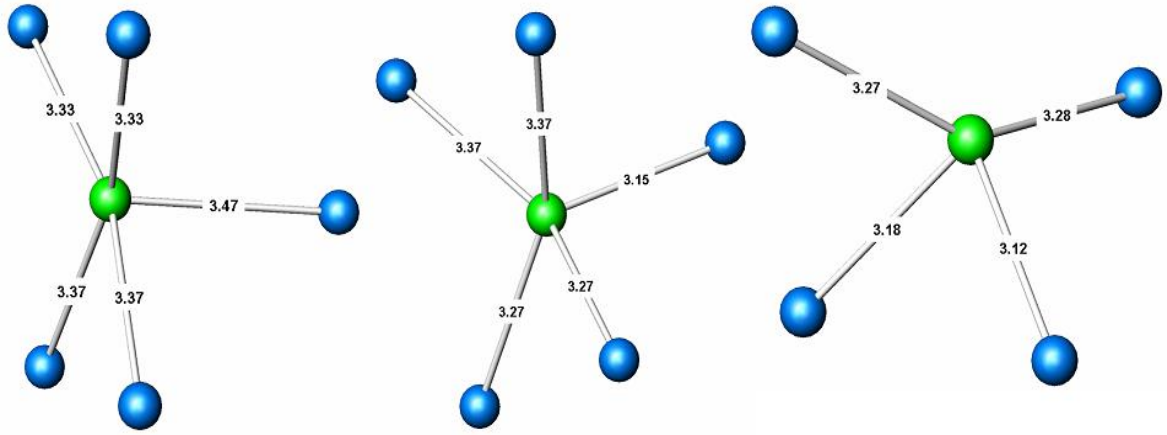

Figure 3.19. Local coordination and Ba-Cl distances of the three crystallographically distinct $ClBa_n$ polyhedra that serve to link individual CBa_3 chains.

Table 3.7. Selected bond angles (°) for $Ba_3Cl_4CO_3$ **(3)**

Atoms	Bond angles/°	Atoms	Bond angles/°
Cl(1)-Ba(1)-Cl(2)	67.446	Cl(1)-Ba(2)-Cl(2)	66.299
Cl(1)-Ba(1)-Cl(3)	2 x 66.347	Cl(1)-Ba(2)-Cl(3)	68.301
Cl(1)-Ba(1)-C(1)	62.301	Cl(1)-Ba(2)-O(1)	68.076
O(1)-Ba(1)-Cl(3)	2 x 73.390	Cl(1)-Ba(2)-Cl(3)	66.419
O(1)-Ba(1)-O(2)	2 x 62.088	Cl(1)-Ba(2)-C(1)	64.377
O(1)-Ba(1)-C(1)	14.269	Cl(1)-Ba(2)-C(1)	69.418
O(1)-Ba(1)-C(1)	63.008	Cl(2)-Ba(2)-Cl(3)	66.669
Cl(3)-Ba(1)-O(2)	2 x 70.269	Cl(2)-Ba(2)-O(2)	74.893
Cl(3)-Ba(1)-O(2)	2 x 76.991	Cl(2)-Ba(2)-Cl(3)	65.367
O(2)-Ba(1)-O(2)	47.717	Cl(2)-Ba(2)-O(2)	72.558
O(2)-Ba(1)-C(1)	2 x 24.141	O(1)-Ba(2)-Cl(3)	70.103
Ba(1)-C(1)-O(1)	31.435	O(2)-Ba(2)-O(2)	47.192
Ba(1)-C(1)-O(1)	51.281	O(1)-Ba(2)-O(2)	61.611
Ba(1)-C(1)-O(2)	2 x 61.092	O(1)-Ba(2)-C(1)	55.733
Ba(2)-C(1)-O(1)	2 x 61.128	O(1)-Ba(2)-C(1)	23.908
Ba(2)-C(1)-O(2)	2 x 63.201	Cl(3)-Ba(2)-O(2)	72.828
Ba(2)-C(1)-O(1)	2 x 47.645	Cl(3)-Ba(2)-O(2)	72.112
Ba(2)-C(1)-O(2)	2 x 39.285	Cl(3)-Ba(2)-O(2)	74.519
$O(1)^{(i)}$-C(1)-O(1)	2 x 119.9(9)	O(2)-Ba(2)-C(1)	24.349
$O(1)^{(i)}$-C(1)-O(2)	2 x 120.0(5)	O(2)-Ba(2)-C(1)	17.322

Neighbouring CBa_6 chains in the [011] and [0-11] directions are linked by Cl(1) ions. Each Cl(1) is coordinated to five Ba^{2+} ions in a square pyramidal geometry. Ba(2) in a given chain is at the apex of the $Cl(1)Ba_5$ pyramid, whose base is formed from Ba(1) ions, two from the same CBa_3 chain, and one from each neighbouring chains in two perpendicular directions. The $Cl(1)Ba_5$ square pyramids share basal edges to form chains directed along [010] in which the direction of the apex alternates along the chain direction (Figure 3.20(a)).

Cl(2) also has a square-pyramidal coordination, having a Ba(2) apex that is shared with the Cl(1)-centred polyhedral chain and a base again formed from Ba(1) ions in neighbouring CBa_3 chains (Figure 3.20(b)). $Cl(2)Ba_5$ square-based pyramids form a zigzag chain directed along [100], which shares both edges and faces with the Cl(1)–containing chains that are aligned in a perpendicular direction. Four-coordinate (2 x Ba(1) and 2 x Ba(2)) Cl(3)) ions complete the cross-linking (Figure 3.21(a)): each tetrahedron containing three barium ions from one CBa_3 chain, with the fourth, located in a neighbouring chain, providing a common vertex that serves to link tetrahedra into a chain along [010]. The resulting three-dimensional structure of $Ba_3Cl_4CO_3$ **(3)** is represented in Figure 3.21(b).

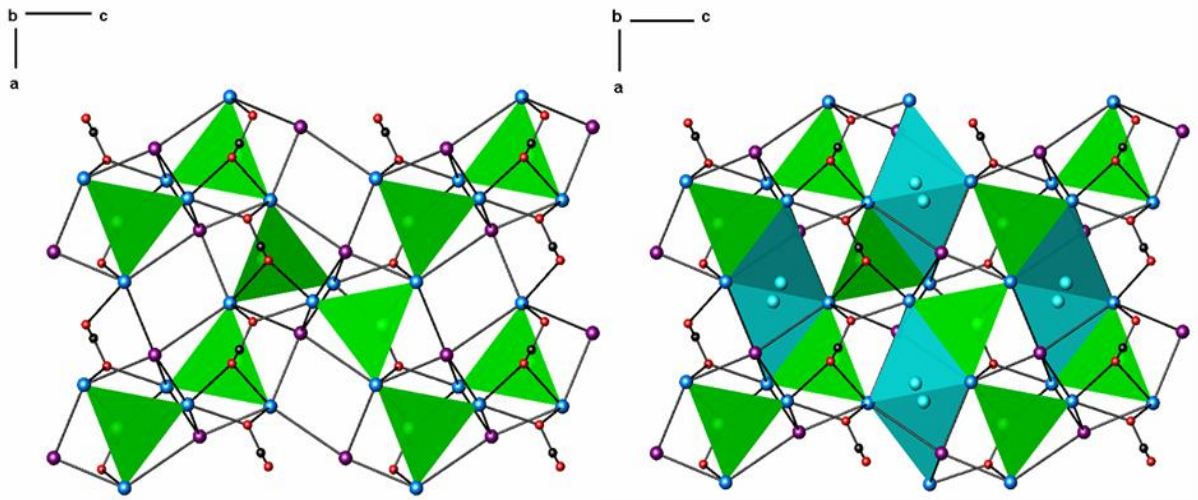

Figure 3.20. (a) Cross-linking of barium carbonate chains by linear chains of Cl(1)-centered square-based pyramids (green) directed along [010] and (b) zigzag chains of Cl(2)-centered square-based pyramids (blue). (Ba atoms, blue; O atoms, red; C atoms black).

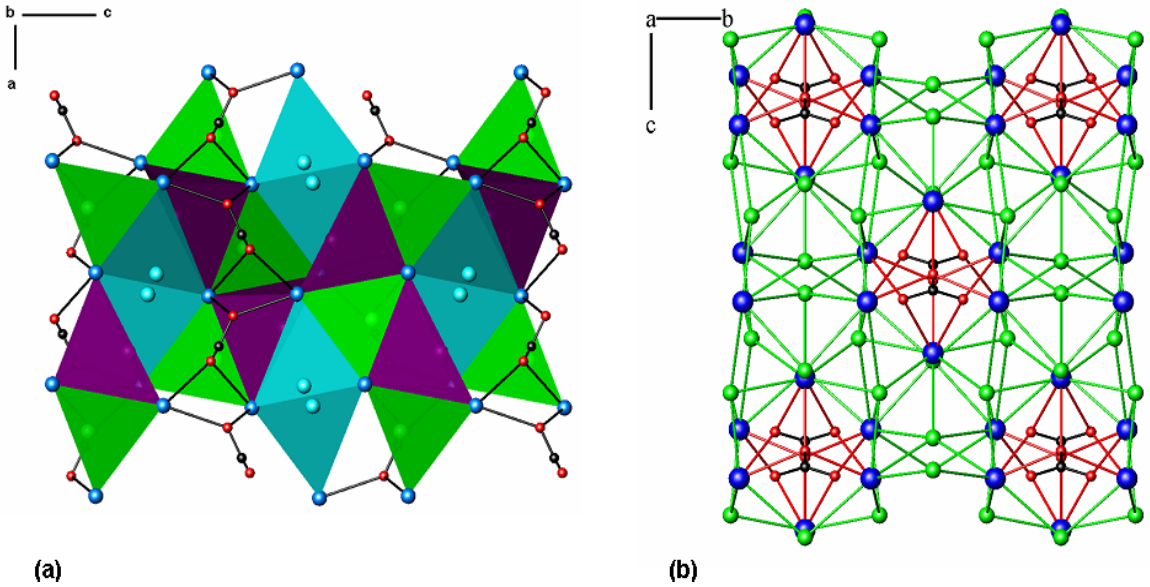

Figure 3.21. (a) Chains of edge-sharing $ClBa_5$ square pyramids and $ClBa_4$ tetrahedra, showing the cross-linking structure of $Ba_3Cl_4CO_3$ **(3)**. (Cl(1) square-pyramids, green; Cl(2) square-based pyramids, blue; Cl(3) tetrahedral, purple) and **(b)** Three-dimensional network of $Ba_3Cl_4CO_3$. (C atoms, black; O atoms, red, Ba atoms, blue; Cl atoms, green).

3.3.5 Discussion

$Ba_3Cl_4CO_3$ **(3)** was first prepared by Frit et *al.* [322] from reaction of $BaCl_2$ and $BaCO_3$ at elevated temperatures (850 °C) in an atmosphere of CO_2. The analogous bromides and iodides, $M_3X_4CO_3$ (M=Ba, Sr; X=Br, I), were subsequently prepared using a similar process [323]. However, the polycrystalline nature of materials prepared by conventional solid-state reactions has, to date, precluded the determination of the crystal structure of these alkaline-earth halide carbonates. During this project the barium carbonate chloride has been successfully synthesised under mild conditions using an ionic liquid ([EMIM] Br). By attempting different reactions in order to produce a single phase product omitting the $CoCl_2{\cdot}6H_2O$ and using $BaCl_2$ instead, the presence of the transition metal chloride was found to be essential for the formation of $Ba_3Cl_4CO_3$ **(3)**. A similar feature has been observed previously in the synthesis under solvothermal conditions of $[C_6H_{20}N_4][Sb_4S_7]$ for which the presence of either cobalt [324] or zinc [325] is required. The synthesis was repeated changing the reaction conditions (temperature, reaction time, molar ratio) in order to obtain a single-phase of this material without success. Due to the impossibility of washing out $BaCO_3$ without dissolving $Ba_3Cl_4CO_3$ **(3)**, the powder

diffraction pattern of the product always revealed the presence of the binary carbonate in the final product.

The carbonate chloride $Ba_3Cl_4CO_3$ **(3)** represents an example of a comparatively rare class of mixed-anion compound. Phosgenite, $Pb_2Cl_2CO_3$, and the isotructural bromide analogues [326] are amongst the small number of carbonate halides whose structures have been determined (Figure 3.22(a)). It adopts a pseudo-layered structure in which two-dimensional $Pb_2Cl_2^{2+}$ slabs are connected by CO_3^{2-} ions [327] in contrast to the complex three-dimensional structure of $Ba_3Cl_4CO_3$. The cations in phosgenite reside in nine-coordinate sites, similar to those in $Ba_3Cl_4CO_3$ **(3)**, both with a monocapped square antiprism geometry. Single-crystals of $Pb_2F_2CO_3$ [328] have also been obtained, but its architecture differs from that of $Pb_2X_2CO_3$ (X=Cl, Br) one, being isotypic with that of the mineral Brenkite, $Ca_2F_2CO_3$ [329], another example of this family of mixed anion compounds (Figure 3.22(b)). Both $Pb_2F_2CO_3$ and $Ba_3Cl_4CO_3$ **(3)** compounds crystallize in the orthorhombic system, but in different space groups. $Pb_2F_2CO_3$ presents a complicated crystal structure in which the building elements are endless spiral chains of edge-sharing FPb_4 tetrahedra, joined by corner-sharing into a three-dimensional network of formula $(PbF)_n^{n+}$. The carbonate groups are situated in the tunnels formed by this network and the Pb^{2+} and Ca^{2+} cations are nine-coordinated, adopting a distorted three-capped trigonal prism arrangement. By contrast, in the structure of $Ba_3Cl_4CO_3$ **(3)**, Ba and Cl ions show a cross-linking structure built up of $BaCl_4$ tetrahedra and $BaCl_5$ square-pyramids, which are linked to each other by sharing both edges and faces, providing the linking between individual barium-carbonate chains to form the three-dimensional structure. Another example of this type of compounds is Tl_3FCO_3 [330], despite the structure of the latter differs from that of the $Ba_3Cl_4CO_3$ **(3)**. Rare-earth fluorocarbonates [331], whose structure is formed by layers of the bastnasite-(Ce) (CeF) and CO_3 layers [332], are also members of the small group of halides carbonates.

Ionothermal synthesis offers a new route for the preparation of materials containing oxy-anions. It has allowed the first structural determination of $Ba_3Cl_4CO_3$ **(3)**, that was previously only obtainable in polycrystalline form by a high temperature reaction, as well as the synthesis of the langbeinite-type phases $(NH_4)_2M_2(SO_4)_3$ (M=Mn, Fe) **(1)-(2)** through an unusual redox process in which sulphur acts as a reducing agent.

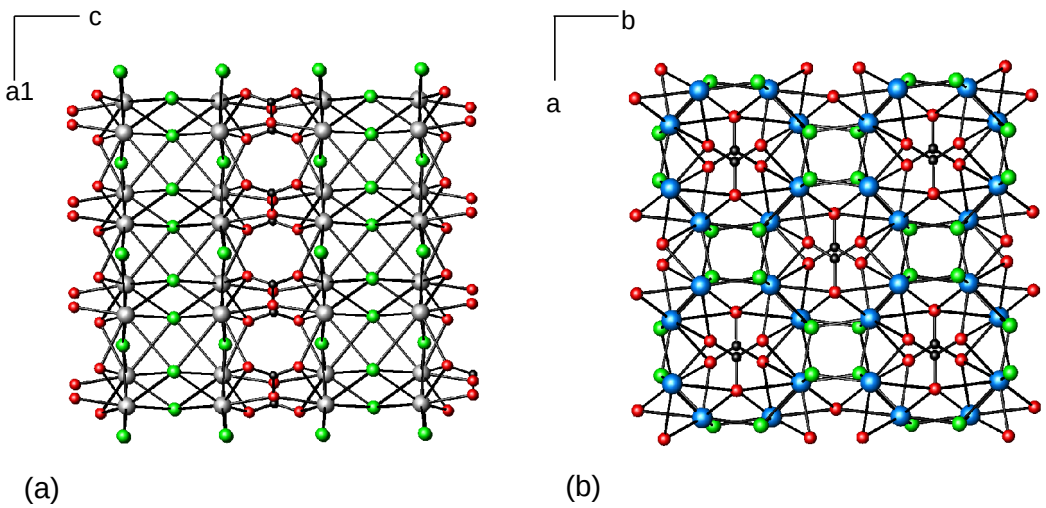

Figure 3.22. (a) Structure of phosphogenite, $Pb_2Cl_2CO_3$ (Pb ions, grey; Cl ions, green; O atoms, red; C atoms, black); (b) Structure of Brenkite, $Ca_2F_2CO_3$ (Ca ions, blue; F ions, green; O atoms, red; C atoms; black).

Chapter 4: Organically-templated transition-metal sulphates

4.1 Introduction

Recently, organic molecules have been employed in the design of novel materials, which has allowed the synthesis of exciting structures and also new properties and applications due to the opportunity of combining both inorganic and organic properties, such as metal coordination and the functionality of the organic component. Following the investigations of Rao and co-workers [150] a wide range of open-framework sulphate structures with different dimensionalities has been reported and most of them have been synthesised under solvothermal conditions in the presence of organic amines [38].

In this research project, solvothermal synthesis has been employed for the preparation of organically-templated transition-metal sulphates. The system MSO_4:amine:H_2SO_4:H_2O has been investigated making use of a wide variety of amines and transition metal sulphates as well as different reaction conditions. After intense investigation of this system, manganese, iron and cobalt sulphates have been successfully prepared in the presence of ethylenediamine and triethylenetetramine. The resulting materials have been characterised and their magnetic properties have been intensively studied.

4.2 Synthesis and characterisation

4.2.1 Synthesis

$[Mn_4(SO_4)_8(OH)_2(H_2O)_2](enH_2)_5$ **(4)**, $[Fe_3(SO_4)_3(OH)_2(H_2O)_2](NH_4)_2$ **(5)**, $[Mn_3(SO_4)_3(OH)_2(trienH_2)]$ **(6)**, $[M(SO_4)(trien)]$ M=Mn, Fe **(7)-(8)**, $[Mn(SO_4)_2](enH_2)$ **(9)**, $[Mn_2(SO_4)_2(en)_2]$ **(10)** and $[Co_3(SO_4)_3(OH)_2](enH_2)$ **(11)** were synthesised under solvothermal conditions employing the corresponding transition-metal sulphate hydrate, sulphuric acid, deionised water and the amine, which were added into a 23 mL Teflon-lined stainless steel autoclave. For the synthesis of $[Mn_4(SO_4)_8(OH)_2(H_2O)_2](enH_2)_5$ **(4)**, a mixture of $MnSO_4 \cdot H_2O$ (0.338 g; 2 mmol), ethylenediamine (0.2 mL; 3 mmol) and H_2SO_4 (0.11 mL; 2 mmol) was loaded in the Teflon liner. 0.036 mL of deionised water were added to form a mixture Mn:en:H_2SO_4:H_2O of molar composition 1:1.5:1:0.5. After stirring the

mixture, the container was closed and heated at 170 °C for 6 days and then cooled to room temperature at a cooling rate of 1°C min^{-1}. The solid product was filtered, washed with deionised water, methanol and acetone and dried in air at room temperature. The product consisted of a mixture of brown powder and colourless crystals of $[Mn_4(SO_4)_8(OH)_2(H_2O)_2](enH_2)_5$ **(4)** that were identified by single-crystal X-ray diffraction. Compounds **(5)-(11)** were synthesised following an analogous procedure and the reaction conditions are displayed in Table 4.1.

4.2.2 Single-crystal diffraction

Single-crystal X-ray diffraction data for $[Mn_4(SO_4)_8(OH)_2(H_2O)_2](enH_2)_5$ **(4)**, $[Fe_3(SO_4)_3(OH)_2(H_2O)_2](NH_4)_2$ **(5)**, $[Mn_3(SO_4)_3(OH)_2(trienH_2)]$ **(6)**, $[M(SO_4)(trien)]$ M=Mn, Fe **(7)-(8)**, $[Mn(SO_4)_2](enH_2)$ **(9)**, $[Mn_2(SO_4)_2(en)_2]$ **(10)** and $[Co_3(SO_4)_3(OH)_2](enH_2)$ **(11)** were collected at 293 K using a Bruker Nonius X8 Apex diffractometer with Mo-Kα radiation (λ=0.71073 Å). Data were processed using the Apex-2 software [289] and the structure was solved by the direct methods program SIR92 [291], which located manganese, iron, cobalt and sulphur atoms and most of the oxygen atoms. Subsequent difference Fourier calculations, to locate the remaining oxygen atoms as well as nitrogen and carbon atoms, and least-squares refinements were carried out using the CRYSTALS suite of programs [292]. Some hydrogen atoms were found by difference Fourier maps and the remaining, introduced manually. In the final cycles of refinement, positional and anisotropic thermal parameters for all non-hydrogen atoms were refined. Crystallographic details are given in Table 4.2, Table 4.3, Table 4.4 and Table 4.5. Atoms coordinates and bond distances and angles for **(4)-(11)** are listed in Appendix B and C, respectively.

4.2.3 Analytical Characterisation

Elemental analysis of hand-picked crystals of $[Mn_4(SO_4)_8(OH)_2(H_2O)_2](enH_2)_5$ **(4)**, $[Fe_3(SO_4)_3(OH)_2(H_2O)_2](NH_4)_2$ **(5)**, $[Mn_3(SO_4)_3(OH)_2(trienH_2)]$ **(6)**, $[Fe(SO_4)(trien)]$ **(8)**, $[Mn(SO_4)_2](enH_2)$ **(9)**, $[Mn_2(SO_4)_2(en)_2]$ **(10)** and $[Co_3(SO_4)_3(OH)_2](enH_2)$ **(11)** are summarised in Table 4.6. For **(4)-(6)** and **(8)-(11)** results of CHN analysis are in agreement with the carbon, nitrogen and hydrogen content calculated on the basis of the crystallographically determined formula. $[Mn(SO_4)(trien)]$ **(7)** could not be analytically

characterised due to the impossibility of reproducing the reaction and getting enough material for further characterisation, but its crystal structure was found to be isostructural to that of the iron analogue **(8)**.

Powder X-ray diffraction data for $[Mn_4(SO_4)_8(OH)_2(H_2O)_2](enH_2)_5$ **(4)**, $[Fe_3(SO_4)_3(OH)_2(H_2O)_2](NH_4)_2$ **(5)**, $[Mn_3(SO_4)_3(OH)_2(trienH_2)]$ **(6)**, $Fe(SO_4)(trien)]$ **(8)**, $[Mn(SO_4)_2](enH_2)$ **(9)**, $[Mn_2(SO_4)_2(en)_2]$ **(10)** and $[Co_3(SO_4)_3(OH)_2](enH_2)$ **(11)** were collected over the range $4 \leq 2\theta\ /° \leq 50$ on a ground portion of bulk sample. The observed diffraction patterns were fitted using the predicted peak positions with TOPAS program [288] in order to refine the lattice parameters (Appendix A).

For **(4)**, the diffraction pattern indicates the presence of $[Mn_4(SO_4)_8(OH)_2(H_2O)_2](enH_2)_5$ **(4)** as the majority phase and the peaks can be indexed on the basis of a monoclinic unit cell determined for $[Mn_4(SO_4)_8(OH)_2(H_2O)_2](enH_2)_5$ **(4)** from the single-crystal diffraction study. The peaks that could not be indexed to the manganese sulphate were assigned to ethylenediammonium sulphate.

For **(5)**, the X-ray diffraction pattern indicates that the bulk sample consists of a mixture of $[Fe_3(SO_4)_3(OH)_2(H_2O)_2](NH_4)_2$ **(5)** and iron oxide, Fe_2O_3. Those peaks due to the formation of $[Fe_3(SO_4)_3(OH)_2(H_2O)_2](NH_4)_2$ **(5)** can be indexed on the basis of the orthorhombic unit cell determined from the single-crystal X-ray diffraction data.

The peaks in the powder X-ray diffraction pattern of **(6)** can be assigned to the manganese sulphate $[Mn_3(SO_4)_3(HO)_2(trienH_2)]$ **(6)**, which appears as a single-phase, and indexed on the basis of the orthorhombic unit cell obtained from the single-crystal X-ray diffraction study.

For **(8)**, the diffraction pattern of the bulk sample indicates the presence of $[Fe(SO_4)(trien)]$ as a single-phase. The peaks were indexed on the basis of the monoclinic unit cell determined from the single-crystal X-ray diffraction data and its lattice parameters were refined using TOPAS program [288] (Appedix A).

The powder X-ray diffraction pattern for **(9)** revealed that the product consisted of a mixture of two phases that were identified as $[Mn(SO_4)_2](enH_2)$ **(9)** and $[NH_3(CH_2)_2NH_3][Mn(SO_4)_2(H_2O)_4]$ [333]. Peaks belonging to **(9)** can be indexed on the basis of the monoclinic unit cell determined from the single-crystal diffraction data.

Table 4.1. Reaction conditions for the solvothermal synthesis of compounds **(4)-(11)**

Compound	Reactants and amounts	Mixture and Composition	T / °C	Time/ days	Product
(4)	$MnSO_4 \cdot H_2O$ (0.338 g; 2 mmol); en (0.2 mL; 3 mmol); H_2SO_4 (0.11 mL; 2 mmol); deionised water (0.036 mL; 1 mmol)	Mn:en:H_2SO_4:H_2O 1:1.5:1:0.5	170	6	colourless crystals + brown powder
(5)	$FeSO_4$ (0.608 g; 4 mmol); spermine (0.4 g; 2 mmol); H_2SO_4 (0.11 mL; 2 mmol); deionised water (0.145 mL; 4 mmol)	Fe:sp:H_2SO_4:H_2O 2:1:1:2	175	5	black needles + black powder
(6)	$MnSO_4 \cdot H_2O$ (0.338 g; 2 mmol); trien (0.32 mL; 2 mmol); H_2SO_4 (0.11 mL; 2 mmol); deionised water (0.036 mL; 1 mmol)	Mn:trien:H_2SO_4:H_2O 1:1:1:0.5	170	10	colourless crystals + pale brown powder
(7)	$MnSO_4 \cdot H_2O$ (0.338 g; 2 mmol); trien (0.32 mL; 2 mmol); H_2SO_4 (0.11 mL; 2 mmol); deionised water (0.36 mL; 1 mmol)	Mn:trien:H_2SO_4:H_2O 1:1:1:0.5	170	6	colourless crystals + white powder
(8)	$FeSO_4$ (0.304 g; 2 mmol); trien (0.32 mL, 2 mmol); H_2SO_4 (0.11 mL; 2 mmol); deionised water (0.072 mL; 2 mmol)	Fe:trien:H_2SO_4:H_2O 1:1:1:1	170	5	brown crystals + brown powder
(9)	$MnSO_4 \cdot H_2O$ (0.338 g; 2 mmol); en (0.2 mL; 2 mmol); H_2SO_4 (0.11 mL; 2 mmol); deionised water (0.072 mL; 2 mmol)	Mn:en:H_2SO_4:H_2O 1:1:1:1	160	6	colourless crystals + white powder
(10)	$MnSO_4 \cdot H_2O$ (0.338 g; 2 mmol); en (0.2 mL; 2 mmol) and H_2SO_4 (0.11 mL; 2 mmol); deionised water (0.072 mL; 2 mmol)	Mn:en:H_2SO_4:H_2O 1:1:1:1	175	6	brown crystals + pale brown powder
(11)	$CoSO_4 \cdot 7H_2O$ (0.55 g; 2 mmol); en (0.2 mL; 2 mmol); H_2SO_4 (0.11 mL; 2 mmol); deionised water (0.072 mL; 2 mmol)	Co:en:H_2SO_4:H_2O 1:1:1:1	170	5	dark pink crystals + pale pink crystals

Table 4.2. Crystallographic data for $[Mn_4(SO_4)_8(OH)_2(H_2O)_2](enH_2)_5$ **(4)**, $[Fe_3(SO_4)_3(OH)_2(H_2O)_2](NH_4)_2$ **(5)** and $[Mn_3(SO_4)_3(OH)_2(trienH_2)]$ **(6)**.

Compound number	**(4)**	**(5)**	**(6)**
Temperature / K	293	293	293
M_r	1368.84	561.85	635.24
Crystal Size (mm)	0.30 X 0.30 X 0.32	0.10 X 0.10 X 1.00	0.40 X 0.40 X 1.00
Crystal Habit	Colourless plate	Black needle	Colourless plate
Crystal System	Monoclinic	Orthorhombic	Orthorhombic
Space Group	*$P2_1/c$*	*$Cmc2_1$*	*Pnma*
***a*(Å)**	10.2425(4)	18.2212(9)	10.5493(5)
***b*(Å)**	14.8953(5)	7.6804(3)	22.3799(10)
***c*(Å)**	14.1119(2)	0.9283(4)	7.7373(15)
β(°)	92.259(2)		
V (Å³)	2151.31(13)	1389.43(10)	1826.72(15)
Z	2	4	2
μ (mm^{-1})	1.66	3.64	2.47
ρ_{calc} (g cm^{-3})	2.113	2.686	2.310
Residual electron density (min, max) (e$Å^{-3}$)	-0.38, 0.43	-0.82, 0.54	-0.39, 0.39
Measured data	39265	37456	50195
Unique data	6306	2161	2867
Observed data *(I>3σ(I))*	4422	1824	2474
R_{int}	0.028	0.031	0.023
R(F)	0.027	0.018	0.017
$_wR(F)$	0.029	0.020	0.018

Table 4.3. Crystallographic data for [M(SO_4)(trien)] M=Mn, Fe **(7)-(8)**

Compound number	**(7)**	**(8)**
Temperature / K	293	293
M_r	297.23	298.5
Crystal Size (mm)	0.12 X 0.20 X 0.32	0.14 X 0.20 X 0.60
Crystal Habit	Colourless plate	Brown plate
Crystal System	Monoclinic	Monoclinic
Space Group	$P2_1/n$	$P2_1/n$
***a*(Å)**	7.8614(3)	7.7791(5)
***b*(Å)**	13.3345(4)	13.1085(8)
***c*(Å)**	11.2349(4)	11.4073(8)
β(°)	105.776(2)	105.234(4)
V (Å^3)	1133.37(7)	1122.35(13)
Z	4	4
μ (mm^{-1})	1.36	1.54
ρ_{calc} (g cm^{-3})	1.742	1.764
Residual electron density (min, max) (eÅ^{-3})	-0.29, 0.36	-0.42, 0.30
Measured data	31589	32312
Unique data	3465	6725
Observed data *(I>3σ(I))*	1868	2864
R_{int}	0.035	0.023
R(F)	0.024	0.032
$_wR(F)$	0.025	0.026

Table 4.4. Crystallographic data for $[Mn(SO_4)_2](enH_2)$ **(9)** and $[Mn_2(SO_4)_2(en)_2]$ **(10)**.

Compound number	**(9)**	**(10)**
Temperature / K	293	293
M_r	309.17	422.18
Crystal Size (mm)	0.28 X 0.50 X 0.50	0.24 X 0.30 X 0.40
Crystal Habit	Colourless plate	Brown plate
Crystal System	Monoclinic	Orthorhombic
Space Group	*$P2_1/n$*	*Pbcm*
***a*(Å)**	6.6176(2)	4.8879(2)
***b*(Å)**	5.5457(2)	9.9791(4)
***c*(Å)**	25.8768(10)	14.1036(7)
β(°)	90.542(2)	
V (Å³)	949.62(6)	687.93(5)
Z	4	2
μ (mm^{-1})	1.86	2.18
ρ_{calc} (g cm^{-3})	2.162	2.038
Residual electron density (min, max) (e$Å^{-3}$)	-0.42, 0.33	-0.37, 0.38
Measured data	26022	5559
Unique data	2892	1082
Observed data *($I>3\sigma(I)$)*	2286	894
R_{int}	0.021	0.018
R(F)	0.021	0.018
$_wR(F)$	0.023	0.022

Table 4.5. Crystallographic data for $[Co_3(SO_4)_3(OH)_2](enH_2)$ **(11)**.

Compound number	**(11)**
Temperature / K	293
M_r	562.46
Crystal size (mm)	0.40 X 0.60 X 0.80
Crystal habit	Pink plate
Crystal system	Monoclinic
Space group	*Cm*
***a* (Å)**	11.6795(3)
***b* (Å)**	19.9926(6)
***c* (Å)**	8.9249(3)
β (°)	93.168(1)
V($Å^3$)	2080.81(11)
Z	6
μ(mm^{-1})	4.08
ρ_{calc} (g cm^{-3})	2.692
Residual electron density (min, max) (e$Å^{-3}$)	-0.68, 0.51
Measured data	14191
Unique data	5545
Observed data (I>3σ(I))	5337
R_{int}	0.021
R(F)	0.018
$_wR(F)$	0.020

Table 4.6. CHN analysis for compounds **(4)-(11)**

Compound	Actual (%)			Theoretical (%)		
	C	H	N	C	H	N
(4)	9.2	4.5	11.2	8.8	4.0	10.2
(5)		2.4	4.8		2.5	4.8
(6)	12.2	3.6	9.1	11.3	3.4	8.8
(8)	22.6	5.7	18.0	24.17	6.1	18.8
(9)	7.6	3.5	8.8	7.8	3.3	9.0
(10)	11.2	3.8	13.4	11.4	3.8	13.3
(11)	4.3	4.8	2.2	4.3	5.0	2.1

Powder X-ray diffraction data of **(10)** indicate the presence of $[Mn_2(SO_4)_2(en)_2]$ as the majority phase and some impurity peaks which were identified as ethylenediammonium sulphate. Peaks of **(10)** can be assigned on the basis of the monoclinic unit cell calculated from single-crystal X-ray diffraction study.

Powder X-ray diffraction data of **(11)** revealed the presence of $[Co_3(SO_4)_3(OH)_2](enH_2)$ as the majority phase and the peaks can be indexed on the basis of the monoclinic unit cell obtained from the single-crystal X-ray diffraction data. $[NH_3(CH_2)_2NH_3][Co(SO_4)_2(H_2O)_4]$ [334] was also identified as the minority phase.

Thermogravimetric analysis data were collected under nitrogen on hand-picked crystals of $[Mn_4(SO_4)_8(OH)_2(H_2O)_2](enH_2)_5$ **(4)**, $[Fe_3(SO_4)_3(OH)_2(H_2O)_2](NH_4)_2$ **(5)**, $[Mn_3(SO_4)_3(OH)_2(trienH_2)]$ **(6)**, $Fe(SO_4)(trien)]$ **(8)**, $[Mn(SO_4)_2](enH_2)$ **(9)**, $[Mn_2(SO_4)_2(en)_2]$ **(10)** and $[Co_3(SO_4)_3(OH)_2](enH_2)$ **(11).** In **(4)**, the thermal decomposition process occurs in three steps (Figure 4.1(a)) with a total weight loss of 69.59 % (calculated 77.72 %) which corresponds to the formation of 4/3 of Mn_3O_4 as the final product, as identified by powder X-ray diffraction. The first step of 7.34 % (calc: 6 %) at 100 °C can be assigned to the removal of one mole of ethylenediamine and water, which would yield the formation of $[Mn_4(SO_4)_8(H_2O)_2](enH_2)_4$ as an intermediate product. The second and third steps correspond to the loss of three moles of ethylenediamine, three moles of SO_3 and four moles of water, and one mole of ethylenediamine, one mole of SO_3 and water, respectively. For **(5)**, the weight loss occurs in two steps (Figure 4.1(b)) yielding the formation of two moles of $FeSO_4$ and ½ of Fe_2O_3 as the final products, which were

identified by powder X-ray diffraction. This corresponds to a total weight loss of 29.17 % which is in good agreement with the expected value 31.3 %. The first step of 7.36 % (calc: 6.4 %) at 120 °C is associated to the loss of two moles of water and the second step of 21.81 % (calc: 24.9 %) at 650 °C can be attributed to the removal of two moles of NH_3, two moles of water, one mole of SO_2 and ¼ of oxygen.

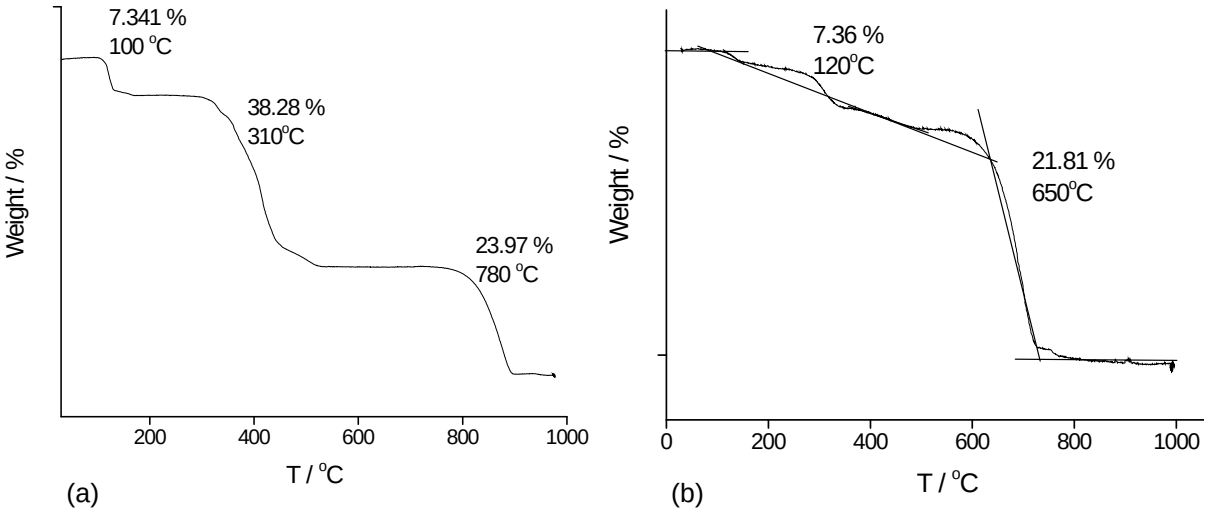

Figure 4.1. Thermogravimetric analysis data for (a) $[Mn_4(SO_4)_8(OH)_2(H_2O)_2](enH_2)_5$ **(4)** and (b) $[Fe_3(SO_4)_3(OH)_2(H_2O)_2](NH_4)_2$ **(5)**.

The decomposition process for **(6)** takes place in two steps (Figure 4.2(a)). The first step (exp: 31.44 %; calc: 29 %) is associated to the removal of two moles of triethylenetetramine and two moles of water at 350 °C, which produces the formation of the intermediate $[Mn_3(SO_4)_3]$. In the second step, the decomposition is completed with the loss of three moles of SO_2 and O_2, which corresponds to a weight loss of 33.81 % (calc: 35.3 %). This is consistent with the formation of Mn_3O_4 as the final product, as identified by powder X-ray diffraction, which corresponds to a weight loss of 65.25 %, which is in excellent agreement with the expected value of 64.3 %. In **(8)** the weight loss occurs in three steps, consistent with the formation of ½ of Fe_2O_3, identified by powder X-ray diffraction, and that corresponds to a total weight loss of 69.1 % which is in agreement with the calculated value 73.8 % (Figure 4.2 (b)). The first step (exp: 23.4 %; calc: 20.13 %) corresponds to the removal of a fraction of the triethylenetetramine that comes out as one mole of ethylenediamine. The second and third weight losses are consistent with the removal of the remaning fraction of the amine, as diethylenediamine, SO_2 and ¼ of oxygen.

The weight loss for **(9)** occurs in three steps (Figure 4.3(a)), in which 1/3 of Mn_3O_4 is obtained as the decomposition product, with a total weight loss of 77.51 %, which is consistent with the expected value of 75.35 %. The first step of 12.65 % (calc: 11.34 %) corresponds to the removal of one mole of NH_3 and one mole of water, and the second of 44.38 % to the removal of one mole of ethylenediamine, NH_3 and CO_2 and one mole of SO_2 and water, which yields the formation of the intermediate $MnSO_4$. In the last step one mole of SO_2 is removed at 794 °C. For **(10)** the decomposition process takes place in two steps with a total weight loss of 64.31 %, which is in good agreement with the calculated value 63.9 %, which corresponds to the formation of 2/3 of Mn_3O_4 as the decomposition product, identified by powder X-ray diffraction (Figure 4.3(b)). In the first weight loss (exp: 28.8 %; calc: 28.5 %) the two moles of ethylenediamine are removed which yields the formation of the intermediate $[Mn_2(SO_4)_2]$. The second step of 35.5 % (calc: 35.4 %) corresponds to the loss of two moles of SO_2 and 2/3 of O_2.

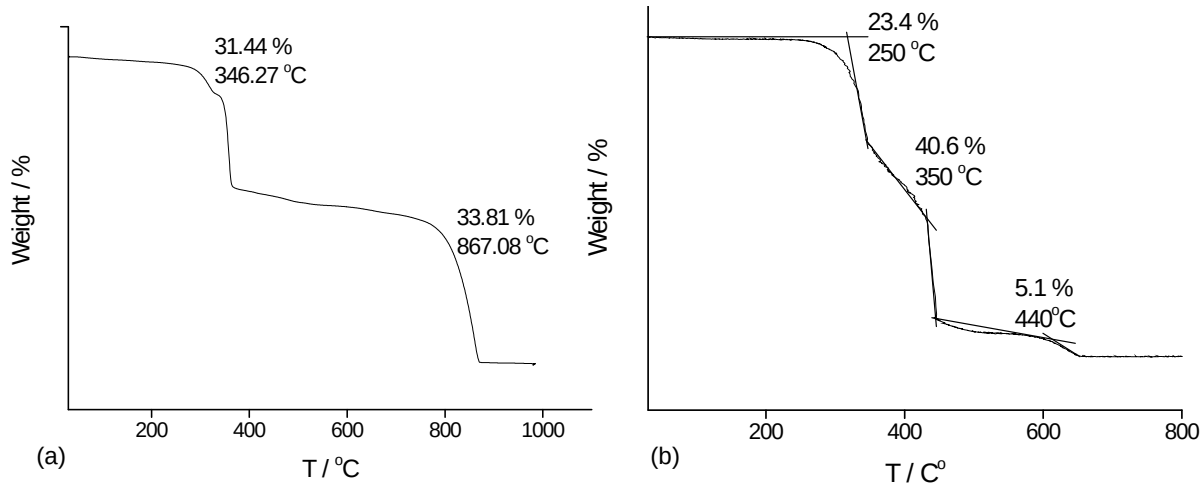

Figure 4.2. Thermogravimetric analysis data for (a) $[Mn_3(SO_4)_3(OH)_2(trienH_2)]$ **(6)** and (b) $[Fe(SO_4)(trien)]$ **(8)**.

For **(11)** the thermal decomposition takes place in two steps (Figure 4.4). The first step of 17.85 % (calc: 17.1 %) is consistent with the loss of a mole of ethylenediamine and two moles of water, which leaves $[Co_3(SO_4)_3]$ as an intermediate product. The second weight loss (exp: 42.74 %; calc: 42.7 %) can be assigned to the removal of three moles of SO_2 and 3/2 of O_2, which yields the formation of three moles of CoO as the final product, which was identified by powder X-ray diffraction. The total weight loss that occurs in the

thermal decomposition is 60.59 %, which is in excellent agreement with the calculated value (59.8 %).

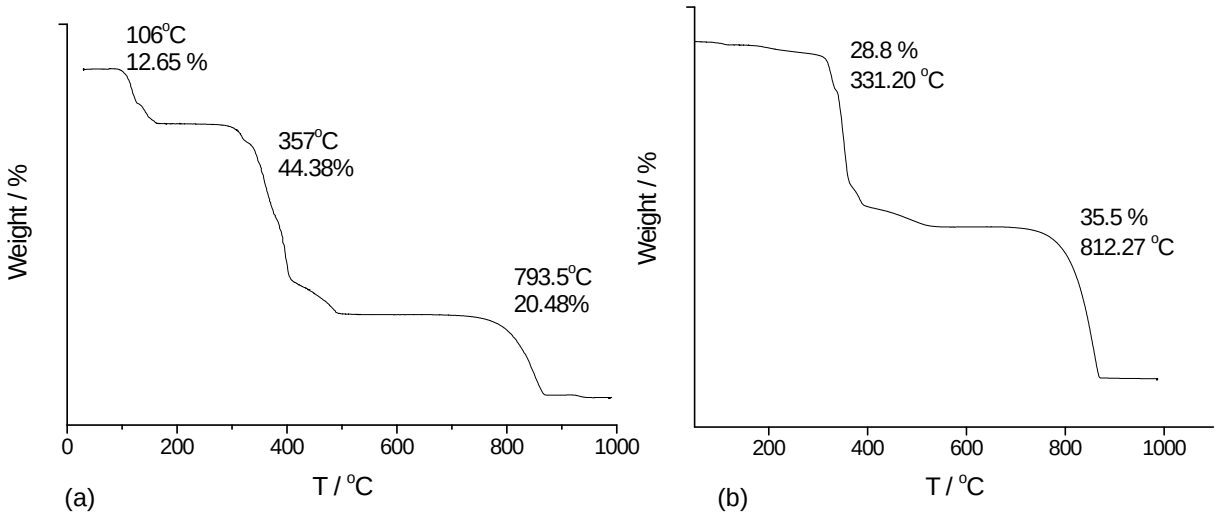

Figure 4.3. Thermogravimetric analysis data for (a) $[Mn(SO_4)_2](enH_2)_2$ **(9)** and (b) $[Mn_2(SO_4)_2(en)_2]$ **(10)**

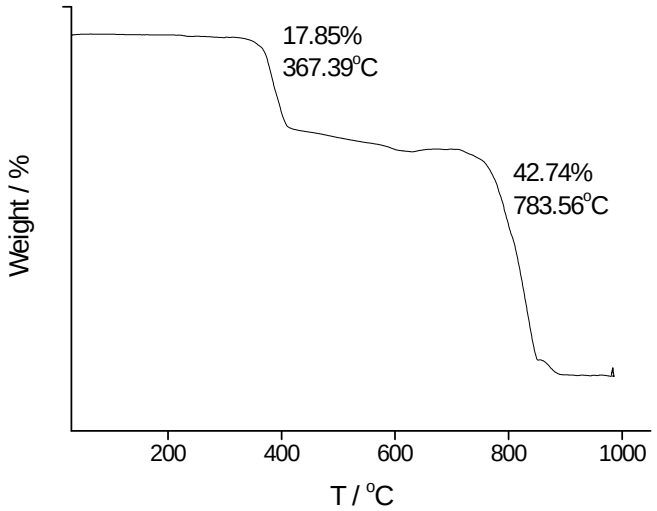

Figure 4.4. Thermogravimetric analysis data for $[Co_3(SO_4)_3(OH)_2](enH_2)$ **(11)**

Infrared spectroscopic data for $[Mn_4(SO_4)_8(OH)_2(H_2O)_2](enH_2)_5$ **(4)**, $[Mn(SO_4)_2](enH_2)$ **(9)**, $[Mn_2(SO_4)_2(en)_2]$ **(10)** and $[Co_3(SO_4)_3(OH)_2](enH_2)$ **(11)** (Figure 4.5) show vibrations appearing in the region between 3260-2930 cm^{-1}, 1680-1530 cm^{-1} and 1350 cm^{-1} which are associated to the presence of ethylenediamine and can be assigned to the N-H stretching, H-N-H bending and C-N stretching vibrations, respectively. The peaks that appear at 866 and 790 cm^{-1} can be assigned to C-H bending. The bands at 1110 cm^{-1}, and the bands at around 600 cm^{-1} are attributed to the asymmetric stretching and

deformation of S-O vibrations and support the presence of the SO_4^{2-} anion. The peak at 3390 cm^{-1} that is observed in **(4)** and **(11)** can be attributed to the presence of O-H vibrations of the hydroxyl group. For $[Fe_3(SO_4)_3(OH)_2(H_2O)_2](NH_4)_2$ **(5)** (Figure 4.6) the peaks at 4117 cm^{-1}, 3924 cm^{-1} and that at 3776 cm^{-1} can be attributed to the N-H stretching of the ammonia cation and O-H stretching of the hydroxyl group. The broad band appearing in the region that goes from 3500-1500 cm^{-1} might be due to presence of water in the structure and the vibrations due to the S-O asymmetric stretching and asymmetric deformation were identified at 1093 cm^{-1} and 588 cm^{-1}.

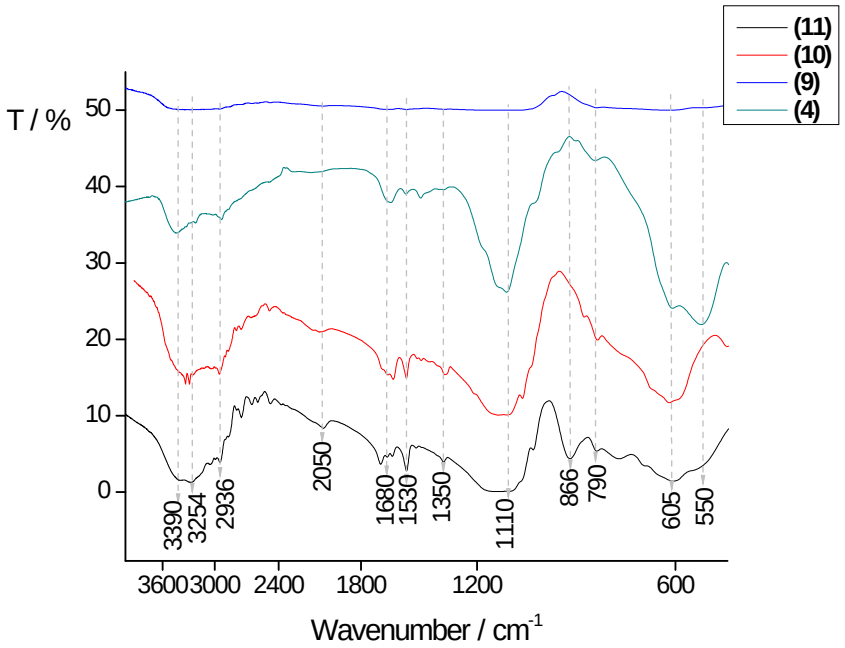

Figure 4.5. Infrared data for $[Mn_4(SO_4)_8(OH)_2(H_2O)_2](enH_2)_5$ **(4)** (green), $[Mn(SO_4)_2](enH_2)$ **(9)** (blue), $[Mn(SO_4)(en)]$ **(10)** (red) and $[Co_3(SO_4)_3(OH)_2](enH_2)$ **(11)** (black).

Infrared spectroscopic data for $[Mn_3(SO_4)_3(OH)_2(trienH_2)]$ **(6)** and $[Fe(SO_4)(trien)]$ **(8)** are shown in Figure 4.7. For **(6)** the broad band at 3252 cm^{-1} can be assigned to the overlapping of two types of bands, those due to the N-H stretching and those other due to O-H stretching in the hydroxyl group. The two peaks at 1640 cm^{-1} and 1504 cm^{-1} can be assigned to the N-H bending, being consistent with the presence of triethylenetetramine. Those bands at 1085 cm^{-1} and 615.5 cm^{-1} are attributed to the asymmetric stretching and asymmetric deformation of S-O vibrations in the SO_4^{2-} anion. For **(8)** N-H stretching and N-H bending bands appear at 3288-2947 cm^{-1} and 1650-1542 cm^{-1}. Those bands attributed

to the asymmetric stretching and asymmetric deformation of S-O vibrations due to the presence of the SO_4^{2-} anion appear at 1094 and 616.6 cm^{-1}. The band at 827 cm^{-1} can be assigned to C-H bending in the amine molecules.

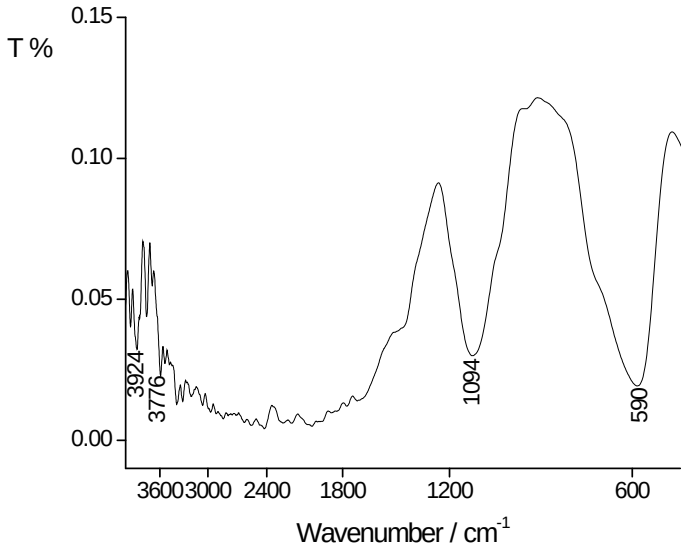

Figure 4.6. Infrared data for $[Fe_3(SO_4)_3(OH)_2(H_2O)_2](NH_4)_2$ **(5)**.

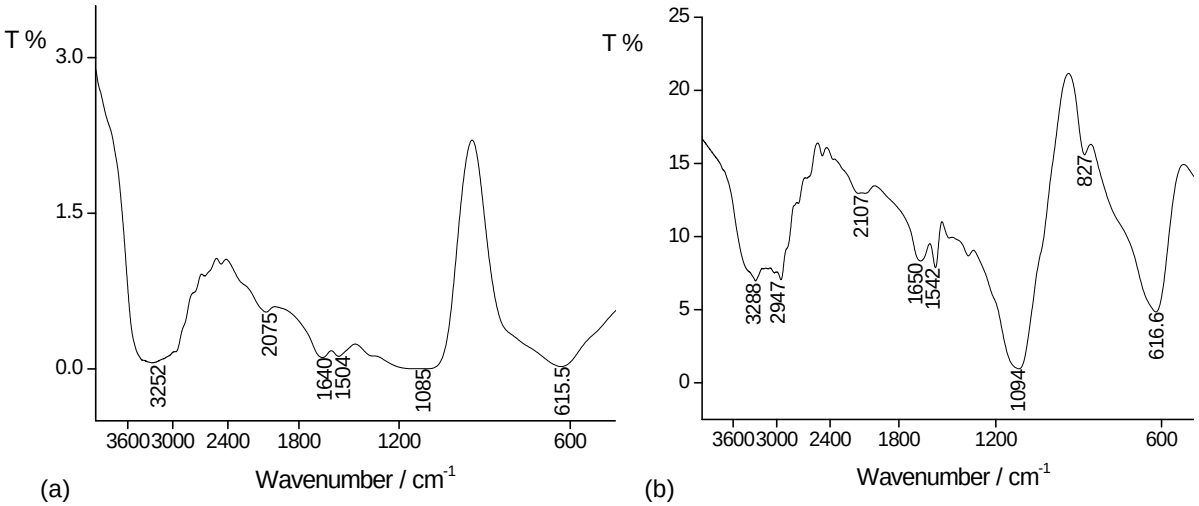

Figure 4.7. Infrared spectroscopic data for (a) $[Mn_3(SO_4)_3(OH)_2(trienH_2)]$ **(6)** and (b) $[Fe(SO_4)(trien)]$ **(8)**.

The UV/Vis diffuse reflectance spectrum for $[Co_3(SO_4)_3(OH)_2](enH_2)$ **(11)** is shown in Figure 4.8. In a cubic field, three spin-allowed transitions are predicted due to the splitting of the free-ion, the ground ^4F term and the ^4P term. A band around 0.99-1.24 eV is usually assigned to the $^4T_{1g}(F) \rightarrow {}^4T_{2g}(F)$ transition and a multiplet structure band observed around 2.48 eV is assigned to the $^4T_{1g}(F) \rightarrow {}^4T_{1g}(P)$ transition. The $^4T_{1g}(F) \rightarrow {}^4A_{2g}(F)$

transition band generally appears as a very weak band at 1.49-1.74 eV. The spectrum of **(11)** exhibits a band at 2.41 eV with a shoulder at 2.62 eV that can be assigned to the $^4T_{1g}(F) \rightarrow {}^4T_{1g}(P)$ transition. The band gap was experimentally calculated from the slope of the curve to be 4.22(5) eV.

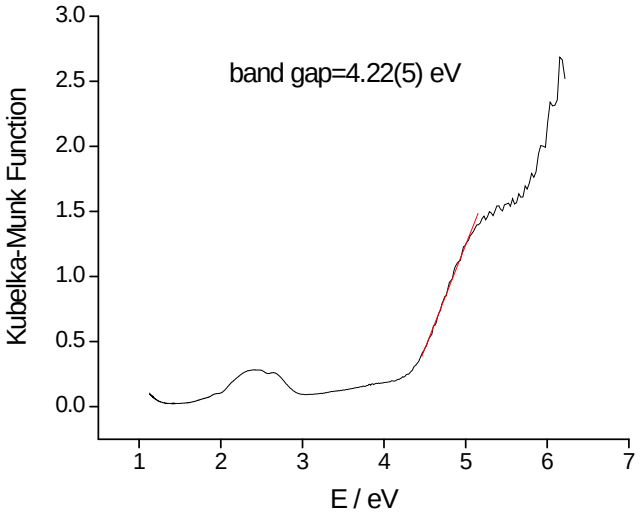

Figure 4.8. UV/Vis spectrum of $[Co_3(SO_4)_3(OH)_2](enH_2)$ **(11).**

4.3 M_4O_{20} building block for the synthesis of $[Mn_4(SO_4)_8(OH)_2(H_2O)_2](enH_2)_5$, $[Fe_3(SO_4)_3(OH)_2(H_2O)_2](NH_4)_2$ and $[Mn_3(SO_4)_3(OH)_2(trienH_2)]$.

4.3.1 Crystal structure description

4.3.1.1 $[Mn_4(SO_4)_8(OH)_2(H_2O)_2](enH_2)_5$ **(4)**

The asymmetric unit of $[Mn_4(SO_4)_8(OH)_2(H_2O)_2](enH_2)_5$ **(4)** contains two crystallographically distinct manganese atoms each of which is six-coordinated. The local coordination scheme for **(4)** is shown in Figure 4.9. Both Mn(1) and Mn(2) are coordinated to four sulphate tetrahedra in a monodentate fashion. The four sulphate tetrahedra coordinated to Mn(1) serve to link the manganese centres, whereas Mn(2) is coordinated to two terminal sulphate tetrahedra. While the coordination environment of Mn(1) is completed by two hydroxyl oxygen atoms, Mn(2) is connected to one hydroxyl oxygen atom and to an oxygen atom of a water molecule. The average Mn(1)-O distance is 2.1843 Å, with the short Mn(1)-O(1) and Mn(1)-O'(1) distances, with values 2.1462(13) Å and 2.1223(13) Å respectively, corresponding to the connection of the manganese centre to two three-coordinated oxygen atoms. Similarly, the average Mn(2)-O distance takes a value of

2.1971 Å with a shortest distance of 2.0890(13) Å, also associated to the linkage of Mn(2) to the three-coordinated oxygen atom O(1). Both average distances are consistent with distances expected on atomic radii and with those previously reported for manganese sulphates [335, 336]. Sulphur-oxygen distances range from 1.4568(16) Å to 1.4867(15) Å, which is in good agreement with the average reported value for an S-O bond in materials containing the oxy-anion of sulphur.

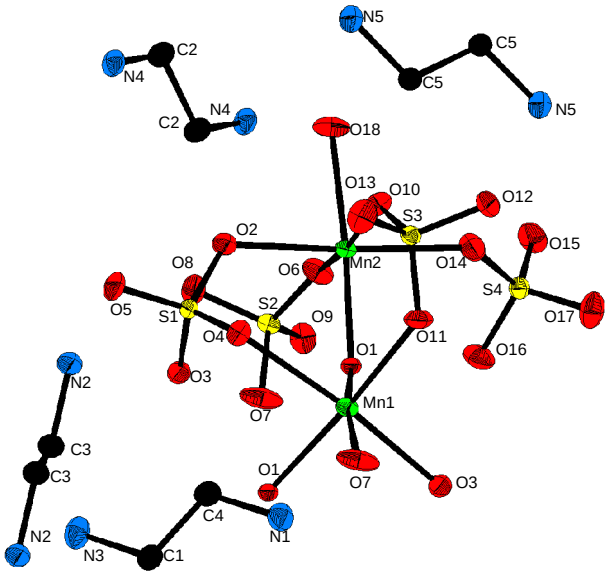

Figure 4.9. Atoms labelling scheme and thermal ellipsoids at 50% probability for $[Mn_4(SO_4)_8(OH)_2(H_2O)_2](enH_2)_5$ **(4)**. Hydrogen atoms have been omitted for clarity.

The structure of $[Mn_4(SO_4)_8(OH)_2(H_2O)_2](enH_2)_5$ **(4)** is built up from isolated $[Mn_4(SO_4)_8(OH)_2(H_2O)_2]^{10-}$ units separated by diprotonated ethylenediamine cations as displayed in Figure 4.10, in which cations and anions are held together in a hydrogen-bond system involving N-H···O interactions (Appendix D). Also O-H···O hydrogen bond interactions between the hydrogen atoms in the water molecules with the oxygen atoms belonging to sulphate groups in adjacent units are present.

Each of these four-metal cluster $[Mn_4(SO_4)_8(OH)_2(H_2O)_2]^{10-}$ units adopt the butterfly-like structure that is shown in Figure 4.11. The core of this unit is a dimer formed by the edge-linkage of two $Mn(1)O_6$ octahedra, in which the two manganese centres are directly connected through a Mn-O-Mn bond *via* two three-coordinated oxygen atoms from a hydroxyl group. The distance between two Mn(1) centres is *ca.* 3.06 Å. The linkage is completed by two sulphate tetrahedra which bridge the two manganese centres through common vertices (Figure 4.11(b)). Each of these sulphate tetrahedra also serves to connect

the dimeric unit to the adjacent Mn(2) centres by vertex-sharing. In addition, the Mn(1)-Mn(1) dimeric unit is connected through the vertices associated with the shared edge to two $Mn(2)O_6$ octahedra. The linkage between Mn(1) and Mn(2) centres is completed by bridging sulphate tetrahedra that share two oxygen atoms with both Mn(1) and Mn(2). As a result of this linkage, a building unit of formula Mn_4O_{20} has been identified (Figure 4.12).

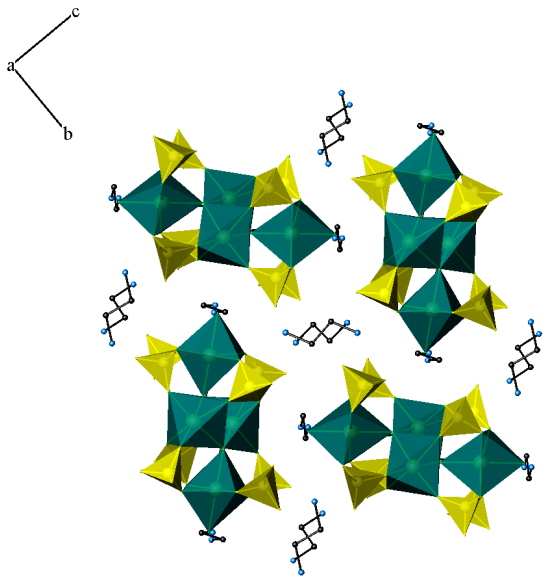

Figure 4.10. Structure of $[Mn_4(SO_4)_8(OH)_2(H_2O)_2](enH_2)_5$ **(4)** in which $[Mn_4(SO_4)_8(OH)_2(H_2O)_2]^{10-}$ isolated units are separated by diprotonated ethylenediamine cations (MnO_6 octahedra, green; SO_4 tetrahedra, yellow; N atoms, blue; C atoms, black).

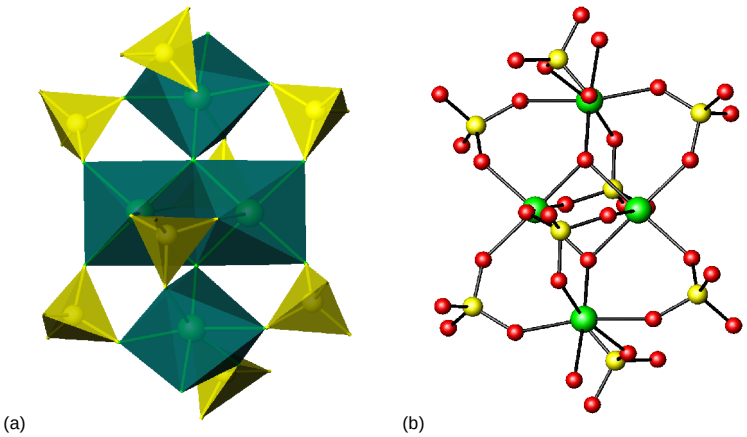

Figure 4.11. (a) Polyhedral representation of the butterfly-like $[Mn_4(SO_4)_8(OH)_2(H_2O)_2]^{10-}$ unit (MnO_6 octahedra, green; SO_4 tetrahedra, yellow); (b) Connectivity between manganese centres to form $[Mn_4(SO_4)_8(OH)_2(H_2O)_2]^{10-}$ unit (Mn atoms, green; S atoms, yellow; O atoms, red).

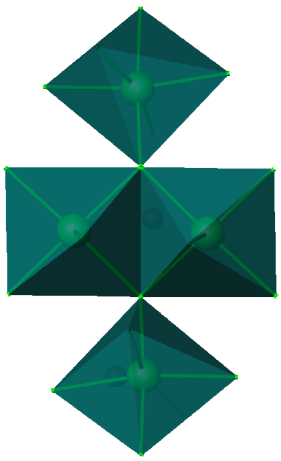

Figure 4.12. Mn_4O_{20} building unit obtained from the connectivity of four MnO_6 octahedra (MnO_6 octahedra, green).

4.3.1.2 $[Fe_3(SO_4)_3(OH)_2(H_2O)_2](NH_4)_2$ **(5)**

The asymmetric unit of $[Fe_3(SO_4)_3(OH)_2(H_2O)_2](NH_4)_2$ **(5)** contains two crystallographically distinct iron atoms, each of which is six-coordinated. Fe(1) is coordinated to four sulphate groups and to two hydroxyl oxygen atoms, in contrast with Fe(2), which is coordinated to three sulphate groups, to two hydroxyl oxygen atoms and to one oxygen from a water molecule. The atoms labelling scheme for the layered $[Fe_3(SO_4)_3(OH)_2(H_2O)_2](NH_4)_2$ **(5)** is displayed in Figure 4.13.

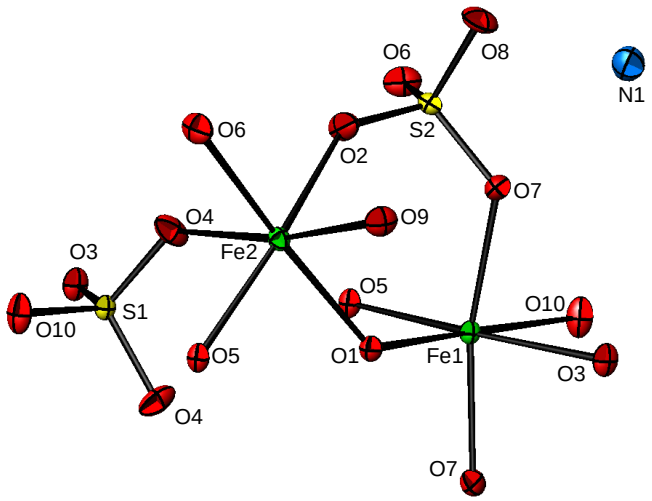

Figure 4.13. Atoms labelling scheme and thermal ellipsoids at 50% probability for $[Fe_3(SO_4)_3(OH)_2(H_2O)_2]$ $(NH_4)_2$ **(5)**. Hydrogen atoms have been omitted for clarity.

The average Fe(1)-O distance is 2.1503 Å which is very close to the average Fe(2)-O distance, which takes a value of 2.1422 Å. The longest Fe(2)-O(9) distance of 2.1962(16) Å is associated with the linkage of Fe(2) to a molecule of water. Those distances are in good agreement with those previously reported for the hydrated iron salt $Fe(SO_4)(H_2O)_7$ [337] and for the organically-templated $[(C(NH_2)_3]_2[Fe(H_2O)_6(SO_4)_2]$ [338] and are comparable to those expected from the sum of their ionic radii. S-O distances, with values that range from 1.4610(17) Å to 1.4865(15) Å, are consistent with the mean S-O distance of 1.473 Å.

The structure of $[Fe_3(SO_4)_3(OH)_2(H_2O)_2](NH_4)_2$ **(5)** is constructed from chains obtained by the connectivity of Fe_4O_{20} building units, analogous to those identified in $[Mn_4(SO_4)_8(OH)_2(H_2O)_2](enH_2)_5$ **(4)** (Figure 4.14). In contrast to **(4)**, only one sulphate tetrahedron ($S(2)O_4$) serves to connect, *via* vertex-sharing, the two Fe(2) centres that form the central dimeric unit, in which the Fe(2)-Fe(2) distance is *ca.* 3.06 Å. Two adjacent Fe_4O_{20} building units are joined together by vertex-sharing a common $Fe(1)O_6$ octahedron. The linkage between building units is completed *via* sulphate tetrahedra through sharing vertices, resulting in the formation of a chain running along [001] direction (Figure 4.14(c)).

Adjacent chains are in turn connected into anionic layers along the *b*-axis through bridging SO_4 tetrahedra (Figure 4.15). A sulphate tetrahedron that bridges one $Fe(1)O_6$ and one $Fe(2)O_6$ in one chain provides the connection between adjacent chains by linking to a FeO_6 octahedron in a neighbouring chain. The linkage between adjacent chains is completed by O-H···O hydrogen bonding interactions between water molecules of one chain and oxygen atoms of sulphate groups in a neighbouring chain.

The structure is completed by charge-balancing NH_4^+ cations that are located in the space between the layers alternating along the crystallographic *a*-axis (Figure 4.16). Cations and anions are held together through hydrogen-bond interactions involving N-H···O bonds (Appendix D).

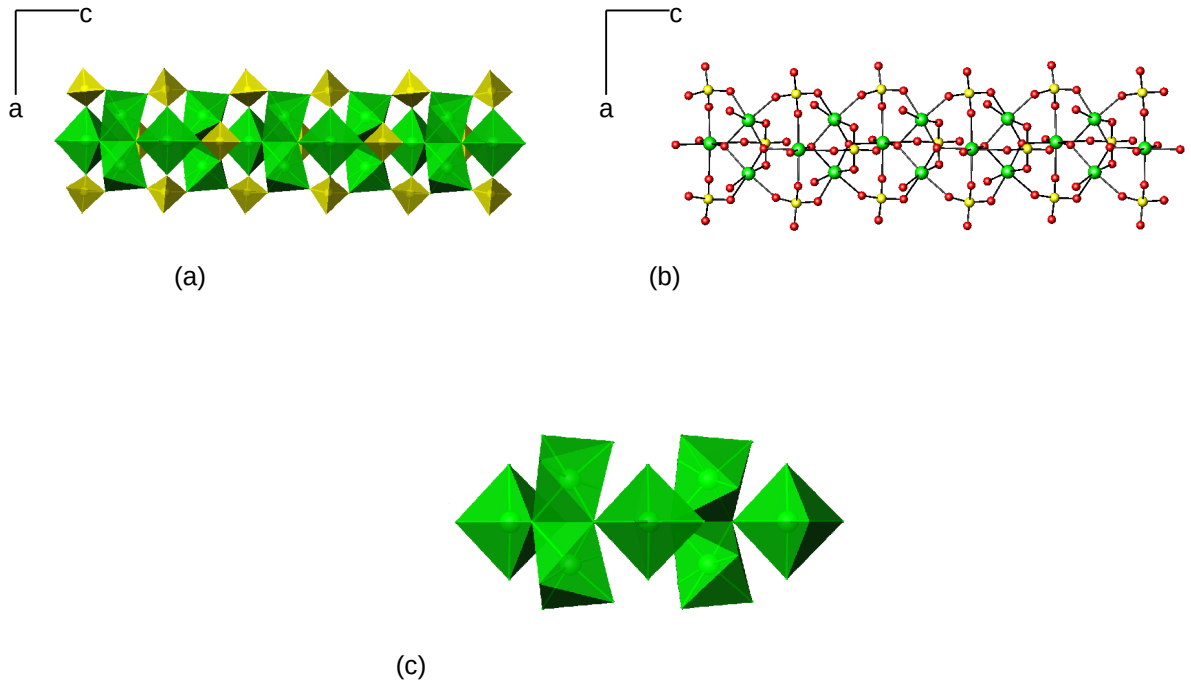

Figure 4.14. (a) Polyhedral representation of a chain in $[Fe_3(SO_4)_3(OH)_2(H_2O)_2](NH_4)_2$ **(5)** formed by edge- and vertex-linking FeO_6 octahedra and bridging SO_4 tetrahedra (FeO_6 octahedra, green; SO_4 tetrahedra, yellow); (b) ball and stick representation of the structure of the chain running along [001] (Fe, green; S, yellow; O, red); (c) Connectivity of two adjacent Fe_4O_{20} building units (FeO_6 octahedra, green).

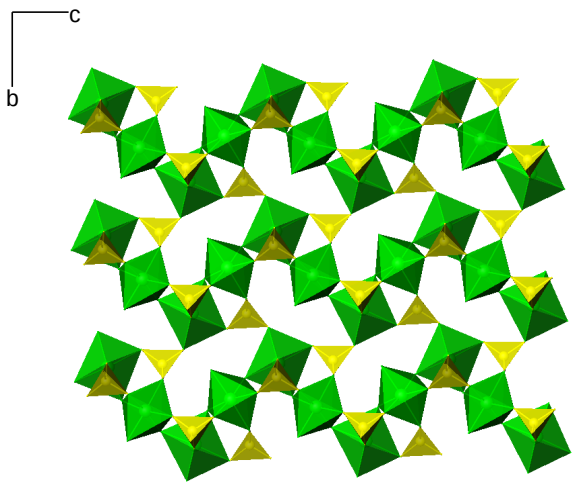

Figure 4.15. A layer in $[Fe_3(SO_4)_3(OH)_2(H_2O)_2](NH_4)_2$ **(5)** parallel to the *bc* plane constructed from the connectivity of neighbouring chains (FeO_6 octehedra, green; SO_4 tetrahedra, yellow).

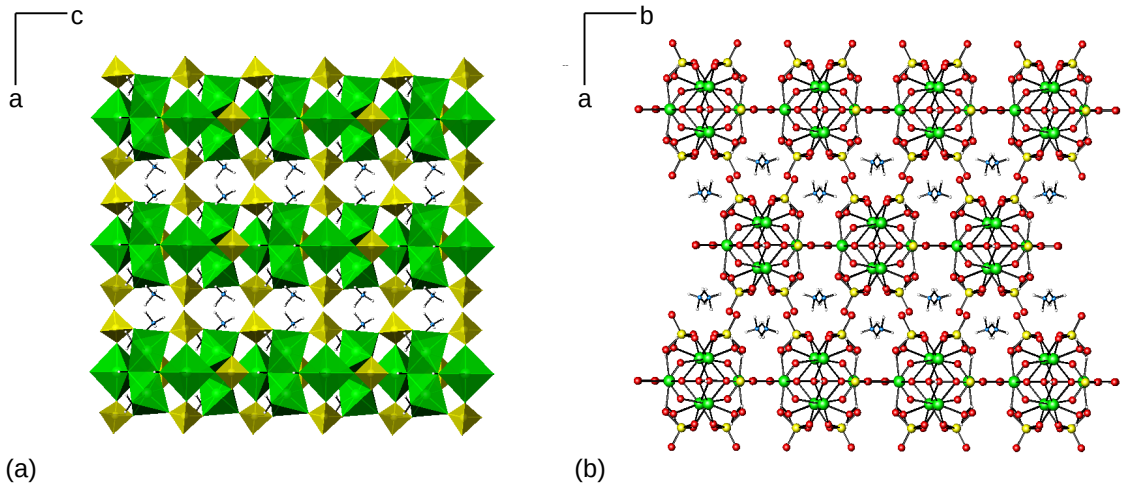

Figure 4.16. Two different representations of the layered structure of $[Fe_3(SO_4)_3(OH)_2(H_2O)_2](NH_4)_2$ **(5)** (a) polyhedral representation of the layered in the *ac* plane (FeO_6 octahedra, green; SO_4 tetrahedra, yellow, N, blue; H, white); (b) ball and stick representation of the layers in the *ab* plane (Fe, green; S, yellow; O, red; N, blue; H, white).

4.3.1.3 $[Mn_3(SO_4)_3(OH)_2(trienH_2)]$ **(6)**

The local coordination scheme for $[Mn_3(SO_4)_3(OH)_2(trienH_2)]$ **(6)** is shown in Figure 4.17.

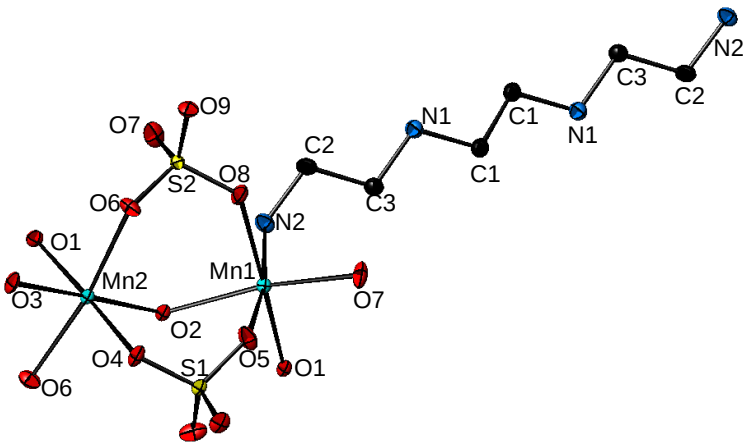

Figure 4.17. Atoms labelling scheme and thermal ellipsoids at 50% probability for $[Mn_3(SO_4)_3(OH)_2(trienH_2)]$ **(6)**. Hydrogen atoms have been omitted for clarity.

The asymmetric unit of $[Mn_3(SO_4)_3(OH)_2(trienH_2)]$ **(6)** contains two crystallographically distinct manganese atoms. Mn(1) is coordinated to three sulphate tetrahedra, to two hydroxyl oxygen atoms and to the amine molecule through a Mn-N bond.

Mn(2) is coordinated to four sulphate groups and to two hydroxyl oxygen atoms. The average Mn(1)-O distance takes a value of 2.2043 Å in comparison to Mn(2)-O with an average value of 2.1966 Å, distances that are consistent with those expected from the sum of their ionic radii and with those observed in previously reported manganese sulphates [335, 336]. The distance Mn(1)-N is 2.2982(9) Å which is in agreement with the expected Mn-N distance calculated from their covalent radii. S-O distances take values ranging from 1.4675(9) Å to 1.4854(10) Å and are concurrent with those reported for sulphate-containing substances.

The structure of $[Mn_3(SO_4)_3(OH)_2(trienH_2)]$ **(6)** is constructed from chains analogous to those observed in the structure of $[Fe_3(SO_4)_3(OH)_2(H_2O)_2](NH_4)_2$ **(5)**. In the structure of **(6)**, $Mn_4O_{18}N_2$ building units are connected through edge- and vertex-sharing MnO_6 and MnO_5N octahedra and bridging SO_4 tetrahedra that serve to complete the linkage *via* vertex-sharing along the crystallographic *a*-axis (Figure 4.18). The Mn(1)-Mn(1) distance within the central dimer that constitute the core of the building unit is *ca.* 3.26 Å. Chains are in turn connected into layers *via* vertex-linking SO_4 tetrahedra in an identical manner as in the structure of $[Fe_3(SO_4)_3(OH)_2(H_2O)_2](NH_4)_2$ **(5)** (Figure 4.19).

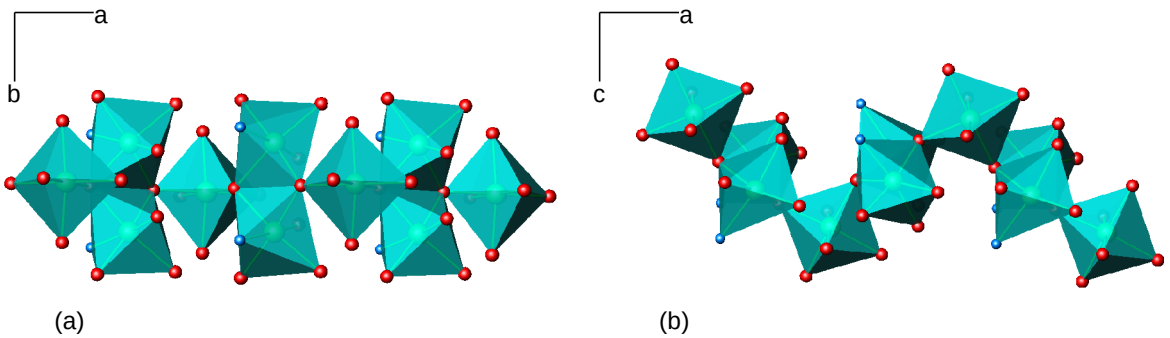

Figure 4.18. (a) Chain made up of three $Mn_4O_{18}N_2$ building units directed along the *a*-axis; (b) Transversal view of the linkage of three tetrameric building units along the *a*-axis; (MnO_6 and MnO_5N octahedra, blue; SO_4 tetrahedra, yellow; O, red; N, blue).

In comparison with the structure of $[Fe_3(SO_4)_3(OH)_2(H_2O)_2](NH_4)_2$ **(5)**, in which ammonia cations are located between the layers, in the structure of $[Mn_3(SO_4)_3(OH)_2(trienH_2)]$ **(6)** the diprotonated triethylenetetramine cations ($trienH_2^{2+}$) are directly coordinated to the metal centre through a Mn(1)-N covalent bond. Each $trienH_2^{2+}$ cation is coordinated to two Mn(1) centres in adjacent layers to form a three-dimensional

structure (Figure 4.20). The amine cations interact with the inorganic layers through N-H···O hydrogen bonds (Appendix D).

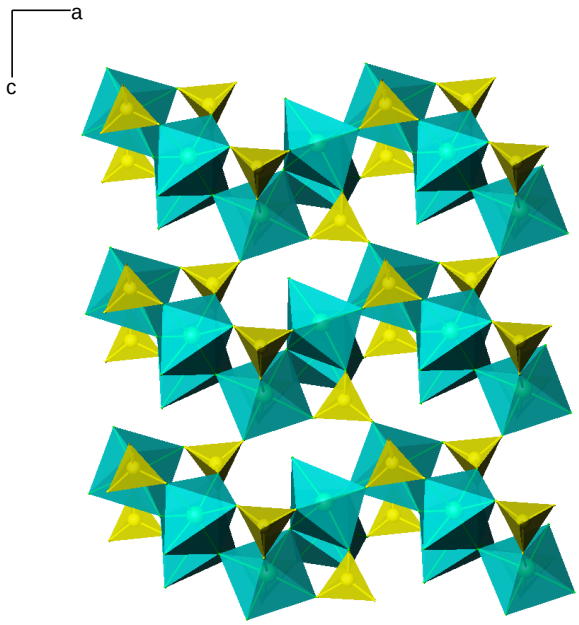

Figure 4.19. A layer in $[Mn_3(SO_4)_3(HO)_2(trienH_2)]$ **(6)** in the *ac* plane (MnO_6 and MnO_5N octahedra, blue; SO_4 tetrahedra, yellow).

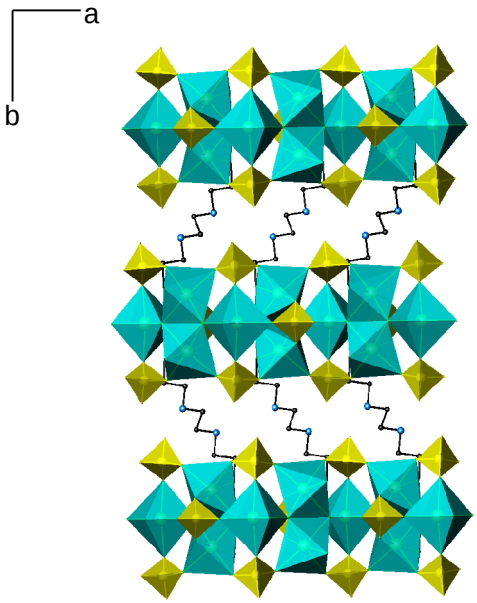

Figure 4.20. Three-dimensional structure of $[Mn_3(SO_4)_3(OH)_2(trienH_2)]$ **(6)** (MnO_6 and MnO_5N octahedra, pale blue; SO_4 tetrahedra, yellow; N atoms, dark blue; C atoms, black).

4.3.2 Magnetic Properties

Magnetic susceptibility data for $[Mn_4(SO_4)_8(OH)_2(H_2O)_2](enH_2)_5$ **(4)** at 1000 G are shown in Figure 4.21. The reciprocal magnetic susceptibility plot as a function of temperature shows an anomaly below 20 K. Above this temperature, the paramagnetic region can be fitted according to the Curie-Weiss equation with a Weiss constant of -10.70(3) K, which suggests antiferromagnetic interactions. The effective magnetic moment calculated from the fitting of the Curie-Weiss law to the linear region is 6.34(1) μ_B, which is close but a bit high compared to the spin-only value for Mn^{2+} ion. The Curie constant, magnetic moment and Weiss constant are summarised in Table 4.7.

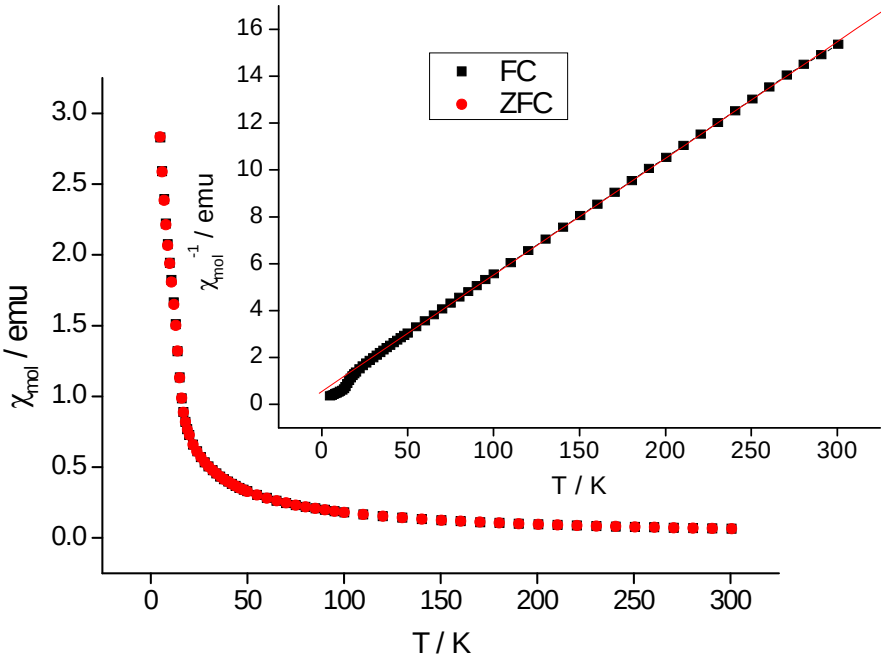

Figure 4.21. Zero field-cooled (Zfc)/ Field-cooled (Fc) susceptibility data and inverse susceptibility data (inset) for $[Mn_4(SO_4)_8(OH)_2(H_2O)_2](enH_2)_5$ **(4)**. The red line shows the fit to the Curie-Weiss law.

$[Mn_4(SO_4)_8(OH)_2(H_2O)_2](enH_2)_5$ **(4)** displays a decrease in the effective magnetic moment, as measured by the quantity $(8\chi T/4)^{1/2}$, as the temperature is lowered from 300 K to 5 K (Figure 4.22). The magnetic moment decreases slowly from 6.26 μ_B to 5.39 μ_B on cooling from 300 K to 20 K temperature after which it increases rapidly to 6.32 μ_B at 12 K. From 12 K to 5 K the magnetic moment decreases rapidly to 5.32 μ_B.

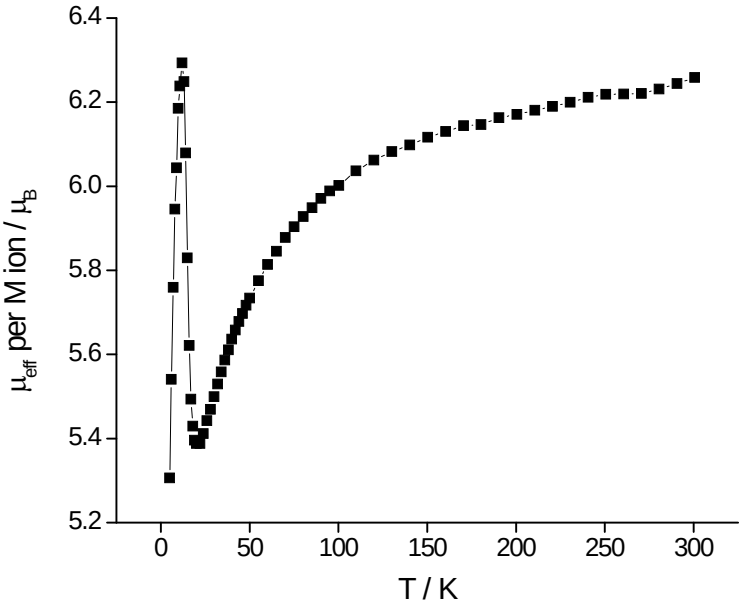

Figure 4.22. Effective magnetic moment per Mn ion for $[Mn_4(SO_4)_8(OH)_2(H_2O)_2](enH_2)_5$ **(4)** as a function of temperature at 1000 G.

Magnetic susceptibility data for $[Fe_3(SO_4)_3(OH)_2(H_2O)_2](NH_4)_2$ **(5)** at 100 G over the range of temperature 2-300 K (Figure 4.23) show a divergence between the field-cooled and zero field-cooled data below 122 K. Below this temperature, the zero field-cooled susceptibility decreases from 5.7 e.m.u at 122 K to 2.2 e.m.u at 46 K. Below 46 K the susceptibility abruptly increases to a value of 19.44 e.m.u at 34 K, after which it decreases again to 10.7 at 2 K. In the field-cooled plot, the susceptibility shows a small anomaly below 122 K, but it remains practically constant down to 45 K, temperature after which it sharply increases to 23.1 e.m.u at 30 K. Below 30 K it decreases to 19.1 e.m.u at 2 K. The reciprocal magnetic susceptibility curve is not linear and therefore the experimental values of the Curie constant, Weiss constant and effective magnetic moment could not be determined.

The magnetisation as a function of field at 5 K per Fe^{2+} ion is shown in Figure 4.24(a). The magnetisation increases with increasing field until it reaches a saturated value at around 6000 G of 0.01196(11) μ_B, obtained from the extrapolation to 1/H=0 in the plot of M *vs* 1/H (Figure 4.24(b)), suggesting that spontaneous magnetisation occurs.

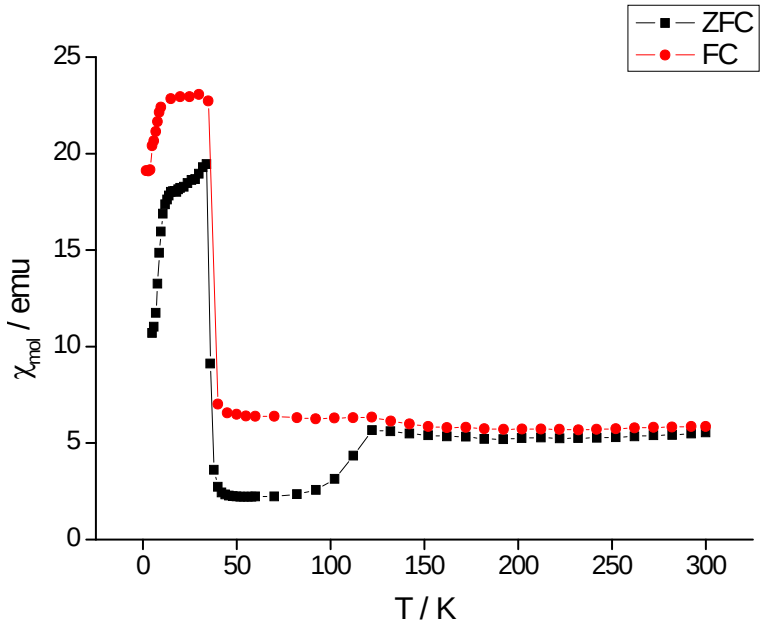

Figure 4.23. Zero field-cooled (Zfc)/ Field-cooled (Fc) susceptibility data for $[Fe_3(SO_4)_3(OH)_2(H_2O)_2](NH_4)_2$ **(5)**.

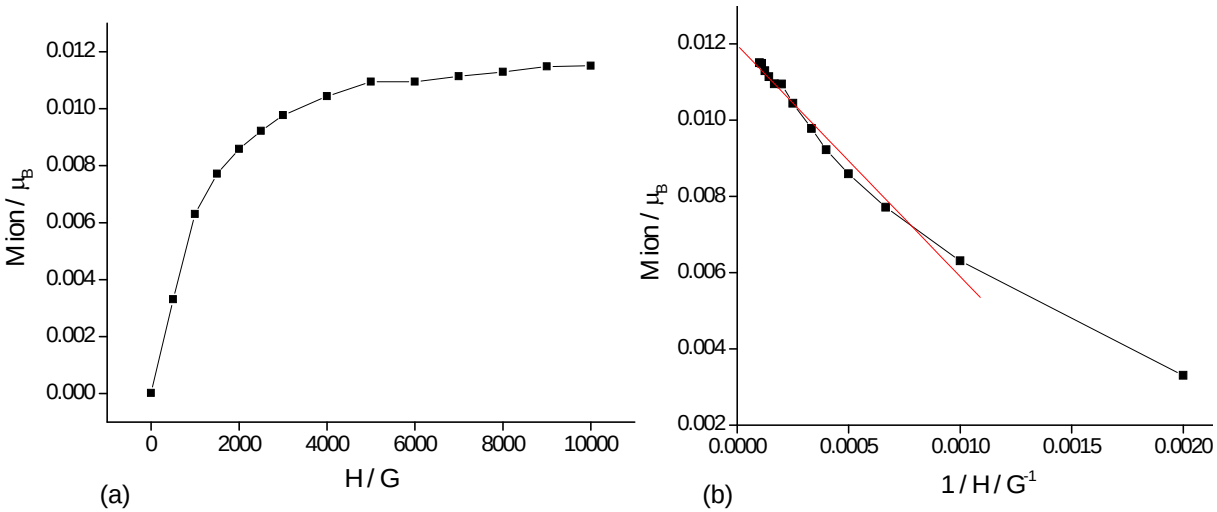

Figure 4.24. (a) Magnetic moment per Fe^{2+} ion for $[Fe_3(SO_4)_3(OH)_2(H_2O)_2](NH_4)_2$ **(5)** as a function of field at 5 K; (b) Magnetic moment per Fe^{2+} ion as a function of reciprocal field at 5 K.

Magnetic susceptibility data for $[Mn_3(SO_4)_3(OH)_2(trienH_2)]$ **(6)** at 100 G (Figure 4.25) show a small divergence between the zero field-cooled and field-cooled susceptibility plots below 13 K. The zero field-cooled reciprocal magnetic susceptibility as a function of temperature shows a discontinuity at *ca.* 55 K and a second discontinuity is observed at *ca.*

14 K, the latter corresponding to the temperature at which the zero field-cooled and the field-cooled susceptibility data diverge. Above 55 K the reciprocal magnetic susceptibility data can be fitted to the Curie-Weiss law, with a negative value for the Weiss constant (-70.45(1) K) which is characteristic of antiferromagnetic interactions. The effective magnetic moment (μ_{eff}=5.721(1) μ_B) calculated for the manganese ion in $[Mn_3(SO_4)_3(HO)_2(trienH_2)]$ **(6)** is consistent with the spin-only value of 5.92 μ_B. The Curie constant, magnetic moment and Weiss constant are listed in Table 4.7.

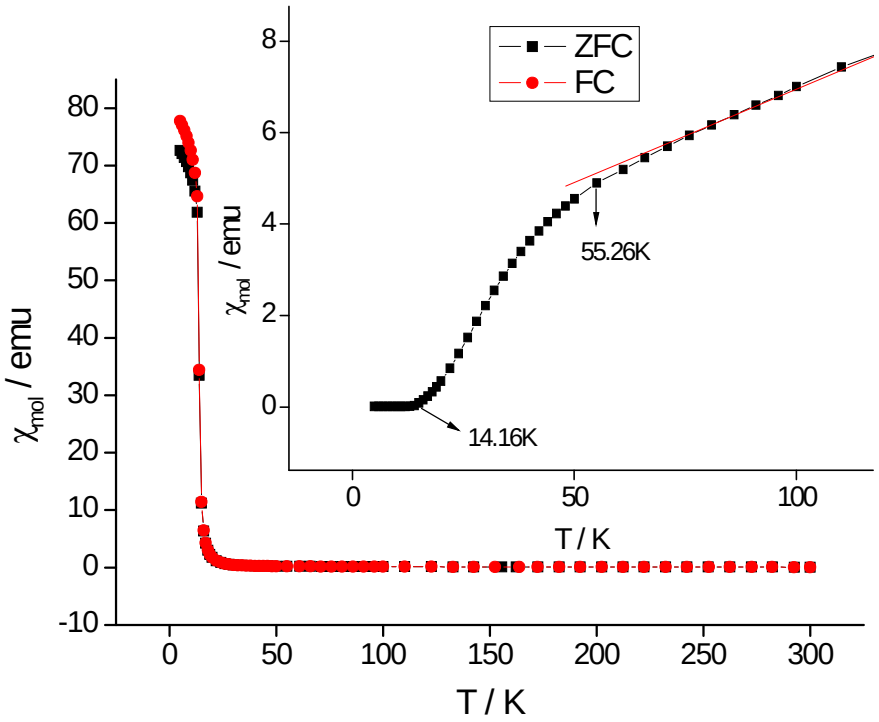

Figure 4.25. Zero field-cooled (Zfc)/ Field-cooled (Fc) susceptibility data and inverse susceptibility data (inset) for $[Mn_3(SO_4)_3(OH)_2(trienH_2)]$ **(6)**. The red line shows the fit to the Curie-Weiss law.

The effective magnetic moment per manganese ion decreases slowly from 7.29 μ_B to 5.53 μ_B on cooling from 300 K to 36 K (Figure 4.26), temperature below which it increases abruptly to 46.31 μ_B at 13 K. Below this temperature, it decreases slowly reaching a value of 3.1 μ_B at 5 K.

The magnetisation per manganese ion as a function of field at 5 K (Figure 4.27(a)) increases with increasing field and it saturates at high field with a saturation of the

magnetic moment per manganese ion of 0.01561(12) μ_B (Figure 4.27(b)), suggesting the existence of spontaneous magnetisation at 5 K.

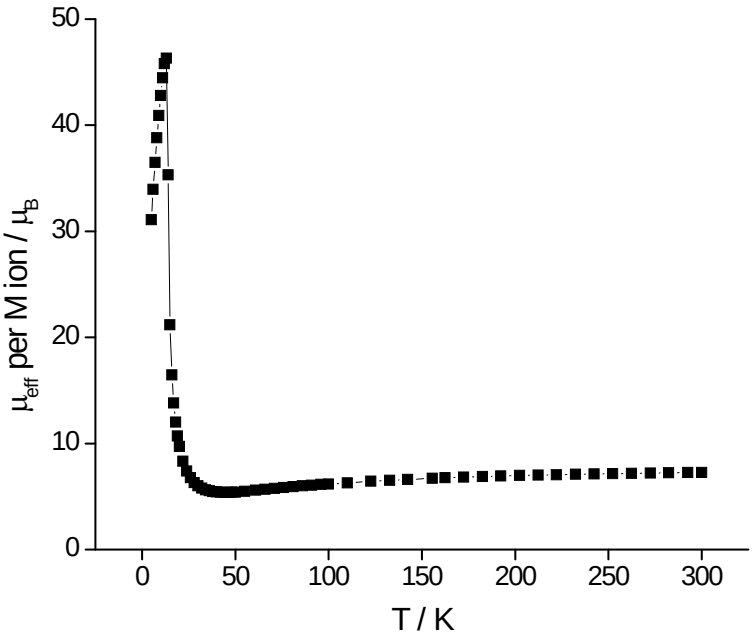

Figure 4.26. Effective magnetic moment per Mn^{2+} ion for $[Mn_3(SO_4)_3(OH)_2(trienH_2)]$ **(6)** as a function of temperature at 100 G.

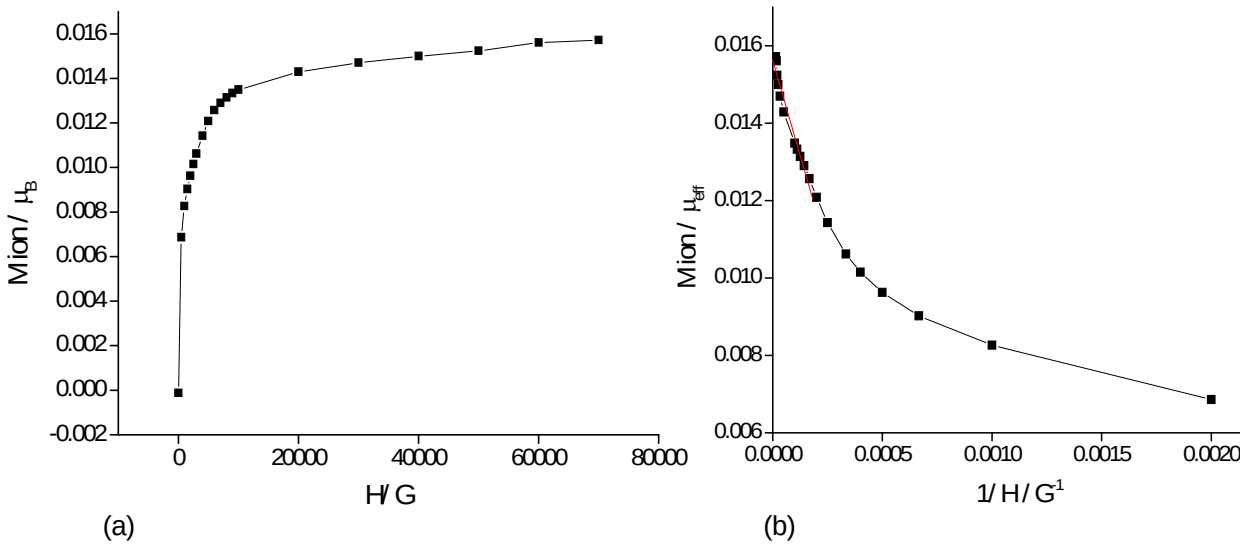

Figure 4.27. Magnetic moment per Mn^{2+} ion for $[Mn_3(SO_4)_3(OH)_2(trienH_2)]$ **(6)** as a function of field at 5 K.

Table 4.7. Curie constants, magnetic moments and Weiss constants for $[Mn_4(SO_4)_8(OH)_2(H_2O)_2](enH_2)_5$ **(4)** and $[Mn_3(SO_4)_3(OH)_2(trienH_2)]$ **(6)**

Compound	C / cm^3 K mol^{-1}	μ_{eff} per M ion / μ_B	μ_{so} / μ_B	θ / K
(4)	20.08(1)	6.34(1)	5.92	-10.70(3)
(6)	24.546(2)	5.721(1)	5.92	-70.45(1)

4.4 The layered structure of $[M(SO_4)(trien)]$ for M=Mn and Fe

4.4.1 Crystal structure description

The local coordination scheme for $[M(SO_4)(trien)]$ M=Mn, Fe **(7)-(8)** is shown in Figure 4.28.

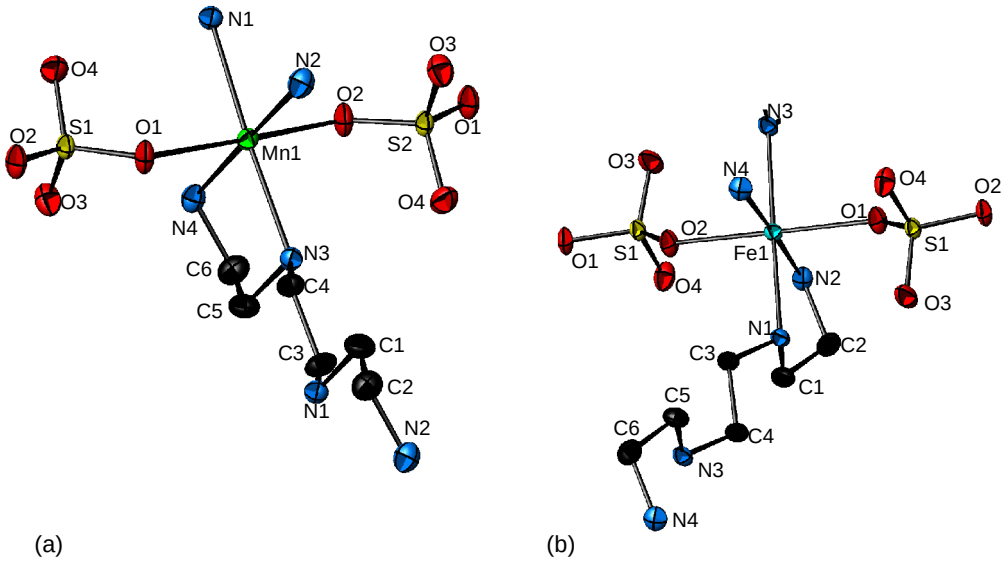

Figure 4.28. Atoms labelling scheme and thermal ellipsoids at 50 % probability of $[M(SO_4)(trien)]$ (a) =Mn **(7)**; (b) M=Fe **(8)**.

In the asymmetric unit of $[M(SO_4)(trien)]$ M=Mn, Fe **(7)-(8)** there is one crystallographically distinct metal ion coordinated to two sulphate anions in a monodentate fashion and to two nitrogen atoms of trien amine. In $[Mn(SO_4)(trien)]$ **(7)**, the average Mn-O distance is 2.2298 Å, which is in good agreement with Mn-O distances previously observed for other manganese sulphate compounds [335, 336]. These distances are also consistent with those expected from the sum of their ionic radii. For the iron analogue **(8)**, the average Fe-O distance is 2.1701 Å, which is similar to those found in hydrated iron

salts, such as $Fe(SO_4)(H_2O)_7$ [337]. Mn-N distances lay in the range 2.2402(17)- 2.3069(15) Å. Similar distances have been observed in manganese nitride [339], while Fe-N distances range from 2.1855(17) Å to 2.2549(15) Å, with an average Fe-N distance 2.2218 Å. The average S-O distance for both manganese **(7)** and iron **(8)** analogues lies in the range of typical values reported for other sulphate materials.

The structure of $[M(SO_4)(trien)]$ M=Mn, Fe **(7)-(8)** is formed by inorganic chains directed along the *b*-axis, in which each metal centre is connected to the adjacent one *via* a bridging sulphate tetrahedron through vertex-sharing. Each metal centre is also coordinated to four nitrogen atoms which belong to two different amine molecules, which results in M-N-C-C-N five-membered rings. Simultaneously, these amines serve to cross-link chains into layers parallel to the *ab* plane (Figure 4.29), in which eight-membered rings apertures are observed.

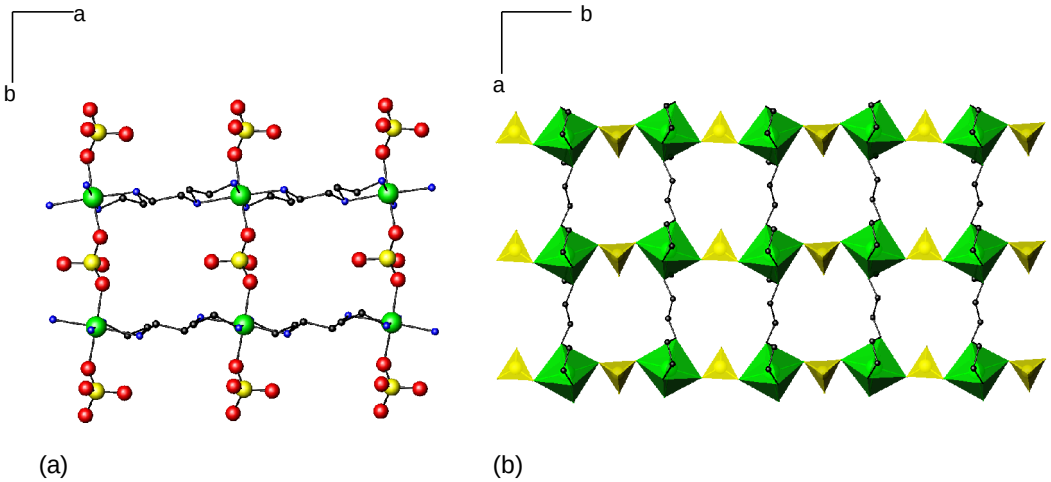

Figure 4.29. (a) Ball and stick representation of one layer in $[M(SO_4)(trien)]$ M=Mn, Fe **(7)-(8)** (M, green; S, yellow; O, red; N, blue; C, black); (b) Polyhedral representation of one layer in $[M(SO_4)(trien)]$ M=Mn, Fe **(7)-(8)**, showing the linkage between MO_2N_4 octahedra and SO_4 tetrahedra to form a chain (MO_2N_4 octahedra, green; SO_4 tetrahedra, yellow; C atoms, black).

Layers are stacked along the *c*-axis (Figure 4.30) and they are held together through hydrogen-bonding interactions in which the hydrogen atoms attached to nitrogen interact with oxygen atoms from the sulphate groups (Appendix D). The distances between two consecutive layers for the manganese **(7)** and the iron **(8)** sulphate analogues are *ca*. 8.3 Å

and 7.8 Å, respectively, consistent with trends associated to the metal radius, since manganese is larger that iron.

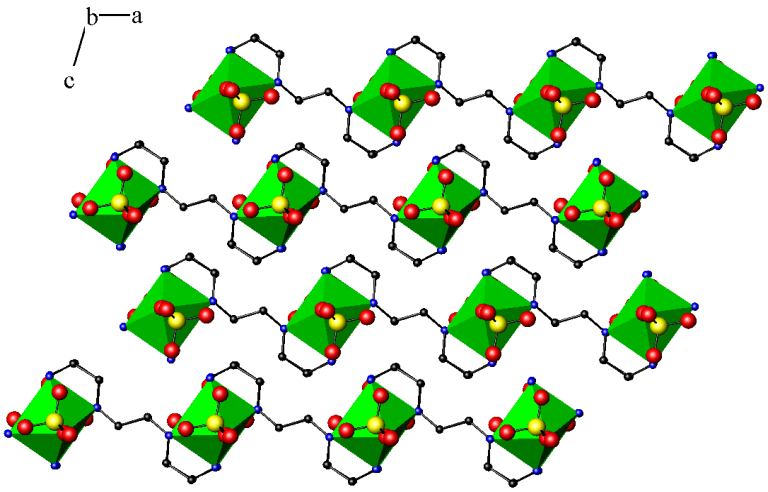

Figure 4.30. Parallel layers in $[M(SO_4)(trien)]$ M=Mn, Fe **(7)-(8)** running along the *c*-axis (MO_6 octahedra, green; S, yellow; O, red; N, blue; C, black).

4.5 Two-dimensional and three-dimensional structures with ethylenediamine: $[Mn(SO_4)_2](enH_2)$ and $[Mn_2(SO_4)_2(en)_2]$

4.5.1 Crystal structure description

4.5.1.1 $[Mn(SO_4)_2](enH_2)$ **(9)**

The asymmetric unit of $[Mn(SO_4)_2](enH_2)$ **(9)** contains one crystallographically distinct six-coordinated manganese atom which is connected to one sulphate group in a bidentate fashion and to four sulphate groups in a monodentate mode. The local coordination scheme for $[Mn(SO_4)_2](enH_2)$ **(9)** is shown in Figure 4.31. Mn-O distances range from 2.1070(9) Å to 2.3854(11) Å, with the longest Mn-O distances Mn-O(5)= 2.3854(11) Å and Mn-O(6)= 2.2446(10) Å associated with the sulphate group linked in a bidentate mode. The average Mn-O distance of 2.2021 Å is consistent with that previously reported for the ethylenediamine-templated manganese sulphate $(C_2N_2H_{10})Mn(SO_4)_2(H_2O)_4$ [336]. The average sulphur-oxygen distance of 1.4764 Å is in good agreement with that expected in materials containing the sulphate oxy-anion.

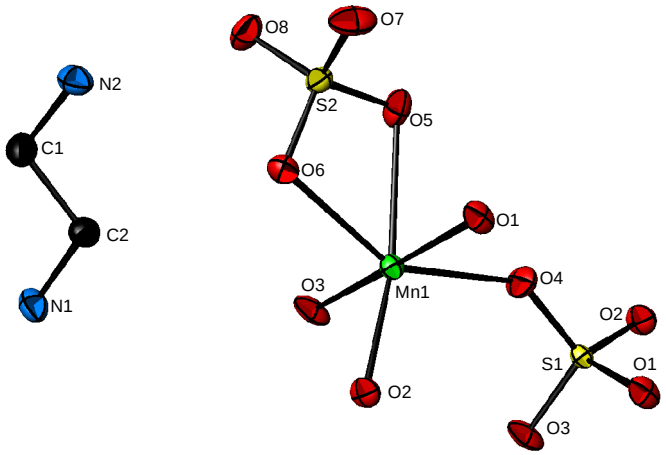

Figure 4.31. Atoms labelling scheme and thermal ellipsoids at 50% probability for $[Mn(SO_4)_2](enH_2)$ **(9)**. Hydrogen atoms have been omitted for clarity.

In the structure of $[Mn(SO_4)_2](enH_2)$ **(9)**, adjacent manganese centres are linked to each other *via* bridging SO_4 tetrahedra by sharing vertices. The bidentate sulphate anion shares an edge with each MnO_6 octahedron but does not participate in the linkage between metal centres. Each metal centre shares three of its monodentate sulphate groups with three neighbouring manganese centres along the *b*-axis, generating a double chain (Figure 4.32). The linkage between adjacent manganese centres results in the formation of $(Mn\text{-}O\text{-}S\text{-}O)_2$ eight-membered rings.

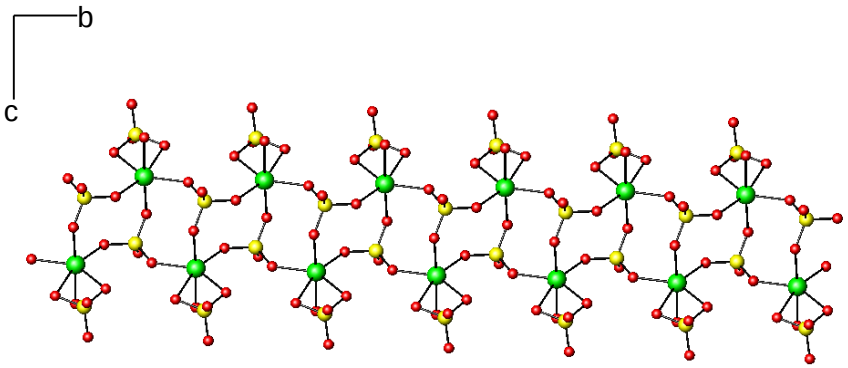

Figure 4.32. Double chain in $[Mn(SO_4)_2](enH_2)$ **(9)** as a result of the linkage between adjacent Mn centres (Mn atoms, green; S atoms; yellow; O atoms; red).

Double chains are linked into layers along the *a*-axis through the connection of adjacent MnO_6 octahedra *via* the fourth monodentate sulphate that does not take part in the formation of the double chain, which results in the generation of apertures of four-membered rings (Figure 4.33).

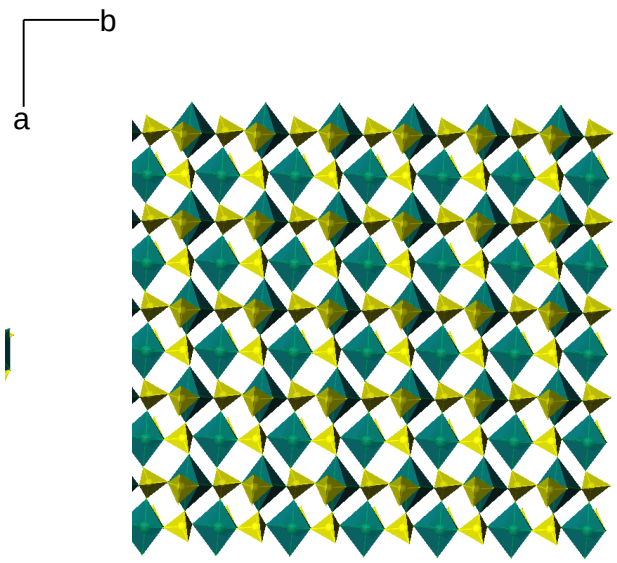

Figure 4.33. Polyhedral representation of a layer of $[Mn(SO_4)_2](enH_2)$ **(9)** parallel to the *ab* plane in which four-membered rings are generated (MnO_6 octahedra, green; SO_4 tetrahedra, yellow).

Inorganic $[Mn(SO_4)_2]^{2-}$ layers alternate with diprotonated ethylenediamine cations along the *c*-axis (Figure 4.34) and are held together through hydrogen bond interactions in which hydrogen atoms coordinated to terminal nitrogen atoms of the amine interact with the oxygen atoms of the sulphate anions (Appendix D).

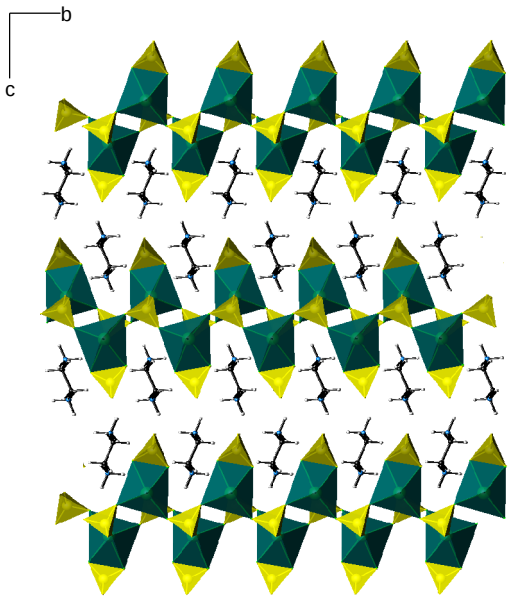

Figure 4.34. Layered structure of $[Mn(SO_4)_2](enH_2)$ **(9)** in which diprotonated ethylenediamine cations occupy the interlayer space (MnO_6 octahedra, green; SO_4 tetrahedra, yellow; C atoms, black; N atoms, blue; H atoms, white).

4.5.1.2 $[Mn_2(SO_4)_2(en)_2]$ **(10)**

The local coordination scheme for $Mn_2(SO_4)_2(en)_2$ **(10)** is depicted in Figure 4.35. The asymmetric unit of $[Mn_2(SO_4)_2(en)_2]$ **(10)** consists of one crystallographically distinct six-coordinated manganese ion connected to one sulphate group in a bidentate mode, to two sulphate groups in a monodentate fashion and to two amine molecules through an Mn-N bond. The average Mn-O distance is 2.2418 Å with the longest distance Mn-O(1)= 2.3115(8) Å associated with the linkage of the manganese ion to a bidentate sulphate group. This bond length lies out of the range of the typically observed Mn-O distances. However, Mn-O(2) and Mn-O(3) distances of 2.1667(11) Å and 2.1776(12) Å respectively, are consistent with those previously reported for manganese sulphate materials [335, 336]. The manganese-nitrogen distance takes the value Mn-N(1)= 2.2205(9) Å that is in good agreement with those expected from the sum of their covalent radii and with those previously observed in manganese nitride [339]. S-O bond lengths are consistent with the mean S-O distances reported for other sulphate materials.

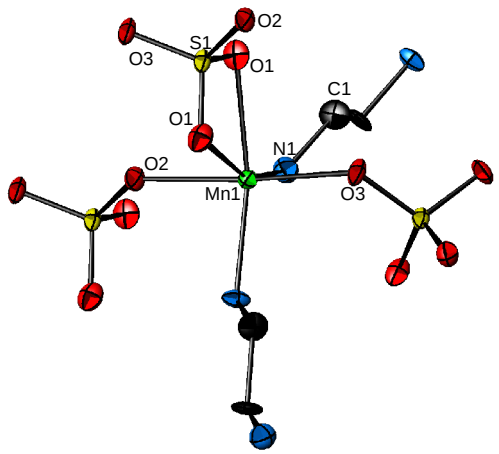

Figure 4.35. Atoms labelling scheme and thermal ellipsoids at 50% probability for $Mn_2(SO_4)_2(en)_2$ **(10)**. Hydrogen atoms have been omitted for clarity.

The structure of $Mn_2(SO_4)_2(en)_2$ **(10)** can be visualised as being derived from chains obtained from the connection of adjacent metal centres by sharing one bridging SO_4 tetrahedron (Figure 4.36). Each MnO_4N_2 octahedron links the neighbouring octahedron *via* a bidentate SO_4 tetrahedron that shares an edge with the mentioned octahedron and a vertex with the adjacent MnO_4N_2 octahedron along the *b*-axis (Figure 4.37(a)).

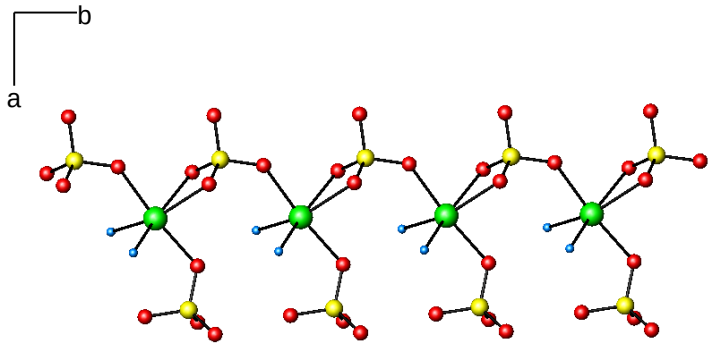

Figure 4.36. Connectivity between adjacent manganese centres through sulphate groups along the *b*-axis (Mn atoms, green; S atoms, yellow; O atoms, red; N atoms, blue).

Each chain is connected to the adjacent chain *via* the bidentate group that serves to link two consecutive metal centres within the chain through vertex-sharing. It results in a layer built up from MnO_4N_2 octahedra joined together through edge- and vertex-sharing SO_4 tetrahedra laying parallel to the *ab* plane, in which channels of six-membered rings are obtained as a result of this connectivity.

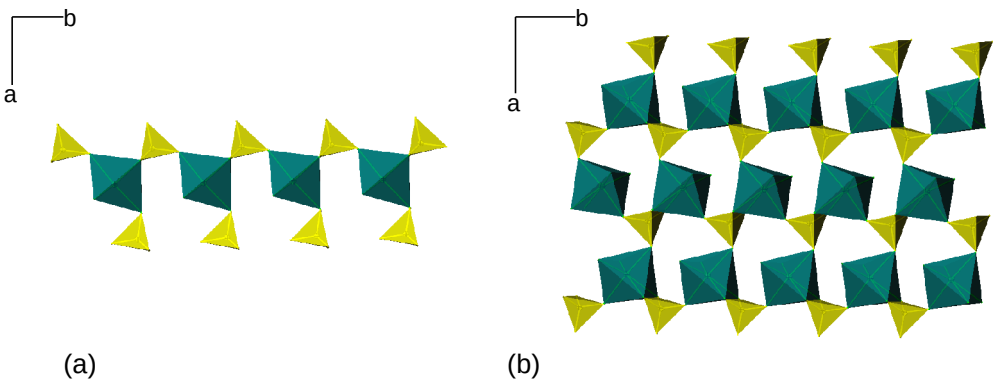

Figure 4.37. (a) Polyhedral representation of chains in $Mn_2(SO_4)_2(en)_2$ **(10)** running along the *b*-axis; (b) $Mn(SO_4)$ layer parallel to the *ab* plane in which the formation of six-membered rings are observed (MnO_4N_2 octahedra, green; SO_4 tetrahedra, yellow).

$[Mn_2(SO_4)_2]$ inorganic layers are in turn linked into a three-dimensional network through the connection of the amine to the metal centre by a manganese-nitrogen bond. Each metal centre is connected to two ethylenediamine molecules, oriented in opposite directions, generating neutral layers through covalent Mn-N bonding. The result is the hybrid manganese sulphate possessing a three-dimensional structure depicted in Figure 4.38. A space filling representation of the three dimensional structure of $[Mn_2(SO_4)_2(en)_2]$

(10) calculated from the van der Waals radii of the atoms (Figure 4.39) indicates that voids of *ca. 2*.8 x 4.7 Å are present.

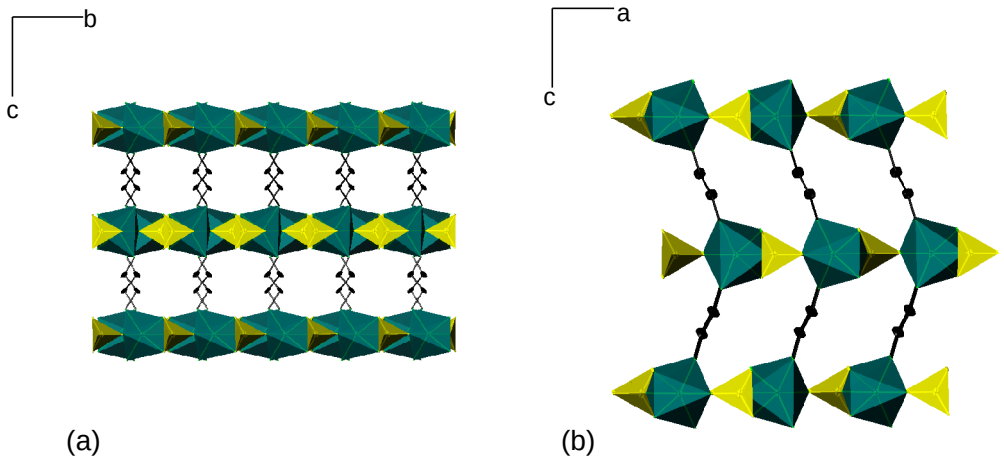

Figure 4.38. Two different views of the three-dimensional structure of $[Mn_2(SO_4)_2(en)_2]$ **(10)** showing the connectivity of the ethylenediamine molecules to the metal centre (a) along the *bc* plane; and (b) along the *ac* plane (MnO_4N_2 octahedra, green; SO_4 tetrahedra, yellow; C atoms, black).

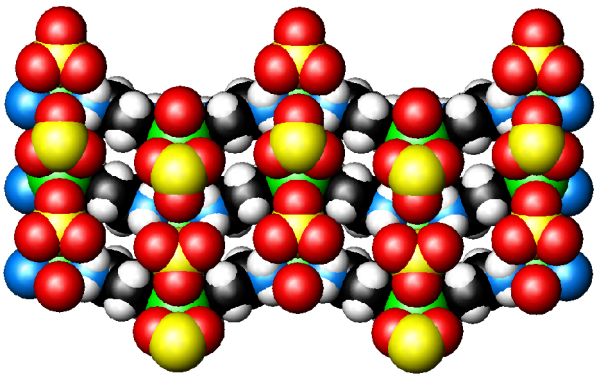

Figure 4.39. Space filling representation of the three-dimensional structure of $[Mn_2(SO_4)_2(en)_2]$ **(10)** (Mn atoms, green; S atoms, yellow; O atoms, red; N atoms, blue; C atoms, black; H atoms, white).

4.5.2 Magnetic properties

Magnetic susceptibility data collected at 100 G for $[Mn(SO_4)_2](enH_2)$ **(9)** and $[Mn_2(SO_4)_2(en)_2]$ **(10)** are shown in Figure 4.40 and Figure 4.41. For both compounds a divergence between the zero field-cooled and the field-cooled susceptibilities is observed. The reciprocal magnetic susceptibility data for $[Mn(SO_4)_2](enH_2)$ **(9)** shows two discontinuities at 40.8 K and 17 K, respectively. Similar anomalies are observed at 45 K

and 17 K in the reciprocal magnetic susceptibility plot for $[Mn_2(SO_4)_2(en)_2]$ **(10)**. In both materials, those discontinuities correspond to the temperature at which zero field-cooled and field-cooled susceptibilities diverge. For both materials, the reciprocal magnetic susceptibility data follow the Curie-Weiss equation above 40-45 K, with a negative value for the Weiss constant. The Curie constants, magnetic moments and Weiss constants for both compounds are listed in Table 4.8. The effective magnetic moment for the manganese ion in $[Mn(SO_4)_2](enH_2)$ **(9)** is very close to the spin-only value for Mn^{2+}, whereas that of manganese in $[Mn_2(SO_4)_2(en)_2]$ **(10)** is 4.84(1) μ_B, which is lower than the spin-only value for a Mn^{2+} ion in high spin configuration. The Weiss constants are both negative with a higher value for that of $[Mn_2(SO_4)_2(en)_2]$ **(10)** of -13.33(2) K, suggesting stronger antiferromagnetic interactions.

Table 4.8. Curie constants, magnetic moments and Weiss constants for $[Mn(SO_4)_2](enH_2)$ **(9)** and $[Mn_2(SO_4)_2(en)_2]$ **(10)**.

Compound	C / cm^3 K mol^{-1}	μ_{eff} per M ion / μ_B	μ_{so} / μ_B	θ / K
(9)	4.105(1)	5.73(1)	5.92	-9.97(2)
(10)	2.932(1)	4.84(1)	5.92 (*hs*) 1.73 (*ls*)	-13.33(2)

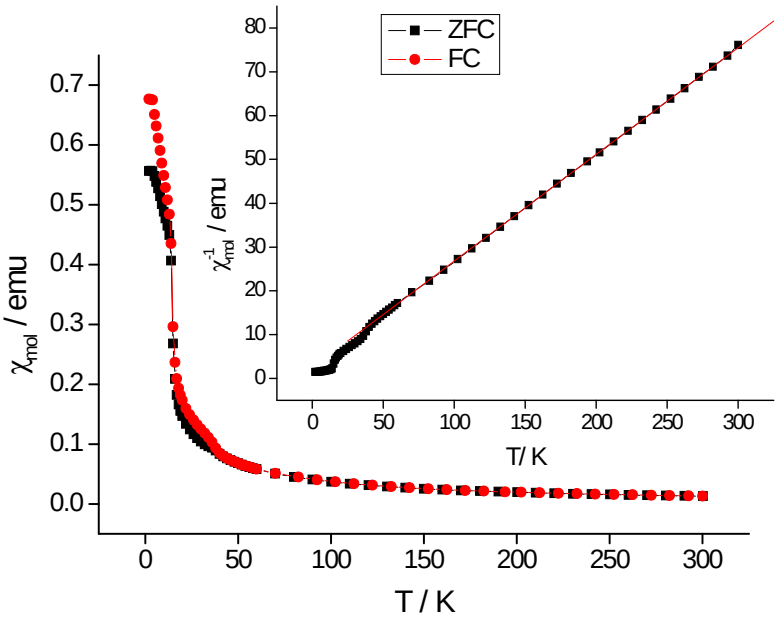

Figure 4.40. Zero field-cooled (Zfc)/ Field-cooled (Fc) susceptibility data and inverse susceptibility data (inset) for $[Mn(SO_4)_2](enH_2)$ **(9)**. The red line shows the fit to the Curie-Weiss law.

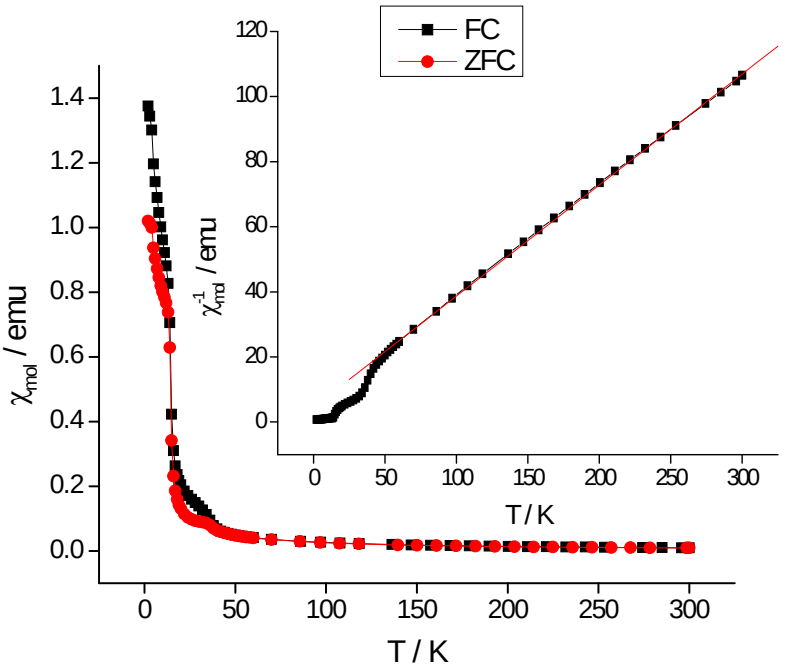

Figure 4.41. Zero field-cooled (Zfc)/ Field-cooled (Fc) susceptibility data and inverse susceptibility data (inset) for $[Mn_2(SO_4)_2(en)_2]$ **(10)**. The red line shows the fit to the Curie-Weiss law.

For both $[Mn(SO_4)_2](enH_2)$ **(9)** and $[Mn_2(SO_4)_2(en)_2]$ **(10)** the effective magnetic moment, measured by the quantity $(8\chi T/n)^{1/2}$, decreases on cooling from 300 K to 2 K (Figure 4.42). For $[Mn(SO_4)_2](enH_2)$ **(9)** the magnetic moment decreases smoothly from 5.61 μ_B to 5.16 μ_B from 300 K to 42 K, temperature at which the magnetic moment slightly increases to 5.20 μ_B. After this peak, it continues decreasing to 5.84 μ_B at 20 K. Below this temperature an abrupt increase in the magnetic susceptibility is observed and it reaches a maximum value of 6.84 μ_B at 13 K, temperature after which it decreases dramatically to 2.98 μ_B at 2 K. The effective magnetic moment of $[Mn_2(SO_4)_2(en)_2]$ **(10)** decreases slowly from 4.75 μ_B to 4.41 μ_B at 50 K, temperature after which it starts increasing from 4.41 μ_B to 5.77 μ_B from 50 K to 28 K, when it stabilizes, and below 20 K it starts increasing again to a maximum value of 9.27 μ_B at 13 K. Below this temperature, the magnetic moment drops dramatically to 4.69 μ_B at 2 K.

The magnetisation as a function of field of $[Mn(SO_4)_2](enH_2)$ **(9)** was measured at 5 K (Figure 4.43). A linear increase of the magnetic moment per manganese ion with increasing field is observed up to 10,000 G, field after which a slight curvature is observed, but no saturation is identified manifesting that no spontaneous magnetisation occurs at 5 K.

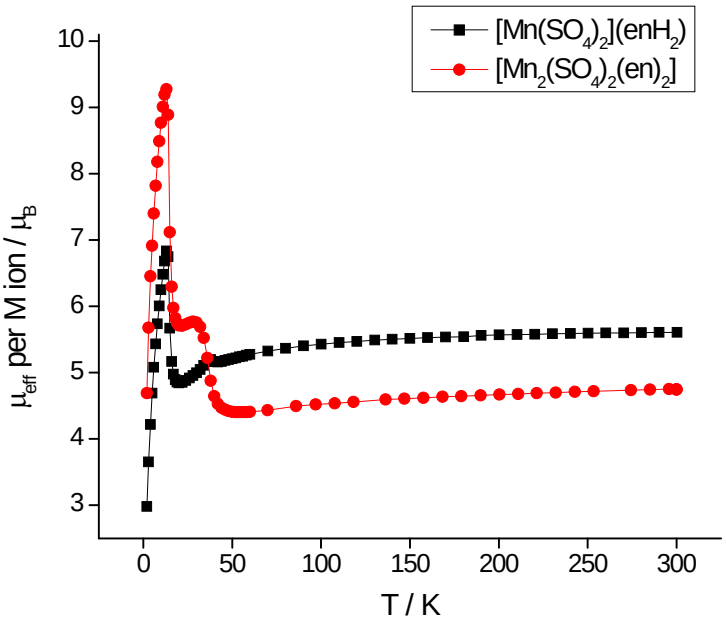

Figure 4.42. Effective magnetic moment per M ion for $[Mn(SO_4)_2](enH_2)$ **(9)** and $[Mn_2(SO_4)_2(en)_2]$ **(10)** as a function of temperature at 100 G.

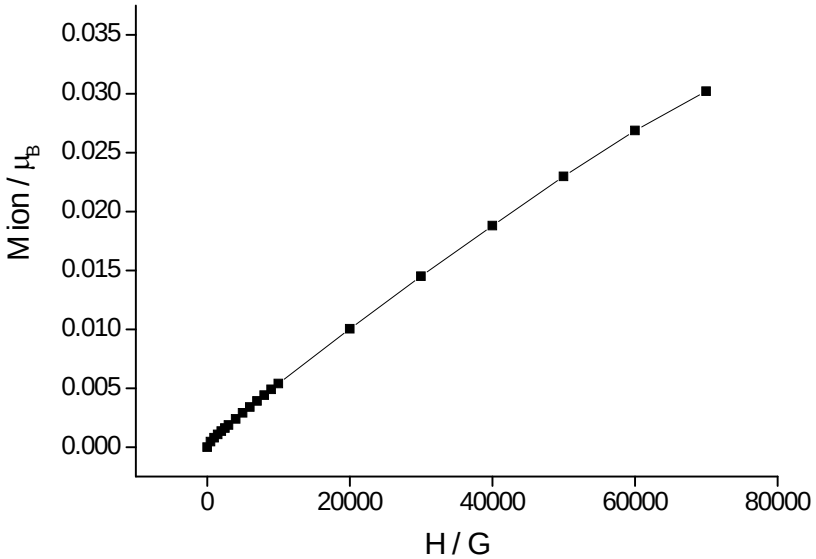

Figure 4.43. Magnetic moment per Mn^{2+} ion for $[Mn(SO_4)_2](enH_2)$ **(9)** as a function of field at 5 K.

4.6 $[Co_3(SO_4)_3(OH)_2](enH_2)$ triangles

4.6.1 Crystal structure description

The local coordination scheme for $[Co_3(SO_4)_3(OH)_2](enH_2)$ **(11)** is given in Figure 4.44. The asymmetric unit of **(11)** contains five crystallographically distinct six-coordinated

cobalt ions. Each cobalt centre is coordinated to four sulphate groups in a monodentate fashion and to two oxygen atoms from hydroxyl groups. Both ethylenediamine cations are disordered and N(2) and N(1) and N(5) can occupy two different positions in which the occupancy of N(2) is 0.5000 and the occupancy of N(1) and N(5) is 0.7034 and 0.2966, respectively. C(2)-N(2) distance is 1.484(6) Å and C(3)-N(1) and C(3)-N(5) distances are 1.438(5) Å and 1.431(9) Å, correspondingly. The average Co-O distance takes a value of *ca.* 2.1166 Å, which is consistent with those reported for the cobalt sulphate materials $Co_3(SO_4)_2(OH)_2(H_2O)_2$ [340] and $[(C(NH_3)_3]_2[Co(SO_4)_2(H_2O)_6]$ [338]. The longest Co-O distances *ca.* 2.22-2.26 Å are associated with the presence of three-coordinated oxygen atoms. S-O distances, with a mean value of 1.4775 Å, lie in the range of those distances expected in materials containing the oxy-anion of sulphur.

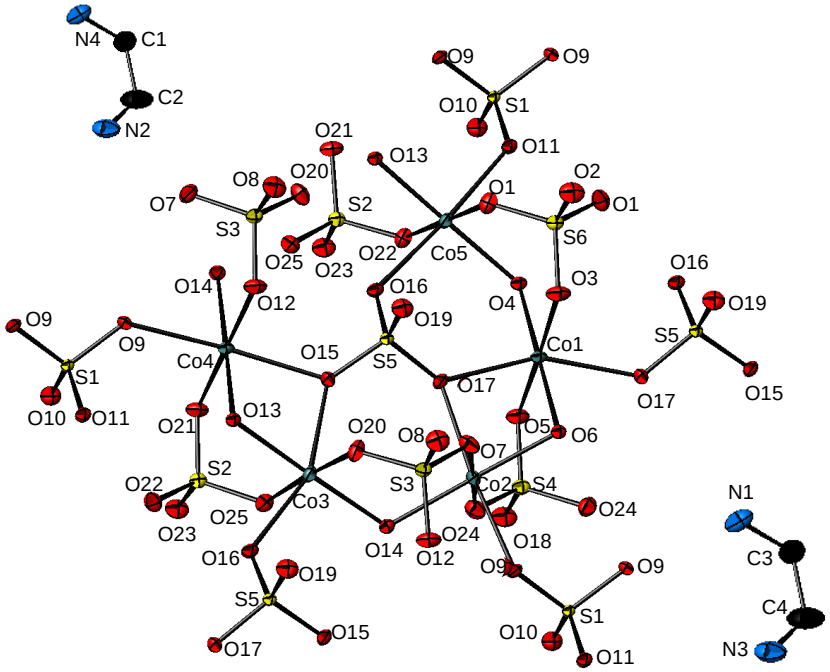

Figure 4.44. Atoms labelling scheme and thermal ellipsoids at 50% probability of $[Co_3(SO_4)_3(OH)_2](enH_2)$ **(11)**. Hydrogen atoms have been omitted for clarity.

Cobalt centres coordinated through bridging sulphate groups and hydroxyl groups form triangles of edge-sharing CoO_6 octahedra (Figure 4.45). Each of the three cobalt centered-octahedra occupying the corners of the triangle are linked by sharing one three-coordinated oxygen atom from a hydroxyl group and one sulphate tetrahedron. Simultaneously, the linkage between two adjacent edge-sharing CoO_6 octahedra is completed by one more sulphate tetrahedron that is connected to them by vertex-sharing.

Each of these three edge-sharing CoO_6 octahedra units connect to a neighbouring unit by sharing edges through one hydroxyl group, *via* a three-coordinated oxygen atom, and through two vertex-linking sulphate tetrahedra. As a result a sulphate tetrahedron remains in the centre of the triangle limited by the nine edge-sharing CoO_6 octahedra that form this triangle. The distances between cobalt centres range from *ca.* 3.2 Å to 3.6 Å. The shortest Co-Co distances of *ca.* 3.2 Å correspond to the distances between cobalt centres at the vertices of the triangle (*ca.* Co(3)-Co(5)=3.18 Å, Co(4)-Co(3)=3.21 Å and Co(2)-Co(1)=3.22 Å).

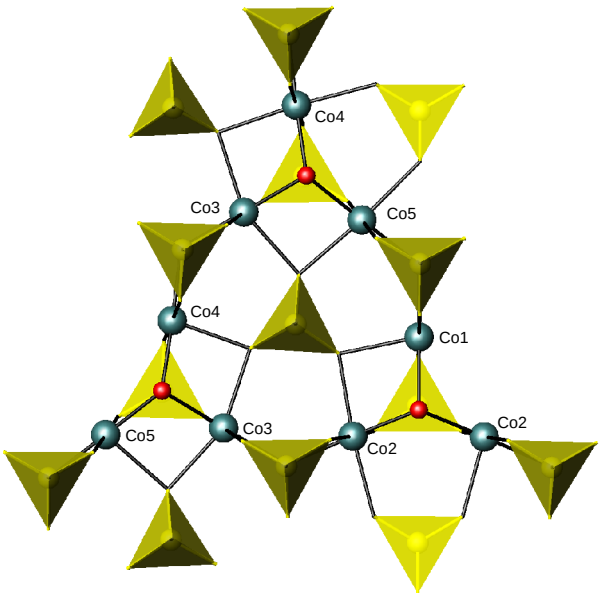

Figure 4.45. Connectivity between Co atoms within one triangle in the layered structure of $[Co_3(SO_4)_3(OH)_2](enH_2)$ **(11)** (Co atoms, grey; O atoms, red; SO_4 tetrahedra, yellow).

Neighbouring triangles of CoO_6 octehedra are coordinated in the *ab* plane to form a complex layer as shown in Figure 4.46. The linkage is made by vertex-sharing CoO_6 tetrahedra and SO_4 tetrahedra, creating another three-metal-centre unit in which the distance between the metal centres varies from 3.49 Å to 3.52 Å. Diprotonated ethylenediamine cations occupy the space between the layers and they alternate along the *c*-axis (Figure 4.47). Nearby cations and anions are held together in a hydrogen bond system in which N-H···O bonds are present (Appendix D).

By representing only the cobalt centres within one layer the topology shown in Figure 4.48 is obtained. Such a layer consisting of hexagonal tungsten bronze sheets

constitutes what is named the Kagome-type lattice, which represents a special case of magnetic system in which spin-magnetic frustration is been observed.

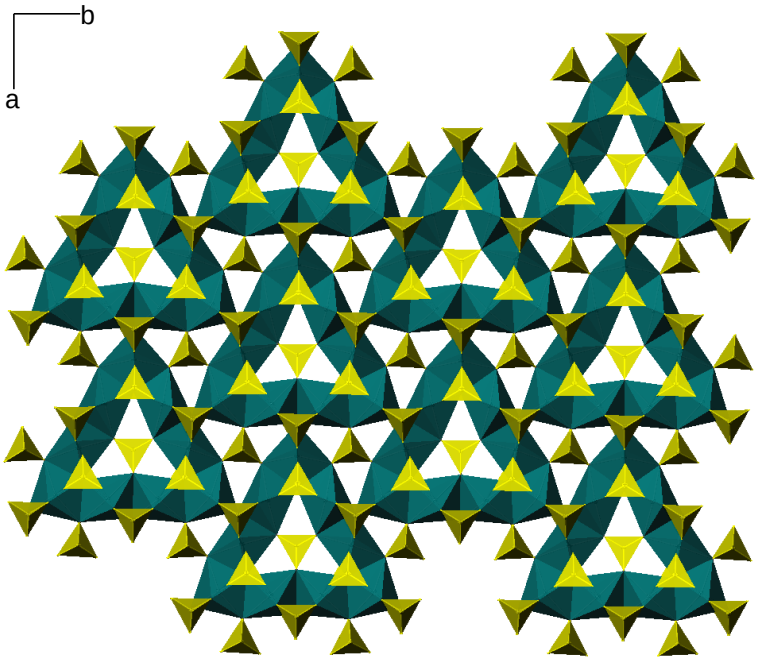

Figure 4.46. One layer in $[Co_3(SO_4)_3(OH)_2](enH_2)$ **(11)** parallel to the *ab* plane obtained from the connectivity of adjacent triangles through corner-linking CoO_6 octahedra and SO_4 tetrahedra (CoO_6 octahedra, green; SO_4 tetrahedra, yellow).

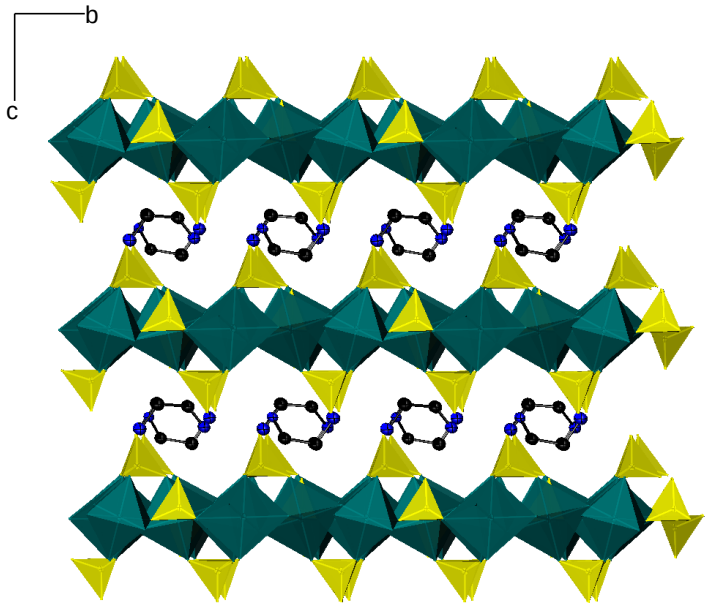

Figure 4.47. Alternating $[Co_3(SO_4)_3(OH)_2]^{2-}$ layers and diprotonated ethylenediamine cations along the *c*-axis (CoO_6 octahedra, green; SO_4 tetrahedra, yellow; C atoms, black; N atoms, blue)

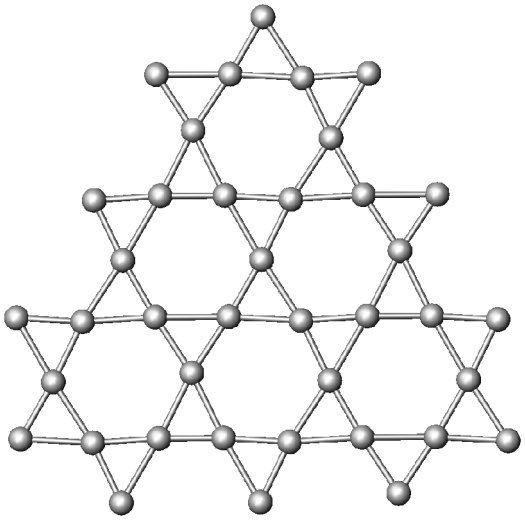

Figure 4.48. (a) Representation of the linkage between metal centres in one layer of $[Co_3(SO_4)_3(OH)_2](enH_2)$ **(11)**

4.6.2 Magnetic Properties

Magnetic susceptibility data at 1000 G and 100 G for $[Co_3(SO_4)_3(OH)_2](enH_2)$ **(11)** are displayed in Figure 4.49 and Figure 4.50, respectively. At 1000 G, the reciprocal magnetic susceptibility shows a discontinuity at 15 K, which is also found in the magnetic susceptibility data. At 100 G, a divergence between the zero field-cooled and field-cooled susceptibility plots is observed. In addition, the reciprocal magnetic susceptibility shows discontinuities at *ca.* 16 K and 10 K, the former being the temperature at which a slight curvature of the magnetic susceptibility data is found and the latter that at which the divergence between the zero field-cooled and the field-cooled magnetic susceptibility is observed. At both fields, the linear region above 16 K was fitted to the Curie-Weiss law yielding a negative value for the Weiss constant. Curie constants, magnetic moments and Weiss constants at 100 G and 1000 G (Table 4.9) suggest they are not strongly dependent of field. The effective magnetic moment of Co^{2+} is higher than the spin-only value calculated for Co^{2+}, but is in good agreement with previously reported values (4.3 μ_B to 5.2 μ_B).

The effective magnetic moment per cobalt ion as measured by the quantity $(8\chi T/3)^{1/2}$ (Figure 4.51) decreases on cooling from 300 K to 5 K at both fields. While at 1000 G the effective magnetic moment decreases slowly from 4.93 μ_B to 1.8 μ_B when

lowering the temperature from 300 K to 5 K, at 100 G the effective magnetic moment decreases smoothly from 300 K to 13 K from 4.93 μ_B to 2.37 μ_B, temperature after which it sharply increases to 2.57 μ_B at 10 K. Below 10 K it decreases rapidly to 1.83 μ_B at 5 K.

The magnetisation per cobalt ion as a function of field at 5 K (Figure 4.52) indicates that the magnetization increases linearly with increasing field. This suggests that no spontaneous magnetisation at 5 K occurs.

Table 4.9. Curie constants, magnetic moments and Weiss constants for $[Co_3(SO_4)_3(OH)_2](enH_2)$ **(11)** at 1000 G and 100 G.

$[Co_3(SO_4)_3(OH)_2](enH_2)$ **Field / G**	**C / cm^3 K mol^{-1}**	**μ_{eff} per M ion / μ_B**	**μ_{so} / μ_B**	**θ / K**
1000	10.333(2)	5.25(1)	3.87	-43.48(2)
100	11.042(2)	5.426(1)	3.87	-60.91(3)

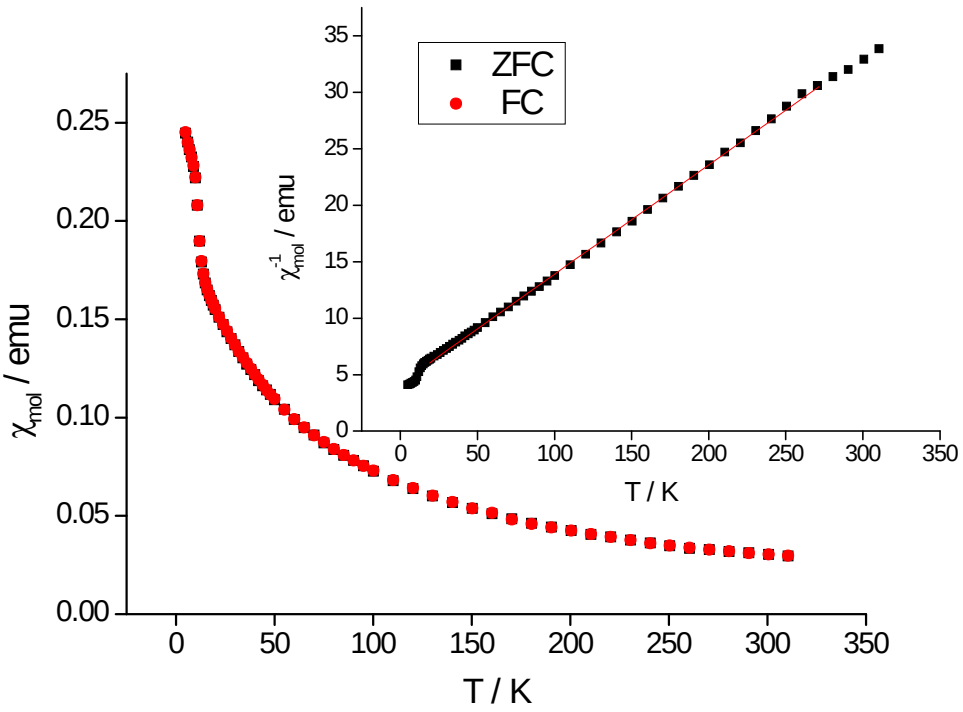

Figure 4.49. Zero field-cooled (Zfc)/ Field-cooled (Fc) susceptibility data and inverse susceptibility data (inset) for $[Co_3(SO_4)_3(OH)_2](enH_2)$ **(11)** at 1000 G. The red line shows the fit to the Curie-Weiss law.

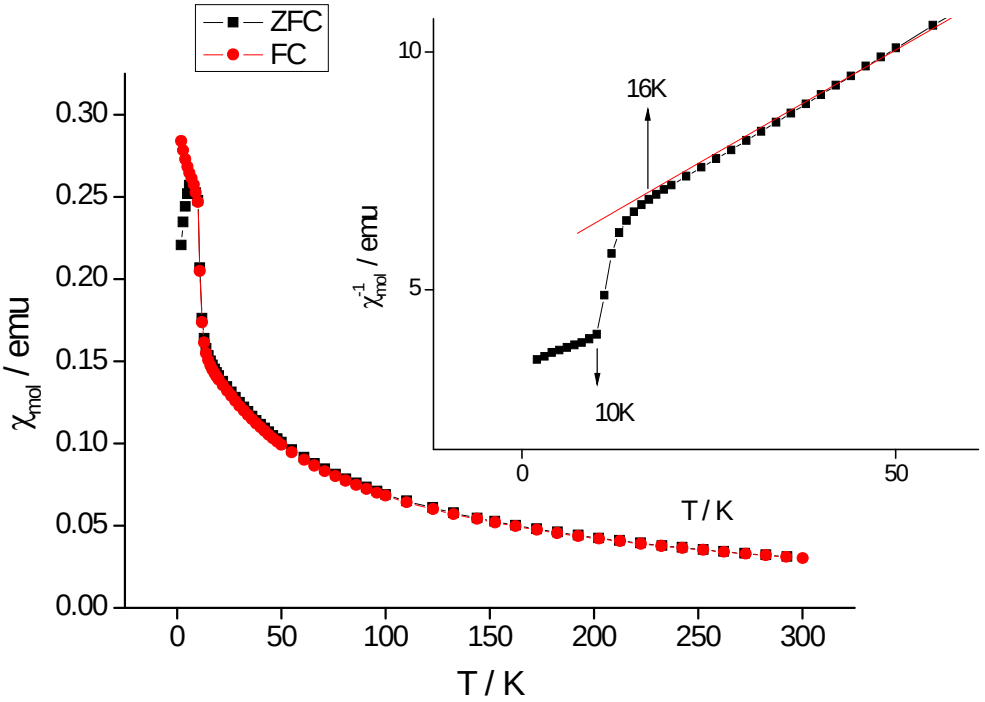

Figure 4.50. Zero field-cooled (Zfc)/ Field-cooled (Fc) susceptibility data and field-cooled inverse susceptibility data (inset) for $[Co_3(SO_4)_3(OH)_2](enH_2)$ **(11)** at 100 G. The red line shows the fit to the Curie-Weiss law.

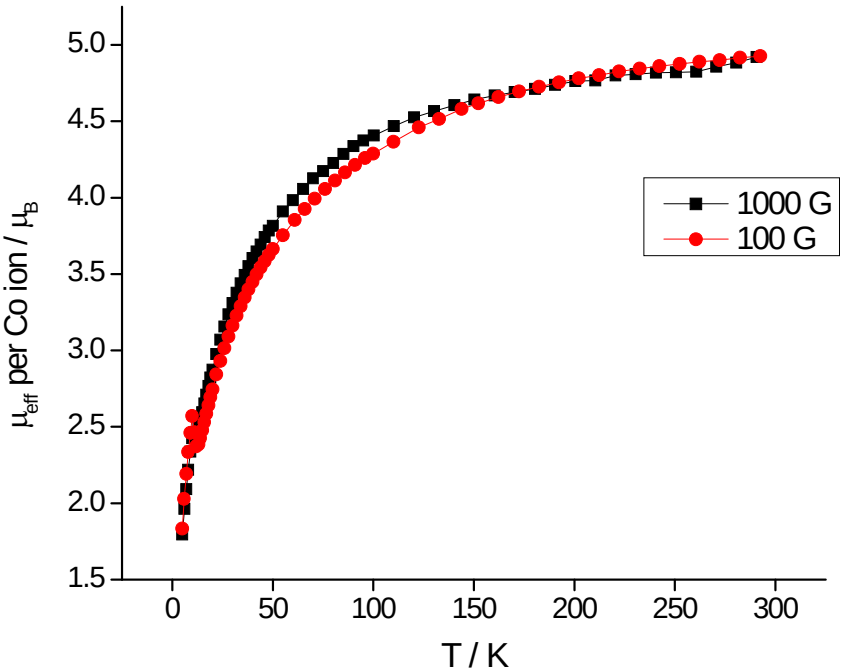

Figure 4.51. Effective magnetic moment per Co^{2+} ion for $[Co_3(SO_4)_3(OH)_2](enH_2)$ **(11)** as a function of temperature at 1000 G and 100 G.

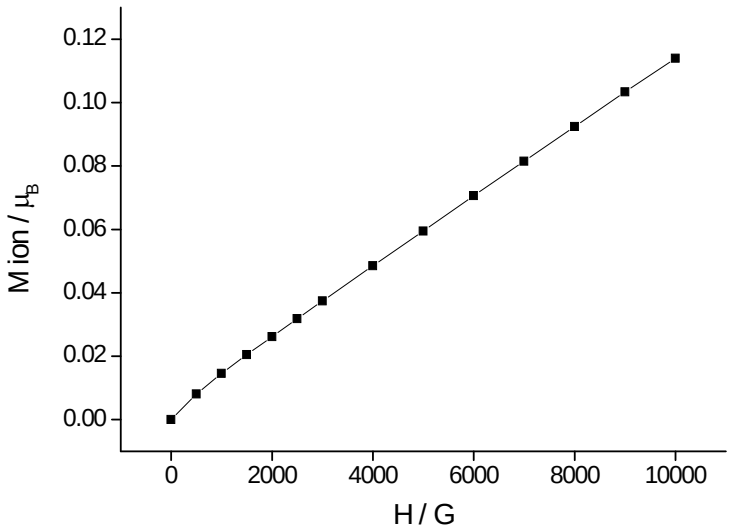

Figure 4.52. Magnetic moment per Co^{2+} ion for $[Co_3(SO_4)_3(OH)_2](enH_2)$ **(11)** as a function of field at 5 K.

4.7 Discussion

To date, most of the sulphate structures have been obtained by making use of an excess of fluoride ions to form an M-O/F-M network. In this project, the system MSO_4:amine:H_2SO_4:H_2O has been investigated as a route for the preparation of organically-templated transition metal sulphates. A wide variety of amines has been employed and the reactions have been conducted in digestion bombs at temperatures between 160 °C and 180 °C. Regardless of the considerable number of amines employed, the affinity of ethylenediamine and triethylenetetramine to participate in the generation of transition metal sulphates under these reaction conditions has been demonstrated with the synthesis of the materials described in this chapter. $[Mn_4(SO_4)_8(OH)_2(H_2O)_2](enH_2)_5$ **(4)**, $[Mn(SO_4)_2](enH_2)$ **(9)**, $[Mn_2(SO_4)_2(en)_2]$ **(10)** and $[Co_3(SO_4)_3(OH)_2](enH_2)$ **(11)** have been prepared in the presence of ethylenediamine. It has been found as a diprotonated molecule, balancing the charge of the inorganic moieties, or directly linked to the metal centre as occurs in $[Mn_2(SO_4)_2(en)_2]$ **(10)**, in which the amine molecules are linked to the manganese centre through a Mn-N bond to form a hybrid three-dimensional structure. Triethylenetetramine has been successfully employed for the generation of hybrid structures as examplified by the synthesis of the three-dimensional manganese sulphate $[Mn_3(SO_4)_3(OH)_2(trienH_2)]$ **(6)** and the layered materials $[M(SO_4)(trien)]$ M=Mn, Fe **(7)-(8)**. The use of spermine allowed the preparation of the layered iron sulphate

$[Fe_3(SO_4)_3(OH)_2(H_2O)_2](NH_4)_2$ **(5)**, in which the amine breaks down to produce ammonium cations NH_4^+ that occupy the space between the layers. In all the materials described in this chapter, the metal centre adopts an octahedral coordination. Thermogravimetric studies reveal that at high temperatures all of these materials decompose to form the oxides Mn_3O_4, Fe_2O_3 and CoO, with the exception of the iron sulphate $[Fe_3(SO_4)_3(OH)_2(H_2O)_2](NH_4)_2$ **(5)** which decompose to produce the corresponding oxide and $FeSO_4$.

4.7.1 M_4O_{20} building unit

$[Mn_4(SO_4)_8(OH)_2(H_2O)_2](enH_2)_5$ **(4)** was prepared under solvothermal conditions in the presence of ethylenediamine. Its structure consists of isolated anionic four-metal clusters whose charge is balanced by diprotonated ethylenediamine cations. Other examples of sulphates containing isolated units obtained in the presence of an organic amine are those of $[NH_3(CH_2)_2NH_3][M(SO_4)_2(H_2O)_4]$ (M=Mn, Fe, Co) [333, 334, 336], $[C_4N_2H_{12}][M(H_2O)_6](SO_4)_2$ [341] (M=Mn, Ni, Fe, Cu) and $[C_6N_2H_{14}][Fe(H_2O)_6](SO_4)_2$ [342]. Crystalline products of these materials were obtained from aqueous solution and slow evaporation at room temperature, with the exception of $[NH_3(CH_2)_2NH_3][Co(SO_4)_2(H_2O)_4]$ that was prepared under solvothermal conditions. All these structures consist of isolated $[M(SO_4)_2(H_2O)_4]^{2-}$ anions, in which MO_6 octahedra are surrounded by two SO_4 tetrahedra connected by vertex-sharing, or $[M(H_2O)_6]$ and SO_4^{2-} anions and amine cations linked together by hydrogen bond interactions. In contrast to those structures, the structure of $[Mn_4(SO_4)_8(OH)_2(H_2O)_2](enH_2)_5$ **(4)** comprises units formed by the connectivity of four MnO_6 octahedra that are coordinated to each other *via* both vertex- and edge-linking octahedra generating a three-coordinated oxygen atom, and vertex-sharing SO_4 tetrahedra. This linkage has resulted in the identification of a building unit with general formula M_4O_{20}. Attempts to link these building units together in order to obtain higher-dimensional structures were successful and produced the two-dimensional iron sulphate $[Fe_3(SO_4)_3(OH)_2(H_2O)_2](NH_4)_2$ **(5)** and the hybrid three-dimensional manganese sulphate $[Mn_3(SO_4)_3(OH)_2(trienH_2)]$ **(6)**. In these two materials, two consecutive M_4O_{20} (or $M_4O_{18}N_2$) building units are fused together to form chains by sharing one terminal octahedron. Chains are in turn connected into layers *via* vertex-linking sulphate tetrahedra. In addition, in $[Mn_3(SO_4)_3(OH)_2(trienH_2)]$ **(6)** the structure is completed by diprotonated triethylenetetramine cations that are directly connected to the

metal centre through a Mn-N bond to form a hybrid three-dimensional network. This building unit was first discovered in the iron phosphate $[Fe_2(OH)(H_2PO_4)(HPO_4)_2(PO_4)]\cdot 0.5H_2O$ [343] (Figure 4.53), in which the tetramer M_4O_{20} is constructed in an identical manner as observed in $[Mn_4(SO_4)_8(OH)_2(H_2O)_2](enH_2)_5$ **(4)**. The only difference is the existence of PO_4 tetrahedra instead of SO_4 tetrahedra. In the one-dimensional structure of $[Fe_2(OH)(H_2PO_4)(HPO_4)_2(PO_4)]\cdot 0.5H_2O$, adjacent tetramers are connected into chains by vertex-sharing SO_4 tetrahedra, while in $[Fe_3(SO_4)_3(OH)_2(H_2O)_2](NH_4)_2$ **(5)** and $[Mn_3(SO_4)_3(OH)_2(trienH_2)]$ **(6)** the connectivity to form the chains is made through edge- and vertex-linking MO_6/MO_5N octahedra.

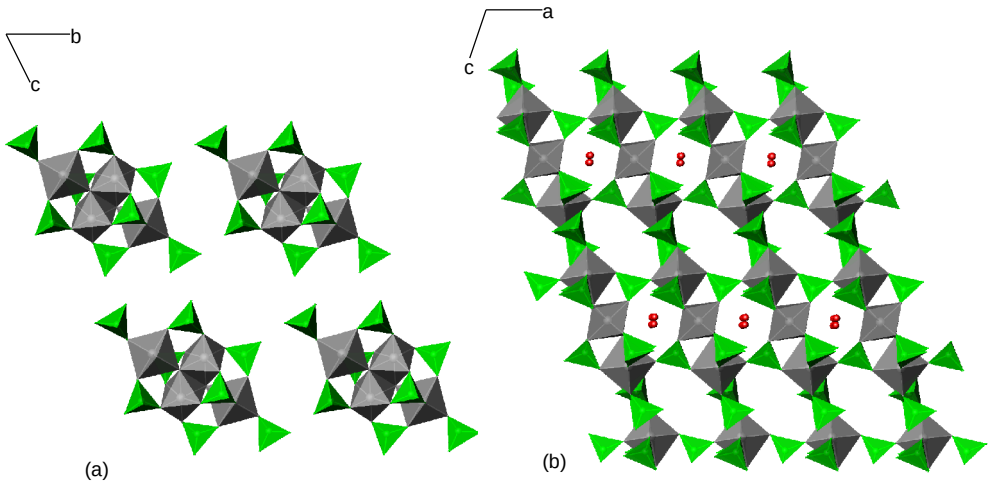

Figure 4.53. (a) Tetranuclear iron cluster in $[C_4N_2H_{12}]_{1.5}[Fe_2(OH)(H_2PO_4)(HPO_4)_2(PO_4)]\cdot 0.5H_2O$; (b) Chains formed by the linkage of tetranuclear clusters (FeO_6 octahedra, grey; PO_4 tetrahedra, green) [343].

The same layers from which the structures of $[Fe_3(SO_4)_3(OH)_2(H_2O)_2](NH_4)_2$ **(5)** and $[Mn_3(SO_4)_3(OH)_2(trienH_2)]$ **(6)** are constructed has also been identified in the nickel sulphate $[C_4N_2H_{12}][Ni_3F_2(SO_4)_3(H_2O)_2]$, whose framework is built up from NiO_4F_2 octahedra and SO_4 tetrahedra, with the diprotonated piperazine cations occupying the interlayer space (Figure 4.54) [188]. The analogous nickel sulphates obtained in the presence of 1,4-diazabicyclo[2.2.2]octane (DABCO) and 1,3-diaminopropane (DAP) display the same layered structure [188]. These structures can be compared to the structures of the minerals sulfoborite $Mg_3(SO_4)[B(OH)_4]_2(OH)F$ [344] and amarantite $[Fe_2(SO_4)_2O]\cdot 7H_2O$ [345] (Figure 4.55). Sulfoborite is constructed from layers of MgO_6 octahedra, SO_4 tetrahedra and BO_4 tetrahedra that link together by edge- and vertex-linking

to form a three-dimensional network in which the M_4O_{20} building unit is present. Conversely, in the mineral amarantite M_4O_{20} building units are linked to each other *via* vertex-linking SO_4 tetrahedra to form chains parallel to [100].

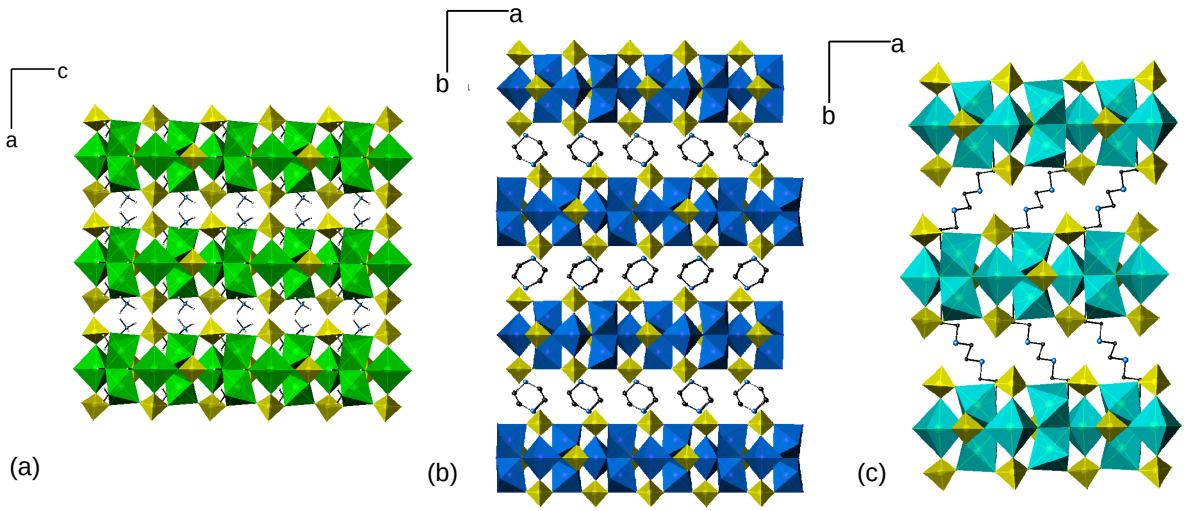

Figure 4.54. Comparison between the layered structures of (a) $[Fe_3(SO_4)_3(OH)_2(H_2O)_2](NH_4)_2$ **(5)** (FeO_6 octahedra, green; SO_4 tetrahedra, yellow; N, blue; H, white); (b) $[C_4N_2H_{12}][Ni_3F_2(SO_4)_3(H_2O)_2]$ (NiF_2O_4 octahedra, blue; SO_4 tetrahedra, yellow; N, blue; C, black; H, white) [188]; (c) $[Mn_3(SO_4)_3(HO)_2(trienH_2)]$ **(6)** (MnO_6 and MnO_5N octahedral, blue; SO_4 tetrahedra, yellow; N, blue; C, black; H, white).

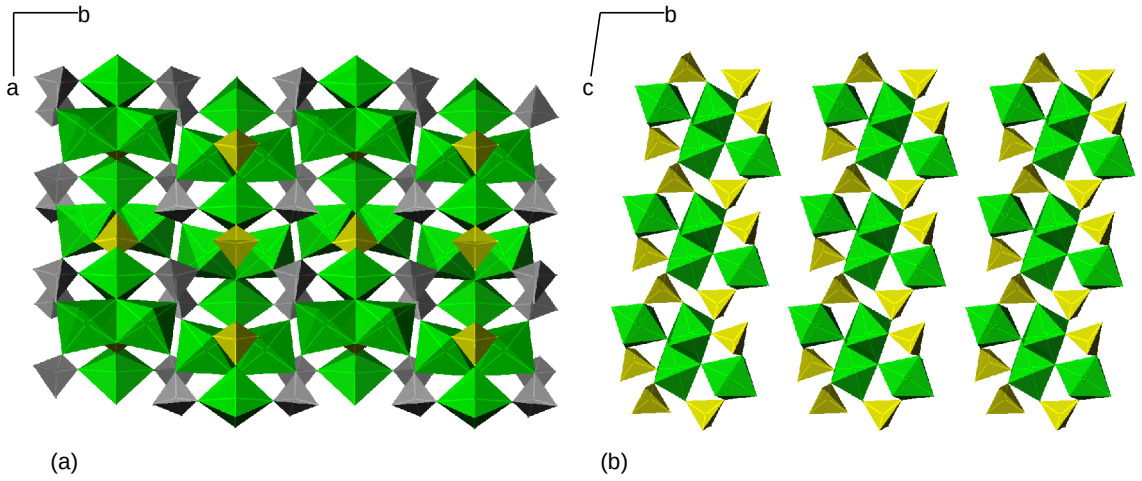

Figure 4.55. (a) A layer in the structure of sulfoborite [344] (MgO_5F octahedra, green; SO_4 tetrahedra, yellow; BO_4 tetrahedra, grey); (b) Parallel chains in the structure of amarantite [345] (FeO_6 octahedra, green; SO_4 tetrahedra, yellow).

4.7.2 The family [M(SO$_4$)(trien)] (M=Mn, Fe)

Motivated by the synthesis of the hybrid sulphate [Mn$_3$(SO$_4$)$_3$(HO)$_2$(trienH$_2$)] **(6)**, attempts to prepare other novel hybrid materials in the presence of triethylenetetramine lead to the synthesis of the family of layered sulphates [M(SO$_4$)(trien)] (M=Mn, Fe) **(7)-(8)**. The manganese analogue **(7)** was obtained under analogous conditions employed for the synthesis of [Mn$_3$(SO$_4$)$_3$(HO)$_2$(trienH$_2$)] **(6)** with only a decrease in reaction time, demonstrating that products obtained in the solvothermal syntheses are extremely influenced by variables such as the reaction time. Similar reaction conditions yielded the synthesis of the iron analogue **(8)**, confirming the ability of triethylenetetramine to act as a template for the preparation of hybrid materials.

The structure of [M(SO$_4$)(trien)] M=Mn, Fe **(7)-(8)** consists of chains built up from MO$_2$N$_4$ octahedra and SO$_4$ tetrahedra linked by vertex-sharing. The resulting chains are comparable to those observed in [Zn(SO$_4$)(H$_2$O)$_2$(C$_{10}$N$_2$H$_8$)] [154] in which chains of ZnO$_4$N$_2$ octahedra and SO$_4$ tetrahedra link through shared vertices and in which the two nitrogen atoms are provided by 2,2-bypiridine ligands (Figure 4.56). This single stranded chain is analogous to those chains observed in the mineral chalcanthite [155]. [NH$_2$(CH$_2$)$_4$NH$_2$][(VO)(H$_2$O)(SO$_4$)$_2$] displays a similar chain structure in which VO$_5$(H$_2$O) octahedra bridged by SO$_4$ tetrahedra in a *trans* fashion form a simple one-dimensional chain [156]. In contrast to the structure of [M(SO$_4$)(trien)] M=Mn, Fe **(7)-(8)**, each octahedron is surrounded by three sulphate tetrahedra. Those bridging VO$_5$(H$_2$O) octahedra are coordinated by vertex-linking, while those sulphate tetrahedra that do not participate in the linkage to form the chains are connected in a bidentate fashion by edge-sharing (Figure 4.56(b)).

The most remarkable feature of this structure is the unusual linkage of the organic amine to the metal centre since the amine is bidentate to each metal centre generating Mn-N-C-C-N five-membered rings.

4.7.3 Ethylenediamine for the preparation of two- and three-dimensional manganese sulphates

The successful use of triethylenetetramine for the generation of hybrid novel structures inspired the use of other templates to obtain similar structures. The use of ethylenediamine yielded [Mn(SO$_4$)$_2$](enH$_2$) **(9)** and the hybrid compound [Mn$_2$(SO$_4$)$_2$(en)$_2$]

(10). They were obtained under similar conditions but by increasing the reaction temperature the formation of the hybrid material was favoured.

The novel characteristic associated to the layered $[Mn(SO_4)_2](enH_2)$ **(9)** is the presence of bidentate sulphate tetrahedra that are linked to MnO_6 octahedra *via* edge-sharing. The existence of bidentate sulphates is not very common among the transition-metal sulphate family in comparison to the rare-earth sulphates that will be described in the next chapter. The connectivity between MnO_6 octahedra and SO_4 tetrahedra to form the double chains that are connected into layers (Figure 4.57(a)) resembles that observed in the iron sulphate $[NH_3(CH_2)_2NH_3][FeF_3(SO_4)]$ [163]. In that structure, alternating FeF_3O_3 octahedra and SO_4 tetrahedra form a ladder running along the crystallographic *a*-axis, in which each octahedron shares vertices with three bridging ligands, generating four-membered rings (Figure 4.57(b)). The structure of $[Mn(SO_4)_2](enH_2)$ **(10)** can also be compared to that of $[C_4N_2H_{12}][Fe_2(SO_4)_3(OH)_2(H_2O)_3]\cdot H_2O$ [161] in which linear chains are built from FeO_6 octahedra in which two SO_4 tetrahedra share corners with adjacent octahedra, resulting in an infinite chain containing four-membered rings (Figure 4.57(c)).

The structure of the hybrid material $[Mn_2(SO_4)_2(en)_2]$ **(10)** consists of a three-dimensional network that can be compared to the structure of $[Mn(SO_4)_2](enH_2)$ **(9)**, in which two sulphate tetrahedra have been substituted by two ethylenediamine molecules that are connected to the metal centre through a Mn-N bond.

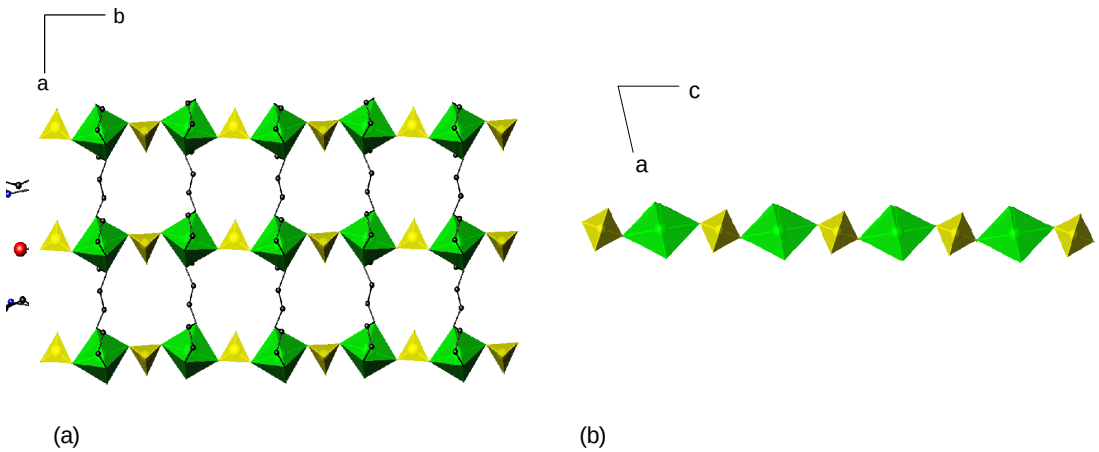

Figure 4.56. (a) Layer in $[M(SO_4)(trien)]$ (M=Mn, Fe) **(7)-(8)** formed by the connectivity of chains of FeO_6 octahedra and SO_4 tetrahedra and trien molecules (FeO_6 octahedra, green; SO_4 tetrahedra, yellow, C, black); (b) Single-stranded chain for $[Zn(SO_4)(H_2O)_2(C_{10}N_2H_8)]$ (ZnN_4O_2 octahedra, green; SO_4 tetrahedra, yellow) [154].

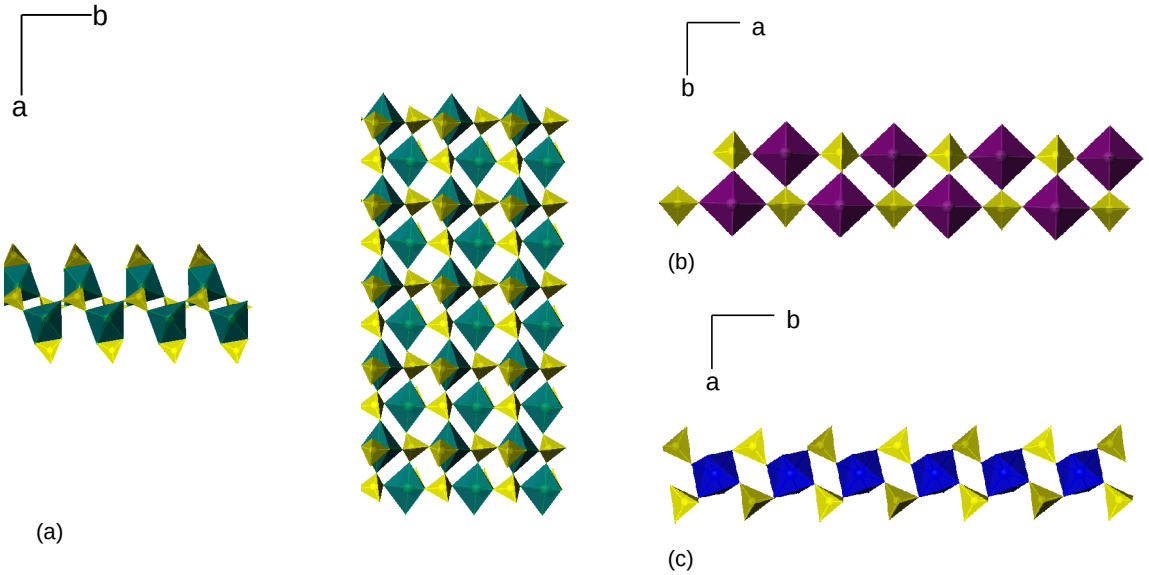

Figure 4.57. (a) Layer in $[Mn(SO_4)_2](enH_2)$ **(9)** (MnO_6 octahedra, green; SO_4 tetrahedra, yellow); (b) Double-stranded chain of $[NH_3(CH_2)_2NH_3][FeF_3(SO_4)]$ (FeF_3O_3 octahedra, purple; SO_4 tetrahedra, yellow) [163]; (c) Chain in $[C_4N_2H_{12}][Fe_2(SO_4)_3(OH)_2(H_2O)_3]\cdot H_2O$ (FeO_6 octahedra, blue; SO_4 tetrahedra, yellow) [161].

In the structure of **(10)** the bidentate sulphate group is also present and serves to connect adjacent MnO_6 octahedra by vertex and edge-linking, in contrast to the structure of $[Mn(SO_4)_2](enH_2)$ **(9)**, in which the bidentate group is a terminal group that does not participate in the formation of the layers. The structure of $[Mn_2(SO_4)_2(en)_2]$ **(10)** can be seen as made up from chains in which each MnO_6 octahedron links the neighbouring octahedron *via* a bidentate SO_4 tetrahedron that shares an edge with that octahedron and a vertex with the adjacent MnO_6 octahedron along the *b*-axis (Figure 4.58(a)). These chains are comparable to those found in $[NH_2(CH_2)_4NH_2][(VO)(H_2O)(SO_4)_2]$ [156] (Figure 4.58(b)), consisting of alternating $VO_5(H_2O)$ octahedra bridged by SO_4 tetrahedra in a *trans* fashion. The bidentate sulphate provides the linkage between adjacent chains to form layers of vertex- and edge-sharing MnO_6 octahedra and SO_4 tetrahedra, which results in the formation of channels of six-membered rings. Those layers resemble those obtained in the three-dimensional cadmium sulphate $[Cd(BIMB)_{0.5}(SO_4)(H_2O)]_n\cdot nH_2O$ [240] in which CdO_6 octahedra and SO_4 tetrahedra are connected by vertex-linking to form layers that are joined to adjacent ones by 1,4-bis(imidazol-1-methyl)benzene (BIMB) generating a hybrid three-dimensional structure (Figure 4.58(c)). The linkage between the amine molecules and

the inorganic layers in $[Mn_2(SO_4)_2(en)_2]$ **(10)** allows the formation of a porous structure with empty cavities of *ca.* 2.7 x 4.7 Å dimensions.

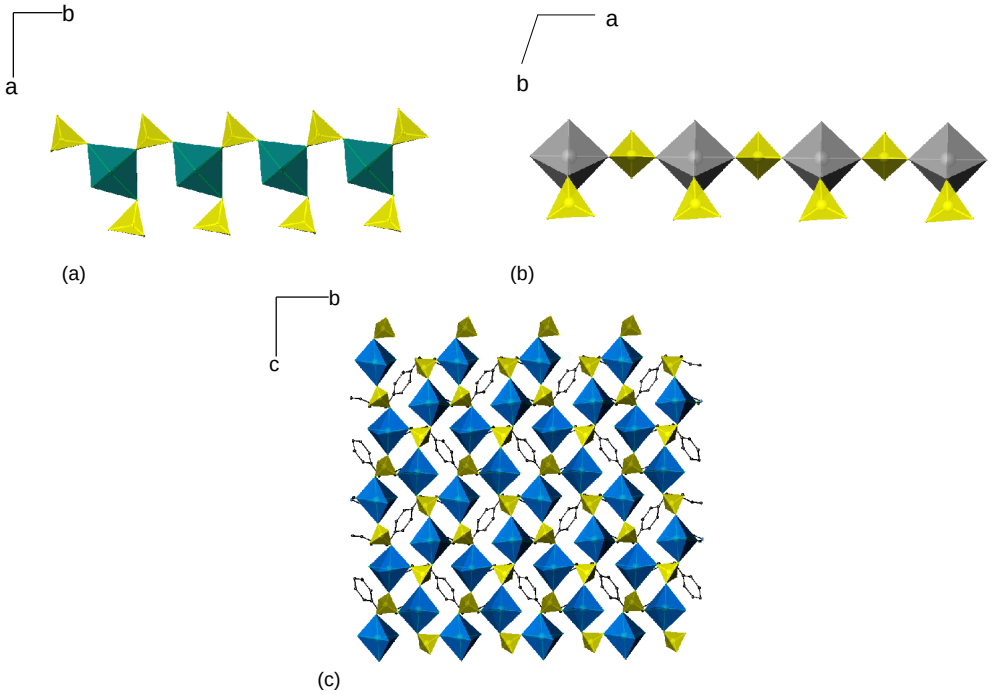

Figure 4.58. (a) Chain in the three-dimensional structure of $[Mn_2(SO_4)_2(en)_2]$ **(10)** (MnO_4N_2 octahedra, green; SO_4 tetrahedra, yellow); (b) Stranded chain in $[NH_2(CH_2)_4NH_2][(VO)(H_2O)(SO_4)_2]$ ($VO_5(H_2O)$, green; SO_4 tetrahedra, yellow) [156]; (c) One layer in $[Cd(BIMB)_{0.5}(SO_4)(H_2O)]_n \cdot nH_2O$ (CdO_6 octahedra, blue; SO_4 tetrahedra, yellow; C, black; N, blue; O, red) [240].

4.7.4 Kagome layers in $[Co_3(SO_4)_3(OH)_2](enH_2)$

A novel cobalt sulphate $[Co_3(SO_4)_3(OH)_2](enH_2)$ **(11)** with an unusual layered structure has been synthesised in the presence of ethylenediamine. The structure consists of $[Co_3(SO_4)_3(OH)_2]^{2-}$ layers which are obtained by CoO_6 octahedra linked together by sharing edges to form triangles. Simultaneously, adjacent triangles are connected to each other *via* vertex-linkage of CoO_6 octahedra and SO_4 tetrahedra (Figure 4.59(a)). Inorganic layers and diprotonated ethylenediamine cations alternate along the crystallographic *c*-axis and they interact with each other in a hydrogen bonded system. This structure constitutes a new example of a Kagome-type lattice, which is a special case of magnetism and important for understanding magnetic frustration in transition metal materials. In $[Co_3(SO_4)_3(OH)_2](enH_2)$ **(11)** frustration arises from the topological arrangement of

magnetic ions in the crystal lattice. Each layer may be visualised by considering only the metal centres and hence consisting of hexagonal tungsten bronze sheets in which one magnetic ion is shared by two adjacent triangles.

Most of the transition-metal sulphates which exhibit the Kagome Lattice belong to the jarosite family, ($K_2[Fe_6^{III}(SO_4)_4(OH)_{12}]$ [218]. The majority of these materials are iron-containing sulphates [220, 221] but recent efforts have lead to the synthesis of cobalt [227], manganese [228] and nickel [226] sulphates possessing the Kagome lattice. In all these materials the layers consist of vertex-sharing MF_4O_2 octahedra and SO_4 tetrahedra linked together through bridging M-F and M-O-S bonds, with the exception of $[NH_3(CH_2)_2NH_2(CH_2)_2NH_2(CH_2)_2NH_3][Fe^{III}Fe_2^{II}F_6(SO_4)_2]$ [221] in which edge-linking FeF_4O_2 octahedra have been identified. The uniqueness of the structure of $[Co_3(SO_4)_3(OH)_2](enH_2)$ **(11)** resides in the structure of the layers and has been described in this thesis for the first time. It constitutes a new Kagome-type lattice consisting of edge-linking CoO_6 octahedra forming triangles which are in turn connected into layers in contrast to the common hexagonal rings observed in the jarosite family (Figure 4.59).

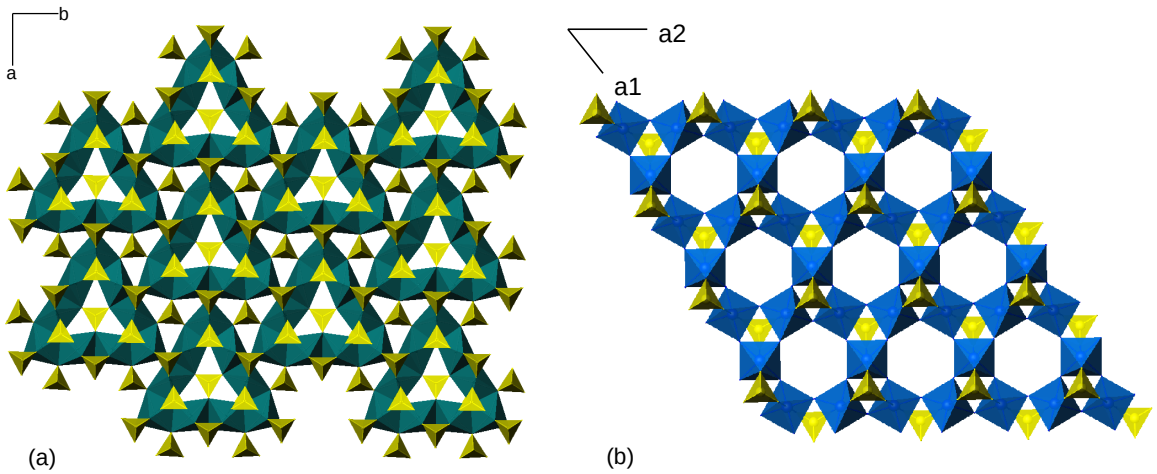

Figure 4.59. (a) Layer in $[Co_3(SO_4)_3(OH)_2](enH_2)$ **(11)** (CoO_6 octahedra, green; SO_4 tetrahedra, yellow); (b) One layer of the jarosite $K_2[Fe_6^{III}(SO_4)_4(OH)_{12}]$ [218] (FeO_6 polyhedra, blue; SO_4 tetrahedra, yellow).

4.7.5 Magnetic properties

Transition metals display a remarkable variety of magnetic properties. The exchange energy between two magnetic dipoles U_{ij} can be expressed as:

$$U_{ij} = {}^{-J_{ij}S_iS_j}\!\!\diagup\!\!_{\hbar^2} \quad (4.1)$$

in which J_{ij} is the exchange coupling constant between the magnetic centre *i* and *j* and *S* refers to the electron spins of *i* and *j*. The coupling is due to quantum mechanical exchange between overlapping orbitals at the two sites. When J_{ij} is positive this corresponds to ferromagnetic exchange and the dipoles tend to align themselves in the same direction. In the situation in which J_{ij} is negative antiferromagnetic exchange occurs and the dipoles tend to align antiparallel. When the exchange interactions involve the intervention of the bridging ligands superexchange happens, which is the dominant source of dipolar coupling in transition metals and most commonly tends to promote antiferromagnetic ordering. The exchange interaction between a pair of open-shell ions decays dramatically with the distance between them.

The manganese sulphate $[Mn_4(SO_4)_8(OH)_2(H_2O)_2](enH_2)_5$ **(4)** shows paramagnetic behaviour at room temperature and the reciprocal magnetic susceptibility plot can be linearly fitted according the Curie-Weiss law over the range 30-300 K. At low temperatures, an anomaly is observed below 20 K. The fitting of the paramagnetic region to the Curie-Weiss law yielded a negative Weiss constant -10.70(3) K, suggesting the origin of the anomaly may be due to the presence of antiferromagnetic correlations. The plot of the magnetic moment as a function of temperature shows a decrease in μ_{eff} as the temperature is lowered, which confirms the antiferromagnetic coupling of Mn-Mn centres which are at a short distance 3.06 Å in the dimer that constitute the central part of the four metal clusters. However a sharp upturn was observed at 12 K, the temperature at which the anomaly in the inverse susceptibility data was observed, and whose origin could not be explained. The effective magnetic moment for Mn^{2+} (μ_{eff}=6.34 μ_B) is slightly higher than the expected spin-only value (μ_{SO}=5.92 μ_B). For systems with a d^5 configuration the orbital angular momentum does not contribute to the magnetic moment [346], therefore the discrepancy between the observed and the spin-only magnetic moment may be attributed to inappropriate processing of magnetic data when significant antiferromagnetic coupling exists or to the presence of impurities.

The layered $[Fe_3(SO_4)_3(OH)_2(H_2O)_2](NH_4)_2$ **(5)** exhibits a complex magnetic behaviour. High-temperature magnetic susceptibility data could not be described by the Curie-Weiss law suggesting that the Curie point is above 300 K and that the material is

magnetically ordered at room temperature. The data obtained reveal that a divergence between the field-cooled and the zero field-cooled susceptibility occurs below 122 K which indicates that this system might be a frustrated system, such as a spin glass, or ferrimagnetically ordered. In $[Fe_3(SO_4)_3(OH)_2(H_2O)_2](NH_4)_2$ **(5)**, if only the iron centres are represented, triangular plaquettes that share both vertices and faces are obtained (Figure 4.60) and they can be rendered frustrated if interactions with adjacent spins are considered. Common and easily observed signatures of spin-glass state are (a) divergence between the zero field-cooled and the field-cooled susceptibility data in d.c. susceptibility; (b) a frequency dependence of the susceptibility below the glass temperature in a.c. susceptibility; (c) the absence of long-range order from neutron diffraction. Therefore, a.c. susceptibility, d.c. susceptibily at high temperatures and at different fields, hysteresis and neutron diffraction measurements are required to determine whether or not this is a frustrated spin-glass system. The decrease of the susceptibility as the temperature decreases in the region that goes from 0-40 K, is usually found in materials that order antiferromagnetically, which suggests that probably the dominant exchange interactions are antiferromagnetic. In **(5)** the magnetisation saturates with increasing field which is a feature of ferromagnetism, but this form of cooperative magnetism is usually characterised by a huge magnetisation. However the maximum susceptibility is 23 e.m.u, which might suggest ferrimagnetic behaviour or competing ferromagnetic and antiferromagnetic interactions, as it has been previously proposed for another organically-templated iron sulphate $[H_3N(CH_2)_2NH_3][Fe_2F_2(SO_4)_2(H_2O)_2]$ [163], which shows a similar transition to that observed in the field-cooled susceptibility data at low temperature. These types of systems in which different competing interactions occur might be helpful for a variety of applications in thermal, mechanical, optical, electrical or magnetic phenomena. The broad nature of the susceptibility data has been described for an iron sulphate with a Kagome layer [225] and was suggested to be caused by magnetic polarizations that might be geometrical in origin. This may also be an indication of low-dimensional antiferromagnetic short-range correlations [347]. More irrefutable data need to be analysed before reaching any conclusion about the magnetic behaviour of $[Fe_3(SO_4)_3(OH)_2(H_2O)_2](NH_4)_2$ **(5)**.

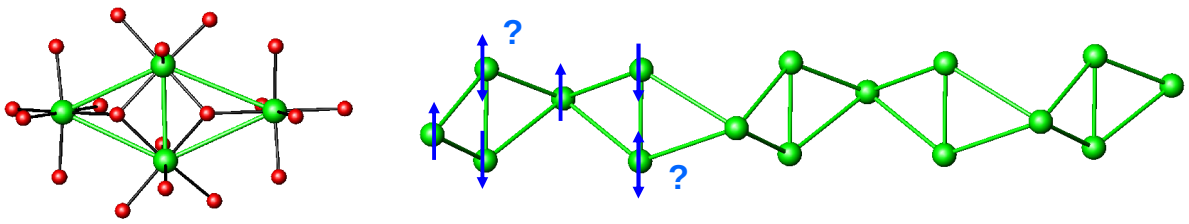

Figure 4.60. (a) Two triangular plaquettes formed by Fe^{2+} centres in the Fe_4O_{20} tetramer; (b) Representation of Fe^{2+} along a chain in **(5)**

For $[Mn_3(SO_4)_3(OH)_2(trienH_2)]$ **(6)** the reciprocal magnetic susceptibility plot was fitted to the Curie-Weiss law over the range 60-300 K, yielding a negative Weiss constant (-70.45(1) K) suggesting that the dominant exchange interactions are antiferromagnetic. Below 60 K, the reciprocal magnetic susceptibility as a function of temperature shows two discontinuities, one at 55 K and a second one at 14 K. At 55 K a sudden increase of the magnetic susceptibility from 0.21 e.m.u at 55 K to 78 e.m.u at 5 K was observed suggesting that $[Mn_3(SO_4)_3(HO)_2(trienH_2)]$ **(6)** undergoes ferromagnetic ordering at this temperature. In addition a divergence between the zero field-cooled and the field-cooled susceptibility plots occurs at 14 K, temperature at which the second discontinuity in the inverse of the magnetic susceptibility data was identified. This is usually an indication of ferrimagnetism or magnetic frustration. In $[Mn_3(SO_4)_3(HO)_2(trienH_2)]$ **(6)** if only the manganese centres are represented a triangular array of spins identical to that observed in **(5)** is obtained, indicating that this system may be a frustrated system that orders ferrimagnetically at low temperature. The magnetisation as a function of field indicates complete saturation occurs at high fields with a saturation value of *ca.* 0.016 μ_B which is consistent with ferrimagnetism. Similar magnetic behaviour has been identified in the layered nickel sulphate $[C_4N_2H_{12}][Ni_3F_2(SO_4)_3(H_2O)_2]$ [188], whose layers, built up from NiO_4F_2 octahedra and SO_4 tetrahedra, are isostructural to the inorganic layers of **(6)**. This material shows magnetic hysteresis at 5 K and a ferrimagnetic transition at low temperature. Ferrimagnetism happens when the crystal lattice contains two distinct magnetic centres in unequal proportions or unequal size. Such might be the case of $[Mn_3(SO_4)_3(OH)_2(trienH_2)]$ **(6)**. A model for ferrimagnetic ordering is shown in Figure 4.61. Exchange interactions are predominantly antiferromagnetic (X-Y) and the ordering within each sublattice (X or Y) is effectively ferromagnetic. Since the two sub-lattices (X and Y) are inequivalent there is a

net magnetisation M_x-M_y in the M_x direction. According to Goodenough rules, atoms in a linear array have oppositely aligned spins and interact antiferromagnetically. In **(6)** such is the case of $Mn(1)O_5N$ octahedra that share edges. In addition, each $Mn(1)O_5N$ octahedron interact ferromagnetically with an adjacent $Mn(2)O_6$ octahedron, resulting in oppositely magnetised arrays of ions with a net magnetisation parallel to that of the most populated sublattice. However, if interactions with other neighbouring spins are considered, this system renders frustrated (Figure 4.62).

The effective magnetic moment per Mn^{2+} ion in $[Mn_3(SO_4)_3(OH)_2(trienH_2)]$ **(6)** (μ_{eff}=5.721(1) μ_B) is close to the spin only value (μ_{so}=5.92 μ_B). The magnetic moment as a function of temperature decreases from room temperature to 50 K, characteristic of antiferromagnetic interactions, but an abrupt increase in the magnetic moment from 5.4 μ_B to 46 μ_B is observed at the temperature at which the proposed transition to ferrimagnetism takes place.

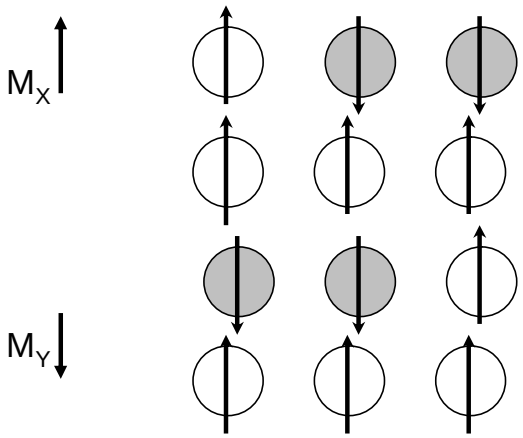

Figure 4.61. Model for ferrimagnetic ordering (X, white; Y, grey).

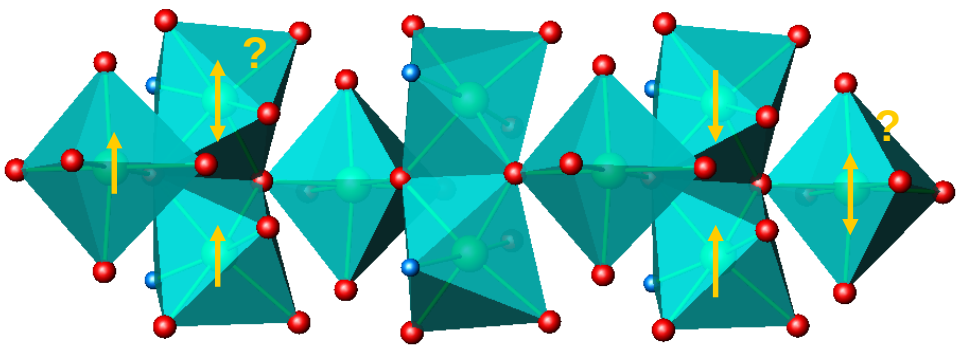

Figure 4.62. Proposed model for ferrimagnetic ordering in **(6)**, showing the two possible arrays of spins that may induce magnetic frustration.

$[Mn(SO_4)_2](enH_2)$ **(9)** and $[Mn_2(SO_4)_2(en)_2]$ **(10)** show similar magnetic behaviour. In the paramagnetic region (50-300 K) the susceptibility follows the Curie-Weiss law with negative Weiss constants of -9.97(2) K and -13.33(2) K, respectively indicating antiferromagnetic exchange interactions. The reciprocal magnetic susceptibility plots show two discontinuities at 41 K and 17 K for $[Mn(SO_4)_2](enH_2)$ **(9)** and at 45 K and 17 K for $[Mn_2(SO_4)_2(en)_2]$ **(10)** which are the temperatures at which the field-cooled and zero-field cooled susceptibility plots for both manganese sulphates show a small divergence. The linear field dependence of the magnetisation at 5 K reveals that no spontaneous magnetisation occurs, which suggests both materials are paramagnetic with only short-range antiferromagnetic correlations *via* superexchange (Mn-O-S-O-Mn) at low temperature. The presence of two discontinuities could be due to one or two phase transitions at low temperature. In order to study the nature of these discontinuities, measurements at higher fields as well as single-crystal structure determination below the temperature at which the transitions occur are required. Similar magnetic behaviour has been identified in a manganese sulphate with a Kagome layer [228]. The effective magnetic moment for Mn^{2+} in $[Mn(SO_4)_2](enH_2)$ **(9)** is 5.73(1) μ_B is close to the spin only value (5.92 μ_B). Surprisingly, in $[Mn_2(SO_4)_2(en)_2]$ **(10)** the effective magnetic moment of the manganese ion was calculated to be 4.84(1) μ_B which is far from the spin only value for a Mn^{2+} ion in a high spin configuration (5.92 μ_B). The origin of this phenomenon could be explained by two different facts: (a) When the internal energy difference between the high-spin and the low spin configuration is small, a transition between the two electronic states can occur when the temperature is varied. When this difference in internal energy is comparable with kT, both the high and the low spin complexes may co-exist as electronic isomers, phenomenon that is known as spin equilibrium, and the relative proportion of complexes is governed by the Boltzmann law; (b) In octahedral complexes involving d^5 configuration there is a chance of ground terms possessing intermediate spin states when the orbital splitting Δ is high enough to induce a transition from the high to the intermediate spin state. In that case, the magnitude of the splitting depends on the nature of the ligand. The stronger the covalent interaction between the metal centre and the ligand is, the greater the orbital splitting. Since in $[Mn_2(SO_4)_2(en)_2]$ **(10)** each manganese centre is covalently linked to two ethylenediamine molecules *via* Mn-N bond and according to the spectrochemical series ethylenediamine is an intermediate to strong-field ligand, which can

be both a σ-donor and π-acceptor, there is a possibility that the splitting of the *d* orbitals [348] is large enough to induce a transition from the high to the intermediate spin-state and therefore the effective magnetic moment can be calculated assuming a Boltzmann distribution.

Magnetic data for $[Co_3(SO_4)_3(OH)_2](enH_2)$ **(11)** were collected at two different fields, 100 G and 1000 G, in order to study the possible frustrated nature of this system. Among the signatures of frustration the most commonly observed is a field-cooled, zero field-cooled divergence. At 1000 G an anomaly was observed at 16 K. Above this temperature the reciprocal magnetic susceptibility was fitted to the Curie-Weiss equation in the paramagnetic region that goes from 16-300 K yielding a negative Weiss constant (-43.48(2) K) suggesting Co-Co antiferromagnetic coupling. At 100 G, the fitting of the paramagnetic region to the Curie-Weiss law also gave a negative Weiss constant -60.91(3) K. An anomaly was also observed in the inverse susceptibility plot at 16 K with a second transition at 9.45 K which confirms the presence of antiferromagnetic correlations. In addition, a divergence between the zero field-cooled and the field-cooled susceptibility plots was observed. The maximum in the zero field-cooled susceptibility data is characteristic of antiferromagnetism and is consistent with the magnetisation as a function of field being linear. Besides the divergence, other manifestation of frustration is given by the magnitude of the ratio θ_c/T_C [207] and for jarosites with appreciable levels of vacancies on the magnetic sub-lattice this ratio typically lies in the range 11-16. For $[Co_3(SO_4)_3(OH)_2](enH_2)$ **(11)** the ratio θ_c/T_C = 8, which is consistent with a magnetically frustrated system. Defective materials with long-range antiferromagnetic order at low temperature adopt the **q**=0 structure below the Neel temperature [224]. The ratio θ_c/T_C increases noticeably when the occupancy of magnetic sites approaches 100 % and the material behaves as a spin glass [222]. However, for **(11)**, with a 100 % coverage of magnetic sites, this parameter is significantly low. Magnetic susceptibility data indicate that magnetic ordering in this material is an antiferromagnetic state, in which both strong and weak antiferromagnetic interactions arising from the differences in connectivity of the octahedra are present. This inequality in the exchange interactions may provide a mechanism for relieving the frustration, allowing an ordered state of the spins in the Kagome lattice (Figure 4.63). The effective magnetic moment for Co^{2+} in $[Co_3(SO_4)_3(OH)_2](enH_2)$ **(11)** (5.25(1) μ_B at 1000 G and 5.426(1) μ_B at 100 G) is higher

that the spin only value (3.87 μ_B) due to the orbital contribution to the ^{4}T ground state, which is expected to give rise to a temperature-dependent contribution to the magnetic moment. $[Co_3(SO_4)_3(OH)_2](enH_2)$ **(11)** displays a magnetic moment that declines as the temperature is lowered and it falls from 4.93 μ_B at 300 K to 1.8 μ_B at 5 K. The effective magnetic moment as a function of temperature plot at 100 G shows an upturn at around 9.4 K coinciding with the temperature at which the anomaly in the inverse susceptibility data is observed.

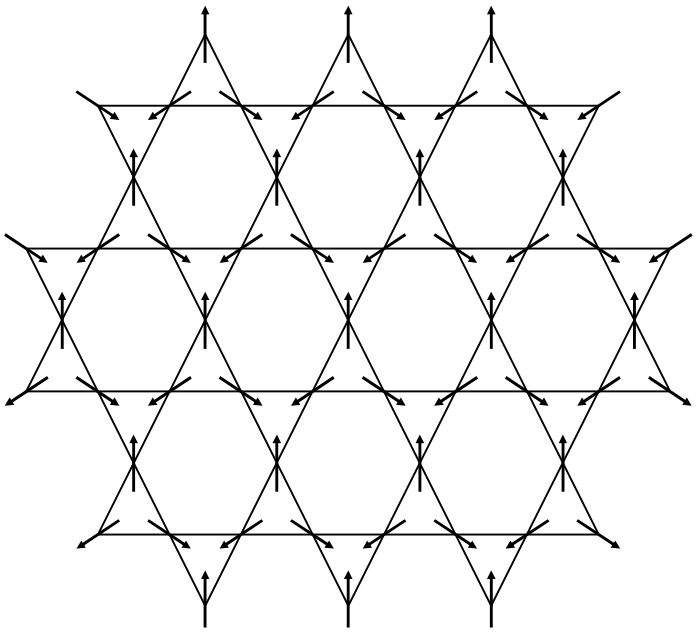

Figure 4.63. Spins of Co^{2+} as a result of an ordered state in the Kagome-lattice

Chapter 5: Organically-templated rare-earth sulphates

5.1 Introduction

Although in recent years emphasis has been given to the synthesis and characterisation of carboxylates [349], oxalates [123, 350] and phosphato-oxalates [131] of rare-earth ions, surprisingly the synthesis of sulphates in the presence of rare-earth ions has been less investigated. The known crystal structures of organically-templated rare-earth sulphates are limited compared to those of the transition metal sulphates and, until five years ago, rare-earth sulphates templated by amines were rarely reported and restricted to inorganic sulphate hydrates [351] and ternary rare-earth sulphates with alkaline metal ions or ammonia [194, 352]. Recently chain, layered and three-dimensional structures of rare-earth sulphates obtained under hydrothermal conditions have been structurally characterised. The research interest in the study of rare-earth sulphates arises from their potential to provide access to novel framework architectures due to their high and diverse coordination numbers as well as from their promising applications.

Making use of solvothermal synthesis, several rare-earth sulphates with different structures and dimensionalities, containing lanthanum, dysprosium, europium, gadolinium, praseodymium and erbium, have been prepared and a full characterisation and description of these structures will be provided in this chapter. In all of these materials, the metal ion is in the trivalent oxidation state, which is the predominant oxidation state in the lanthanide chemistry. Reactions were carried out varying the reaction conditions, including temperature, time, reagents and molar ratio, and using a wide variety of organic amines, such as ethylenediamine, triethylenetetramine, diethylamine, pyrrolidine and piperazine. Several inorganic sulphate hydrates of general formula $Ln_2(SO_4)_3(H_2O)_4$ (Ln=Sm, Pr, Dy, Gd) were obtained in the course of this research project when employing piperazine, diethylamine and pyrrolidine. However, the crystal structure of those materials will not be discussed in this chapter since they are inorganic sulphate hydrates whose structure has been well-established.

Spectroscopic and magnetic susceptibility data were collected for many of these novel amine-templated rare-earth sulphates which allowed a detailed examination of their properties in comparison to those of the organically-templated transition metal sulphates.

5.2 Synthesis and characterisation

5.2.1 Synthesis

Solvothermal synthesis was employed for the preparation of $[La(SO_4)_3](enH_2)_{1.5}$ **(12)**, $[Dy_2(SO_4)_6(H_2O)](trienH_4)_{1.5}$ **(13)**, $[Ln_2(SO_4)_6(enH)_2](enH_2)_2$ (Ln=Pr, Eu, Gd) **(14)-(16)**, $[Ln_2(SO_4)_6(H_2O)_2](enH_2)_3$ (Ln=Er, Dy) **(17)-(18)**, $[Dy(SO_4)_2](enH_2)_{0.5}$ **(19)** and $[Sm_4(SO_4)_{10}(H_2O)_4](pipH_2)_4$, **(20)** using the corresponding rare-earth sulphate hydrate salt, H_2SO_4, deionised water and the amine. For instance, $[La(SO_4)_3](enH_2)_{1.5}$ was synthesised from a mixture of $La_2(SO_4)_3$ (0.55 g; 1 mmol), ethylenediamine (0.2 mL; 3 mmol) and H_2SO_4 (0.11 mL; 2 mmol) which were loaded into a 23 mL Teflon-lined stainless steel autoclave together with 0.072 mL of deionised water to form a mixture La:en:H_2SO_4:H_2O of molar composition 1:1.5:1:1. After stirring the mixture, the container was closed and heated at 170 °C for 5 days and then cooled down to room temperature at a cooling rate of 1 °C min^{-1}. The solid product was filtered, washed with deionised water, methanol and acetone and dried in air at room temperature. The product consisted of a mixture of white powder and colourless crystals of $[La(SO_4)_3](enH_2)_{1.5}$, identified by single-crystal X-ray diffraction. Using an analogous synthetic approach, compounds **(13)-(20)** were prepared and the reactions conditions are summarised in Table 5.1.

5.2.2 Single-crystal diffraction

Single-crystal X-ray diffraction data for **(12)-(20)** were collected at 293 K using a Bruker Nonius X8 Apex diffractometer with Mo-Kα radiation (λ=0.71073 Å). Data were processed using the Apex-2 software [289] and the structure was solved by direct methods using the program SIR92 [291], which located the heavy atoms, lanthanum, dysprosium, praseodymium, europium, gadolinium, erbium and samarium atoms, together with sulphur and most of the oxygen atoms. Subsequent difference Fourier calculations, to locate the remaining oxygen atoms as well as nitrogen and carbon atoms, and least-squares refinements were carried out using the CRYSTALS suite of program [292]. Some hydrogen atoms were found by difference Fourier maps and the remaining introduced manually. In the final cycles of refinement, positional and anisotropic thermal parameters for all non-hydrogen atoms were refined. Crystallographic details for **(12)-(20)** are given in Table 5.2, Table 5.3, Table 5.4 and Table 5.5. Atoms coordinates and selected bond distances and angles for **(12)-(20)** are listed in Appendix B and C, respectively.

Table 5.1. Reaction conditions for the solvothermal synthesis of **(12)-(20)**.

Compound	Reactants and Amounts	Mixture and Composition	T / °C	Time / days	Product
(12)	$La_2(SO_4)_3$ (0.55 g; 1mmol); ethylenediamine (0.2 mL; 3 mmol); H_2SO_4 (0.11 mL; 2 mmol); deionised water (0.072 mL; 2 mmol)	La:en:H_2SO_4:H_2O 1:1.5:1:1	170	5	colourless crystals + white powder
(13)	$Dy_2(SO_4)_3{\cdot}8H_2O$ (0.747 g; 1 mmol); triethylenetetramine (0.33 mL; 2 mmol); H_2SO_4 (0.22 mL; 4 mmol); deionised water (0.145 mL; 4 mmol)	Dy:trien:H_2SO_4:H_2O 2:1:2:2	170	10	colourless crystals + pale brown powder
(14)	$Pr_2(SO_4)_3{\cdot}8H_2O$ (0.588 g; 1mmol); ethylenediamine (0.2 mL; 3 mmol); H_2SO_4 (0.11 mL; 2 mmol); deionised water (0.145 mL; 4 mmol)	Pr:en:H_2SO_4:H_2O 1:1.5:1:2	170	10	green crystals + pale green powder
(15)	$Eu_2(SO_4)_3{\cdot}8H_2O$ (0.194 g; 0.3 mmol); ethylenediamine (0.2 mL; 3 mmol); H_2SO_4 (0.11 mL; 2 mmol); deionised water (0.145 mL; 4 mmol)	Eu:en:H_2SO_4:H_2O 0.30:1.5:1:2	170	10	brown crystals
(16)	$Gd_2(SO_4)_3{\cdot}8H_2O$ (0.197 g; 0.3 mmol); ethylenediamine (0.2 mL; 3 mmol); H_2SO_4 (0.11 mL; 2 mmol); deionised water (0.145 mL; 4 mmol)	Gd:en:H_2SO_4:H_2O 0.30:1.5:1:2	170	10	white crystals + pale brown powder
(17)	$Er_2(SO_4)_3{\cdot}8H_2O$ (0.21 g; 0.3 mmol); ethylenediamine (0.2 mL; 3 mmol); H_2SO_4 (0.11 mL; 2 mmol); deionised water (0.072 mL; 2mmol)	Er:en:H_2SO_4:H_2O 0.30:1.5:1:1	170	5	pink crystals
(18)	$Dy_2(SO_4)_3{\cdot}8H_2O$ (0.25 g; 0.3 mmol); ethylenediamine (0.2 mL; 3 mmol); H_2SO_4 (0.22 mL; 4 mmol); deionised water (0.145 mL; 4 mmol)	Dy:en:H_2SO_4:H_2O 0.30:1.5:2:2	170	5	white crystals + pale brown powder
(19)	$Dy_2(SO_4)_3{\cdot}8H_2O$ (0.747g; 1 mmol); ethylendiamine (0.2 mL; 3 mmol); H_2SO_4 (0.22 mL; 4 mmol); deionised water (0.145 mL; 4 mmol)	Dy:en::H_2SO_4:H_2O 1:1.5:2:2	170	5	colourless crystals + grey powder
(20)	$Sm_2(SO_4)_3{\cdot}8H_2O$ (0.751 g; 1 mmol); piperazine (0.173 g; 2 mmol); H_2SO_4 (022 mL; 4 mmol); deionised water (0.145 mL; 4 mmol)	Sm:pip:H_2SO_4:H_2O 2:1:2:2	170	5	colourless crystals + white powder

Table 5.2. Crystallographic data for $[La(SO_4)_3](enH_2)_{1.5}$ **(12)** and $[Dy_2(SO_4)_6(H_2O)](trienH_4)_{1.5}$ **(13)**.

Compound number	**(12)**	**(13)**
Temperature / K	293	293
M_r	520.27	1144.80
Crystal size (mm)	0.24 X 0.30 X 0.40	0.16 X 0.40 X 0.40
Crystal habit	Colourless plate	Colourless plate
Crystal system	Trigonal	Triclinic
Space group	*R-3c*	*P-1*
***a*(Å)**	17.1571(3)	6.3042(7)
***b*(Å)**		10.8925(12)
***c*(Å)**	16.4207(6)	22.777(2)
α (°)		77.721(5)
β (°)		87.866(5)
γ (°)		84.443(6)
V(Å^3)	4186.10(18)	1520.9(3)
Z	12	2
μ(mm^{-1})	3.58	5.40
ρ_{calc} (g cm^{-3})	2.476	2.500
Residual electron density (min, max) (eÅ^{-3})	-0.34, 0.56	-1.19, 1.13
Measured data	36214	41439
Unique data	1424	9020
Observed data (I>3σ(I))	908	5851
R_{int}	0.027	0.046
R(F)	0.014	0.029
$_wR(F)$	0.015	0.023

Table 5.3. Crystallographic data for $[Ln_2(SO_4)_6(enH)_2](enH_2)_2$ (Ln=Pr, Eu, Gd) **(14)-(16)**.

Compound number	**(14)**	**(15)**	**(16)**
Temperature / K	293	293	293
M_r	1103.02	1126.75	1137.32
Crystal Size (mm)	0.16 X 0.20 X 0.40	0.20 X 0.60 X 0.64	0.20 X 0.20 X 0.80
Crystal Habit	Green plate	Brown plate	White plate
Crystal System	Orthorhombic	Orthorhombic	Orthorhombic
Space Group	*Pna2$_1$*	*Pna2$_1$*	*Pna2$_1$*
***a*(Å)**	19.5310(11)	19.4071(17)	19.3359(6)
***b*(Å)**	6.5898(4)	6.5238(5)	6.5175(2)
***c*(Å)**	25.4281(19)	25.263(2)	25.1950(8)
V (Å^3)	3272.7(4)	3198.5(5)	3175.12(17)
Z	4	4	4
μ (mm^{-1})	3.43	4.38	4.64
ρ_{calc} (g cm^{-3})	2.238	2.340	2.379
Residual electron density (min, max) (eÅ^{-3})	-0.98, 1.73	-1.46, 1.83	-0.91, 1.71
Measured data	25533	25564	24256
Unique data	9025	9558	9493
Observed data *(I>3σ(I))*	4430	5719	6936
R_{int}	0.089	0.077	0.045
R(F)	0.056	0.047	0.036
$_wR(F)$	0.044	0.014	0.032

Table 5.4. Crystallographic data for $Ln_2(SO_4)_6(H_2O)_2](enH_2)_3$ (Ln=Er, Dy) **(17)-(18)**

Compound number	**(17)**	**(18)**
Temperature / K	293	293
M_r	1133.28	1123.76
Crystal Size (mm)	0.24 X 0.24 X 0.30	0.40 X 0.50 X 0.60
Crystal Habit	Pink plate	White plate
Crystal System	Orthorhombic	Orthorhombic
Space Group	*Pbca*	*Pbca*
***a*(Å)**	9.6427(4)	9.6396(5)
***b*(Å)**	19.9307(9)	19.9399(12)
***c*(Å)**	30.3349(13)	30.4327(17)
V (Å^3)	5829.9(4)	5849.5(6)
Z	8	8
μ (mm^{-1})	6.26	5.61
ρ_{calc} (g cm^{-3})	2.582	2.552
Residual electron density (min, max) (eÅ^{-3})	-1.16, 1.32	-1.84, 1.81
Measured data	46544	29738
Unique data	8730	5929
Observed data *(I>3σ(I))*	4970	4795
R_{int}	0.058	0.033
R(F)	0.029	0.033
$_wR(F)$	0.029	0.030

Table 5.5. Crystallographic data for $[Dy(SO_4)_2](enH_2)_{0.5}$ **(19)** and $[Sm_4(SO_4)_{10}(H_2O)_4](pipH_2)_4$ **(20)**

Compound number	**(19)**	**(20)**
Temperature / K	293	293
M_r	385.68	1986.91
Crystal size (mm)	0.20 X 0.20 X 0.80	0.20 X 0.20 X 0.40
Crystal habit	Colourless plate	Colourless plate
Crystal system	Triclinic	Monoclinic
Space group	*P-1*	*$P2_1/c$*
***a* (Å)**	5.3542(2)	19.7936(7)
***b* (Å)**	7.1078(3)	19.3266(7)
***c* (Å)**	9.6853(3)	13.2525(5)
α (°)	87.078(2)	
β (°)	83.585(1)	92.316(2)
γ (°)	80.131(1)	
V(Å^3)	360.67(2)	5065.5(3)
Z	2	4
μ(mm^{-1})	10.96	5.11
ρ_{calc} (g cm^{-3})	3.551	2.605
Residual electron density (min, max) (eÅ^{-3})	-1.32, 0.70	-2.47, 2.51
Measured data	9580	136715
Unique data	2189	15552
Observed data (I>3σ(I))	2104	10019
R_{int}	0.019	0.047
R(F)	0.014	0.022
$_wR(F)$	0.015	0.022

5.2.3 Analytical Characterisation

Results of elemental analysis of hand-picked crystals of $[La(SO_4)_3](enH_2)_{1.5}$ **(12)**, $[Dy_4(SO_4)_{12}(H_2O)_2](trienH_4)_3$ **(13)**, $[Ln_2(SO_4)_6(enH)_2](enH_2)_2$ (Ln=Pr, Eu, Gd) **(14)-(16)**, $[Ln_2(SO_4)_6(H_2O)_2](enH_2)_3$ (Ln=Er, Dy) **(17)-(18)**, $[Dy(SO_4)_2](enH_2)_{0.5}$ **(19)** and $[Sm_4(SO_4)_{10}(H_2O)_4](pipH_2)_4$, **(20)** are summarised in Table 5.6. For **(12)**, **(15), (17)**, **(18)** and **(19)** CHN results are in agreement with the values calculated on the basis of the crystallographically determined formula. However, some discrepancies are observed for **(13)**, **(14)**, **(16)** and **(20)**, which might be associated to the presence of impurities in the sample.

Table 5.6. CHN analysis for compounds **(12)-(20)**

Compound	Actual (%)			Theoretical (%)		
	C	H	N	C	H	N
(12)	6.9	2.9	8.1	7.2	3.0	8.1
(13)	10.6	3.7	8.1	9.5	3.1	7.4
(14)	7.5	3.2	8.4	8.7	3.4	10.1
(15)	9.3	3.9	9.9	8.5	3.4	9.9
(16)	11.0	4.7	11.8	8.5	3.4	9.9
(17)	6.4	3.1	7.5	6.3	3.0	7.4
(18)	6.4	3.1	7.5	6.4	3.1	7.5
(19)	3.2	1.2	3.6	3.1	1.3	3.6
(20)	8.5	2.4	5.0	9.7	2.5	5.6

Powder X-ray diffraction data for $[La(SO_4)_3](enH_2)_{1.5}$ **(12)**, $[Dy_2(SO_4)_6(H_2O)](trienH_4)_{1.5}$ **(13)**, $[Ln_2(SO_4)_6(enH)_2](enH_2)_2$ (Ln=Pr, Eu, Gd) **(14)-(16)**, $[Ln_2(SO_4)_6(H_2O)_2](enH_2)_3$ (Ln=Er, Dy) **(17)-(18)**, $[Dy(SO_4)_2](enH_2)_{0.5}$ **(19)** and $[Sm_4(SO_4)_{10}(H_2O)_4](pipH_2)_4$, **(20)** were collected over the range $4 \leq 2\theta\ /° \leq 50$ on a ground portion of bulk sample. Lattice parameters were refined using TOPAS program [288] (Appendix A).

For **(12)** the powder X-ray diffraction pattern indicates the presence of $La(SO_4)_3(enH_2)_{1.5}$ **(12)** and unreacted $La_2(SO_4)_3$. The peaks can be indexed on the basis of

the trigonal unit cell determined for the lanthanum sulphate from the single-crystal X-ray diffraction data.

Powder X-ray diffraction data of **(13)** indicates the presence of $[Dy_2(SO_4)_6(H_2O)](trienH_4)_{1.5}$ as the majority phase. The peak at 22° could not be identified. The peaks can be indexed on the basis of the triclinic unit cell determined for **(13)** from the single-crystal X-ray diffraction data.

Powder X-ray diffraction data for **(14)-(16)** reveals the presence of $[Ln_2(SO_4)_6(enH)_2](enH_2)_2$ (Ln=Pr, Eu, Gd). PXRD pattern for **(14)** shows it is a single phase. However, for **(15)-(16)** the powder X-ray diffraction pattern indicates the presence in the bulk sample of impurities of $Eu_2(SO_4)_3(H_2O)_4$ in **(15)** and $Gd_2(SO_4)_3(H_2O)_8$ and an unknown phase in **(16)**. The peaks were indexed on the basis of the orthorhombic unit cell determined for $[Ln_2(SO_4)_6(enH)_2](enH_2)_2$ (Ln=Pr, Eu, Gd) from the single-crystal X-ray diffraction study.

For **(17)**, powder X-ray diffraction data reveal the presence of $[Er_2(SO_4)_6(H_2O)_2](enH_2)_3$ **(17)** as a single-phase and the peaks were indexed on the basis of an orthorhombic unit cell determined for $[Er_2(SO_4)_6(H_2O)_2](enH_2)_3$ **(17)** from the single-crystal X-ray diffraction study. However, powder X-ray diffraction data indicate that the dysprosium-containing phase **(18)** consists of a mixture of phases that were identified as $[Dy_2(SO_4)_6(H_2O)_2](enH_2)_3$ **(18)**, as the majority phase, and ethylenediammonium sulphate. Refined lattice parameters for **(18)** on the basis of the orthorhombic unit determined from the single-crystal X-ray diffraction data are listed in Appendix A.

The powder diffraction pattern of **(19)** indicates the presence of a mixture of phases that were identified to be $[Dy(SO_4)_2](enH_2)_{0.5}$ **(19)** and $Dy_2(SO_4)_3(H_2O)_4$. Peaks at low angles could not be indexed to any phase and this might be due to the formation of an organic crystalline phase. Peaks belonging to **(19)** were indexed on the basis of the triclinic unit cell determined for $[Dy(SO_4)_2](enH_2)_{0.5}$ from single-crystal X-ray diffraction data and the lattice parameters were refined using TOPAS program [288].

The powder X-ray diffraction pattern for **(20)** indicates the presence of $[Sm_4(SO_4)_{10}(H_2O)_4](pipH_2)_4$ **(20)** and an unidentified phase. The peaks could be indexed on the basis of the monoclinic unit cell calculated for the samarium sulphate from the single-crystal X-ray diffraction study.

Thermogravimetric analysis data for $[La(SO_4)_3](enH_2)_{1.5}$ **(12)**, $[Dy_2(SO_4)_6(H_2O)](trienH_4)_{1.5}$ **(13)**, $[Ln_2(SO_4)_6(enH)_2](enH_2)_2$ (Ln=Pr, Eu, Gd) **(14)-(16)**, $[Ln_2(SO_4)_6(H_2O)_2](enH_2)_3$ (Ln=Er, Dy) **(17)-(18)**, $[Dy(SO_4)_2](enH_2)_{0.5}$ **(19)** and $[Sm_4(SO_4)_{10}(H_2O)_4](pipH_2)_4$, **(20)** were collected under nitrogen on hand-picked crystals.

For $La(SO_4)_3(enH_2)_{1.5}$ **(12)** the decomposition process occurs in three steps with a total weight loss of 52.4 % (calc: 53.23 %), which is consistent with the formation of $La_2O_2(SO_4)$ as a final product, as identified by powder X-ray diffraction (Figure 5.1(a)). The first weight loss of 8.204 % (calc: 9.0 %) can be attributed to the removal of ½ mol of ethylenediamine, ½ mol of water and ¼ mol of O_2. In the second step, the remaining mol of ethylenediamine together with water and ½ mol of O_2 are removed, with a weight loss of 19.01 % (calc: 16.55 %). The last weight loss of 25.19 % (calc: 27.7 %) at 570 °C is consistent with the extraction of two moles of SO_2 and ½ O_2 to form $La_2O_2(SO_4)$.

The thermal decomposition process for $[Dy_2(SO_4)_6(H_2O)](trienH_4)_{1.5}$ **(13)** (Figure 5.1(b)) takes place in two steps, in which $Dy_2O_2(SO_4)$ has been identified as the final product by powder X-ray diffraction. The total weight loss is 63.95 %, which is consistent with the calculated 60.67 %. The first step at 280 °C (exp: 27.52 %; calc: 28.5 %) can be assigned to the removal of 1.5 moles of triethylenetetramine, four moles of water and O_2. The second weight loss of 36.43 % (calc: 32.17 %) at approximately 550 °C corresponds to the removal of five moles of SO_2 and 3/2 of O_2, which is in good agreement with the formation of $Dy_2O_2(SO_4)$.

The weight losses observed during thermogravimetric analysis for $[Pr_2(SO_4)_6(enH)_2](enH_2)_2$ **(14)** and (b) $[Eu_2(SO_4)_6(enH)_2](enH_2)_2$ **(15)** are shown in Figure 5.2. For **(14)** (Figure 5.2(a) the process takes place in three steps, with a total weight loss of 60.23 %, consistent with the expected 63.01 % in the formation of $Pr_2O_2(SO_4)$ as final product, identified by powder X-ray diffraction. The first and second steps of 25.91 % (calc: 25.8 %) and 28.25 % (calc: 31.4%) respectively occur consecutively and are consistent with the removal of two moles of ethylenediamine, two moles of water and two moles of SO_2 in the first step and two moles of ethylenediamine, two moles of SO_2, water and 5/2 of O_2 in the second step. The last step of 6.07 % (calc: 5.81 %) corresponds to the extraction of SO_2 yielding $Pr_2O_2(SO_4)$ as the final product. For **(15)** the weight loss occurs in two steps (Figure 5.2(b)). The first step of 57.1 % (calc: 53.13 %) can be attributed to the removal of four moles of ethylenediamine, four moles of SO_2, three moles of water and 3/2 of O_2 and the second step (exp: 9.18 %; calc: 8.53 %) to the removal of one mole of SO_2

and O_2. This is consistent with the formation of $Eu_2O_2(SO_4)$, which corresponds to a total weight loss of 66.27 % (calc: 61.7 %). Thermogravimetric data for $[Gd_2(SO_4)_6(enH)_2](enH_2)_2$ **(16)** could not be analysed since the phase consisted of a mixture of crystals, as suggested by elemental analysis, containing $Gd_2(SO_4)_3(H_2O)_8$ and an unknown phase together with $[Gd_2(SO_4)_6(enH)_2](enH_2)_2$ **(16)**.

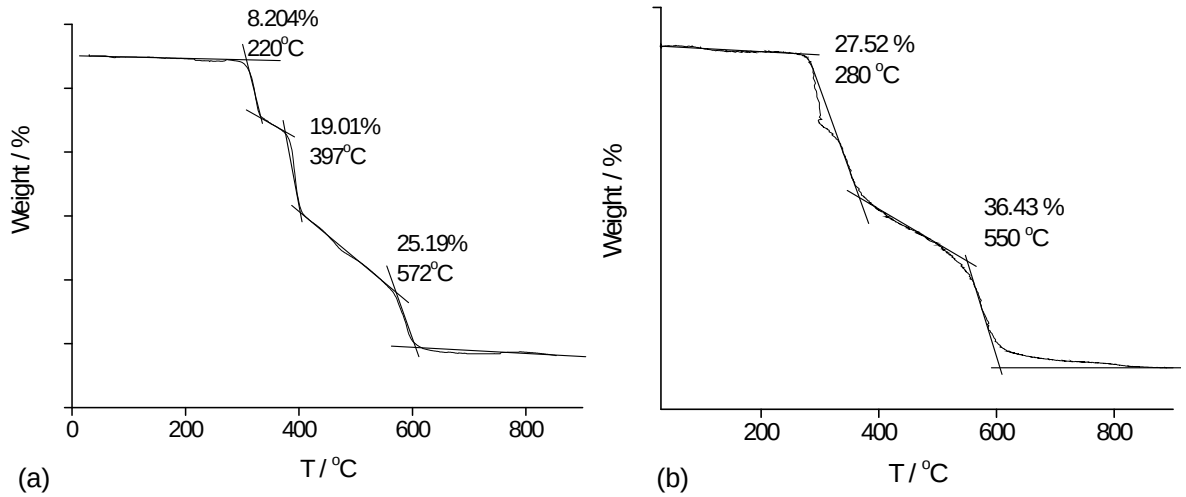

Figure 5.1. Thermogravimetric analysis data for (a) $La(SO_4)_3(enH_2)_{1.5}$ **(12)** and (b) $[Dy_2(SO_4)_6(H_2O)](trienH_4)_{1.5}$ **(13)**

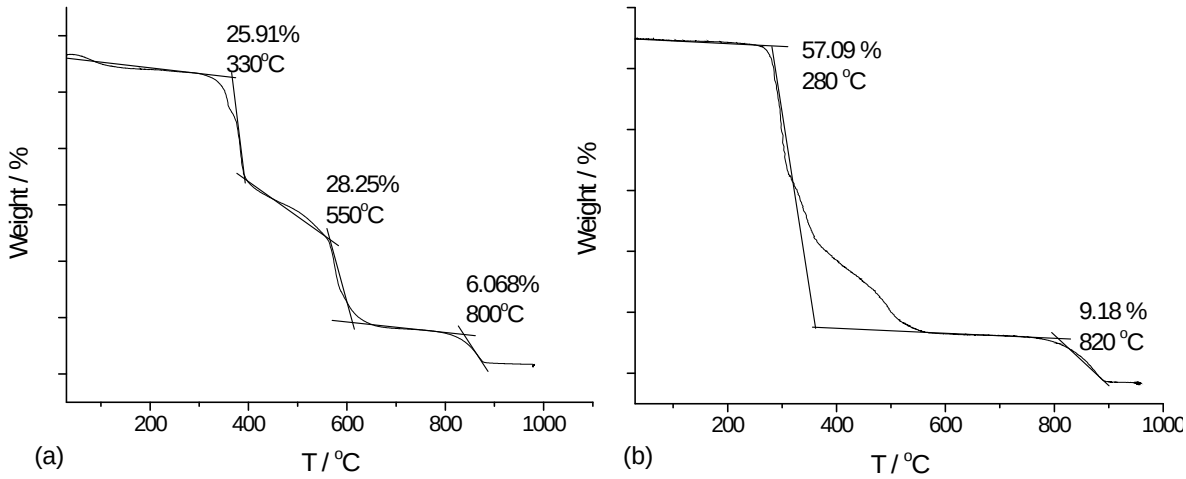

Figure 5.2. Thermogravimetric analysis data for (a) $[Pr_2(SO_4)_6(enH)_2](enH_2)_2$ **(14)** and (b) $[Eu_2(SO_4)_6(enH)_2](enH_2)_2$ **(15)**

Both $[Ln_2(SO_4)_6(H_2O)_2](enH_2)_3$ (Ln=Er, Dy) **(17)-(18)** display the same weight loss profile (Figure 5.3). It takes place in three different steps. The first and second weight

losses at 280 °C and 400 °C respectively occur consecutively and are consistent with the loss of three moles of ethylenediamine, five moles of SO_2, five moles of water and three moles of O_2 (**(17)**: exp: 63 %; calc: 60.6 %; **(18)**: exp: 58.61 %; calc: 61.1 %). The third weight loss can be assigned to the removal of SO_2 and correspond to the formation of Er_2O_3 for **(17)** and Dy_2O_3 for **(18)**, as identified by powder X-ray diffraction. For **(17)** the experimental total weight loss of 69.3 % is consistent with the calculacted value (66.3 %). Similarly, for **(18)** the total weight loss (64.4 %) is also in good agreement with the expected value of 66.8 %.

Thermogravimetric analysis data for $[Dy(SO_4)_2](enH_2)_{0.5}$ **(19)** are shown in Figure 5.4(a). The weight losses occur in four steps which are consistent with the formation of a mixture of phases as final products, Dy_2O_3 and $Dy_2O_2(SO_4)$, which were identified by powder X-ray diffraction. Assuming that of ¼ $Dy_2O_2(SO_4)$ and ¾ of Dy_2O_3 are formed, the calculated weight loss would be 49.1 %, which is in excellent agreement with the experimental value (49.55 %). The first three weight losses (exp: 36.35 %; calc: 37.1 %) are consistent with the removal of half a mole of ethylenediamine, one mol of SO_2, half a mol of water and 5/4 of O_2. The last weight loss of 12.3 % (calc: 12.45 %) can be assigned to the removal of ¾ of SO_2, yielding the formation of Dy_2O_3 and $Dy_2O_2(SO_4)$.

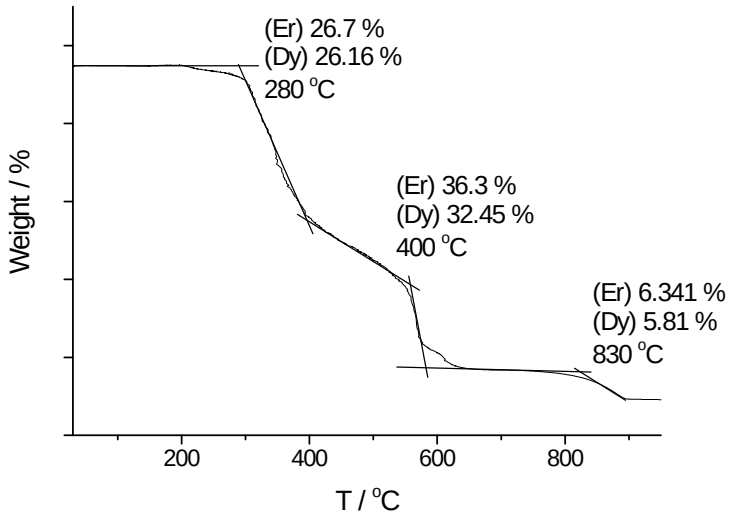

Figure 5.3. Thermogravimetric analysis data for $[Ln_2(SO_4)_6(H_2O)_2](enH_2)_3$ (Ln=Er, Dy) **(17)-(18)**

The thermal decomposition process for $[Sm_4(SO_4)_{10}(H_2O)_4](pipH_2)_4$ **(20)** (Figure 5.4(b)) occurs in three steps with a total weight loss of 53.5 %, which correspond to the formation of $Sm_2O_2(SO_4)$ as final product, identified by powder X-ray diffraction, and that

is consistent with the calculated value of 52.8 %. The first step of 19.68 % (calc: 18.75 %) at 330 °C corresponds to the elimination of two moles of piperazine, four moles of water, two moles of SO_2 and two moles of O_2. In the second step at 560 °C (exp: 29.31 %; calc: 30.2 %), another two moles of piperazine are removed together with three moles of SO_2, four moles of water and five moles of O_2. The last weight loss of 4.46 % (calc: 4.03 %) at 788 °C, is consistent with the formation of two moles of $Sm_2O_2(SO_4)$ and corresponds to the removal of SO_2 and ½ of O_2.

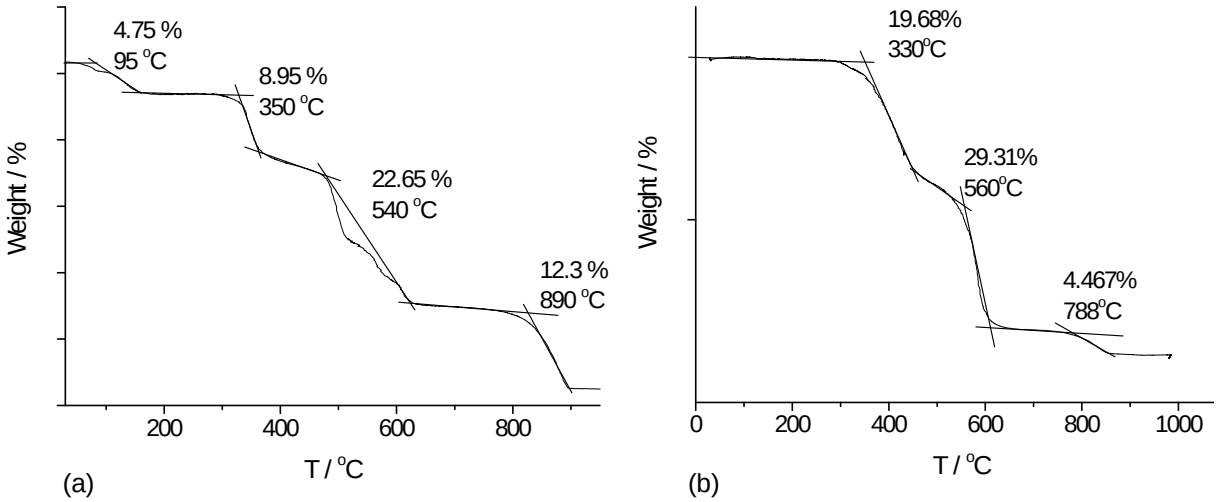

Figure 5.4. Thermogravimetric analysis data for (a) $[Dy(SO_4)_2](enH_2)_{0.5}$ **(19)** and (b) $[Sm_4(SO_4)_{10}(H_2O)_4](pipH_2)_4$ **(20)**.

Infrared spectroscopy for $La(SO_4)_3(enH_2)_{0.5}$ **(12)**, $[Ln_2(SO_4)_6(enH)_2](enH_2)_2$ (Ln=Pr, Eu, Gd) **(14)-(16)**, $[Ln_2(SO_4)_6(H_2O)_2](enH_2)_3$ (Ln=Er, Dy) **(17)-(18)** and $[Dy(SO_4)_2](enH_2)_{0.5}$ **(19)** (Figure 5.5) shows the presence of vibrations at 1090 and 612 cm^{-1} that can be assigned to the asymmetric stretching and asymmetric deformation of S-O vibrations, respectively. Vibrations appearing between 3570-2900 cm^{-1} are characteristic of N-H stretches and those around 1600 cm^{-1} of H-N-H bending modes, supporting the presence of ethylenediamine. The vibrations at 830 cm^{-1} can also be attributed to the amine and are associated with C-H bending along the aliphatic chain.

Infrared spectroscopic data were also used to support the formation of $[Dy_2(SO_4)_6(H_2O)](trienH_4)_{1.5}$ **(13)** and $[Sm_4(SO_4)_{10}(H_2O)_4](pipH_2)_4$ **(20)**. For **(13)** (Figure 5.6) vibrations at 3477 cm^{-1} and 1623 cm^{-1} are attributed to the N-H stretching and H-N-H bending correspondingly. Those bands appearing at 1099, 620 and 502 cm^{-1} can be

assigned to asymmetric stretching and asymmetric and symmetric deformation of S-O vibrations, respectively associated with SO_4^{2-} anion. The band at 803 cm^{-1} is due to C-H vibrations along the aliphatic chain of the amine. For **(20)** (Figure 5.7) the vibrations at 3415, 3178, 2123, 1602 and 1452 cm^{-1} are associated with the presence of the piperazine and correspond to the N-H stretching and H-N-H bending modes. The vibration at 865 cm^{-1} is also attributed to the amine and is due to the C-C stretching. Bands at 1156, 1083 and 691 cm^{-1} can be assigned to the asymmetric and symmetric stretching and asymmetric deformation of S-O due to the existence of the sulphate anion.

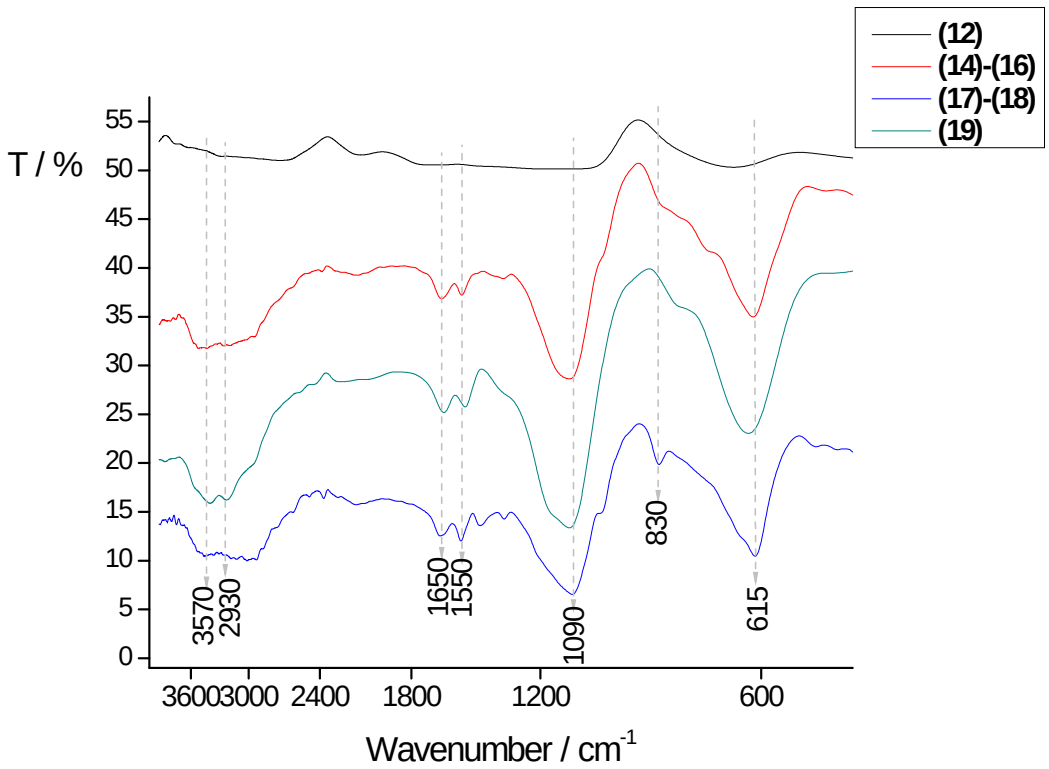

Figure 5.5. Infrared data for $La(SO_4)_3(enH_2)_{0.5}$ **(12)** (black), $[Ln_2(SO_4)_6(enH)_2](enH_2)_2$ (Ln=Pr, Eu, Gd) **(14)-(16)** (red), $[Ln_2(SO_4)_6(H_2O)_2](enH_2)_3$ (Ln=Er, Dy) **(17)-(18)** (blue) and $[Dy(SO_4)_2](enH_2)_{0.5}$ **(19)** (green).

UV/Vis diffuse reflectance studies for the materials containing the ion Dy^{3+} $[Dy_2(SO_4)_6(H_2O)](trienH_4)_{1.5}$ **(13),** $[Dy_2(SO_4)_6(H_2O)_2](enH_2)_3$ **(18)** and $[Dy(SO_4)_2](enH_2)_{0.5}$ **(19)** were performed (Figure 5.8). A set of bands originating in the $^4F_{9/2}$ level appear in the region between 400-500 nm. They may be associated to the transitions $^4F_{9/2} \rightarrow {}^6H_{15/2}$ and $^4F_{9/2} \rightarrow {}^6H_{13/2}$. Bands in the region 300-400 nm are associated to the transition $^6H_{15/2} \rightarrow$

$^6P_{3/2}$, whereas those below 300 nm are attributed to the host absorption. Those bands appearing near the IR region can be assigned to the $^4F_{9/2} \rightarrow {}^6H_{3/2}$ transition [353, 354].

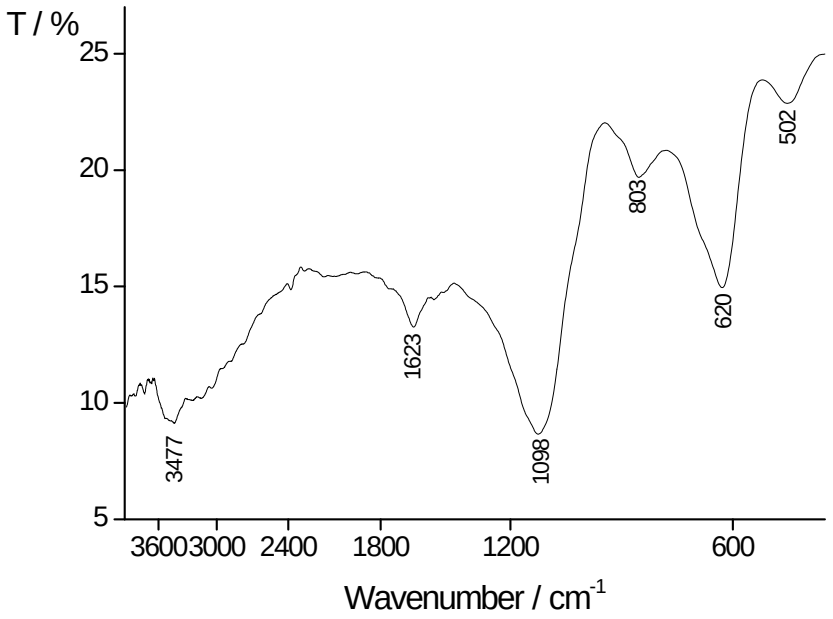

Figure 5.6. Infrared spectroscopic data for $[Dy_2(SO_4)_6(H_2O)](trienH_4)_{1.5}$ **(13)**

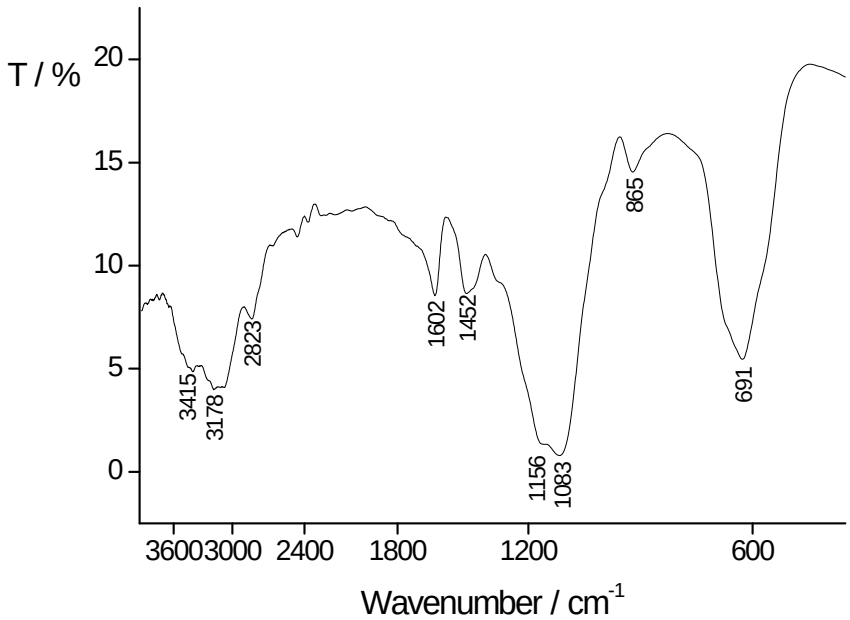

Figure 5.7. Infrared spectroscopic data $[Sm_4(SO_4)_{10}(H_2O)_4](pipH_2)_4$ **(20)**.

UV/Vis diffuse reflectance studies were also performed for the three isostructural $[Ln_2(SO_4)_6(enH)_2](enH_2)_2$ (Ln=Pr, Eu, Gd) **(14)-(16)** materials, but only absorption bands were observed for the $[Pr_2(SO_4)_6(enH)_2](enH_2)_2$ **(14)** phase. These correspond to the f-f transitions of Pr^{3+} (f^2), and they are very sharp (Figure 5.9). The absorption bands at 445,

471, 484 and 592 nm can be assigned to the $^3H_4 \rightarrow {}^3P_2$, $^3H_4 \rightarrow {}^3P_1$, $^3H_4 \rightarrow {}^3P_0$ and $^3H_4 \rightarrow {}^1D_2$ transitions [355].

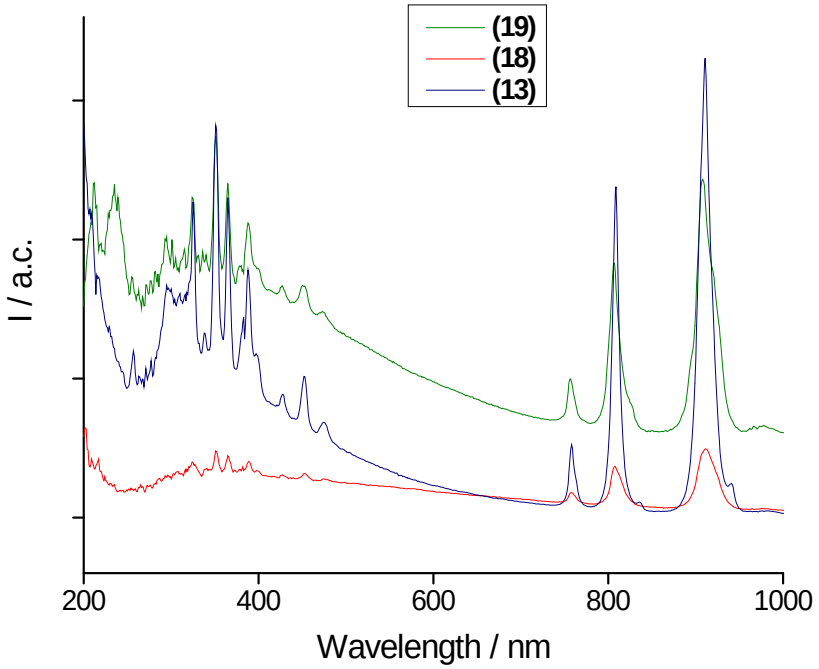

Figure 5.8. UV/Vis spectrum of $[Dy_2(SO_4)_6(H_2O)](trienH_4)_{1.5}$ **(13)**, $[Dy_2(SO_4)_6(H_2O)_2](enH_2)_3$ **(18)** and $[Dy(SO_4)_2](enH_2)_{0.5}$ **(19)**.

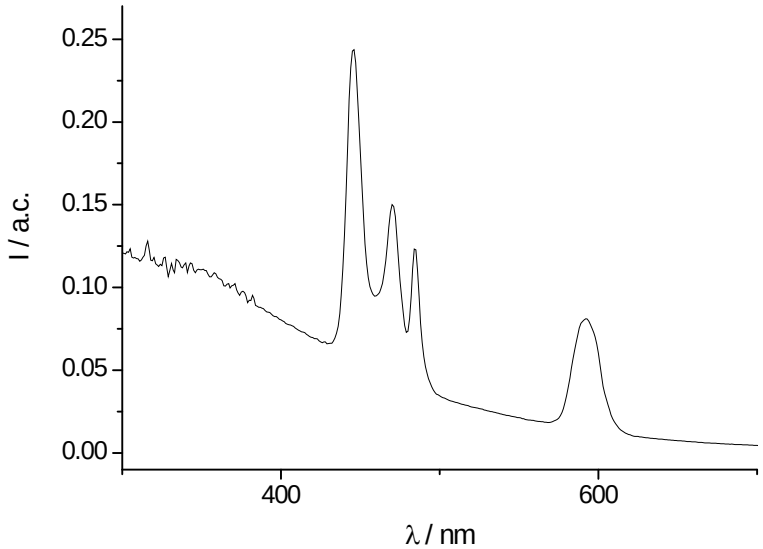

Figure 5.9. UV/Vis spectrum of $[Pr_2(SO_4)_6(enH)_2](enH_2)_2$ **(14)**.

For $[Er_2(SO_4)_6(H_2O)_2](enH_2)_3$ **(6)** the spectrum shows a number of absorption lines, most of them in the visible region that can be assigned to Er^{3+} states. The bands at 365-379 nm, 489 nm, 521 nm, 543 nm and 652 nm are associated to $^4I_{15/2} \rightarrow {}^4G_{11/2}$, $^4I_{15/2} \rightarrow {}^4F_{7/2}$,

$^4I_{15/2} \rightarrow {}^2H_{11/2}$, $^4I_{15/2} \rightarrow {}^4S_{3/2}$ and $^4F_{9/2}$ transitions, respectively [356]. (Figure 5.10). For $[Sm_4(SO_4)_{10}(H_2O)_4](pipH_2)_4$ **(20)** The bands appearing around 400 nm can be assigned to the transitions $^6H_{5/2} \rightarrow {}^4D_{3/2}$, $^6H_{5/2} \rightarrow {}^4D_{1/2}$, $^6H_{5/2} \rightarrow {}^4L_{13/2}$, $^6H_{5/2} \rightarrow {}^4G_{9/2}$ and $^6H_{5/2} \rightarrow {}^4I_{13/2}$, whereas those bands at 950 nm and 1100 nm correspond to the transitions $^6H_{5/2} \rightarrow {}^6F_{11/2}$ and $^6H_{5/2} \rightarrow {}^6F_{9/2}$, respectively [357] (Figure 5.11).

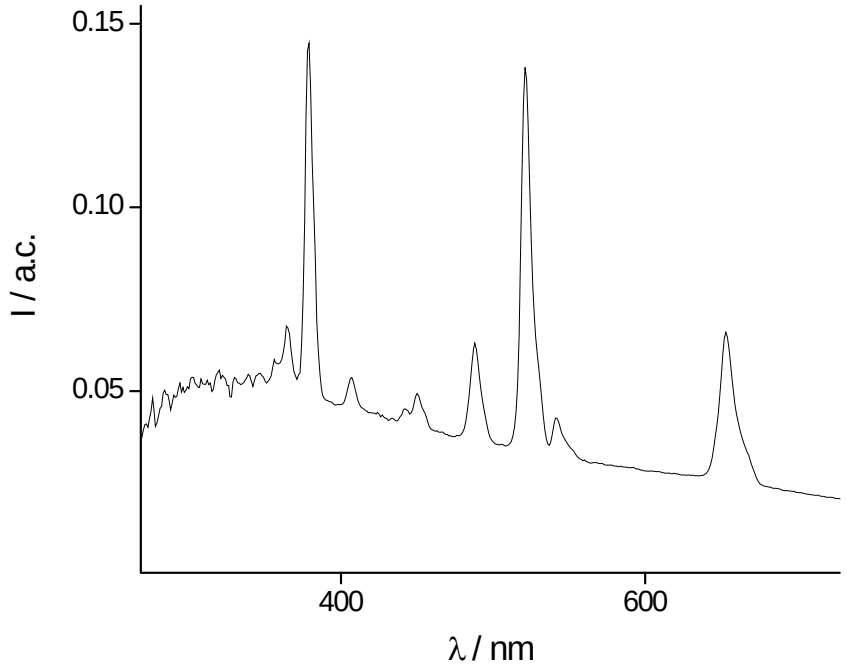

Figure 5.10. UV/Vis spectrum for $[Er_2(SO_4)_6(H_2O)_2](enH_2)_3$ **(17)**.

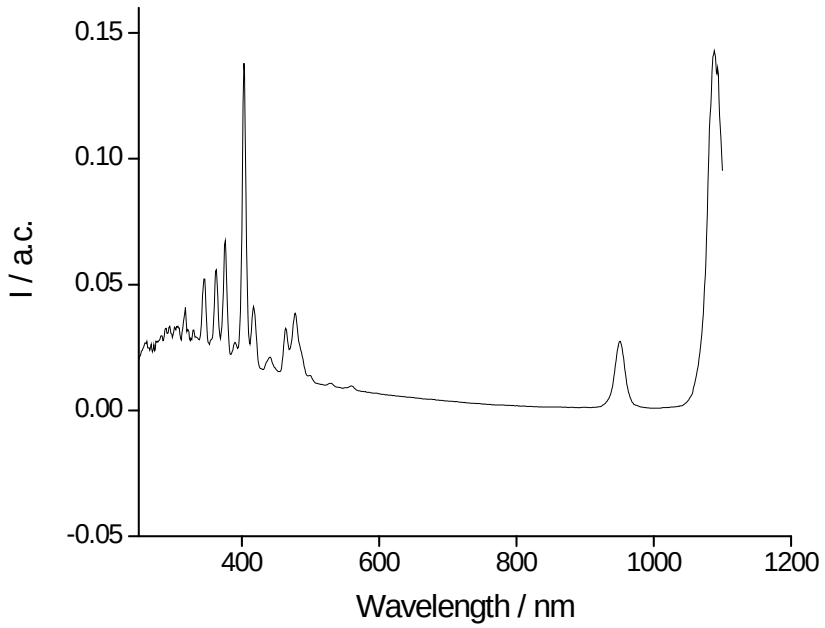

Figure 5.11. UV/Vis spectrum of $[Sm_4(SO_4)_{10}(H_2O)_4](pipH_2)_4$ **(20)**.

5.3 The rare-earth sulphate $[La(SO_4)_3](enH_2)_{1.5}$

5.3.1 Crystal structure description

The local coordination scheme for $[La(SO_4)_3](enH_2)_{1.5}$ **(12)** is shown in Figure 5.12.

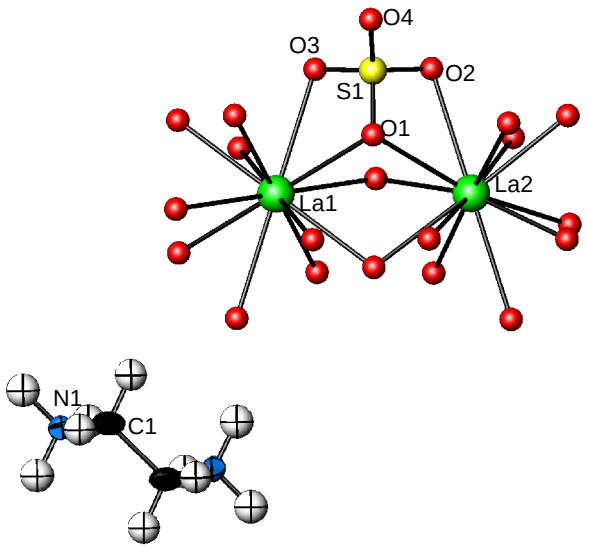

Figure 5.12. Atoms labelling scheme and thermal ellipsoids at 50% probability of $[La(SO_4)_3](enH_2)_{1.5}$ **(12)**.

In the asymmetric unit of $[La(SO_4)_3](enH_2)_{1.5}$ **(12)**, there are two crystallographically distinct lanthanum ions occupying special positions, which are 12-coordinated by oxygen atoms, all of them belonging to sulphate groups (Figure 5.13(a)). The average La-O bond lengths are d(La(1)-O)=2.7021 Å and d(La(2)-O)=2.7059 Å, which are in good agreement with those previously reported [358]. Sulphur-oxygen distances range from 1.4552(13) Å to 1.5041(12) Å. This difference in bond lengths is related to the presence of three different types of oxygen atoms in the structure. O(1) is in a three coordination fashion with two La ions and one sulphur with a longest distance S-O(1)= 1.5041(12) Å forming three-membered rings, whereas the shortest distance is associated to the terminal O(4). Each lanthanum ion is surrounded by six sulphate anions in a bidentate mode. The oxygen atoms arrangement around the La centre is depicted in Figure 5.13(a). Infinite $[La(SO_4)_3]^{3-}$ chains are formed by linking of LaO_{12} and SO_4 tetrahedra (Figure 5.13(b)).

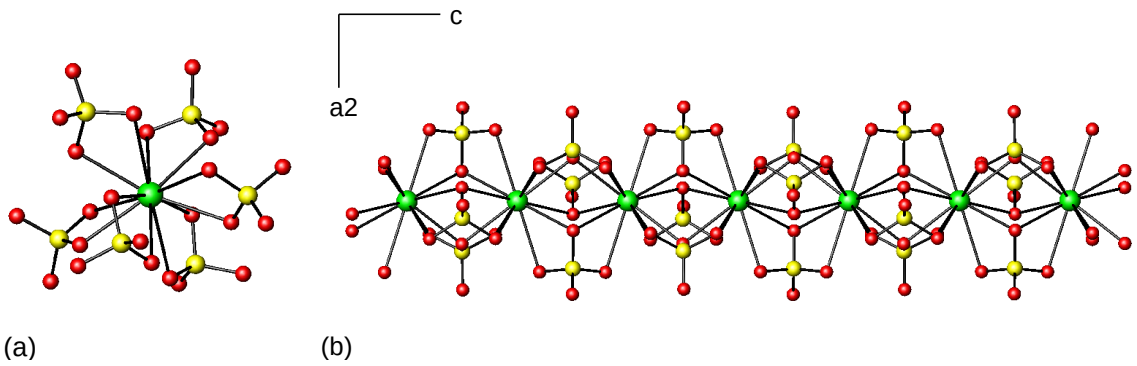

Figure 5.13. (a) Lanthanum centre enviroment in $[La(SO_4)_3](enH_2)_{1.5}$ **(12)**; (b) One-dimensional $[La(SO_4)_3]^{3-}$ in $[La(SO_4)_3](enH_2)_{1.5}$ along the *a*-axis (La centre, green; S atoms, yellow; O atoms; red).

LaO_{12} polyhedra are linked by sharing faces forming a one-dimensional chain, to which SO_4 tetrahedra are connected *via* edge-sharing (Figure 5.14). Two consecutive La(1) and La(2) lanthanum ions are connected by sharing three common sulphate groups in which three O(1) atoms are linked to La(1), La(2) and S belonging to the corresponding sulphate anion. The linkage is completed by each SO_4 tetrahedron sharing one of its oxygen atoms with La(1) and another one with La(2). The ethylenediamine cations occupy the inter-chain space and they interact with the $[La(SO_4)_3]^{3-}$ inorganic chains through hydrogen bonding (Appendix D).

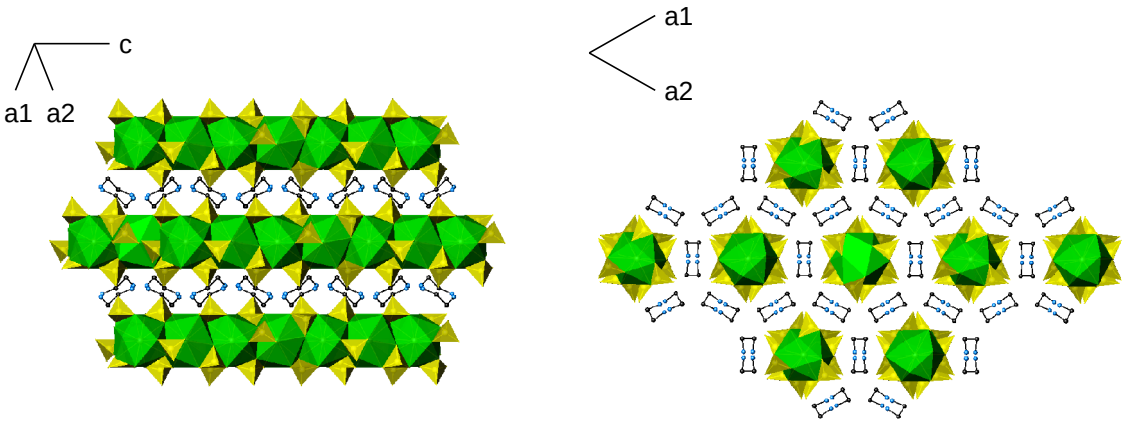

Figure 5.14. Two different polyhedral representations of the structure of $[La(SO_4)_3](enH_2)_{1.5}$ **(12)** (a) along *a*-axis; (b) along *c*-axis (LaO_{12} polyhedra, green; SO_4 tetrahedra, yellow; C, black; N, blue).

5.4 From chains to layers: $[Dy_2(SO_4)_6(H_2O)](trienH_4)_{1.5}$ ribbons

5.4.1 Crystal structure description

The asymmetric unit of $[Dy_2(SO_4)_6(H_2O)](trienH_4)_{1.5}$ **(13)** contains two crystallographically distinct dysprosium atoms each of which is nine-coordinated. The local coordination scheme for $[Dy_2(SO_4)_6(H_2O)](trienH_4)_{1.5}$ **(13)** is shown in Figure 5.15.

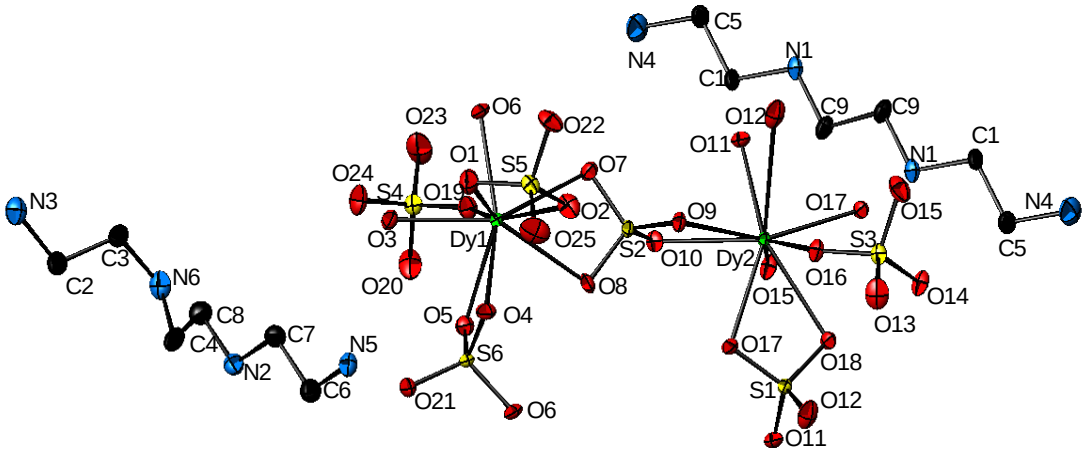

Figure 5.15. Atoms labelling scheme and thermal ellipsoids at 50% probability for $[Dy_2(SO_4)_6(H_2O)](trienH_4)_{1.5}$ **(13)**. Hydrogen atoms have been omitted for clarity.

Dy(1) is connected to three sulphate groups in a bidentate fashion, to two sulphate anions in a monodentate fashion and to one oxygen atom of a molecule of water. Dy(2) is coordinated to two sulphate groups in a bidentate mode, to three sulphate anions in a monodentate fashion and to two water molecules. The average Dy-O distances are consistent with those reported for the dysprosium sulphate hydrate, $Dy_2(SO_4)_3(H_2O)_8$ [359] and they exhibit similar values for each of the two distinct metal centres, d[Dy(1)-O]=2.434 Å and d[Dy(2)-O]=2.418 Å. Sulphur-oxygen distances range from 1.429(12) Å to 1.534(10) Å, which is in good agreement with average reported values for S-O bonds in materials containing the oxy-anion of sulphur.

As it has been described earlier for the one-dimensional structure of $[La(SO_4)_3](enH_2)_{1.5}$ **(12)** (*Section 5.3*), three different types of oxygen atoms are present in the structure of $[Dy_2(SO_4)_6(H_2O)](trienH_4)_{1.5}$ **(13)**. Each $Dy(1)O_9$ is linked to one $Dy(2)O_9$ *via* a bridging sulphate tetrahedron, which is bidentate to both metal centres sharing one edge with each of them. As a result, a dimer is formed that is the basic building block of

this structure (Figure 5.15). Two adjacent building units are directly connected by edge-sharing $Dy(1)O_9$ polyhedra *via* two three-coordinated oxygen atoms which belong to different sulphate tetrahedra. The connectivity between the two adjacent Dy(1) centres is completed by two further sulphate tetrahedra sharing one oxygen atom with each dysprosium centre *via* vertex-linking. The linkage between two adjacent building blocks along the *c*-axis results in the chain that is shown in Figure 5.16(a). Neighbouring chains are linked together along the *a*-axis through edge- and vertex-sharing SO_4 tetrahedra producing a ribbon (Figure 5.16(b)). The structure of the ribbon can be visualised as being made up of two different types of chains: chains formed by the connectivity of Dy(1) centres (double chain that constitute the central part of the ribbon) and those obtained by the linkage of Dy(2) centres (side chains) (Figure 5.17).

The chains on the sides are constructed from $Dy(2)O_9$ polyhedra joined by SO_4 tetrahedra through edge and vertex sharing (Figure 5.17(b)). The central double chain is built up from the connection of Dy(1) centres. Two Dy(1) centres are linked together by edge-sharing along the *c*-axis to form a dimer. The distance between the two metal centres is approximately 3.92 Å. Adjacent dimers are fused together along the *a*-axis forming a double chain *via* edge-sharing sulphate tetrahedra, resulting in the formation of four-membered rings. The connectivity is completed *via* vertex-linking SO_4 tetrahedra. The central double chain is linked by edge-sharing SO_4 tetrahedra to the single chains formed by $Dy(2)O_9$ polyhedra to produce eight-membered ring channels.

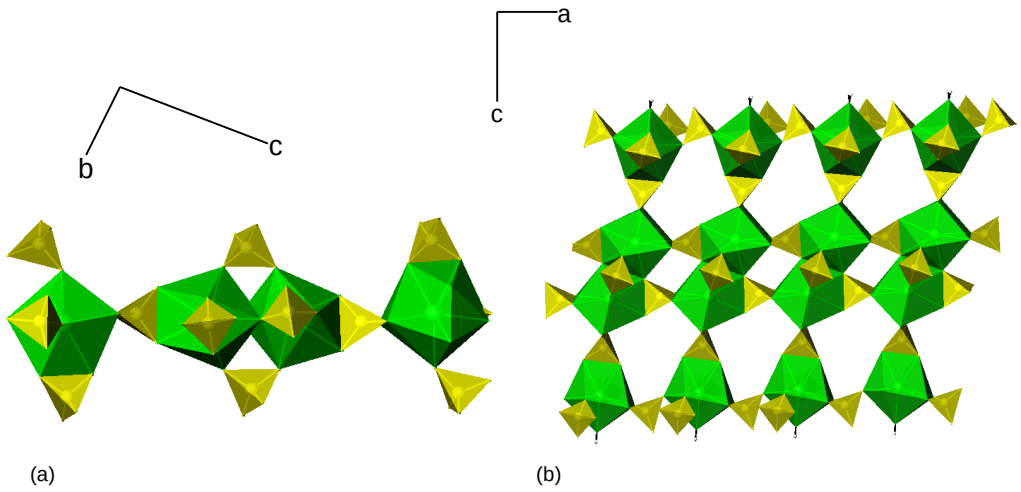

Figure 5.16. (a) Chain resulting of the connectivity between adjacent building unit in $[Dy_2(SO_4)_6(H_2O)](trienH_4)_{1.5}$ **(13)**; (b) View of the ribbon along the *a*-axis (DyO_9 polyhedra, green; SO_4 tetrahedra, yellow; H, white).

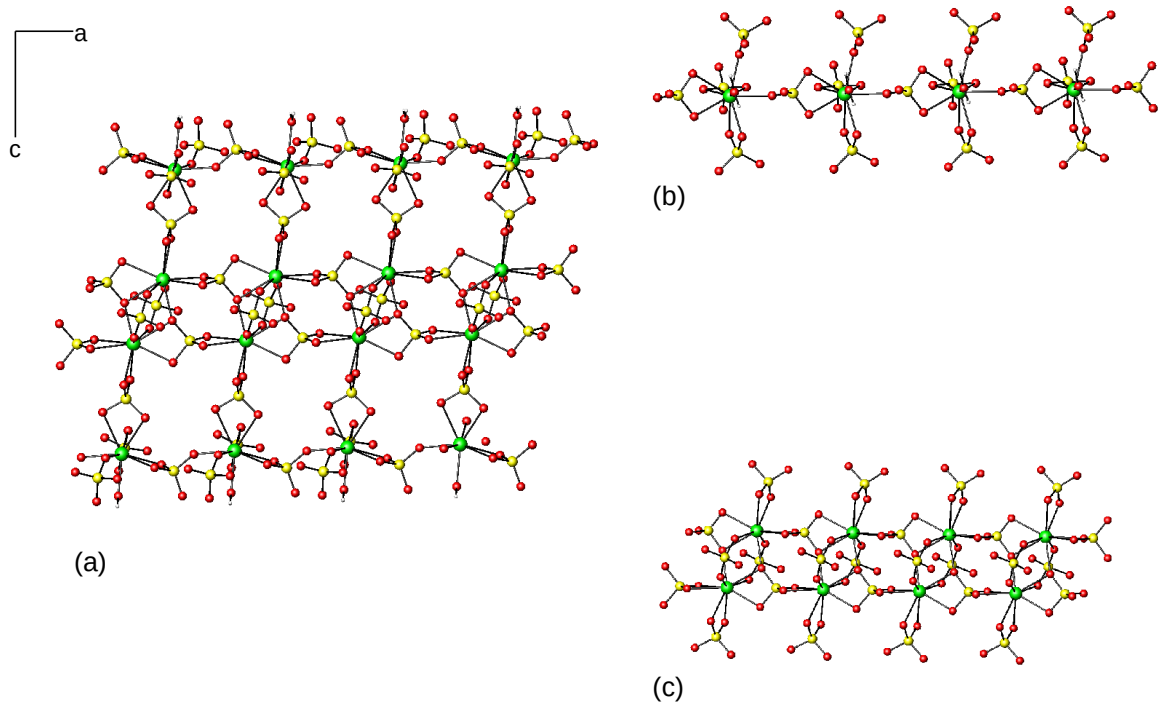

Figure 5.17. (a) Ball and stick representation of the ribbon in $[Dy_2(SO_4)_6(H_2O)](trienH_4)_{1.5}$ **(13)** (b) One-dimensional chain formed by Dy(2); (c) double chain built up from the connectivity between Dy(1) (Dy, green; S, yellow; O, red).

Ribbons are separated by tetraprotonated triethylenetetramine cations, which serve to balance the negative charge of the inorganic framework (Figure 5.18), and they are held together through hydrogen interactions involving N-H···O and O-H···O bond, the latter being due to the presence of terminal water molecules (Appendix D).

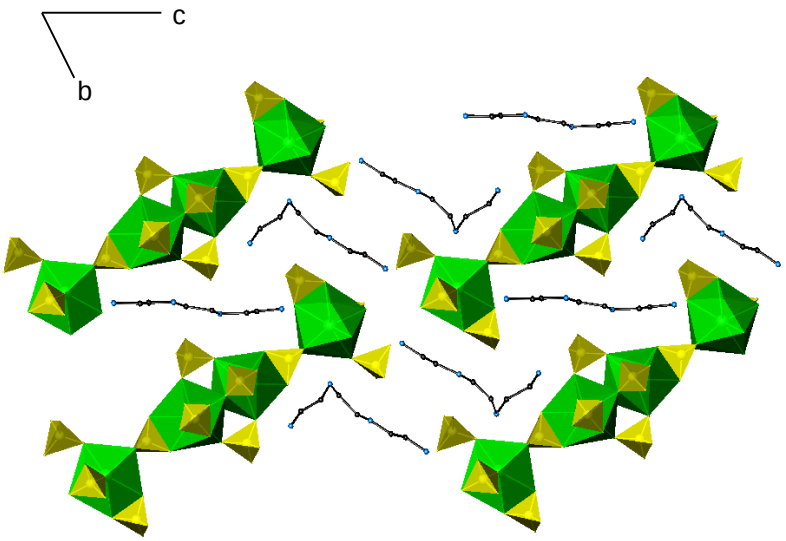

Figure 5.18. Structure of $[Dy_2(SO_4)_6(H_2O)](trienH_4)_{1.5}$ **(13)** in which ribbons are separated by amine cations (DyO_9 polyhedra, green; SO_4 tetrahedra, yellow; N, blue; C, black).

5.5 Layered structures of $[Ln_2(SO_4)_6(enH)_2](enH_2)_2$ (Ln=Pr, Eu, Gd), $[Ln_2(SO_4)_6(H_2O)_2](enH_2)_3$ (Ln=Er, Dy) and $[Dy_2(SO_4)_4](enH_2)$

5.5.1 $[Ln_2(SO_4)_6(enH_2)_2](enH_2)_2$ (Ln=Pr, Eu, Gd) (14)-(16)

5.5.1.1 Crystal structure description

The local coordination scheme for $[Ln_2(SO_4)_6(enH)_2](enH_2)_2$ (Ln=Pr, Eu, Gd) **(14)-(16)** is shown in Figure 5.19. The asymmetric unit of $[Ln_2(SO_4)_6(enH)_2](enH_2)_2$ (Ln=Pr, Eu, Gd) **(14)-(16)** contains two crystallographically distinct Ln atoms, each of them nine-coordinate to three sulphate tetrahedra in a bidentate mode, to one sulphate tetrahedron in a monodentate mode and to the amine through a Ln-N bond. In $[Pr_2(SO_4)_6(enH)_2](enH_2)_2$ **(14)**, the average Pr(1)-O and Pr(2)-O distances do not differ much from each other and take average values of 2.530 Å and 2.527 Å, respectively, which are comparable with those expected on the basis of the sum of their ionic radii and previously reported values in the literature [360, 361]. Pr(1)-N and Pr(2)-N distances are 2.612(12) Å to 2.630(12) Å respectively which is close to the Pr-N distances observed in PrN by Brown and co-workers [362]. Similarly, the average Eu(1)-O and Eu(2)-O and Gd(1)-O and Gd(2)-O distances are very close to each other with average values 2.474 Å and 2.483 Å for the europium analogue **(15)** and 2.475 Å and 2.462 Å for the gadolinium phase **(16)**. These bond distances are in good agreement with those previously reported for europium [359, 363] and gadolinium [364] sulphates. Ln-N distances (Eu(1)-N=2.533(11) Å, Eu(2)-N=2.553(10) Å, Gd(1)-N=2.538(7) Å and Gd(2)-N=2.522(7) Å) are similar to those in the corresponding nitride [365, 366]. Trends connected to the ionic radii of the metal centre are noticeable since Ln-O distances decrease on going from praseodymium to gadolinium as the number of the electrons in the *f* orbitals increases, owing to the lanthanide contraction. S-O bond lengths are consistent with the mean S-O distances reported for other sulphate materials.

In the structure of $[Ln_2(SO_4)_6(enH)_2](enH_2)_2$ (Ln=Pr, Eu, Gd) **(14)-(16)** adjacent Ln(1)-Ln(2) centres are connected by sharing one sulphate group ($S(1)O_4$ and $S(2)O_4$ for **(14)** and **(15)** and $S(1)O_4$ and $S(3)O_4$ for **(16)**) that is bonded to each metal centre in a bidentate fashion forming infinite zig-zag chains along the *a*-axis (Figure 5.20(a)). These chains connect with neighbouring chains along the *b*-axis *via* bridging SO_4 tetrahedra to build the layers.

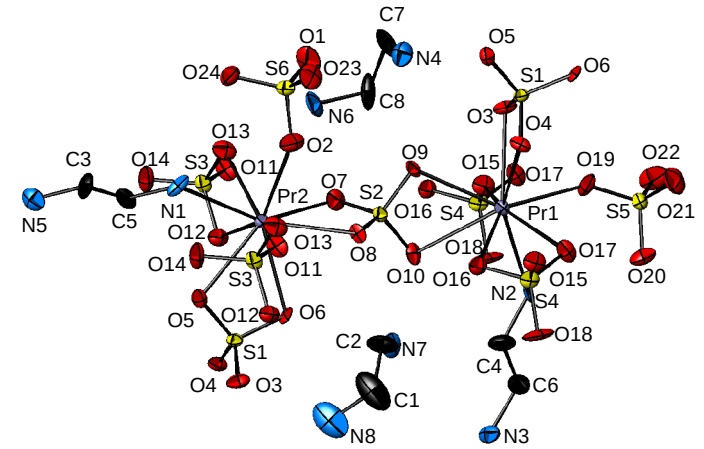

(a) $[Pr_2(SO_4)_6(enH)_2](enH_2)_2$

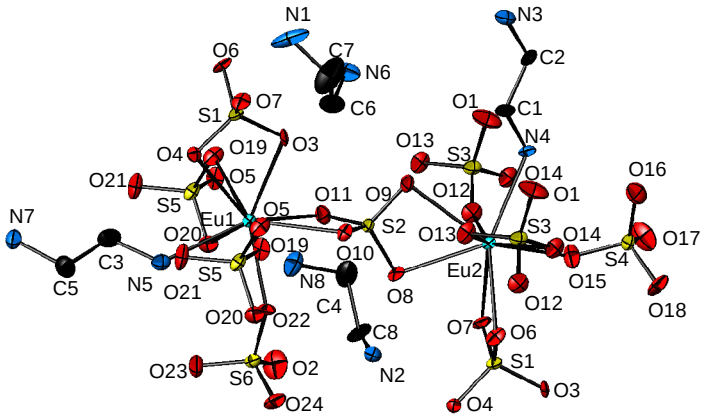

(b) $[Eu_2(SO_4)_6(enH)_2](enH_2)_2$

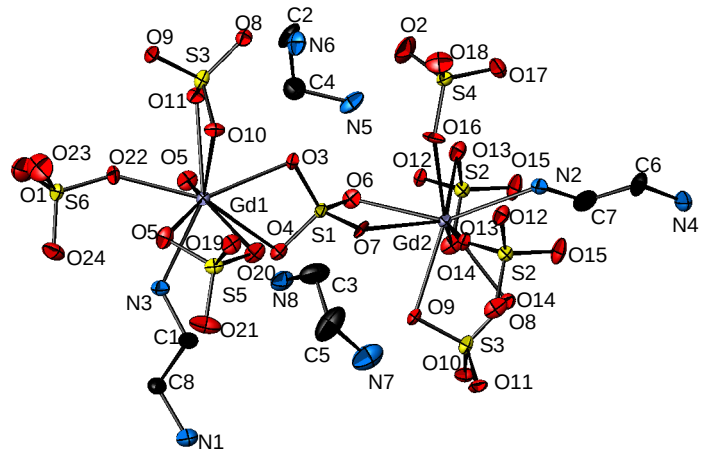

(c) $[Gd_2(SO_4)_6(enH)_2](enH_2)_2$

Figure 5.19. Atoms labelling scheme and thermal ellipsoids at 50% probability for (a) $[Pr_2(SO_4)_6(enH)_2](enH_2)_2$ **(14)**; (b) $[Eu_2(SO_4)_6(enH)_2](enH_2)_2$ **(15)**; and (c) $[Gd_2(SO_4)_6(enH)_2](enH_2)_2$ **(16)**.

Two sulphate groups are involved in the formation of the layer and connect Ln(1)-Ln(1) and Ln(2)-Ln(2) centres (Pr(1)-S(4)O_4-Pr(1); Pr(2)-S(3)O_4-Pr(2); Eu(1)-S(5)O_4-Eu(1); Eu(2)-S(3)O_4-Eu(2); Gd(1)-S(5)O_4-Gd(1); Gd(2)-S(2)O_4-Gd(2)). Sulphate tetrahedra that are coordinated to Ln centres in a bidentate mode connect the adjacent chain in a monodentate fashion sharing one vertex. Those coordinated to Ln centres in a monodentate fashion, connect in a bidentate mode through edge-sharing, giving rise to corrugated layers parallel to the *ab* plane, in which eight-membered rings (LnO_9-SO_4)$_4$ are formed (Figure 5.20(b)).

Protonated ethylenediamine cations directly coordinated to the metal centre together with the remaining sulphate tetrahedron that does not participate in the formation of the layer are projected out of the zig-zag layers pointing alternatively up or down. Diprotonated ethylenediamine cations occupy the space between the layers and alternate with the inorganic layer along the *b*-axis (Figure 5.21). The separation between the layers is *ca.* 9.46 Å, 9.47 Å and 9.46 Å for the praseodymium **(14)**, europium **(15)** and gadolinium **(16)** analogues, respectively. Cations and anions interact together *via* hydrogen bonding (Appendix D).

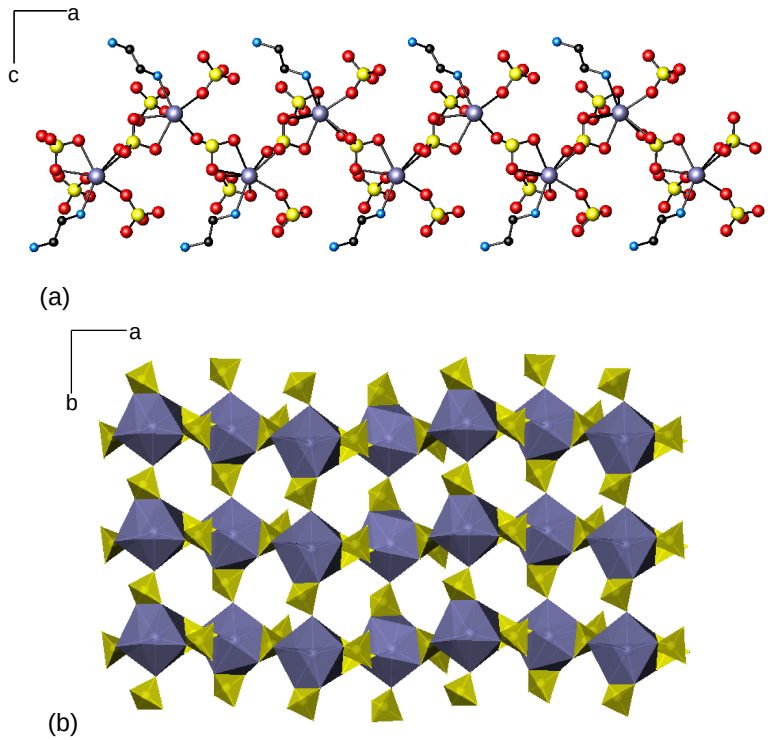

Figure 5.20. (a) Infinite zig-zag chains of [$Ln_2(SO_4)_6(enH)_2$](enH_2)$_2$ (Ln=Pr, Eu, Gd) **(14)-(16)**; (b) A corrugated layer of [$Ln_2(SO_4)_6(enH)_2$](enH_2)$_2$ (Ln=Pr, Eu, Gd) **(14)-(16)** (Ln; purple; S, yellow; O, red; N, blue; C, black).

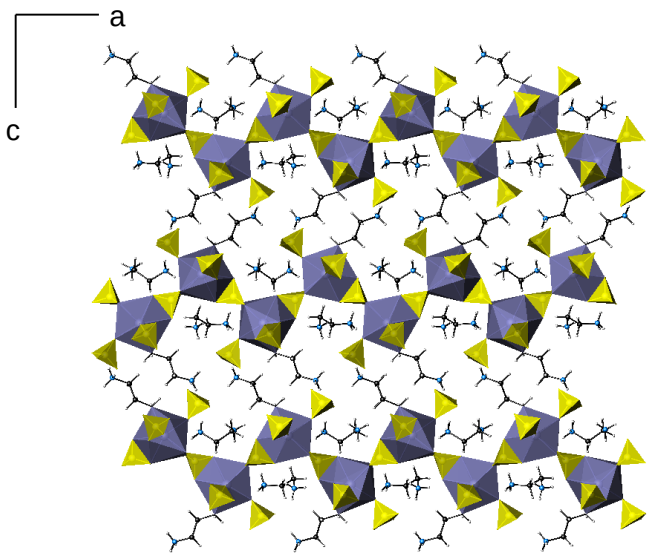

Figure 5.21. Polyhedral representation of the layered structure of $[Ln_2(SO_4)_6(enH)_2](enH_2)_2$ (Ln=Pr, Eu, Gd) **(14)-(16)** (LnO_8N polyhedra; purple; SO_4^{2-} tetrahedra, yellow; N, blue; C, black; H, white).

5.5.2 $[Ln_2(SO_4)_6(H_2O)_2](enH_2)_3$ (Ln=Er, Dy) (17)-(18)

5.5.2.1 Crystal structure description

The local coordination scheme for $[Ln_2(SO_4)_6(H_2O)_2](enH_2)_3$ (Ln=Er, Dy) **(17)-(18)** is depicted in Figure 5.22. In the structure of $[Ln_2(SO_4)_6(H_2O)_2](enH_2)_3$ (Ln=Er, Dy) **(17)-(18)** there are two crystallographically distinct metal centres with different coordination. Ln(1) is nine coordinated to three SO_4 groups (2 x $S(1)O_4$ and $S(2)O_4$ for **(17)** and 2 x $S(1)O_4$ and $S(5)O_4$ for **(18)**) in a bidentate fashion, to two sulphate groups in a monodentate fashion ($S(6)O_4$ and $S(3)O_4$ for **(17)** and $S(2)O_4$ and $S(6)O_4$ for **(18)**) and to one water molecule. In contrast, Ln(2) is eight coordinated to two sulphate anions in a bidentate mode ($S(3)O_4$ and $S(5)O_4$ for **(17)** and $S(2)O_4$ and $S(3)O_4$ for **(18)**), to three sulphate anions in a monodentate fashion ($S(3)O_4$ and 2 x $S(4)O_4$ for **(17)** and $S(2)O_4$ and 2 x $S(4)O_4$ for **(18)**) and to one water molecule.

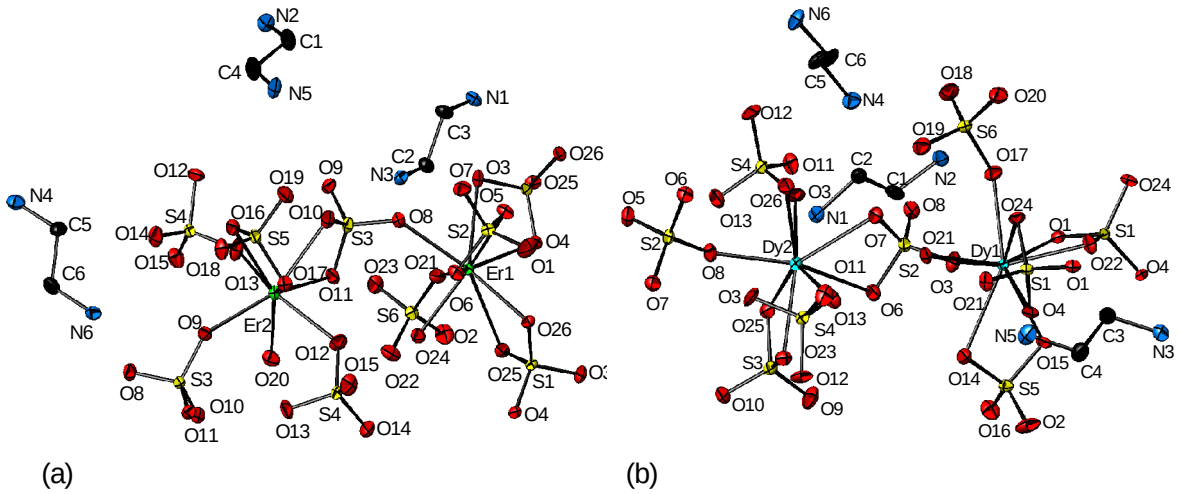

Figure 5.22. Atoms labelling scheme and thermal ellipsoids at 50% probability for $[Ln_2(SO_4)_6(H_2O)_2](enH_2)_3$ (Ln=Er, Dy) **(17)-(18)**. Hydrogen atoms have been omitted for clarity.

The average Ln(1)-O distance (Er(1)-O=2.420 Å, Dy(1)-O=2.433 Å) is greater than the corresponding Ln(2)-O (Er(2)-O=2.373 Å, Dy(2)-O=2.394 Å). For Er(1)-O, distances vary from 2.264(3) Å to the longest distances 2.634(4) Å and 2.607(4) Å, associated to the linkage to bidentate sulphate groups. The same trend is found in the dysprosium analogue **(18)** in which Dy(1)-O distances range from 2.279(3) Å to the longest distances 2.621(3) Å and 2.604(3) Å, also associated with the binding of the metal centre to bidentate sulphate groups. However, longer Ln-O bond distances are not seen for the Ln(2) centres, for which Ln(2)-O distances are comparable with those previously reported for ternary rare-earth sulphates. S-O distances are consistent with the mean S-O distance of 1.473 Å.

The structure of $[Ln_2(SO_4)_6(H_2O)_2](enH_2)_3$ (Ln=Er, Dy) **(17)-(18)** can be visualised as a two-dimensional structure in which layers are constructed from connection of two different types of chain (Figure 5.23). The chain of $Ln(2)O_8$ polyhedra is formed by linkage of each Ln(2) through two bridging SO_4 tetrahedra ($S(2)O_4$ and $S(4)O_4$ for **(17)** and $S(3)O_4$ and $S(4)O_4$ for **(18)**) both by edge- and vertex-sharing (Figure 5.23(b)). This connectivity results in the formation of four-membered rings of $Ln(2)O_8$ polyhedra and SO_4 tetrahedra. Chain formed by Ln(1) centres contains $Ln(1)O_9$ polyhedra connected through edge-sharing a common sulphate tetrahedron $S(1)O_4$, which is bidentate, forming a zig-zag chain running along the *a*-axis (Figure 5.23(c)).

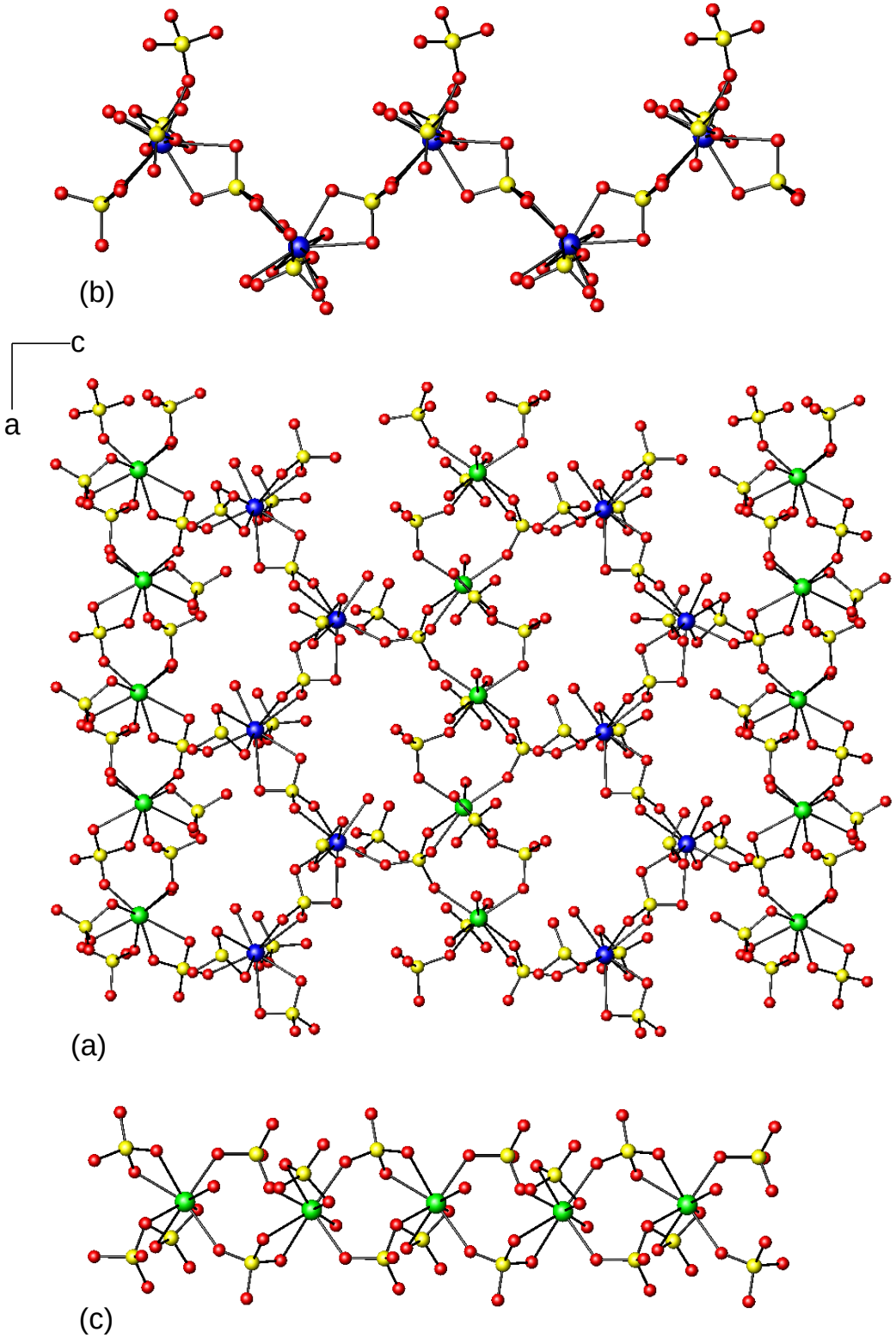

Figure 5.23. (a) Layer of $[Ln_2(SO_4)_6(H_2O)_2](enH_2)_3$ (Ln=Er, Dy) **(17)-(18)** showing the connectivity between the two different type of chains (b) Chain of $Ln(1)O_9$ polyhedra; and (c) Chain of $Ln(2)O_8$ polyhedra (Ln(1), blue; Ln(2), green; S, yellow; O, red).

Chains are fused together to form $[Ln_2(SO_4)_6(H_2O)_2]^{6-}$ layers. One of the sulphate tetrahedra that provide the connection between $Ln(2)O_8$ polyhedra to form the infinite chains, binds the adjacent zig-zag chains by sharing one vertex with $Ln(1)O_9$ polyhedra to form layers running parallel to the *ac* plane. The connectivity between SO_4 tetrahedra and $Ln(1)O_9$ and $Ln(2)O_8$ is responsible for the formation of ten-membered rings (Figure 5.24(a)). Layers are stacked directly above one another along the *b*-axis, with a separation distance of *ca.* 9.98 Å in each case, with the diprotonated ethylenediamine cations in the space between them. Cations and anions are held together in a hydrogen-bond system (Figure 5.24(b)). The geometry of the H-bond interactions is depicted in Appendix D.

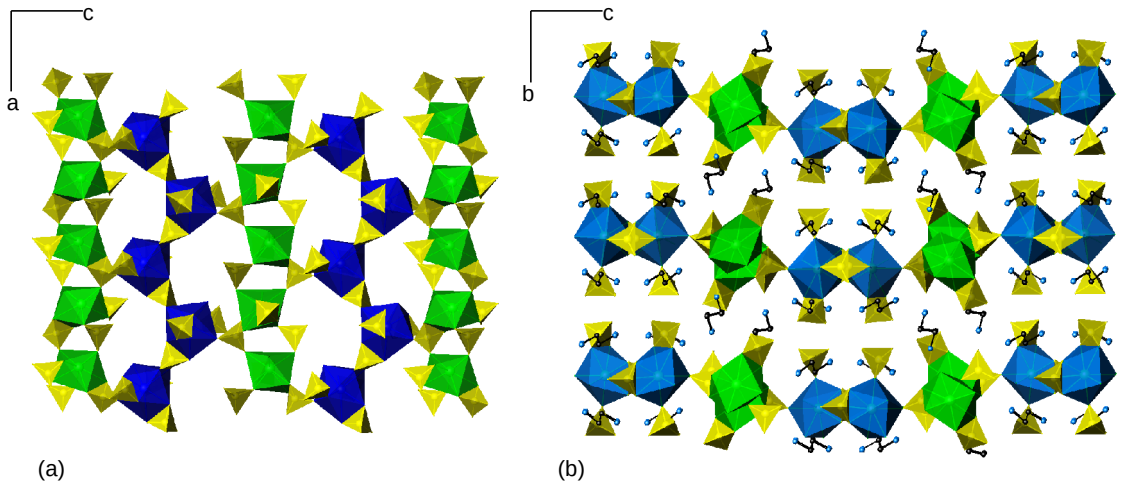

Figure 5.24. (a) Polyhedral representation of a layer of $[Ln_2(SO_4)_6(H_2O)_2](enH_2)_3$ (Ln=Er, Dy) **(17)-(18)**; (b) Stacking of layers along *b*-axis for $[Ln_2(SO_4)_6(H_2O)_2](enH_2)_3$ (Ln=Er, Dy) **(17)-(18)** ($Ln(1)O_9$ polyhedra, blue; $Ln(2)O_8$ polyhedra, green; SO_4 tetrahedra, yellow; N, blue; C, black) H atoms have been omitted for clarity.

5.5.3 $[Dy(SO_4)_2](enH_2)_{0.5}$ (19)

5.5.3.1 Crystal structure description

The atoms labelling scheme is depicted in Figure 5.25. In the asymmetric unit of $[Dy(SO_4)_2](enH_2)_{0.5}$ **(19)** there is one crystallographically distinct dysprosium atom, which is nine-coordinated by oxygen atoms from the sulphate groups. Dy-O distances range from 2.2984(11) Å to 2.5664(10) Å, with an average Dy-O distance of 2.4283 Å. They are consistent with Dy-O distances previously reported for $Dy_2(SO_4)_3(H_2O)_8$ [359]. S-O distances range from 1.4435(11) Å to 1.5076(10) Å.

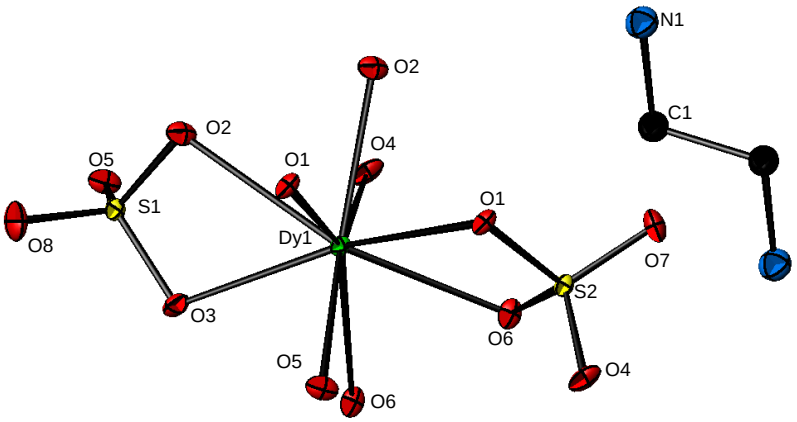

Figure 5.25. Atoms labelling scheme and thermal ellipsoids at 50% probability of $[Dy(SO_4)_2](enH_2)_{0.5}$ **(19)**. Hydrogen atoms have been omitted for clarity.

This difference in bond lengths is related to the presence of three different types of oxygen atoms in the structure. Each sulphate tetrahedron has one terminal oxygen atom, with the shortest S-O bond length. The longest S-O distance is associated with the presence of three-coordinate oxygen atoms, and on the basis of this type of connectivity, two different types of sulphate tetrahedron can be distinguished. $S(1)O_4$ tetrahedra has one three-coordinated oxygen atom and two two-coordinated oxygen atoms, whereas $S(2)O_4$ comprises two three-coordinated oxygen atoms and one two-coordinated oxygen atom. Each SO_4 tetrahedra shares an edge and one vertex with metal-centered polyhedra leaving one of the vertices of the SO_4 tetrahedron unconnected.

The connectivity between two centres produces $[Dy_2(SO_4)_4]$ units that can be seen as the building unit of this structure. Neighbouring units are linked together by edge-sharing DyO_9 polyhedra and bridging $S(1)O_4$ and $S(2)O_4$ tetrahedra through one of the two three-coordinated oxygen atoms to form a chain running along the *a*-axis (Figure 5.26).

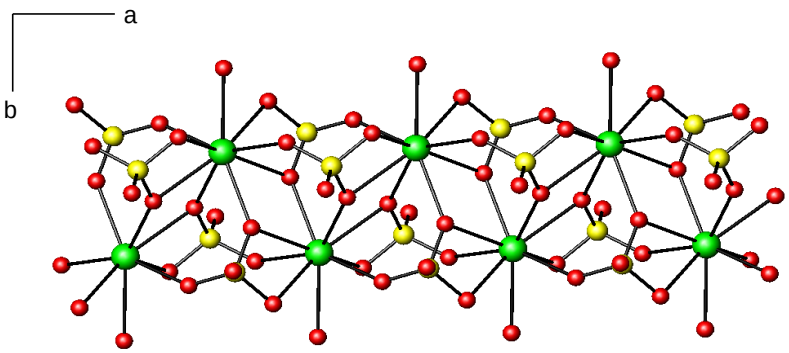

Figure 5.26. Chain formed by linking building units in $[Dy(SO_4)_2](enH_2)_{0.5}$ **(19)** (Dy ions, green; S, yellow, O, red).

Chains are in turn connected into layers *via* the second three-coordinated oxygen atom in $S(2)O_4$ tetrahedra and edge-sharing DyO_9 polyhedra. It results in the formation of four-membered rings between the chains, involving two DyO_9 polyhedra and two SO_4 tetrahedra. (Figure 5.27(a)).

The inorganic layers are stacked along the *c*-axis separated by the diprotonated ethylenediamine molecules forming a three-dimensional network (Figure 5.28) in which inorganic layers and organic cations are held together through hydrogen-bond interactions (Appendix D). The separation distance between two consecutive layers is *ca.* 9.68 Å.

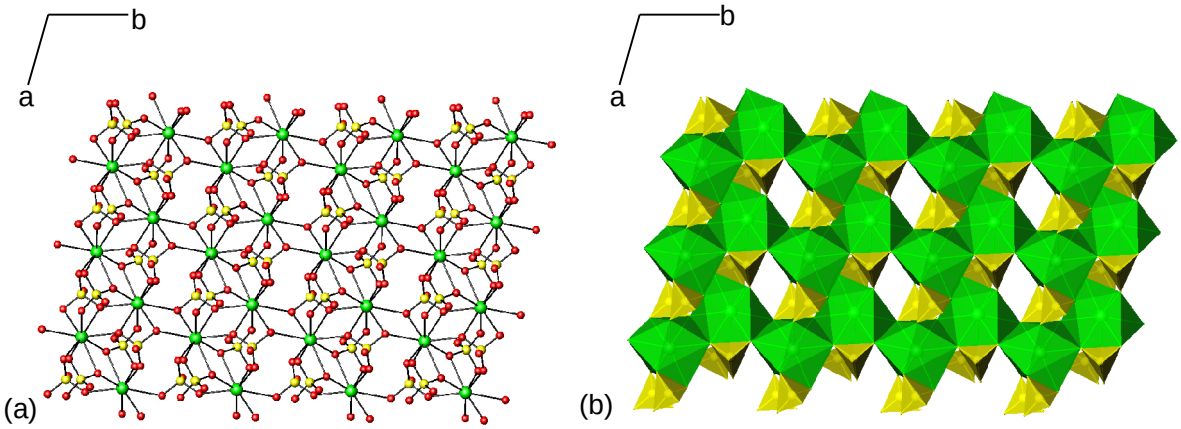

Figure 5.27. A layer formed by linking of the chains in $[Dy(SO_4)_2](enH_2)_{0.5}$ **(19)** (a) ball and stick representation (Dy ions, green; S, yellow, O, red); (b) polyhedral representation (DyO_9 polyhedra, green; SO_4 tetrahedra, yellow).

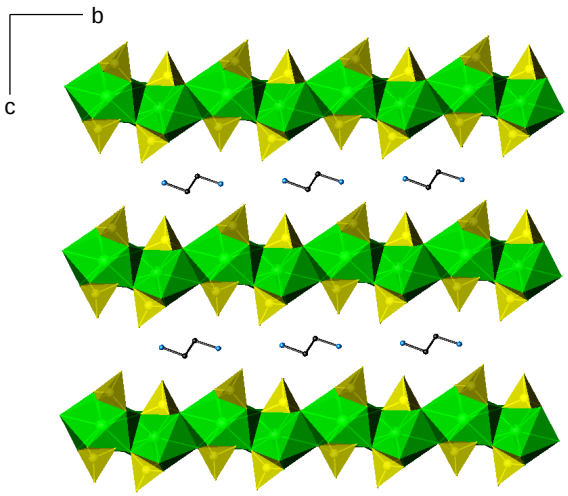

Figure 5.28. Packing of alternating $[Dy(SO_4)_2]^+$ layers and amine molecules along the *c*-axis (DyO_9 polyhedra, green; SO_4 tetrahedra, yellow; C, black; N, black) Hydrogen atoms have been omitted for clarity.

5.6 Three-dimensional structure of $[Sm_4(SO_4)_{10}(H_2O)_4](pipH_2)_4$

5.6.1 Crystal structure description

The local coordination scheme for $[Sm_4(SO_4)_{10}(H_2O)_4](pipH_2)_4$ **(20)** is shown in Figure 5.29. The asymmetric unit of $[Sm_4(SO_4)_{10}(H_2O)_4](pipH_2)_4$ **(20)** contains four crystallographically distinct samarium ions, three of them being nine coordinate and the fourth eight-coordinate. The coordination sphere of each Sm(2), Sm(3) and Sm(4) has three bidentate sulphate anions, two monodentate sulphate anions and one molecule of water. However, Sm(1) is eight coordinate and its coordination environment consists of two bidentate sulphate groups, three monodentate sulphate anions and one molecule of water. The average Sm-O distances for Sm(1)-O, Sm(2)-O, Sm(3)-O and Sm(4)-O are 2.444 Å, 2.503 Å, 2.520 Å and 2.487 Å, respectively.

The long Sm(3)-O(18) distance of 2.938(4) Å has not been found in any other of the Sm-O bonds present within this structure, the longest distances for Sm(1)-O, Sm(2)-O and Sm(4)-O bonds being 2.543(3) Å, 2.607(3) Å and 2.584(3) Å respectively. These latter values are consistent with bond lengths observed in the samarium sulphate $Sm_2(SO_4)_3(H_2O)_8$ [367]. The long Sm(3)-O(18) distance lies out of this range and corresponds to the coordination of Sm(3) to an oxygen atom belonging to a bidentate sulphate anion. S-O distances are in good agreement with those reported for sulphates.

In the asymmetric unit, the four crystallographically distinct samarium ions are interconnected through edge and corner sharing SO_4 tetrahedra which results in the formation of an eight-membered ring. $Sm(3)O_9$ is linked to $Sm(2)O_9$ and $Sm(4)O_9$ *via* two edge-sharing SO_4 tetrahedra, whereas $Sm(1)O_8$ is linked to $Sm(2)O_9$ and $Sm(4)O_9$ in two different ways; to Sm(2) by edge-sharing SO_4 tetrahedra while one sulphate tetrahedra that shares one edge with $Sm(4)O_8$ links the two metal centres by sharing one vertex with $Sm(1)O_9$ polyhedra (Figure 5.29).

On the basis of the existence of two different types of polyhedra, the structure can be seen as formed by merging of two different motifs. The first motif that is found in this structure is the one-dimensional chain built up from $Sm(1)O_8$ polyhedra and bridging SO_4 tetrahedra, in which $Sm(1)O_8$ polyhedra and vertex-linking SO_4 tetrahedra alternate along the *c*-axis (Figure 5. 30(a)). Simultaneously, each $Sm(1)O_8$ polyhedron shares three sulphate tetrahedra *via* edge and vertex-linking with three neighbouring SmO_9 polyhedra in the *ab* plane (Figure 5. 30(b)).

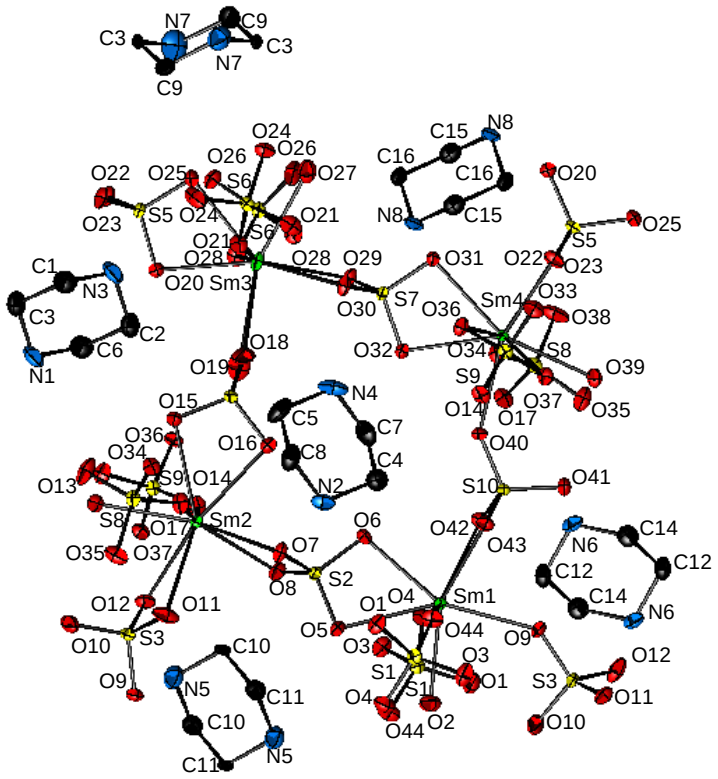

Figure 5.29. Atoms labelling scheme and thermal ellipsoids at 50% probability of $[Sm_4(SO_4)_{10}(H_2O)_4](pipH_2)_4$ **(20)**. Hydrogen atoms have been omitted for clarity.

The second motif is that formed by connection of SmO_9 polyhedra. SmO_9 polyhedra are linked *via* edge- and vertex-sharing SO_4 tetrahedra, alternatively, to form one chain. Each chain is connected to an adjacent chain through bridging edge-sharing SO_4 tetrahedra. The result is a double chain in which eight-membered rings, involving four SmO_9 polyhedra and four SO_4 tetrahedra, are obtained. Layers are produced by the linkage of consecutive double chains through edge-sharing SO_4 tetrahedra which creates twelve-membered rings containing six sulphate tetrahedra and six SmO_9 polyhedra (Figure 5.31(a)). These layers are in turn connected to each other through edge-linking SO_4 tetrahedra along the *b*-axis forming a three-dimensional motif (Figure 5.31(b)).

Chains built up from $Sm(1)O_8$ polyhedra serve to link adjacent three-dimensional motifs *via* edge- and vertex-linking sulphate tetrahedra (Figure 5.32) to form a three-dimensional network in which channels of eight- and twelve-membered rings are produced. The diprotonated piperazinium cations occupy cavities within the structure (Figure 5.33). Both cations and anions are held together in a hydrogen-bonded system (Appendix D).

A space filling representation of the three-dimensional structure of $[Sm_4(SO_4)_{10}(H_2O)_4](pipH_2)_4$ **(20)** was calculated from the van der Waals' radii of the atoms and it is shown in Figure 5.34. Cavities are entirely occupied by diprotonated piperazinium cations. However, the removal of the cations could afford an empty space within the structure of dimensions *ca*. 9.9 x 6.1 Å.

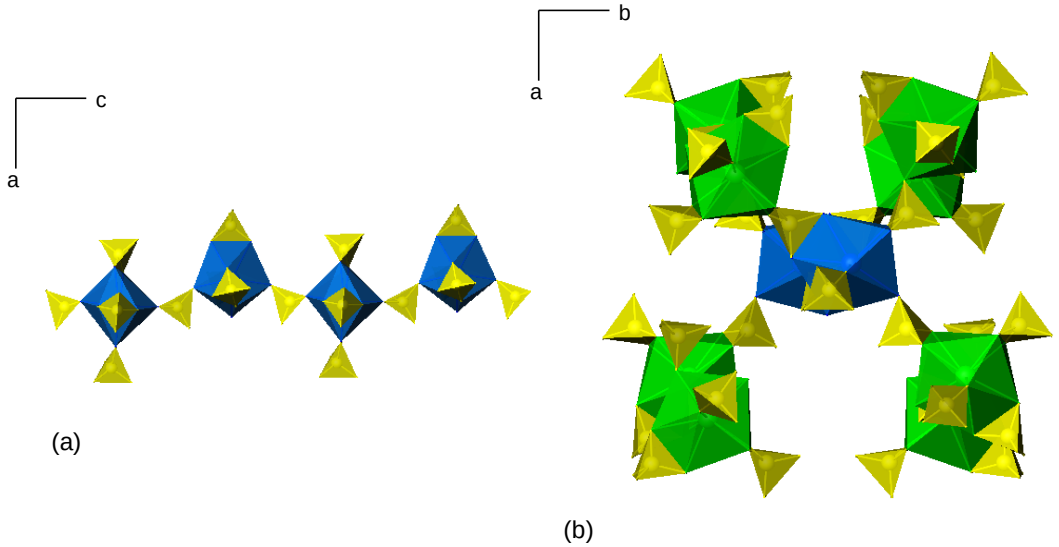

Figure 5. 30. (a) Chain in $[Sm_4(SO_4)_{10}(H_2O)_4](pipH_2)_4$ **(20)** built up from $Sm(1)O_8$ polyhedra and SO_4 tetrahedra; (b) Linkage between SmO_8 and SmO_9 polyhedra through edge- and vertex-sharing SO_4 tetrahedra (SmO_8 polyhedra, blue; SmO_9 polyhedra, green; SO_4 tetrahedra, yellow).

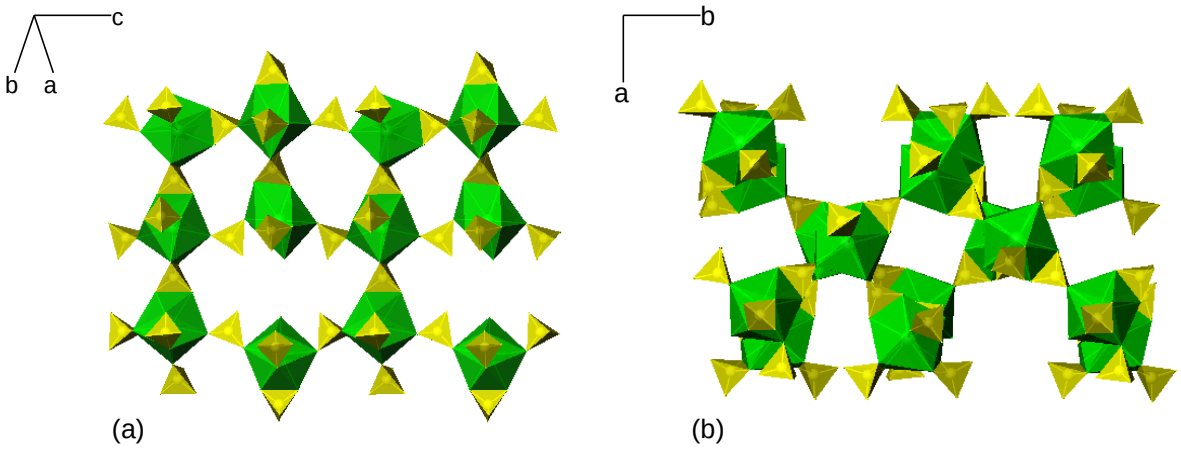

Figure 5.31. (a) View of the 3D motif in the *ab* plane in $[Sm_4(SO_4)_{10}(H_2O)_4](pipH_2)_4$ **(20)** made up of SmO_9 and SO_4 tetrahedra to form 8- and 12-membered rings; (b) View in the *ab* plane in $[Sm_4(SO_4)_{10}(H_2O)_4](pipH_2)_4$ **(20)** (SmO_9 polyhedraa, green; SO_4 tetrahedra, yellow).

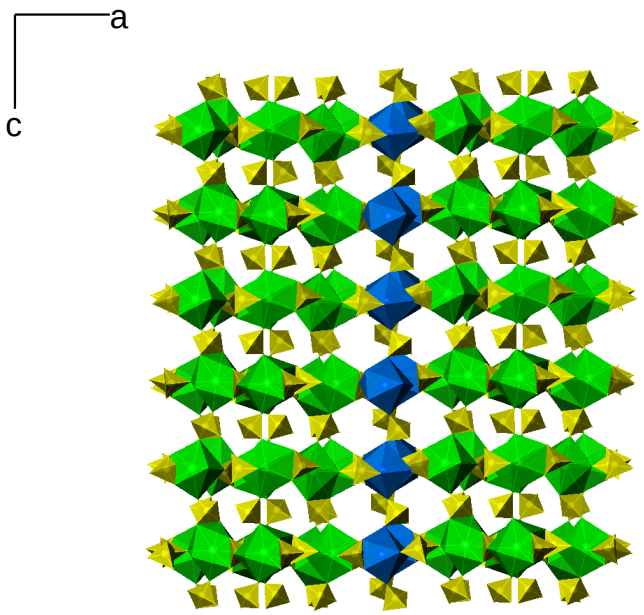

Figure 5.32. Connection between SmO_8 and SmO_9 polyhedra through edge-sharing and vertex-sharing SO_4 tetrahedra parallel to the *ac* plane (SmO_8 polyhedra, blue; SmO_9 polyhedra, green; SO_4 tetrahedra, yellow).

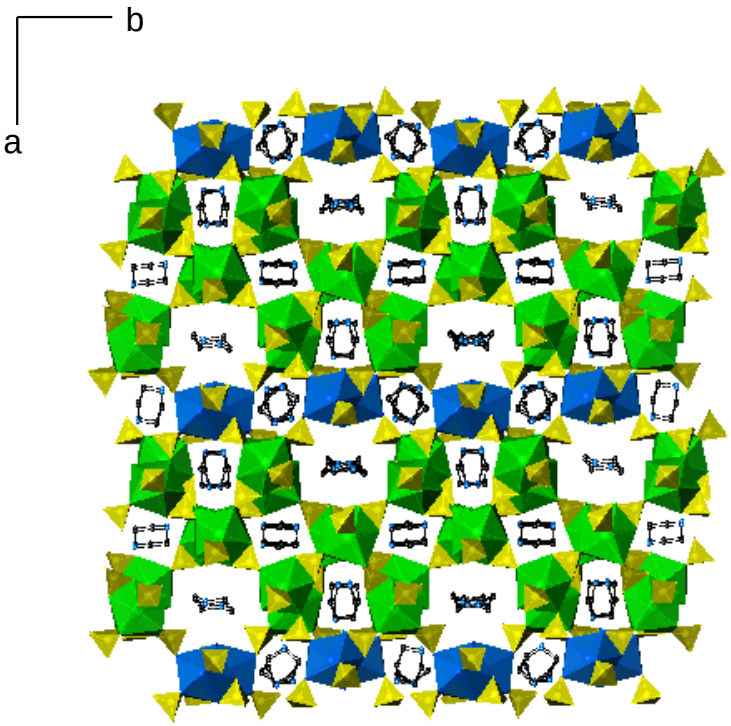

Figure 5.33. Three-dimensional structure of $[Sm_4(SO_4)_{10}(H_2O)_4](pipH_2)_4$ **(20)** (SmO_9 polyhedra; green; SmO_8 polyhedra, blue; SO_4 tetrahedra, yellow; N, blue; C, black).

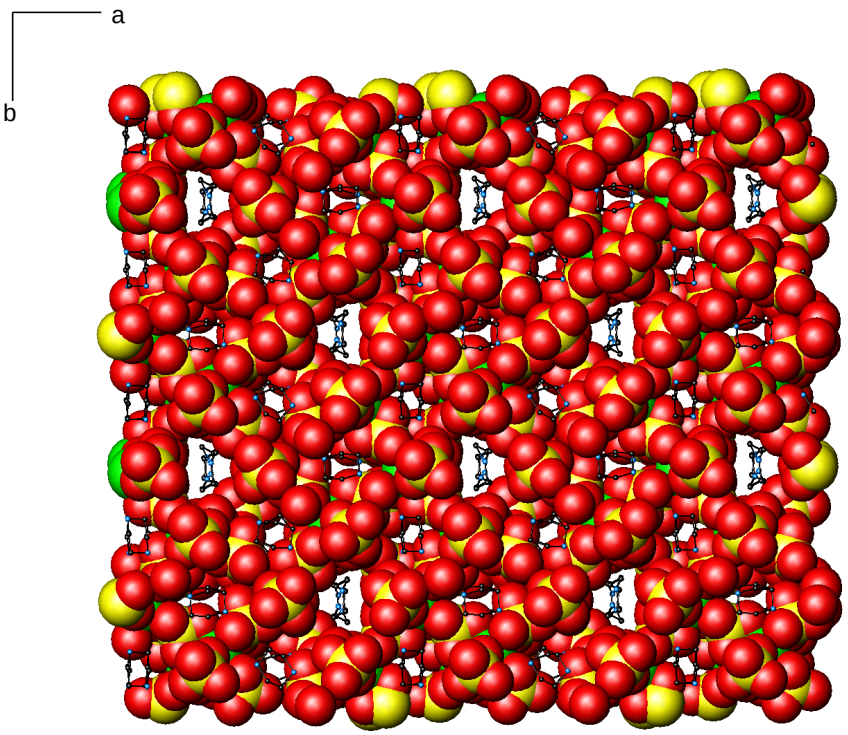

Figure 5.34. Space filling representation of the structure of $[Sm_4(SO_4)_{10}(H_2O)_4](pipH_2)_4$ **(20)** in the *ab* plane without applying the van der Waals' radii to nitrogen, carbon and hydrogen (Sm, green; S, yellow; O, red; N, blue; C, black; H, white).

5.7 Magnetic properties of the organically-templated rare-earth sulphates

Magnetic susceptibility data at 100 G for $[Dy_2(SO_4)_6(H_2O)](trienH_4)_{1.5}$ **(13)**, $[Eu_2(SO_4)_6(enH)_2](enH_2)_2$ **(15)**, $[Ln_2(SO_4)_6(H_2O)_2](enH_2)_3$ (Ln=Er, Dy) **(17)-(18)**, $[Dy(SO_4)_2](enH_2)_{0.5}$ **(19)** and $[Sm_4(SO_4)_{10}(H_2O)_4](pipH_2)_4$ **(20)** are shown in Figure 5.35. Magnetic susceptibility data indicate paramagnetic behaviour for each material with the exception of $[Sm_4(SO_4)_{10}(H_2O)_4](pipH_2)_4$ **(20)** that does not follow the Curie-Wiess law in the range of temperatures measured (5-300 K). The field-cooled suceptibility for **(20)** smoothly increases from 0.013 e.m.u. at 300 K to 0.020 e.m.u. at 41.5 K, temperature after which it abruptly increases 0.064 e.m.u. at 5 K. The reciprocal magnetic susceptibility slowly decreases on cooling from 74 e.m.u. at 300 K to 60.88 e.m.u. at 73.5 K. Below this temperature, it rapidly decreases to 15.6 e.m.u. at 5 K. The reciprocal susceptibility as a function of temperature also shows a slight curvature at low temperature for $[Eu_2(SO_4)_6(enH)_2](enH_2)_2$ **(15)** and $[Er_2(SO_4)_6(H_2O)_2](enH_2)_3$ **(17)**.

The Curie and Weiss constants as well as the effective magnetic moments were determined by fitting the linear section of the reciprocal susceptibility plots to the Curie-Weiss law. The Curie constants, effective magnetic moments and Weiss constants are summarised in Table 5.7. The effective magnetic moments for dysprosium, europium and erbium are in agreement with the calculated and previously observed magnetic moments [368]. The Weiss constants are all negative, suggesting antiferromagnetic exchange interactions, with the exception of that of $[Dy(SO_4)_2](enH_2)_{0.5}$ **(19)** that is positive but very close to zero.

Table 5.7. Summary of the Curie constants, magnetic moments and Weiss constants.

Comp.	Fitting range / K	C / cm^3 K mol^{-1}	μ_{eff} per M ion / μ_B	$g(J(J+1))^{-1/2}$ / μ_B		θ / K
				(A) (without TIP)*	**(B)** (with TIP)*	
(13)	5-300	46.297(3)	9.623(1)	10.63	10.63	-3.901(4)
(15)	100-300	4.602(2)	4.291(1)	0	[≈3.45]#	-29.134(2)
(17)	5-300	22.650(1)	9.518(2)	9.57	9.57	-15.728(2)
(18)	5-300	27.359(3)	10.461(3)	10.63	10.63	-4.043(2)
(19)	5-300	25.720(1)	10.143(1)	10.63	10.63	0.107(1)

(* TIP= additional contribution from *temperature independent paramagnetism*)
(# As originally estimated by Van Vleck)

The majority of the materials exhibits a decrease of the effective magnetic moment as the temperature is lowered from 300 K to 5 K. For $[Dy_2(SO_4)_6(H_2O)](trienH_4)_{1.5}$ **(13)** (blue triangles) the effective magnetic moment remains constant on cooling down to 100 K when it starts decreasing from 9.623(1) μ_B at room temperature to 8.253(4) μ_B at 5 K (Figure 5.36). Similar behaviour has been observed for $[Dy_2(SO_4)_6(H_2O)_2](enH_2)_3$ **(18)** (red circles) for which the effective magnetic moment remains constant on cooling to 60 K, temperature after which the magnetic moment decreases from 10.461(3) μ_B to 8.770(3) μ_B at 5 K. For the analogous erbium phase $[Er_2(SO_4)_6(H_2O)_2](enH_2)_3$ **(17)** (black squares) the magnetic moment decreases slowly and continuously from 9.518(2) μ_B to 8.415(2) μ_B on cooling from 300 K to 60 K, where the magnetic moment decreases rapidly to 6.053(2) μ_B at 5 K (Figure 5.36). Different behaviour has been found in $[Dy(SO_4)_2](enH_2)_{0.5}$ **(19)** (green

triangles), in which the effective magnetic moment increases slightly on cooling from 10.143(1) μ_B at 300 K to 10.261(5) μ_B at 31 K, before decreasing abruptly to 7.945(4) μ_B at 5 K, indicating a possible magnetic transition (Figure 5.36).

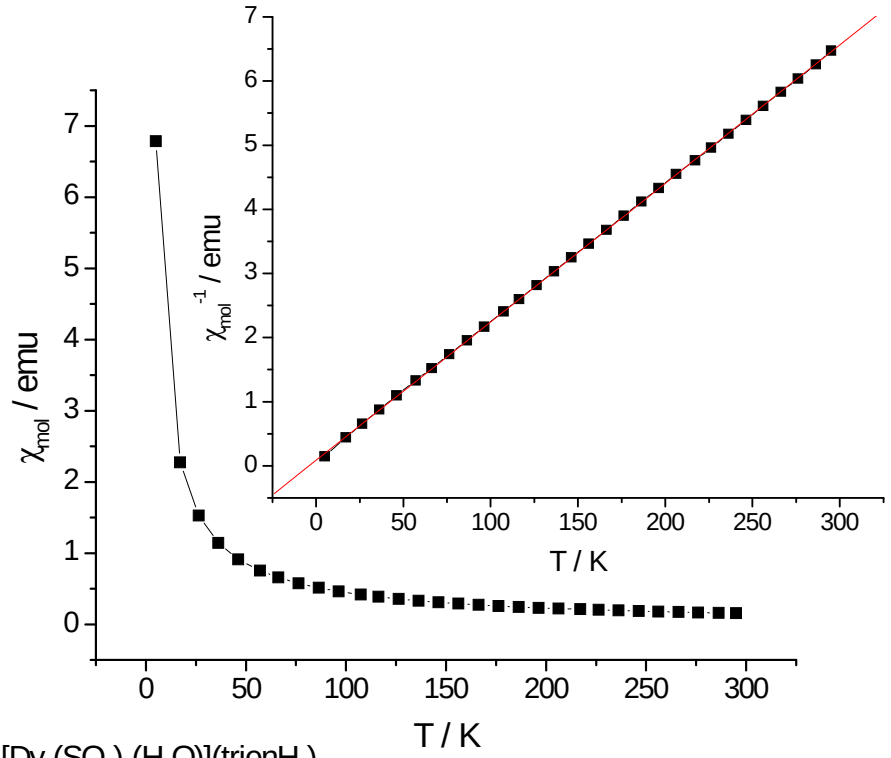

(a) $[Dy_2(SO_4)_6(H_2O)](trienH_4)_{1.5}$

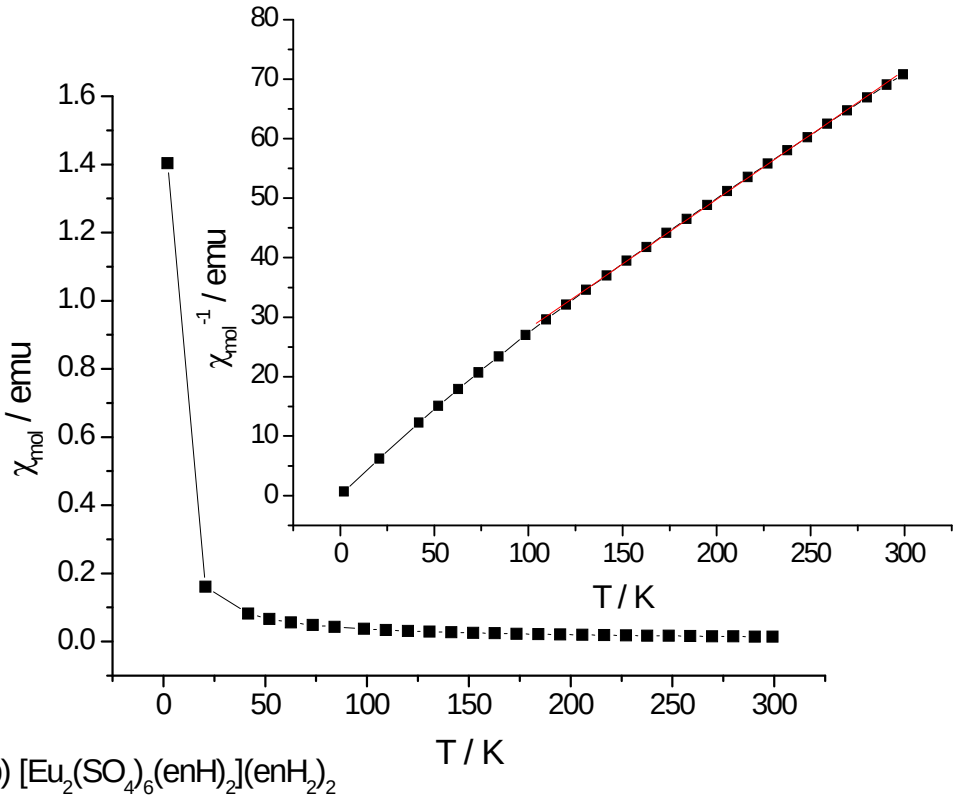

(b) $[Eu_2(SO_4)_6(enH)_2](enH_2)_2$

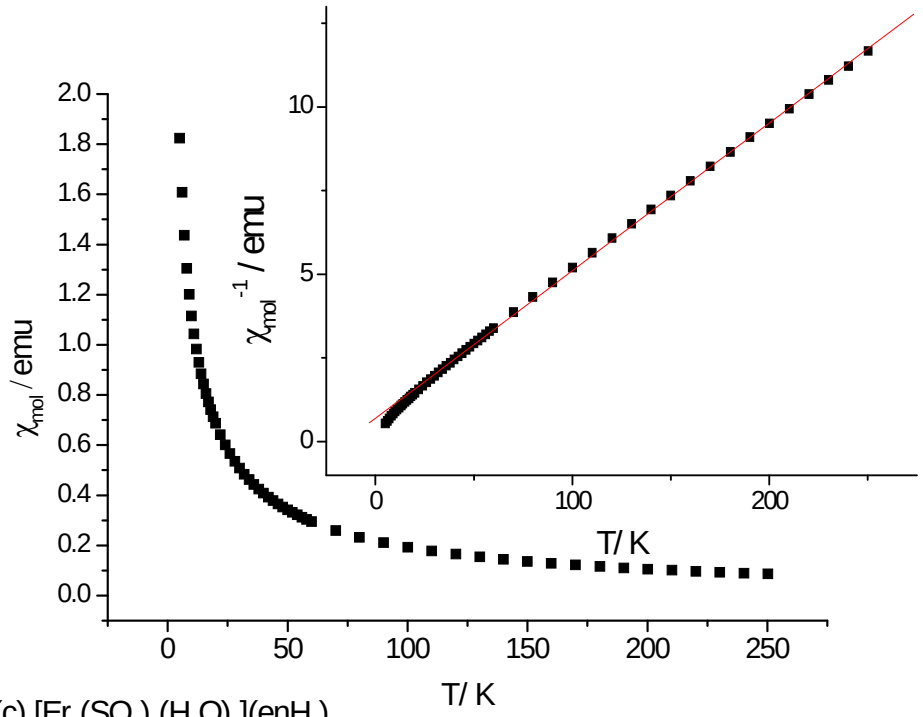

(c) $[Er_2(SO_4)_6(H_2O)_2](enH_2)_3$

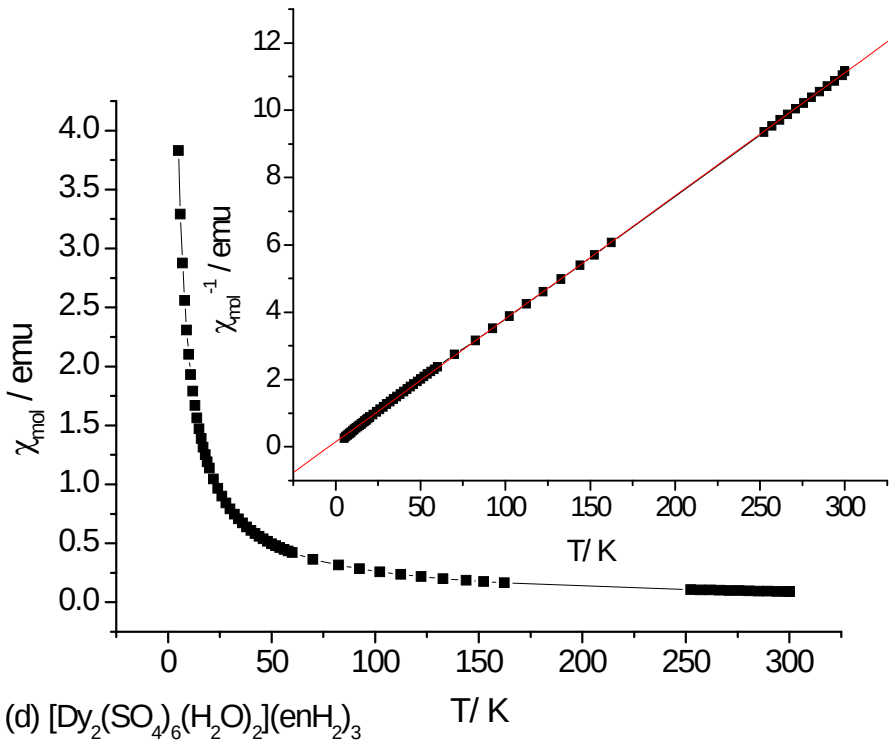

(d) $[Dy_2(SO_4)_6(H_2O)_2](enH_2)_3$

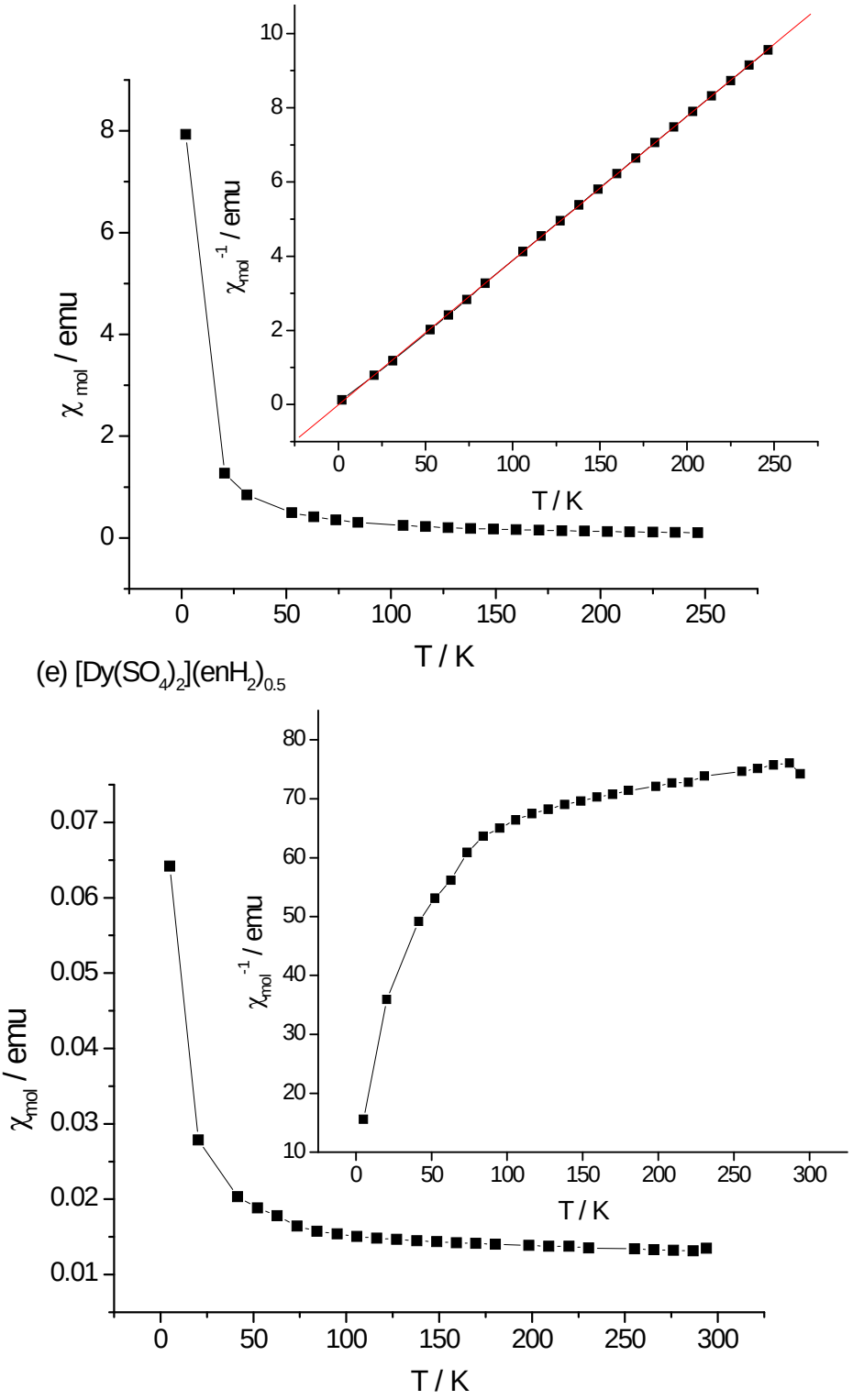

Figure 5.35. Field-cooled (Fc) magnetic susceptibility data and inverse susceptiblity data (inset) for (a) $[Dy_2(SO_4)_6(H_2O)](trienH_4)_{1.5}$ **(13)**; (b) $[Eu_2(SO_4)_6(enH)_2](enH_2)_2$ **(15)**; (c) $[Er_2(SO_4)_6(H_2O)_2](enH_2)_3$ **(17)**; (d) $[Dy_2(SO_4)_6(H_2O)_2](enH_2)_3$ **(18)**; (e) $[Dy(SO_4)_2](enH_2)_{0.5}$ **(19)**; and (f) $[Sm_4(SO_4)_{10}(H_2O)_4](pipH_2)_4$ **(20)**. The red solid lines show the fit to the Curie-Weiss law.

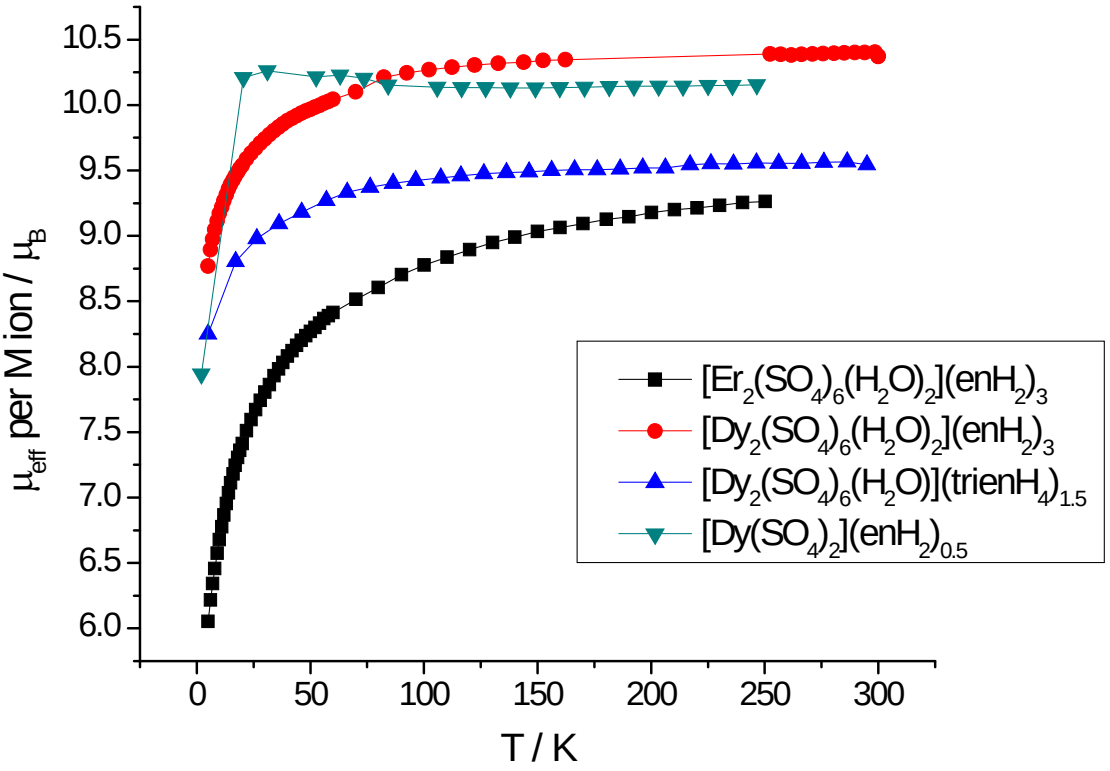

Figure 5.36. Effective magnetic moment per M ion as a funtion of temperature for $[Dy_2(SO_4)_6(H_2O)](trienH_4)_{1.5}$ **(13)**, $[Dy(SO_4)_2](enH_2)_{0.5}$ **(18)** and $[Ln_2(SO_4)_6(H_2O)_2](enH_2)_3$ (Ln=Er, Dy) **(17)-(18)** at 100 G between 5-300 K.

For $[Eu_2(SO_4)_6(enH)_2](enH_2)_2$ **(15)** and $[Sm_4(SO_4)_{10}(H_2O)_4](pipH_2)_4$ **(20)** (Figure 5.37), the effective magnetic moment continuously decreases from 300 K to 5 K. The magnetic moment of $[Eu_2(SO_4)_6(enH)_2](enH_2)_2$ decreases slightly from 4.155(4) μ_B at 300 K to 3.346(3) μ_B at 5 K and that of $[Sm_4(SO_4)_{10}(H_2O)_4](pipH_2)_4$ continuously decreases from 300 K in which μ_{eff} is 2.031(4) μ_B to a value of 0.802(1) μ_B at 5 K.

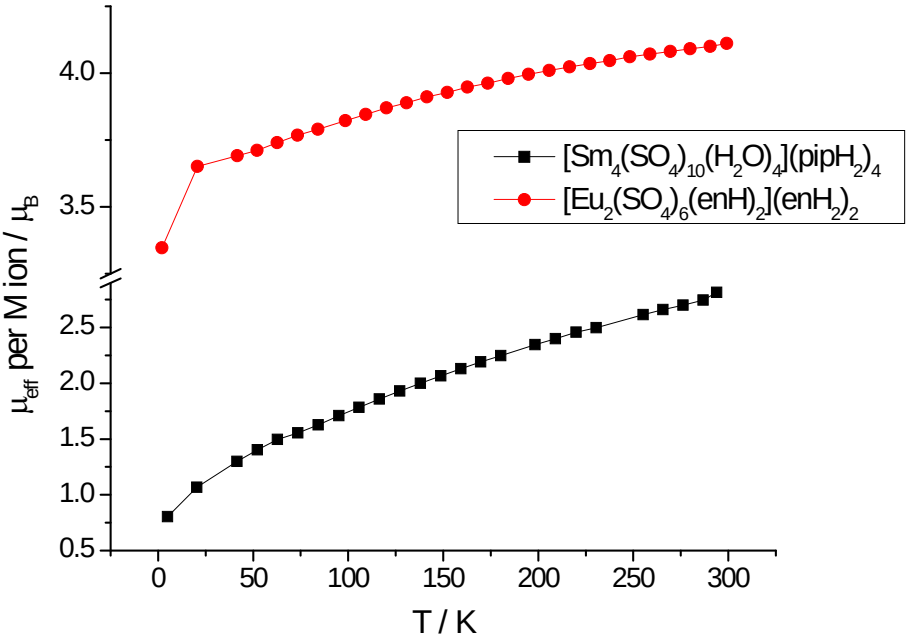

Figure 5.37. Effective magnetic moment per M ion as a function of temperature for $[Sm_4(SO_4)_{10}(H_2O)_4](pipH_2)_4$ **(20)** and $[Eu_2(SO_4)_6(enH)_2](enH_2)_2$ **(15)** at 100 G between 5-300 K

5.8 Discussion

In this research project, solvothermal synthesis has been employed for the preparation of organically-templated rare-earth sulphates, in which a wide variety of amines as well as reaction conditions for the system $Ln_2(SO_4)_3$-H_2SO_4-H_2O-amine have been investigated. Using ethylendiamine as a template the formation of layered structures was favoured and the rare-earth sulphates $[Ln_2(SO_4)_6(enH)_2](enH_2)_2$ (Ln=Pr, Eu, Gd) **(14)-(16)**, $[Ln_2(SO_4)_6(H_2O)_2](enH_2)_3$ (Ln=Er, Dy) **(17)-(18)** and $[Dy(SO_4)_2](enH_2)_{0.5}$ **(19)** as well as the one-dimensional lanthanum sulphate $[La(SO_4)_3](enH_2)_{1.5}$ **(12)** were obtained. The use of triethylenetetramine for the synthesis of rare-earth sulphates resulted in the formation of the dysprosium sulphate $[Dy_2(SO_4)_6(H_2O)](trienH_4)_{1.5}$ **(13)** but attempts to synthesise other structures employing this amine failed indicating a most limitating chemistry of this amine in the rare-earth crystals compared to the transition metal sulphates described in Chapter 4. The three-dimensional samarium sulphate $[Sm_4(SO_4)_{10}(H_2O)_4](pipH_2)_4$ **(20)** was prepared in the presence of piperazine as well as the rare-earth sulphate hydrates $Ln_2(SO_4)_3(H_2O)_4$ (Ln=Dy, Gd). Further investigations employing other amines led to the synthesis of two

other rare-earth sulphate hydrates, $Sm_2(SO_4)_3(H_2O)_4$ and $Pr_2(SO_4)_3(H_2O)_4$ which were obtained using diethylamine and pyrrolidine, respectively.

Several common characteristic have been observed in the crystal structures of the organically-templated rare-earth sulphates illustrated in this chapter. The ethylenediamine-templated one-dimensional lanthanum sulphate, $[La(SO_4)_3](enH_2)_{1.5}$ **(12)**, displays a unique crystal structure in comparison with the others, as the lanthanum ion shows a high coordination number, twelve, with each La^{3+} ion being surrounded by six sulphate anions all of them coordinated to the metal centre in a bidentate mode. This particular coordination has not been observed in the other materials investigated in this chapter, in which besides bidentate sulphate groups, sulphate anions coordinated to the metal centre in a monodentate fashion are also present. Such high coordination numbers are confined to compounds of the larger and lighter atoms, for instance lanthanum and cerium, and are only achievable with ligands like NO_3^- and SO_4^{2-}, with eight and nine being the more characteristic coordination numbers. This very high coordination environment has only been found in organically-templated rare-earth sulphates in which this ion is present. The structure of $[La(SO_4)_3](enH_2)_{1.5}$ **(12)** can be compared to that of a lanthanum sulphate of formula $[La(SO_4)_3]H_2O[C_4N_3H_{16}]$ synthesised by Xin and co-workers [182], which constitutes the first example of a rare-earth sulphate in which the LaO_{12} polyhedra linked together by sharing faces. They are analogues with an isostructural one-dimensional structure. This material is built up from infinite $[La(SO_4)_3]^{3-}$ chains. In contrast to the structure of **(12)**, the inorganic chains are held together by DETA (diethylenetriamine) cations in a hydrogen-bonded system. In addition, the three-membered rings formed as a result of the three-coordinated oxygen atoms that serve to connect two adjacent La^{3+} centres have been reported in organically-templated metal phosphates [369, 370]. The same type of connectivity between metal centres through three-coordinate oxygen ions have been observed in the layered rare-earth sulphates $[Ln_2(SO_4)_4][C_2N_2H_{10}]$ (Ln=La, Nd), $[La_2(SO_4)_4][C_3N_2H_{12}]$ [191] and $[Ln(INO)(H_2O)(SO_4)]_n$ (INO=isonicotinate-N-oxide) (Ln=La, Ce, Pr) [241]. In common with $[La(SO_4)_3](enH_2)_{1.5}$ **(12)** they contain three-coordinate oxygen ions although there are only two crystallographically distinct species in these materials, whereas in $[La(SO_4)_3(enH_2)_{1.5}$ three of these oxygens connect La(1) and La(2). However, the coordination environment of Ln in $[Ln_2(SO_4)_4][C_2N_2H_{10}]$, $[La_2(SO_4)_4][C_3N_2H_{12}]$ and $[Ln(INO)(H_2O)(SO_4)]_n$, in which Ln is nine or eight-

coordinated, differs from that of $[La(SO_4)_3](enH_2)_{1.5}$ **(12)**, in which each La ion is twelve-coordinated.

$[Dy_2(SO_4)_6(H_2O)](trienH_4)_{1.5}$ **(13)** was obtained under solvothermal conditions employing trien amine as a template. Its structure comprises two different types of chains, those in which DyO_9 polyhedra are connected by SO_4 tetrahedra linked by edge and vertex sharing; and those in which the same chains are fused together forming a double chain that represents the central part of the ribbon. The first type of chain is comparable to that found in the quasi-layer structure of $[La_2(H_2O)_4(SO_4)_4]\cdot 2H_2O$ [192]. In this structure $La(1)O_{10}$ polyhedra are connected by vertex- and edge-sharing SO_4 tetrahedra in a similar manner as the DyO_9 polyhedra are connected in **(13)** despite the coordination around the metal differing from that of the lanthanum sulphate. Similar chains have also been reported for the rare-earth sulphates $[Ln_2(SO_4)_4(H_2O)_4][C_6N_2H_{14}][SO_4][C_2N_2H_8][H_2O]_3$ (Ln=La, Pr, Nd) [191]. In this structure, neighbouring chains are linked together in a zig-zag fashion to form an extended layer, while in $[Dy_2(SO_4)_6(H_2O)](trienH_4)_{1.5}$ **(13)** chains are connected to the central double chain. It gives rise to a different structure as the result of the fusion of two consecutive chains to form ribbons. In the double chain, DyO_9 polyhedra are directly coordinated by sharing one edge since the binding between them is made through two three-coordinated oxygen atoms. As previously mentioned in the discussion of the structure of the one-dimensional lanthanum sulphate $[La(SO_4)_3](enH_2)_{1.5}$ **(12)**, the presence of the three-coordinate oxygen ions has been previously found in other structures such as organically-templated metal phosphates [369, 370], in the cerium phosphate-sulphate, $[Ce(PO_4)(HSO_4)(H_2O](enH_2)$ [195] and in the layered rare-earth sulphates $[Ln_2(SO_4)_4][C_2N_2H_{10}]$ (Ln=La, Nd), $[La_2(SO_4)_4][C_3N_2H_{12}]$ [191] and $[Ln(INO)(H_2O)(SO_4)]_n$ (Ln=La, Ce, Pr) [340]. These structures share in common with $[Dy_2(SO_4)_6(H_2O)](trienH_4)_{1.5}$ **(13)** the existence of two-coordinated oxygen atoms that serve to join the two metal centres. In contrast to $[Dy_2(SO_4)_6(H_2O)](trienH_4)_{1.5}$ **(13)**, in which the double chains simply constitute the central part of the ribbon, in these structures the double chains link one another to form infinite layers of LnO_x polyhedra and SO_4 tetrahedra that are bridged *via* vertex and edge-linking (Figure 5.38).

$[Dy_2(SO_4)_6(H_2O)]^{6-}$ has been found to be the building unit of the three-dimensional structure of $[Nd_2(SO_4)_4(H_2O)_2][C_4N_2H_{12}]$ [188], in which each unit connects an adjacent unit through edge-sharing SO_4 tetrahedra.

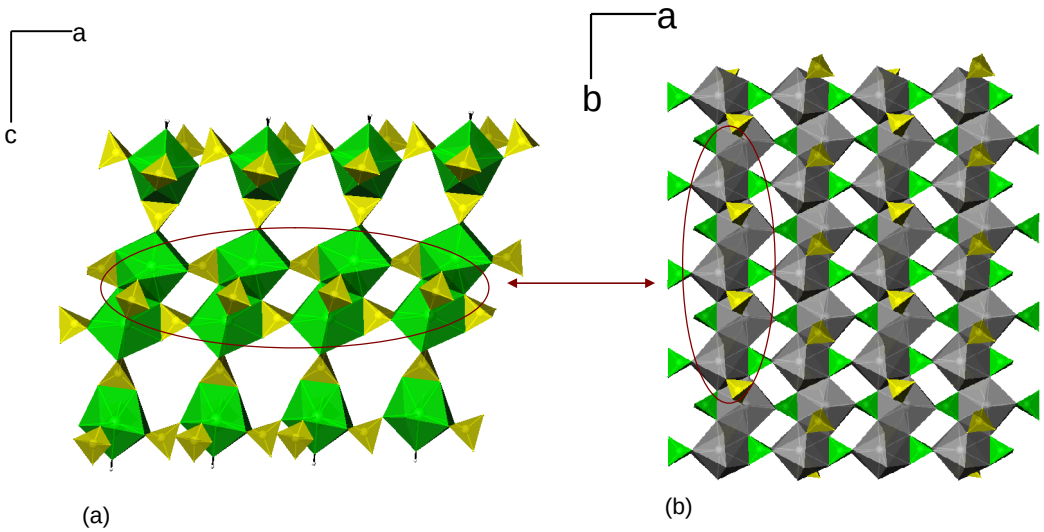

Figure 5.38. Comparison between (a) $[Dy_2(SO_4)_6(H_2O)](trienH_4)_{1.5}$ **(13)** and (b) layer formed by edge-sharing CeO_9 polyhedra through three-coordinated oxygen atoms in $[Ce(PO_4)(HSO_4)(H_2O](enH_2)$ (DyO_9 polyhedra, green; CeO_9 polyhedra, grey; SO_4 tetrahedra, yellow; PO_4 tetrahedra, green).

A wide variety of novel layered amine-templated rare-earth sulphates have been prepared over recent years. In this research project, $[Ln_2(SO_4)_6(enH)_2](enH_2)_2$ (Ln=Pr, Eu, Gd) **(14)-(16)**, $[Ln_2(SO_4)_6(H_2O)_2](enH_2)_3$ (Ln=Er, Dy) **(17)-(18)** and $[Dy(SO_4)_2](enH_2)_{0.5}$ **(19)** have been synthesised under solvothermal conditions in the presence of ethylenediamine. The structure of $[Ln_2(SO_4)_6(enH)_2](enH_2)_2$ (Ln=Pr, Eu, Gd) **(14)-(16)** comprises layers which are built up from the connection of zig-zag chains in which LnO_8N polyhedra link together through bridging edge- and vertex-sharing SO_4 tetrahedra, forming eight-membered rings. The novel feature of this structure is the existence of two different types of ethylendiamine cations within the structure. Protonated amine molecules are directly connected to the metal centre through Ln-N bonds acting as ligands, whilst diprotonated ethylenediamine molecules occupy the interlayer space and interact with the layers *via* hydrogen bonding. Among the rare-earth sulphates this feature has also been observed in the neodymium sulphate $[Nd(H_2O)(SO_4)_2][N_2H_5]$ [194], in which the hydrazine molecule is coordinated to the metal centre. This material also displays a corrugated layer built up from ladder-like zig-zag chains connected through SO_4 tetrahedra sharing vertices and edges. The linkage between neighbouring chains to form the corrugated layers in $[Ln_2(SO_4)_6(enH)_2](enH_2)_2$ (Ln=Pr, Eu, Gd) **(14)-(16)** is comparable to the connectivity in

those chains obtained in $[Dy_2(SO_4)_6(H_2O)](trienH_4)_{1.5}$ **(13)**, in which each LnO_9 polyhedron links the next polyhedron through a sulphate ion that is bidentate to one metal centre and is coordinated in a monodentate fashion to the adjacent metal centre (Figure 5.39). Analogous layers have been found in $[Ln_2(SO_4)_4(H_2O)_4][C_6N_2H_{14}]_{12}[SO_4][C_2N_2H_8][H_2O]_3$ (Ln=La, Pr, Nd) [191] in which zig-zag chains have also been identified. In $[Ln_2(SO_4)_6(enH)_2](enH_2)_2$ (Ln=Pr, Eu, Gd) **(14)-(16)** the interlayer spacing ranges from *ca.* 9. 46 Å in the gadolinium sulphate to *ca.* 9.47 Å for the europium analogue, which are shorter distances than the observed 12.78 Å in $[Ln_2(SO_4)_4(H_2O)_4][C_6N_2H_{14}]_{12}[SO_4][C_2N_2H_8][H_2O]_3$ (Ln=La, Pr, Nd). This may be associated with the presence of the larger DABCO molecules in the latter. Similar corrugated layers have been found in other rare-earth sulphate compounds, including the layered lanthanum sulphates $[C_2N_2H_{10}][La_2(H_2O)_4(SO_4)_4]\cdot 2H_2O$ [192] and $[La_2(H_2O)_2(SO_4)_6][C_2N_2H_{10}]_3\cdot 4H_2O$ [193].

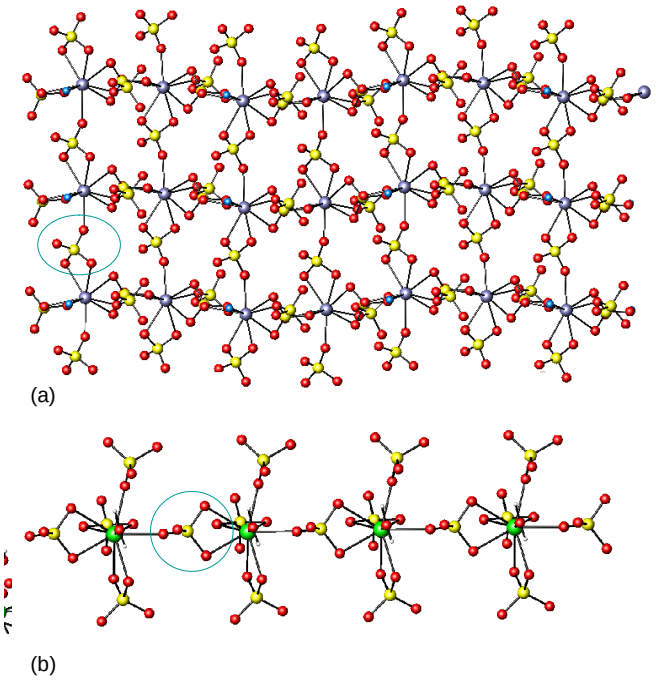

Figure 5.39. (a) Connectivity between adjacent zig-zag chains to form one layer in $[Ln_2(SO_4)_6(enH)_2](enH_2)_2$ (Ln=Pr, Eu, Gd) **(14)-(16)**; (b) Side chains in the quasi-layer of $[Dy_2(SO_4)_6(H_2O)](trienH_4)_{1.5}$ **(13)**.

The layered structure of $[Ln_2(SO_4)_6(H_2O)_2](enH_2)_3$ (Ln=Er, Dy) **(17)-(18)** is constructed from two different types of chains. The zig-zag chains are comparable to those chains observed in $[Ln_2(SO_4)_6(enH)_2](enH_2)_2$ (Ln=Pr, Eu, Gd) **(14)-(16)**. The connectivity of LnO_8 polyhedra to form the second type of chains is similar to that found in

$[Ln(INO)(H_2O)(SO_4)]_n$ (Ln=Dy, Ho) [241], in which two sulphate groups connect adjacent metal centered polyhedra creating channels of four-membered rings. In $[Ln_2(SO_4)_6(H_2O)_2](enH_2)_3$ (Ln=Er, Dy) **(17)-(18)** the two sulphate tetrahedra bridging adjacent LnO_8 are linked to the metal-centered polyhedra by shared vertices except for one that is sharing an edge with the polyhedron. In contrast, in $[Ln(INO)(H_2O)(SO_4)]_n$ (Ln=Dy, Ho), each sulphate tetrahedron is linked *via* edge sharing to one metal centered polyhedron and by vertex-sharing to the adjacent one. This type of connectivity in which two SO_4 tetrahedra serve as a linkage between metal polyhedra generating channels of four-membered rings has also been observed in transition metal sulphates [161, 163], and phosphates [171] as well as in some uranium sulphates [172]. Two examples of this type of linkage by vertex-sharing SO_4 tetrahedra are illustrated in Figure 5.40(a and b), in comparison to those chains found in $[Ln_2(SO_4)_6(H_2O)_2](enH_2)_3$ (Ln=Er, Dy) **(17)-(18)** (Figure 5.40(c)) in which the linkage to generate the four-membered rings is made through both vertex- and edge-sharing SO_4 tetrahedra.

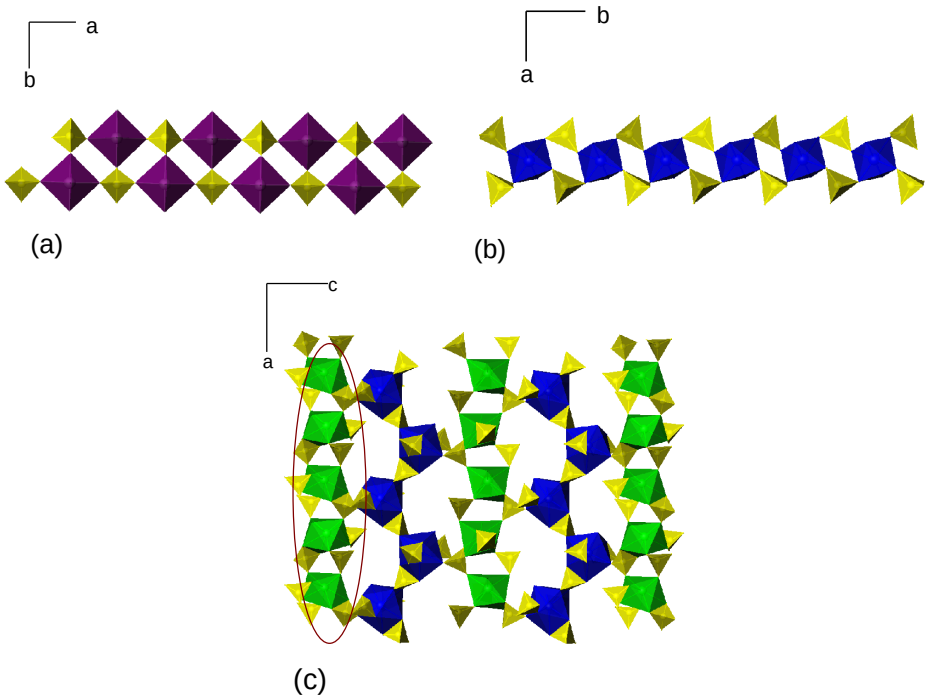

Figure 5.40. (a) Double chain of $[NH_3(CH_2)_2NH_3][FeF_3(SO_4)]$ (FeF_3O_3 octahedra, purple; SO_4 tetrahedra, yellow) [163]; (b) Chains in $[C_4N_2H_{12}][Fe_2(SO_4)_3(OH)_2(H_2O)_3]\cdot H_2O$ (FeO_6 octahedra, blue; SO_4 tetrahedra, yellow) [161]; (c) Double chains connected by zig-zag chains in $[Ln_2(SO_4)_6(H_2O)_2](enH_2)_3$ (Ln=Er, Dy) **(17)-(18)** in which four-membered rings channels are generated.

The structure of $[Dy(SO_4)_2](enH_2)_{0.5}$ **(19)** is isostructural with that of $[Ln_2(SO_4)_4](C_2N_2H_{10})$ [191], both obtained in the presence of ethylenediamine. The most remarkable feature of these structures is the presence of three three-coordinate oxygen ions that prior to the synthesis of $[Ln_2(SO_4)_4](C_2N_2H_{10})$ had only been observed in lanthanum sulphates [182]. The presence of the three-coordinated oxygen atom in that structure constituted the first example of an infinite two-dimensional Ln-O-Ln linkage formed by three-coordinate oxygen ions of sulphate. Its existence in other materials has been previously reviewed when discussing the structure of $[La(SO_4)_3](enH_2)_{1.5}$ **(12)**. The connectivity between the two metal centres that constitute the building unit of this structure is comparable to that observed in the central double chain of the quasi-layer in $[Dy_2(SO_4)_6(H_2O)](trienH_4)_{1.5}$ **(13)**, manifesting the tendency of the dysprosium anion to adopt this coordination environment. Other structures displaying this type of connectivity have been described in the discussion of the structure of $[Dy_2(SO_4)_6(H_2O)](trienH_4)_{1.5}$ **(13)**. In contrast to the structure of **(13)**, adjacent chains in $[Dy(SO_4)_2](enH_2)_{0.5}$ **(19)** are connected to each other making use of three-coordinate oxygen atoms that act as bridging units.

In the three layered structures described in this section of chapter 5, the separation between the layers appears to be very similar, of the order of *ca.* 9.4 Å for $[Ln_2(SO_4)_6(enH)_2](enH_2)_2$ (Ln=Pr, Eu, Gd) **(14)-(16)**, *ca.* 9.9 Å for $[Ln_2(SO_4)_6(H_2O)_2](enH_2)_3$ (Ln=Er, Dy) **(17)-(18)** and *ca*. 9.7 Å for $[Dy(SO_4)_2](enH_2)_{0.5}$ **(19)** which is consistent with the presence of ethylenediamine cations in the interlayer space in each of them.

Only a few three-dimensional rare-earth sulphate networks have been reported to date. $[Sm_4(SO_4)_{10}(H_2O)_4](pipH_2)_4$ **(20)**, synthesised in the presence of piperazine under solvothermal conditions, represents a novel structure. It has been found that the use of piperazine as a template plays an important role in the preparation of three-dimensional structures in which it is accommodated in the cavities within the network, as illustrated by the examples $La_2(H_2O)_2(C_4H_{12}N_2)_2(SO_4)_4$ [193] and $[C_4N_2H_{12}][Ce_8(SO_4)_{16}(H_2O)_8]$ [239]. A common characteristic that has been found in most of the three-dimensional rare-earth sulphates reported to date is the existence of eight-membered rings [188, 193, 239]. As occurs in the structure of the samarium sulphate $[Sm_4(SO_4)_{10}(H_2O)_4](pipH_2)_4$ **(20)** here described, a neodymium sulphate of formula $[Nd_2(SO_4)_4(H_2O)_2][pipH_2]$ [188] that was also obtained in the presence of piperazine, displays a three-dimensional structure built up from

twelve-membered ring apertures surrounding eight-membered rings. It differs from **(20)** in the linkage between LnO_9 polyhedra and SO_4 tetrahedra, as two NdO_9 polyhedra are linked by edge-sharing and they are simultaneously connected to adjacent pairs of polyhedra *via* bridging SO_4 tetrahedra.

Chains obtained from the connectivity of SmO_8 polyhedra and SO_4 tetrahedra in $[Sm_4(SO_4)_{10}(H_2O)_4](pipH_2)_4$ **(20)** resemble the side chains observed in the structure of $[Dy_2(SO_4)_6(H_2O)](trienH_4)_{1.5}$ **(13)**, with the difference that in this structure SO_4 tetrahedra bridge DyO_9 polyhedra by sharing edges and vertices, whereas in the structure of the samarium sulphate the connection is made *via* vertex-linking (Figure 5.41). The connectivity between the metal centres to form chains *via* sulphate anions, can also be compared to that of the chains formed in $[N_2C_{10}H_{10}][UO_2(SO_4)_2]\cdot H_2O$ [174], in which there are double chains of UO_7 polyhedra (Figure 5.42).

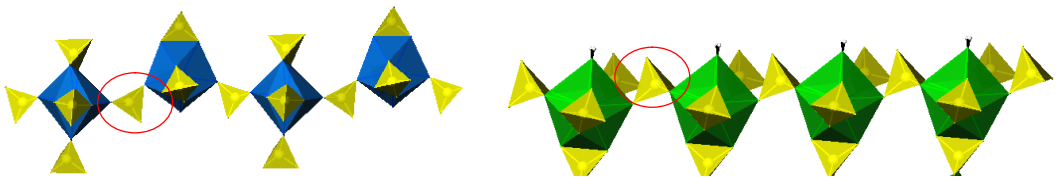

(a) (b)

Figure 5.41. Comparison of the connectivity in the chains formed by (a) SmO_8 polyhedra and SO_4 tetrahedra in $[Sm_4(SO_4)_{10}(H_2O)_4](pipH_2)_4$ **(20)**; and (b) DyO_9 polyhedra and SO_4 tetrahedra in $[Dy_2(SO_4)_6(H_2O)](trienH_4)_{1.5}$ **(13)** (SmO_8 polyhedra, blue; DyO_9 polyhedra green; SO_4 tetrahedra, yellow).

Similar eight-membered rings obtained from the connection of adjacent SmO_9 polyhedra and SO_4 tetrahedra to form the double chain in $[Sm_4(SO_4)_{10}(H_2O)_4](pipH_2)_4$ **(20)** have been observed in the three-dimensional structure of $[Ln_2(H_2O)_2(SO_4)_5][C_2N_2H_{10}]_2$ (Ln=Pr, La, Nd) [188]. In contrast to the samarium sulphate, the linkage between four metal centered polyhedra to generate the eight-membered rings is made through edge-sharing SO_4 tetrahedra, whereas in $[Sm_4(SO_4)_{10}(H_2O)_4](pipH_2)_4$ **(20)** they are connected alternatively both by edge and vertex linking. The connection of double chains to form the three-dimensional motifs containing apertures bounded by twelve-membered rings in **(20)** appears to be the first instance of the formation of this type of motifs.

As observed from thermogravimetric analysis data, the first decomposition step that takes place at 330 °C, results in the removal of diprotonated piperazine cations. That could afford cavities within this network with 9.9 Å of diameter, assuming the structure does not collapse.

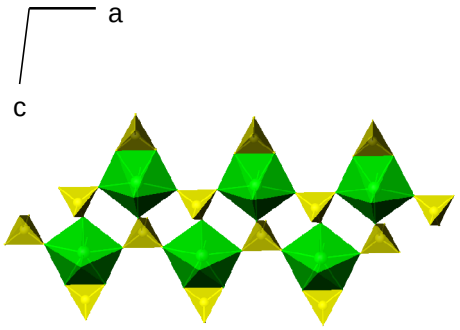

Figure 5.42. Double chain in $[N_2C_{10}H_{10}][UO_2(SO_4)_2]\cdot H_2O$ (UO_7 polyhedra, green; SO_4 tetrahedra, yellow).

5.8.1 Magnetism

Magnetic properties of rare-earth compounds differ from those of transition metals as they depend on the electrons of the incomplete 4*f* subshell. Materials are paramagnetic and the dominant interactions are long-range and dipolar in nature. The electronic states of the rare-earths may be described by using the Russell-Saunders coupling scheme. The 4*f* electrons of rare-earth ions are buried in the inner electron core and hence, they are shielded from their chemical environments. Therefore, spin-orbit coupling is substantial in the 4*f* subshell and much larger than the crystal field, in comparison to transition metals whose *d* electrons are exposed directly to the influence of neighbouring groups. As a result, the spin-only equation used to calculate the predicted magnetic moments for transition metals is not valid and the Hund-Landé equation (Eq. 5.1) is applicable for the calculation of expected magnetic moments.

$$\mu_{eff} = g\sqrt{J(J+1)}\mu_B \qquad (5.1)$$

For the most part of the lanthanide series magnetic properties are determined solely by the ground state since the separation between adjacent states is sufficient to cause the first excited state of the Ln^{III} ion to be thermally inaccessible. In such cases the Hund-

Landé equation works remarkably well, with the exception of Eu^{3+} and Sm^{3+}, which display experimental values much greater that those calculated from the equation. The reason for these discrepancies is associated with the unusually small energy separation between the lower multiplet states; consequently at room temperature a significant population of the excited states will invalidate the Hund-Landé equation. The close spacing of the lowest multiplet levels of the $4f^6$ and $4f^5$ ions suggests a second order Zeeman effect in the ground multiplet due to mixing between electronic states.

Whilst weaker than the effects of the spin-orbit coupling, crystal field effects in the lanthanide elements cannot be ignored. The effects of the crystal field are only considered for the ground state and they result in a further splitting of the 4*f* orbital energy levels by the electrostatic field of the ligands. The outcome depends on the *f*-electron configuration, the symmetry of the crystal field and the strength of the electrostatic perturbation and the spin-orbit interaction. The spin-orbit coupling tends to resist the effects of the crystal field [346]. The crystal field effects are insignificant for compounds involving $4f^7$ (Gd^{3+}) and $4f^6$ (Eu^{3+}) ions because for Gd^{3+} the ground term ^8S is an orbital singlet (L=0) and Eu^{3+} has a singlet J=0 ground state. The level J=1 will split in crystal field of lower symmetry than octahedral but since in $4f^6$ ions the excited multiplet has a second order role, it will not be affected by moderate crystal fields.

Magnetic susceptibility data for $[Dy_2(SO_4)_6(H_2O)](trienH_4)_{1.5}$ **(13)**, $[Eu_2(SO_4)_6(enH)_2](enH_2)_2$ **(15)**, $[Dy(SO_4)_2](enH_2)_{0.5}$ **(19)**, $[Ln_2(SO_4)_6(H_2O)_2](enH_2)_3$ (Ln=Er, Dy) **(17)-(18)** show paramagnetic behaviour that can be fitted according to the Curie-Weiss equation. $[Dy(SO_4)_2](enH_2)_{0.5}$ **(19)** exhibits a positive Weiss constant of the order 0.107(1) K, which is very close to zero, suggesting no magnetic interactions. For the remaining phases, the Curie-Weiss expression yields negative values for the Weiss constant which points out antiferromagnetic interactions are present between the rare-earth ions.

For $[Sm_4(SO_4)_{10}(H_2O)_4](pipH_2)_4$ **(20)** the reciprocal magnetic susceptibility could not be fitted according to the Curie-Weiss law in the range of temperatures measured (5-300 K), which indicates that this material is magnetically ordered at room temperature. The magnetic susceptibility increases as the temperature is lowered, suggesting ferromagnetic interactions. However, ferromagnetism is generally characterised by a huge magnetisation and the susceptibility of **(20)** is 0.065 e.m.u. at 5 K, which indicates possible ferrimagnetic behaviour at low temperatures. Ferrimagnetism is usually characterised by a divergence between the zero field-cooled and the field-cooled susceptibility. Therefore zero field-

cooled and field-cooled magnetic susceptibility data are required. More conclusive data will be also obtained by analysing magnetic susceptibility at different fields as well as the magnetisation as a function of field measurements.

The experimental values of the magnetic moment of Er^{3+} and Dy^{3+} ions for the phases $[Dy_2(SO_4)_6(H_2O)](trienH_4)_{1.5}$ **(13)**, $[Dy(SO_4)_2](enH_2)_{0.5}$ **(19)** and $[Ln_2(SO_4)_6(H_2O)_2](enH_2)_3$ (Ln=Er, Dy) **(17)-(18)** are in good agreement with the values calculated making use of the Hund-Landé equation and with those previously observed [371]. However, for $[Eu_2(SO_4)_6(enH)_2](enH_2)_2$ **(15)** and $[Sm_4(SO_4)_{10}(H_2O)_4](pipH_2)_4$ **(20)** there is a deviation from the Hund-Landé equation with experimental values much higher than the calculated ones, due to the second order Zeeman Effect in the ground state multiplet. The magnetic properties for Eu^{3+} and Sm^{3+} at room temperature can be explained by allowing for the thermal population of the first excited multiplet (J=1) under an applied magnetic field. Hence, the effective magnetic moment of the two-level system, which is strongly dependent on temperature, is given by [346]

$$\mu_{eff}^2 = \frac{(24 + (13.5(\lambda / kT) - 1.5)e^{-(\lambda / kT)}}{(\lambda / kT)(1 + 3e^{-(\lambda / kT)})} \tag{5.2}$$

where λ is the spin-coupling constant. Therefore, for Eu^{3+} with a value for λ=355 cm^{-1} (first multiplet interval as determined by atomic spectroscopy) and T=300 K [346], the effective magnetic moment is calculated to be 3.26 μ_B. This is consistent with the magnetic moment of Eu^{3+} for $[Eu_2(SO_4)_6(enH)_2](enH_2)_2$ **(15)** (4.291(1) μ_B), for which λ was experimentally calculated to be 298.43(2) cm^{-1} from the plot of μ_{eff}^2 as a function of temperature (Figure 5.43(a)), and with previously experimentally reported values [371]. However, for Sm^{3+} **(20)** with a greater multiplet interval (993 cm^{-1}) at T=300 K [346] the effective moment is predicted to be 1.62 μ_B. The plot of the effective magnetic moment per Sm^{3+} ion as a function of temperature gives a value at 300 K of 2.815 μ_B, with a spin-coupling constant of λ=689.28(2) cm^{-1}, which is higher than the observed experimental values [371]. All these rare-earth materials show a decrease of the magnetic moment as the temperature is lowered. Besides the antiferromagnetic interactions, the decrease in the effective magnetic moment originates in the thermal depopulation of Stark levels derived from the splitting of the free ion ground state by crystal field [372, 373]. In the case of the Eu^{3+}, the effective magnetic moment decreases upon cooling due to the depopulation of the Stark levels. At the lowest

temperature, the value of the magnetic moment should be close to zero, which indicates a *J*=0 ground state of the europium-ion. However, this value was not reached, suggesting that this phenomenon might occur at temperatures below 5 K. On the other hand, for $[Dy(SO_4)_2](enH_2)_{0.5}$ **(19)** the effective magnetic moment slightly increases upon cooling from 10.143(1) to 10.261(5) μ_B before it starts gradually decreasing. This might be due to strong dipole-dipole interactions, which are the dominant interactions between rare-earth ions.

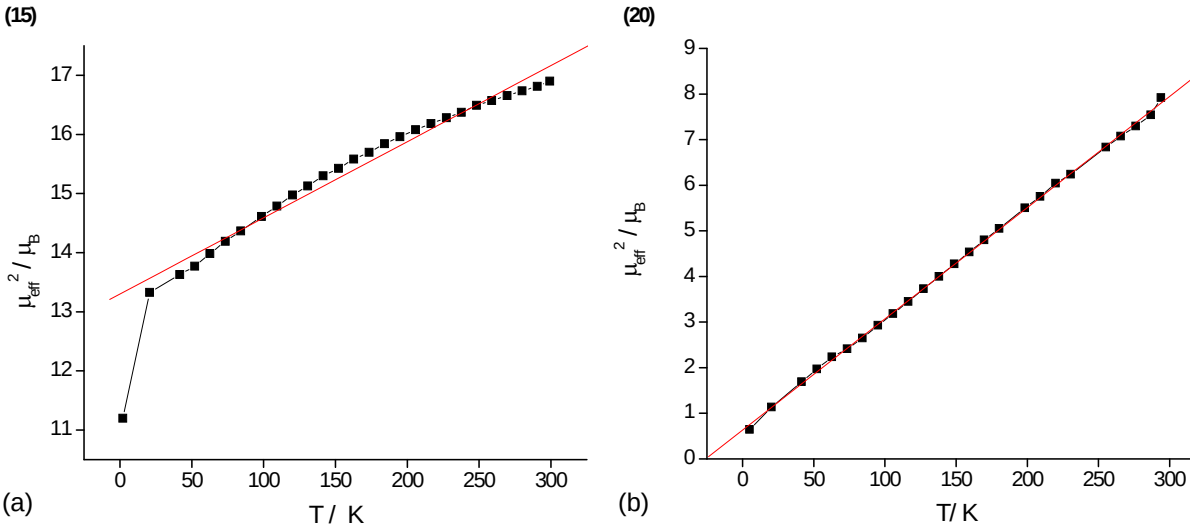

Figure 5.43. μ_{eff}^2 as a function of temperature for (a) $[Eu_2(SO_4)_6(enH)_2](enH_2)_2$ **(15)** and (b) $[Sm_4(SO_4)_{10}(H_2O)_4](pipH_2)_4$ **(20)**.

Chapter 6: Concluding Remarks and Further Work

6.1 Synthesis and crystal structures

Most recent research efforts in solid state chemistry have focused on the design and prediction of new structures and materials using a wide range of synthetic methods. The aim of this research project concentrated on the use of solvothermal and ionothermal synthesis for the generation of novel materials containing oxy-anions. Special attention has been payed to the study of the sulphate anion for the design of novel materials and its versatility as a building unit has been demonstrated with the synthesis of structures of different dimensionalities obtained through appropriate usage of the organic and inorganic components and the reaction conditions.

Ionothermal synthesis has been established as a new route for the preparation of materials containing oxy-anions. The crystal structure of a member of the family of mixed-anion materials $M_3X_4CO_3$ (M=Ba, Sr; X=Br, I) has been successfully determined for the first time by preparing single-crystals of $Ba_3Cl_4CO_3$ **(3)** under mild conditions in the presence of 1-ethyl-3-methylimidazolium bromide ([EMIM] Br) ionic liquid. Prior to this synthesis the polycrystalline nature of materials prepared by conventional solid-state reaction by a high temperature route, had precluded the determination of the crystal structure of these alkaline-earth halide carbonates. Two langbeinite-type phases $(NH_4)_2M_2(SO_4)_3$ M=Mn, Fe **(1)-(2)** have also been obtained in a straight forward low-temperature synthesis in the presence of [EMIM] Br through an unusual redox process in which sulphur is oxidised to sulphate. In this reaction the ionic liquid is believed to remain unreacted. However, it plays an important role in the synthetic route since it provides the suitable conditions for the reaction to take place. The synthesis of these materials demonstrates the potential of ionic liquids for the discovery of crystalline materials that could not be accessible using conventional techniques and its potential as an alternative synthetic route for existing materials, illustrating the wide range of open possibilities in materials chemistry. For $(NH_4)_2Mn_2(SO_4)_3$ **(1)** differential scanning calorimetry measurements were attempted in order to look for possible phase transitions at low temperatures in view of the fact that many of the langbeinite-type phases undergo phase transitions to ferroelastic or ferroelectric behaviour as the temperature is lowered. The anomaly showed by DSC measurements at 226 K, what in principle was believed to be a

phase transition, may be due to an order-disorder transition associated with motional dynamics of the ammonium and/or sulphate ions when lowering the temperature since at 100 K its crystal structure was solved to remain cubic.

Solvothermal methods have been successfully employed for the preparation of novel organically-templated transition metal and rare-earth sulphates, including the synthesis of hybrid inorganic-organic sulphates, confirming solvothermal synthesis as the preferred synthetic approach for the generation of this type of materials. This provides potential for a variety of applications and chemical properties due to the possibility of combining both the inorganic (conducting, semiconducting, magnetic and luminescent behaviour) and the organic functionalities (ferroelastic, hyperpolarizable and polymerizable behaviour).

After the works of Rao and co-workers in the preparation of a family of cadmium sulphates, the synthesis of organically transition-metal sulphates became a very challenging area of study. In this project, the system MSO_4:amine:H_2SO_4:H_2O was investigated for the generation of these materials, employing a wide variety of amines and transition-metal sulphates as well as different reaction conditions. The affinity of ethylenediamine and triethylenetetramine to participate in the generation of transition metal sulphates has been demonstrated yielding numerous new architectures with novel topologies and magnetic properties. Triethylenetetramine has been successfully employed for the generation of hybrid structures revealing the potential of this organic moiety to act as a linker between inorganic units. Under similar reaction conditions two different structures were obtained in the presence of triethylenetetramine: the novel three-dimensional manganese sulphate $[Mn_3(SO_4)_3(OH)_2(trienH_2)]$ **(6)** and the layered materials $[M(SO_4)(trien)]$ M=Mn, Fe **(7)-(8)**, demonstrating how small variations in factors such as reaction time alter significantly the crystalline products obtained. In these materials the amine is found linking inorganic layers or chains respectively, through covalent M-N bonding. In **(7)** and **(8)** the amine displays a unique connectivity to the metal centre in a bidentate fashion generating Mn-N-C-C-N five-membered rings. The crystal structure of **(6)** consists of chains made up from $Mn_4O_{18}N_2$ building blocks that are in turn connected into layers. The same building unit, of general formula M_4O_{20}, has been successfully incorporated into the structure of the four-metal cluster $[Mn_4(SO_4)_8(OH)_2(H_2O)_2](enH_2)_5$ **(4)**, built up from isolated units Mn_4O_{20} bridged by SO_4 tetrahedra, and in the layered iron sulphate $[Fe_3(SO_4)_3(OH)_2(H_2O)_2](NH_4)_2$ **(5)**, which were obtained making use of ethylenediamine and spermine, respectively. In

these two structures the amine acts as a space filler enhancing the hydrogen-bond interactions between the organic component and the framework species. Previous examples of materials containing this building unit are the one-dimensional iron phosphate $[Fe_2(OH)(H_2PO_4)(HPO_4)_2(PO_4)].0.5H_2O$ [343], the mineral sulfoborite [344] and amarantite [345] and the piperazine-templated nickel sulphate $[C_4N_2H_{12}][Ni_3F_2(SO_4)_3(H_2O)_2]$ [188]. The use of ethylenediamine also fruitfully produces the sulphates $[Mn(SO_4)_2](enH_2)$ **(9)**, $[Mn_2(SO_4)_2(en)_2]$ **(10)** and $[Co_3(SO_4)_3(OH)_2](enH_2)$ **(11)**. The structures of $[Mn(SO_4)_2](enH_2)$ **(9)** and $[Mn_2(SO_4)_2(en)_2]$ **(10)** are built up from layers comprising MnO_6 octahedra and SO_4 tetrahedra that link together sharing vertices and edges. Both structures, in which bidentate sulphate groups are present, characteristic that is very rare among the transition metal sulphates, are related to each other and both were obtained under similar conditions. Only an increase in the reaction temperature favoured the formation of the hybrid material. In $[Mn(SO_4)_2](enH_2)$ **(9)**, layers are separated by diprotonated ethylenediamine cations which are acting as space fillers, and by the substitution of two sulphate tetrahedra by two ethylenediamine molecules, the structure of $[Mn_2(SO_4)_2(en)_2]$ **(10)** was obtained. In **(10)** adjacent layers are linked *via* ethylenediamine molecules into a porous hybrid three-dimensional network with empty cavities of *ca.* 2.7 x 4.7 Å. $[Co_3(SO_4)_3(OH)_2](enH_2)$ **(11)** constitutes the first example of a novel Kagome-type layer with a unique connectivity within the layer, consisting of edge-linking CoO_6 octahedra to form triangles which are connected *via* edge-sharing octahedra. This type of connectivity differs from that of the common hexagonal rings observed in the jarosite family. Fluoride ions were not incorporated into the reaction mixture in the formation of **(11)** which represents an advantage in comparison with the synthesis of the majority of the jarosites that, to date, have been obtained using an excess of fluoride ions producing layers of vertex- or edge-sharing MF_4O_2 octahedra and SO_4 tetrahedra.

Rare-earth ions have been widely employed in the synthesis of carboxylates [349], oxalates [123, 350] and phosphate-oxalates [131] due to their ability to form porous materials and to their promising applications. However, the preparation of rare-earth sulphates has been less investigated. For that purpose, the system $Ln_2(SO_4)_3$:H_2SO_4:H_2O:amine has been explored, yielding the synthesis of a wide variety of novel rare-earth sulphates with diverse dimensionalities in which the rare-earth element exhibits different coordination geometries, confirming the potential of the solvothermal method for the synthesis of these materials. Using ethylenediamine the formation of layered

materials was enhanced, while the use of triethylenetetramine, which had proved itself as a suitable template for the synthesis of hybrid transition metal sulphates, only resulted in the formation of the ribbon-like dysprosium sulphate $[Dy_2(SO_4)_6(H_2O)](trienH_4)_{1.5}$ **(13)**. Also piperazine yielded the synthesis of the three dimensional $[Sm_4(SO_4)_{10}(H_2O)_4](pipH_2)_4$ **(20)**, amine that has been previously widely used in the generation of three-dimensional rare-earth sulphates. The crystal structures of the rare-earth sulphates obtained in this project share common characteristics, the most remarkable feature being the presence of bidentate sulphate anions. The ethylenediamine-templated one-dimensional lanthanum sulphate, $[La(SO_4)_3](enH_2)_{1.5}$ **(12)**, displays a unique structure in which La^{3+} ions exhibit a high coordination environment and three-coordinated oxygen atoms exist, which are rarely observed in rare-earth sulphates. This distinctive characteristic has also been found in the structure of $[Dy(SO_4)_2](enH_2)_{0.5}$ **(19)** and the ribbon $[Dy_2(SO_4)_6(H_2O)](trienH_4)_{1.5}$ **(13)**. In $[Dy(SO_4)_2](enH_2)_{0.5}$ **(19)** three-coordinated oxygen atoms provide the linkage between adjacent centres into chains that are in turn connected *via* three-coordinated oxygen atoms into layers, while in $[Dy_2(SO_4)_6(H_2O)](trienH_4)_{1.5}$ **(13)** the ribbon-like layers are made up from two different type of chains being the central double chain formed by adjacent metal centres connected through three-coordinated oxygen atoms. The double chain is connected to the single side chains by edge-sharing SO_4 tetrahedra which resemble to those found in the novel layered $[Ln_2(SO_4)_6(enH)_2](enH_2)_2$ (Ln=Pr, Eu, Gd) **(14)-(16)**. The structure of this material constitutes one of the few examples reported in which the amine is directly connected to the metal centre. Layers are built up from zig-zag chains which are comparable to those found in $[Ln_2(SO_4)_6(H_2O)_2](enH_2)_3$ (Ln=Er, Dy) **(17)-(18)**, which is an example of a novel structure in which these chains are cross-linked with infinite chains formed from LnO_8 polyhedra and SO_4 tetrahedra. $[Sm_4(SO_4)_{10}(H_2O)_4](pipH_2)_4$ **(20)** displays a novel genuinely three-dimensional structure in which channels of eight and twelve-membered rings are generated and occupied by piperazine cations.

6.2 Magnetic properties

One the motives for stydying transition-metal based frameworks is associated to the possibility of making frameworks that exhibit some of the properties of condensed compounds of the transition metals, such as ferromagnetism, ferroelectricity or conductivity. Also the synthesis of rare-earth frameworks may provide access to optical

and magnetic materials. For that reason one of the aims of this project was to investigate the magnetic properties of the transition-metal and rare-earth sulphates synthesised. While in transition-metal compounds magnetic interactions typically take place by superexchange, magnetic interactions between rare-earth ions are dipolar.

Magnetic measurements for $(NH_4)_2M_2(SO_4)_3$ M=Mn, Fe **(1)-(2)** showed both materials are paramagnetic with dominant antiferromagnetic exchange interactions. For **(1)** a discontinuity at 45 K was observed. EPR and magnetic measurements at different fields performed in Argentina indicate that the discontinuity might be due to a ferromagnetic transition.

Magnetic measurements showed that $[Mn_4(SO_4)_8(OH)_2(H_2O)_2](enH_2)_5$ **(4)** is paramagnetic with antiferromagnetic interactions at low temperature, whereas $[Fe_3(SO_4)_3(OH)_2(H_2O)_2](NH_4)_2$ **(5)** exhibits a complex magnetic behaviour. High-temperature magnetic susceptibility data could not be linearly fitted according to the Curie-Weiss law since the Curie point is above the range of temperatures measured (2-300 K). It is believed to be a frustrated system with ferrimagnetic behaviour. However the lack of data does not allow a conclusion and further measurements at high temperature and higher fields need to be done, including neutron diffraction measurements, to study its magnetic structure and understand its properties. In $[Mn_3(SO_4)_3(OH)_2(trienH_2)]$ **(6)** a triangular array of spins identical to that found in **(5)** has been observed. In fact, magnetic measurements for **(6)** indicate that this system may be a frustrated system that undergoes a ferrimagnetic transition at low temperature. $[Co_3(SO_4)_3(OH)_2](enH_2)$ **(11)** is an example of a frustrated system possessing the Kagome lattice, in which magnetic frustration arises from the topological arrangement of magnetic ions in the crystal lattice. Magnetic measurements at 100 G prove that this is a frustrated system in which cobalt centres interact antiferromagnetically. It is believed that the differences in connectivity of the octahedra within the layer cause an inequality in the exchange interactions, providing a mechanism for relieving the frustration and, consequently, allowing an ordered state of the spins in the Kagome lattice. It would be interesting to perform neutron diffraction measurements to study its magnetic structure and obtain more details about its properties. A profound study of these three materials would represent a significant contribution for the comprehension of spin frustration related magnetic properties as well as for the understanding of their relationship to the intrinsic magnetic moment of the magnetic ions.

$[Mn(SO_4)_2](enH_2)$ **(9)** and $[Mn_2(SO_4)_2(en)_2]$ **(10)** are both paramagnetic with short-range antiferromagnetic correlations at low temperature. The two discontinuities at *ca.* 40 K and 17 K in the reciprocal magnetic susceptibility indicate the possibility of one or more phase transitions. In order to study these transitions, single-crystal X-ray diffraction determination at low temperature and magnetic measurements at different fields are required. The effective magnetic moment of **(10)** was calculated to be 4.81(1) μ_B which is lower than the spin-only value for Mn^{2+} in high spin configuration. The origin of this phenomenon can be explained by assuming a high-spin/low-spin equilibrium governed by a Boltzmann distribution.

All the organically-templated rare-earth sulphates described in Chapter 5 show paramagnetic behaviour, with the exception of $[Sm_4(SO_4)_{10}(H_2O)_4](pipH_2)_4$ **(20)**, with a negative value for the Weiss constant which indicates antiferromagnetic exchange interactions. $[Dy(SO_4)_2](enH_2)_{0.5}$ **(19)** exhibits a positive Weiss constant, very close to zero, which suggests the absence of magnetic interactions. Reciprocal magnetic susceptibility data for $[Sm_4(SO_4)_{10}(H_2O)_4](pipH_2)_4$ **(20)** can not be fitted to the Curie-Weiss law at high temperatures which indicates this material is magnetically-ordered at room temperature. Magnetic data indicate possible ferrimagnetism but more data at different fields as well as zero field-cooled and field-cooled measurements need to be collected before reaching a conclusion. The experimental magnetic moments for Er^{3+} and Dy^{3+} ion for $[Dy_2(SO_4)_6(H_2O)](trienH_4)_{1.5}$ **(13)**, $[Dy(SO_4)_2](enH_2)_{0.5}$ **(19)** and $[Ln_2(SO_4)_6(H_2O)_2](enH_2)_3$ (Ln=Er, Dy) **(17)-(18)** correspond to those obtained using the Hund-Landé equation. However, the magnetic moments for Eu^{3+} and Sm^{3+} for $[Eu_2(SO_4)_6(enH)_2](enH_2)_2$ **(15)** and $[Sm_4(SO_4)_{10}(H_2O)_4](pipH_2)_4$ **(20)** shows a deviation from the Hund-Landé equation due to the second order Zeeman effect in the ground multiplet by which the thermal population of the first excited multiplet (J=1) under an applied magnetic field is allowed.

6.3 Further work

Future work on the synthesis of organically-templated sulphates could be directed towards the formation of mixed transition and rare-earth metal sulphates which might provide access to interesting structures with novel topologies and give rise to potential applications obtained from the combination of those associated to rare-earth elements, such as ion exchange, fluorescence, separation of lanthanide elements and ion conduction, and

those properties attributed to the incorporation of transition metals into the framework, such as magnetic or conducting behaviour. The role of the ionic liquid could also be explored as a route for the generation of this type of materials because it may provide access to compounds with new morphologies and exciting properties due to the versatility of the ionothermal method and its potential to prepare materials that are difficult to be obtained under hydrothermal conditions. One of the future goals should focus on expanding the scope of research in this area towards the design of other transition metal and rare-earth materials containing oxy-anions. Special effort should be spent in the synthesis of materials containing germanates, vanadates, molydates and borates, because they remain relatively unexplored, as well as in the generation of materials containing more than one type of oxy-anions to form hybrid structures. The combination of these ligands with transition metals or rare-earth metals would offer the possibility of discovering new materials with attractive properties that can exhibit diverse applications.

APPENDIX A: Powder X-ray diffraction data

Refinement of lattice parameters for $(NH_4)_2Mn_2(SO_4)_3$ **(1)**

Lattice parameters / Å	Parameters obtained for SCXRD	Refined parameter in TOPAS
a	10.1818(2)	10.2190(22)

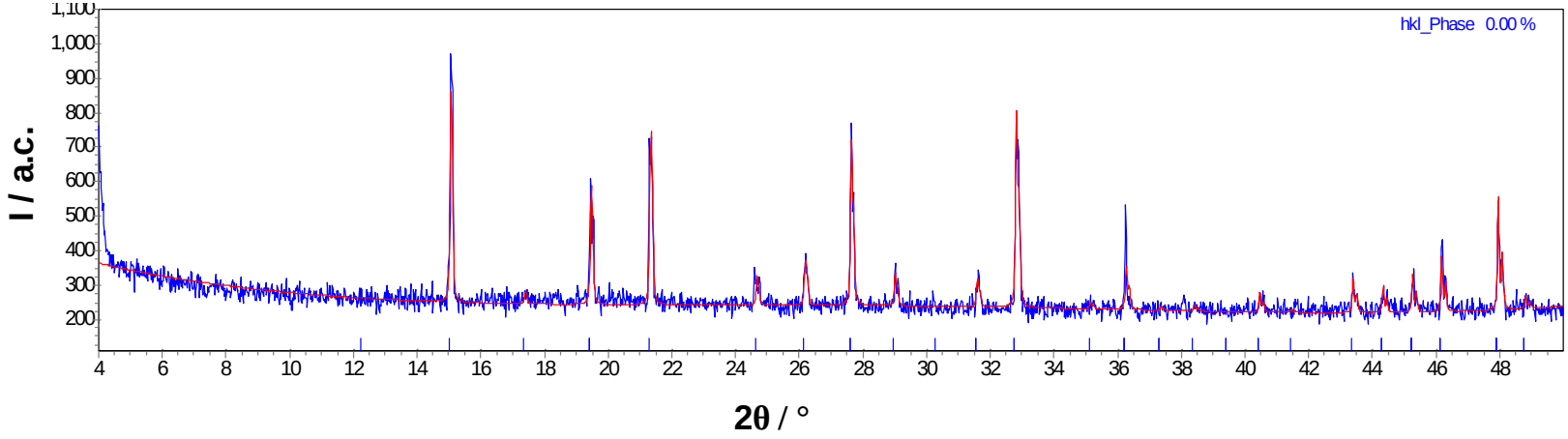

Comparison between refined (red) and observed (blue) powder X-ray diffraction pattern for **(1)**

Refinement of lattice parameters for $(NH_4)_2Fe_2(SO_4)_3$ **(2)**

Lattice parameters / Å	Parameters obtained for SCXRD	Refined parameter in TOPAS
a	10.1575(10)	10.1005(37)

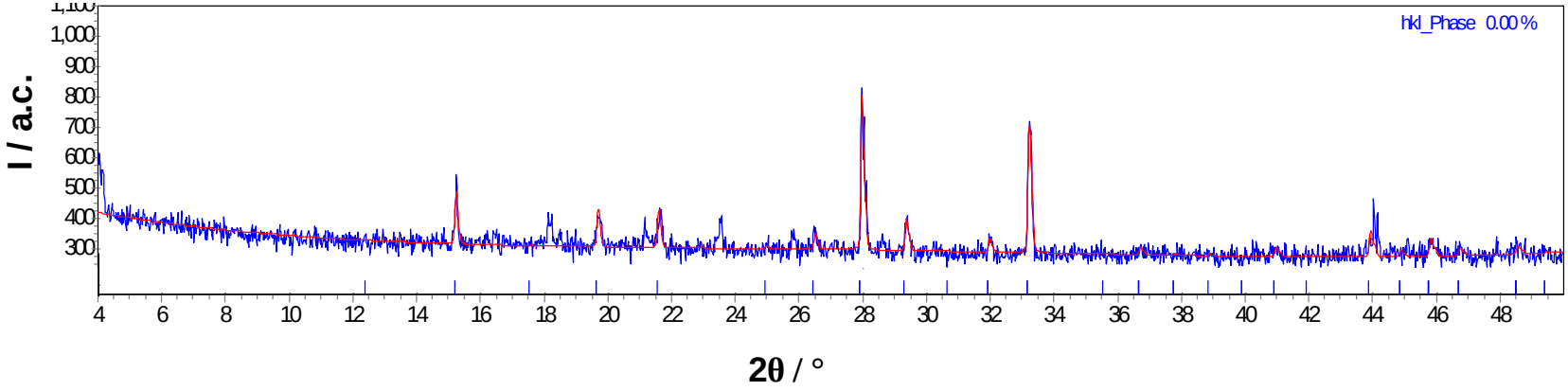

Comparison between refined (red) and observed (blue) powder X-ray diffraction pattern for **(2)**

Refinement of lattice parameters for $Ba_3Cl_4CO_3$ **(3)**.

Lattice parameters / Å	Parameters obtained for SCXRD	Refined parameter in TOPAS
a	8.4074(11)	8.4262(16)
b	9.5886(12)	9.6143(20)
c	12.4833(15)	12.4835(12)

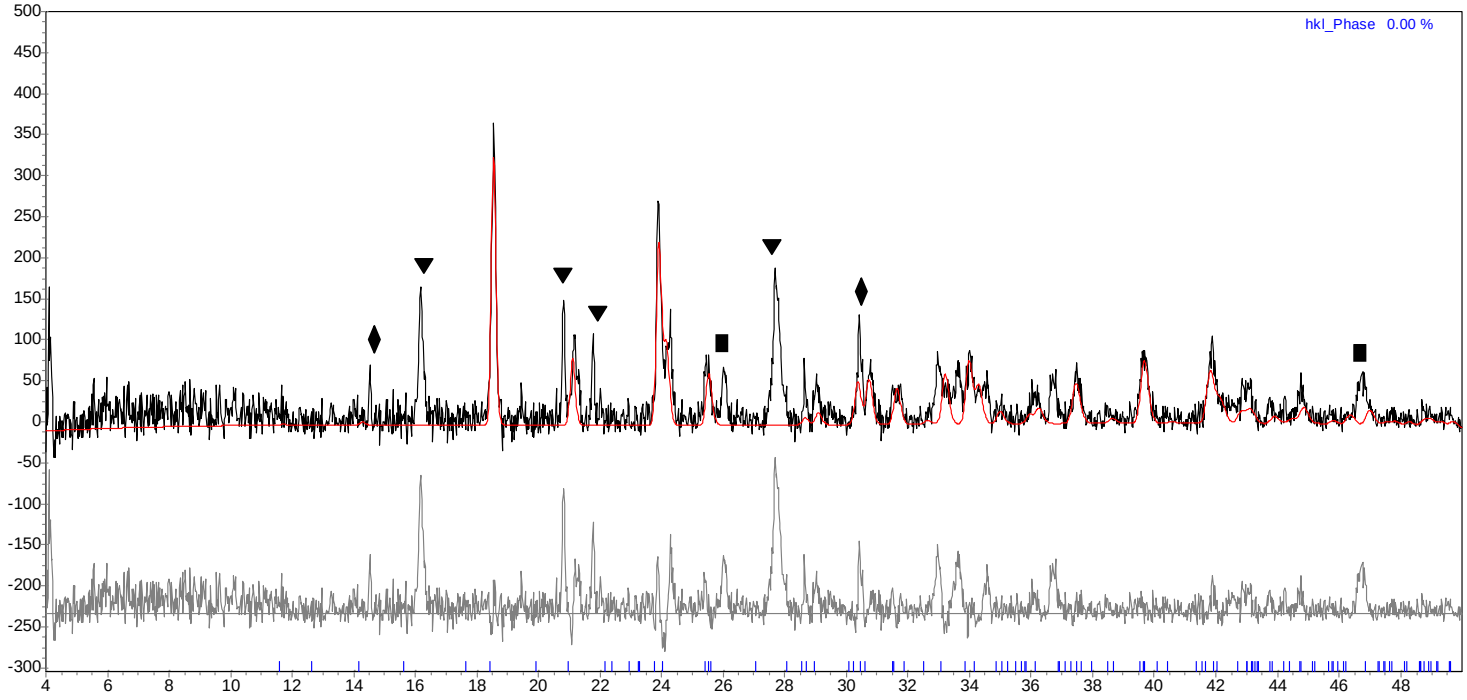

Comparison between refined (red) and observed (blue) powder X-ray diffraction pattern for **(3)**
(▼ 1-ethyl-3methylimidazolium bromide; ■ $BaCO_3$; and ♦ $CoCl_2$)

Refinement of lattice parameters for $[Mn_4(SO_4)_8(OH)_2(H_2O)_2](enH_2)_5$ **(4)**

Lattice parameters / Å	Parameters obtained for SCXRD	Refined parameter in TOPAS
a	10.2425(4)	10.2025(30)
b	14.8953(5)	14.9094(57)
c	14.1119(2)	14.1384(53)
β	92.259(2)	91.914(33)

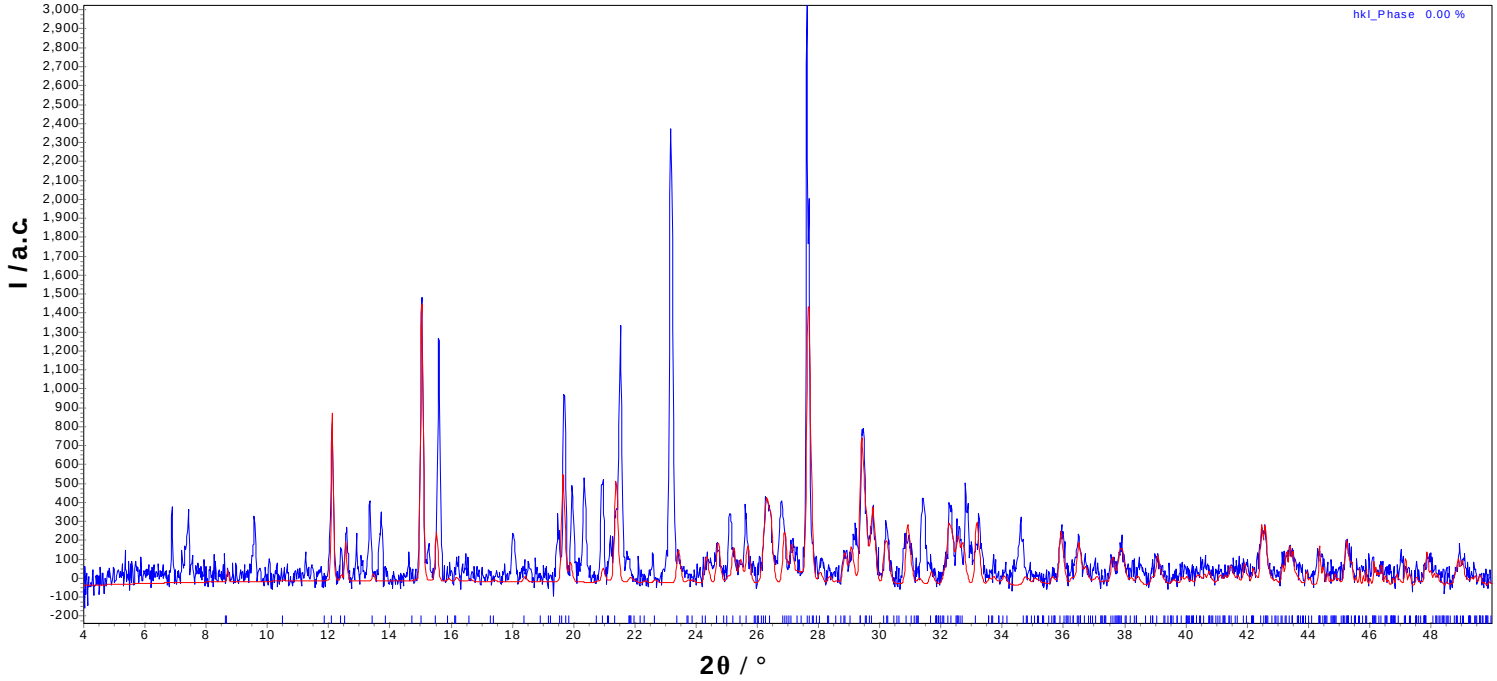

Comparison between refined (red) and observed (blue) powder X-ray diffraction pattern for **(4)**

Refinement of lattice parameters for $[Fe_3(SO_4)_3(OH)_2(H_2O)_2](NH_4)_2$ **(5)**

Lattice parameters / Å	Parameters obtained for SCXRD	Refined parameter in TOPAS
a	18.2212(9)	18.2334(37)
b	7.6804(3)	7.6790(12)
c	9.9283(4)	9.9210(20)

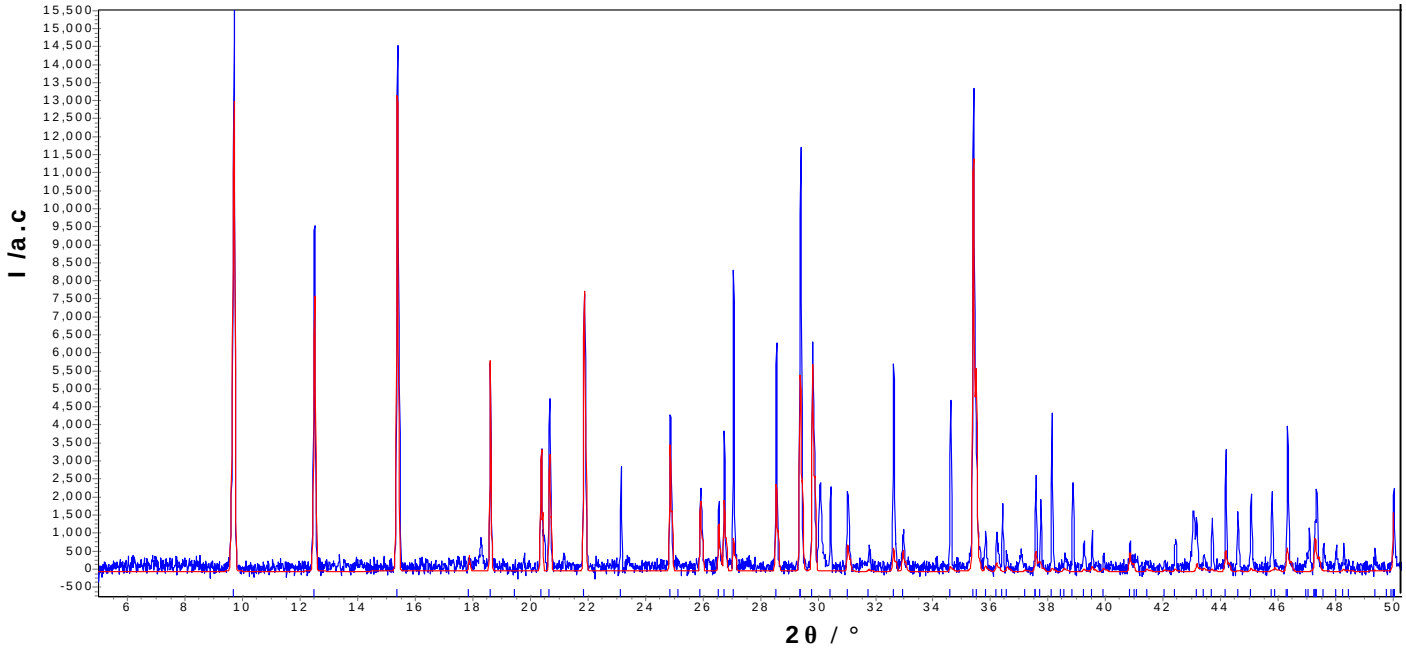

Comparison between refined (red) and observed (blue) powder X-ray diffraction pattern for **(5)**

Refinement of lattice parameters for $[Mn_3(SO_4)_3(OH)_2(trienH_2)]$ **(6)**

Lattice parameters / Å	Parameters obtained for SCXRD	Refined parameter in TOPAS
a	10.5493(5)	10.5734(15)
b	22.3799(10)	22.4277(30)
c	7.7373(15)	7.7501(12)

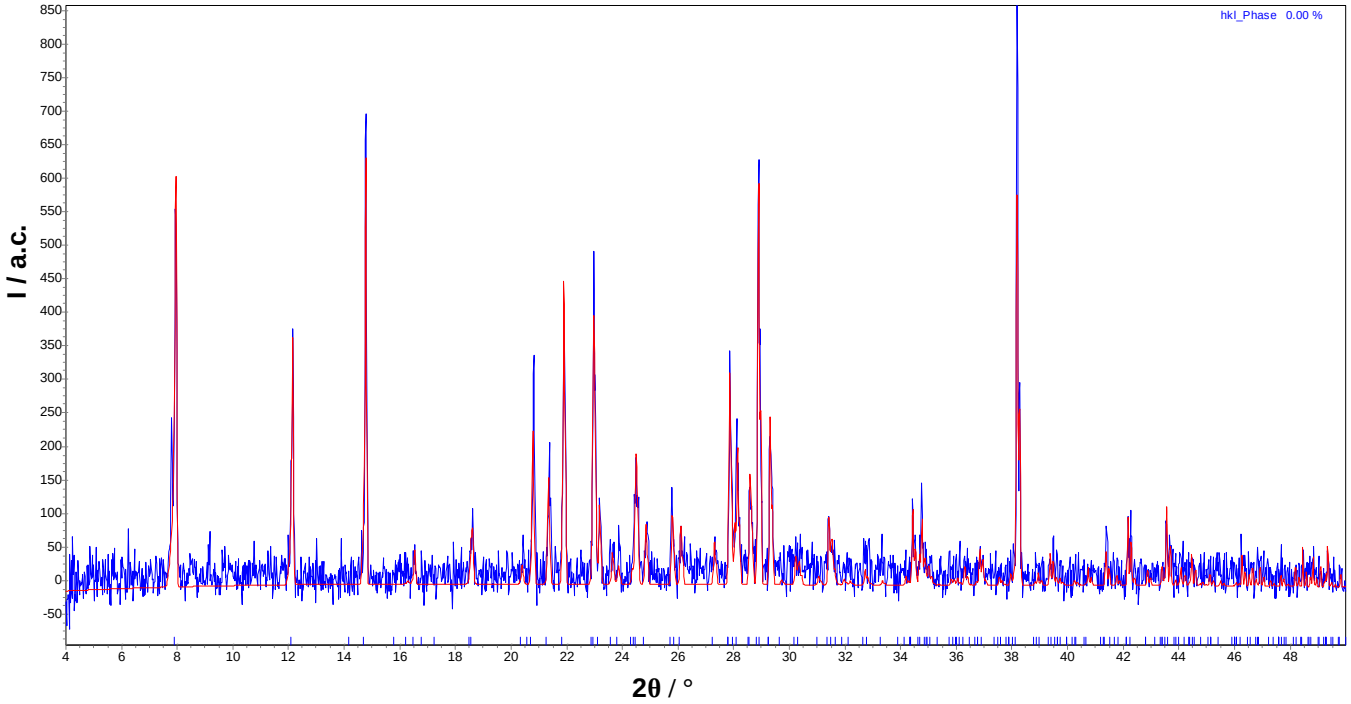

Comparison between refined (red) and observed (blue) powder X-ray diffraction pattern for **(6)**.

Refinement of lattice parameters for [Fe(SO_4)(trien)] **(8)**

Lattice parameters / Å	Parameters obtained for SCXRD	Refined parameter in TOPAS
a	7.7791(5)	7.7999(22)
b	13.1085(8)	13.1338(35)
c	11.4073(8)	11.4275(37)
β	105.234(4)	105.296(21)

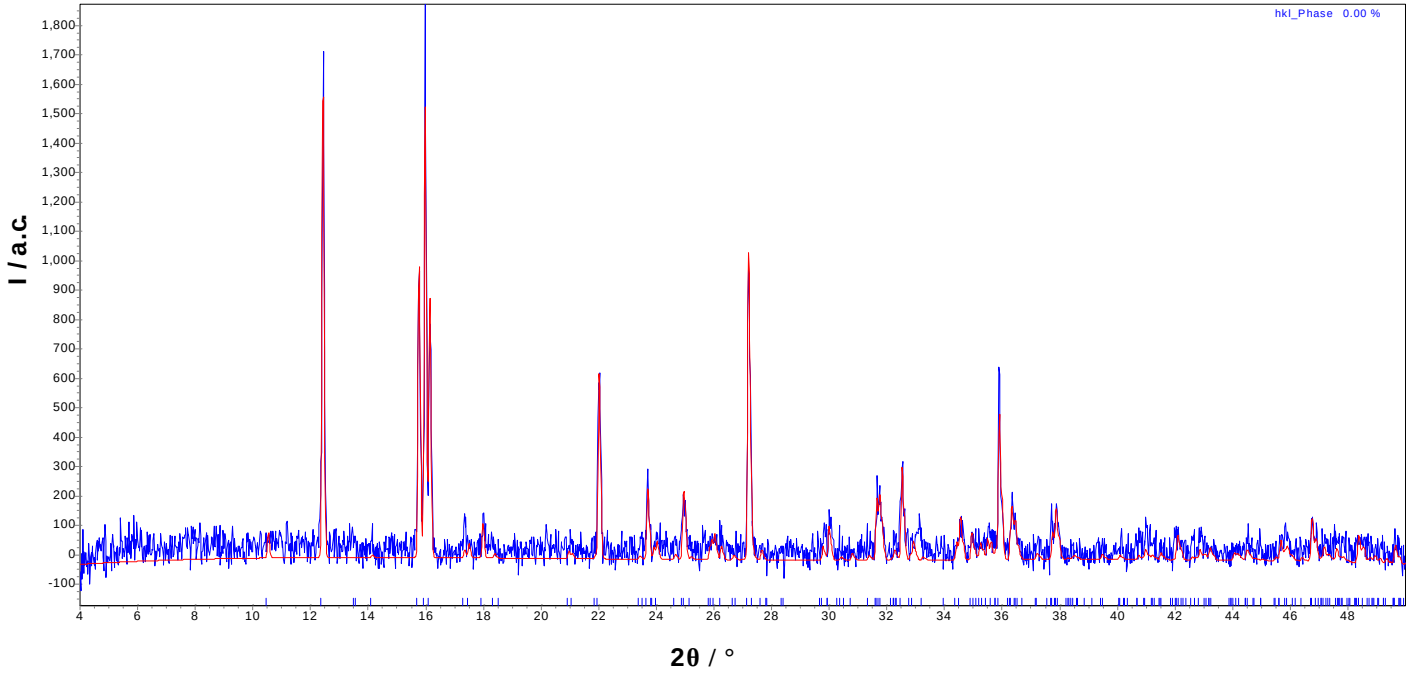

Comparison between refined (red) and observed (blue) powder X-ray diffraction pattern for **(8)**.

Refinement of lattice parameters for $[Mn(SO_4)_2](enH_2)$ **(9)**

Lattice parameters / Å	Parameters obtained for SCXRD	Refined parameter in TOPAS
a	6.6176(2)	6.6429(49)
b	5.5457(2)	5.5692(45)
c	25.8768(10)	25.9377(17)
β	90.542(2)	90.713(42)

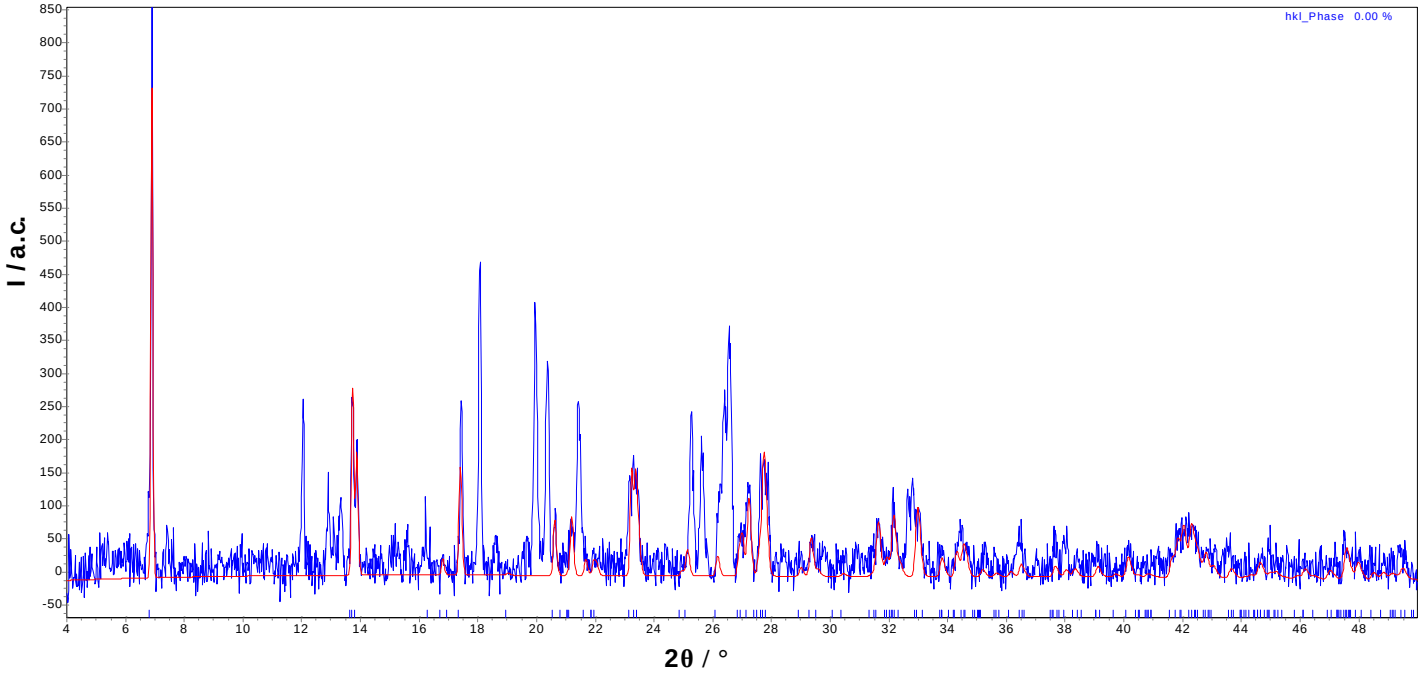

Comparison between refined (red) and observed (blue) powder X-ray diffraction pattern for **(9)**

Refinement of lattice parameters for $[Mn_2(SO_4)_2(en)_2]$ **(10)**

Lattice parameters / Å	Parameters obtained for SCXRD	Refined parameter in TOPAS
a	4.8879(2)	4.9039(20)
b	9.9791(4)	9.9904(39)
c	14.1036(7)	14.1562(55)

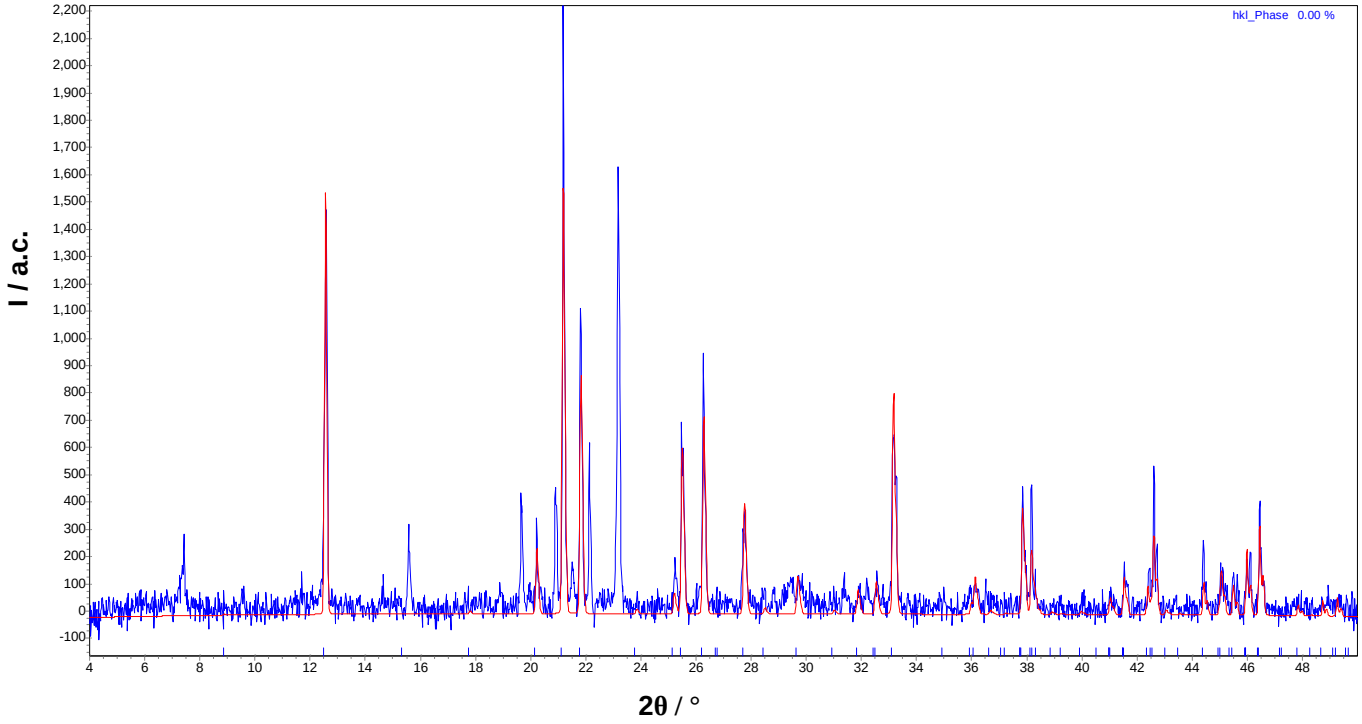

Comparison between refined (red) and observed (blue) powder X-ray diffraction pattern for **(10)**

Refinement of lattice parameters for $[Co_3(SO_4)_3(OH)_2](enH_2)$ **(11)**

Lattice parameters / Å	Parameters obtained for SCXRD	Refined parameter in TOPAS
a	11.6795(3)	11.6959(56)
b	19.9926(6)	20.0369(13)
c	8.9249(3)	8.9443(53)
β	93.1680(10)	93.0659(32)

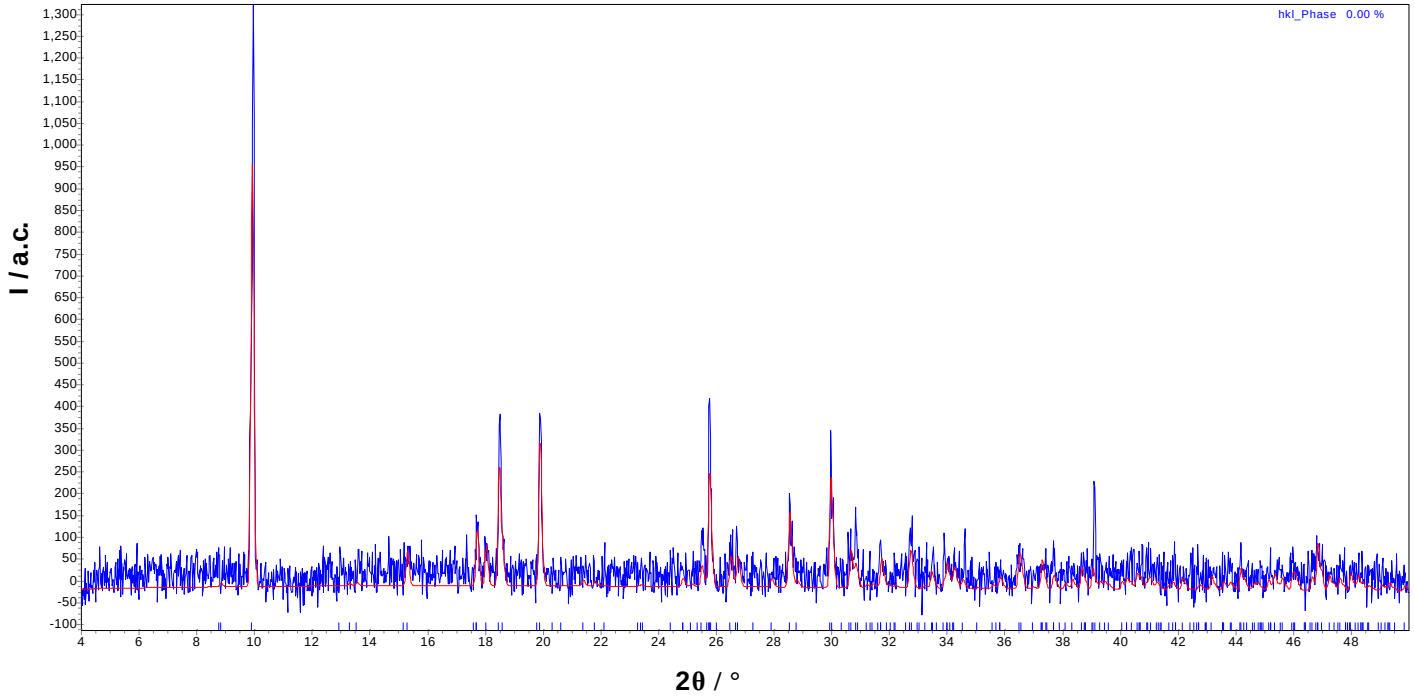

Comparison between refined (red) and observed (blue) powder X-ray diffraction pattern for **(11)**

Refined lattice parameters for $[La(SO_4)_3](enH_2)_{1.5}$ **(12)**

Lattice parameters / Å	Parameters obtained for SCXRD	Refined parameter in TOPAS
a	17.1571(3)	17.2068(13)
c	16.4207(6)	16.4778(15)

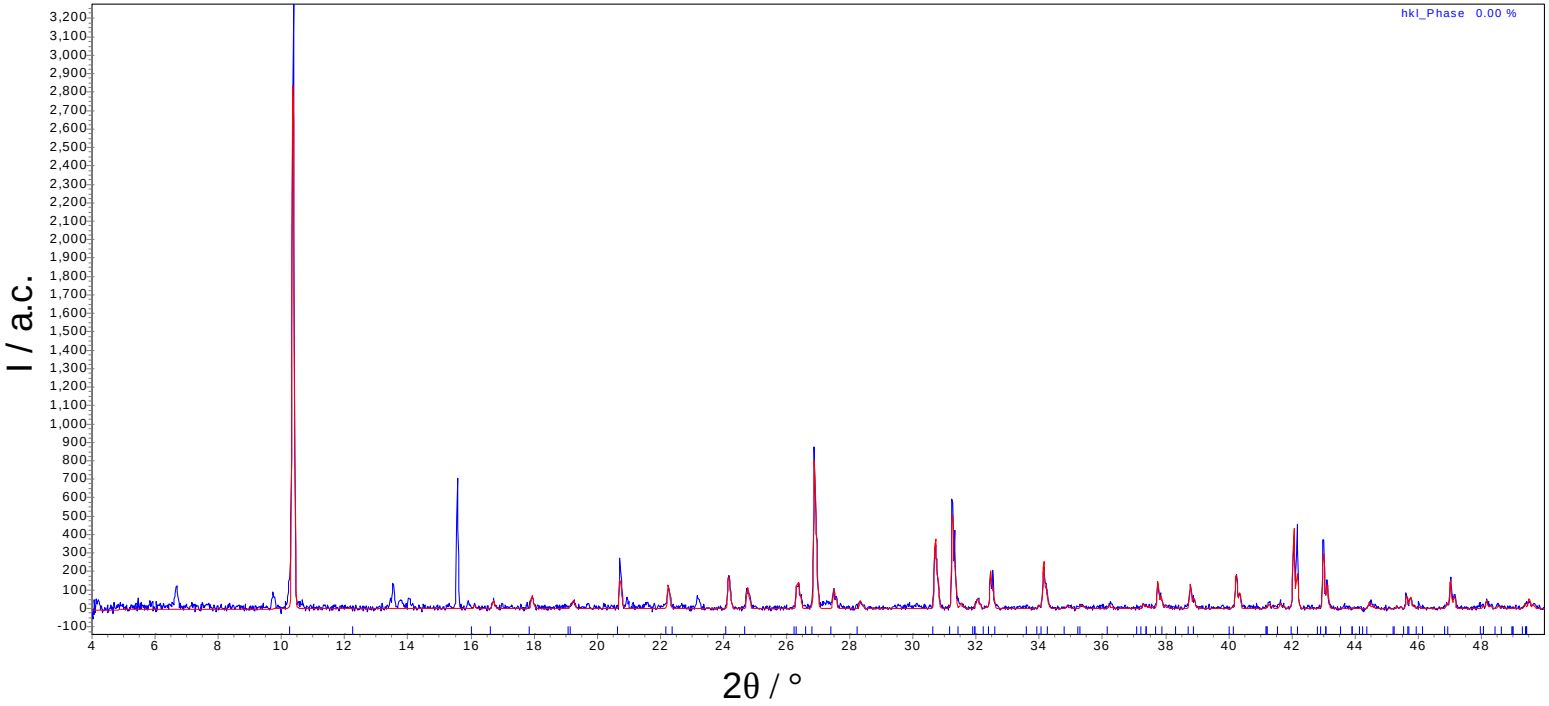

Comparison between refined (red) and observed (blue) powder X-ray diffraction data for **(12)**

Refined lattice parameters for $[Dy_2(SO_4)_6(H_2O)](trienH_4)_{1.5}$ **(13)**

Lattice parameters / Å	Parameters obtained for SCXRD	Refined parameter in TOPAS
a	6.2954(2)	6.3118(11)
b	10.8869(4)	10.9078(28)
c	22.7441(7)	22.7745(47)
α	77.893(2)	77.939(16)
β	87.936(2)	87.902(18)
γ	84.336(10)	84.336(18)

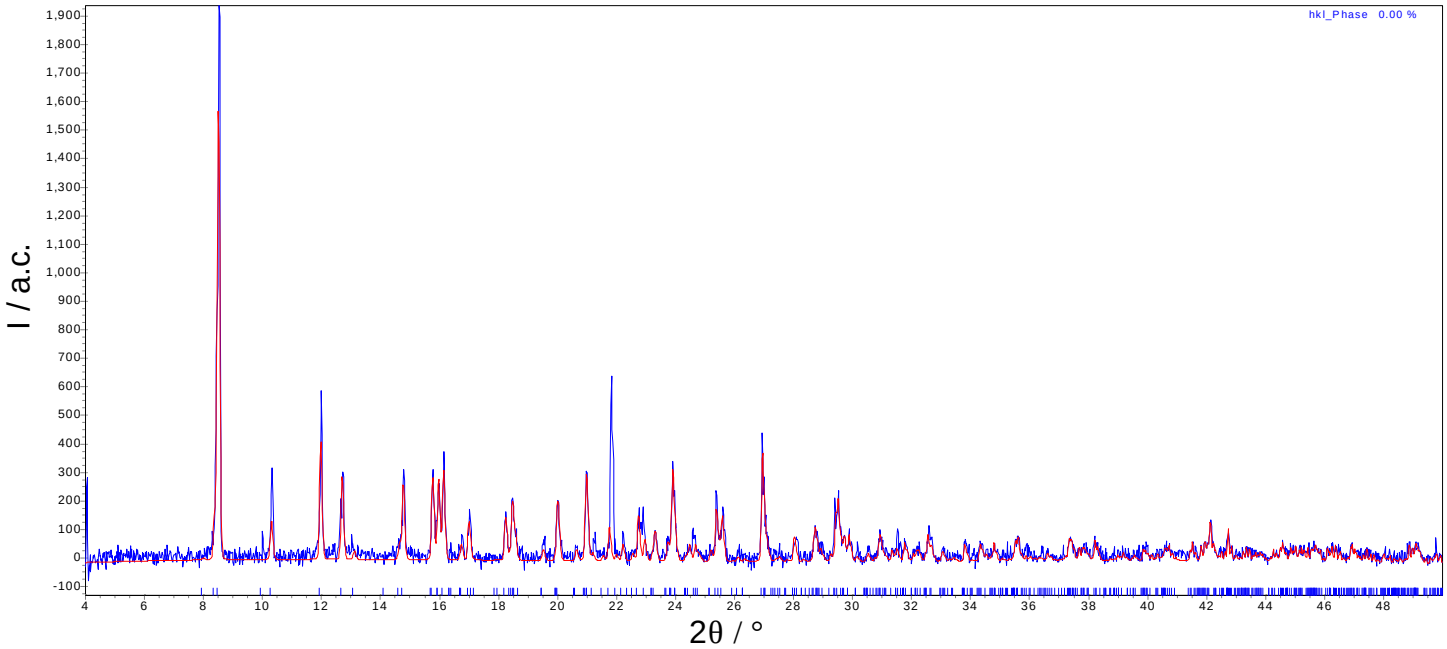

Comparison between refined (red) and observed powder X-ray diffraction data for **(13)**

Refined lattice parameters for $[Pr_2(SO_4)_6(enH)_2](enH_2)_2$ **(14)**

Lattice parameters / Å	Parameters obtained for SCXRD	Refined parameter in TOPAS
a	19.5310(11)	19.5855(42)
b	6.5898(4)	6.5917(18)
c	25.4281(19)	25.5520(69)

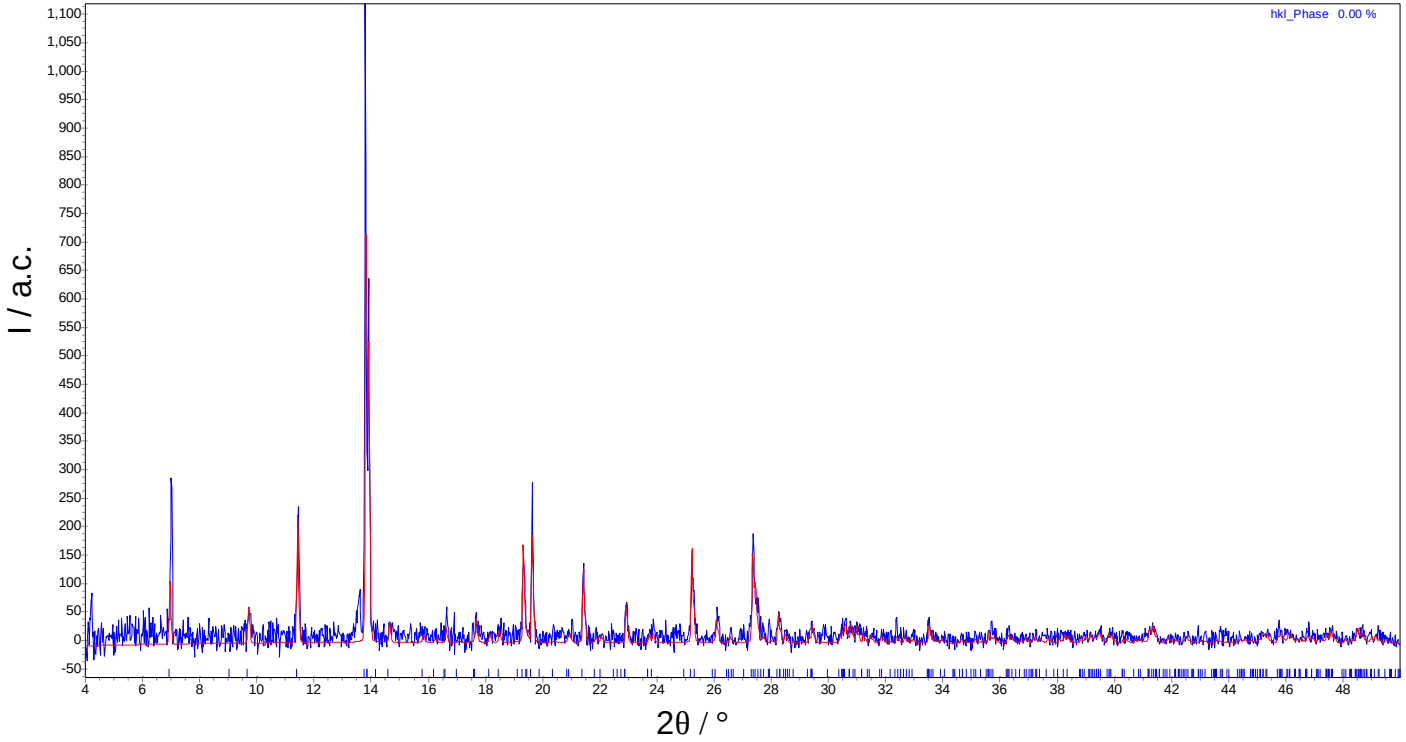

Comparison between refined (red) and observed (blue) powder X-ray diffraction data for **(14)**

Refined lattice parameters for $[Eu_2(SO_4)_6(enH)_2](enH_2)_2$ **(15)**

Lattice parameters / Å	Parameters obtained for SCXRD	Refined parameter in TOPAS
a	19.4071(17)	19.4188(57)
b	6.5238(5)	6.5419(11)
c	25.263(2)	25.3453(82)

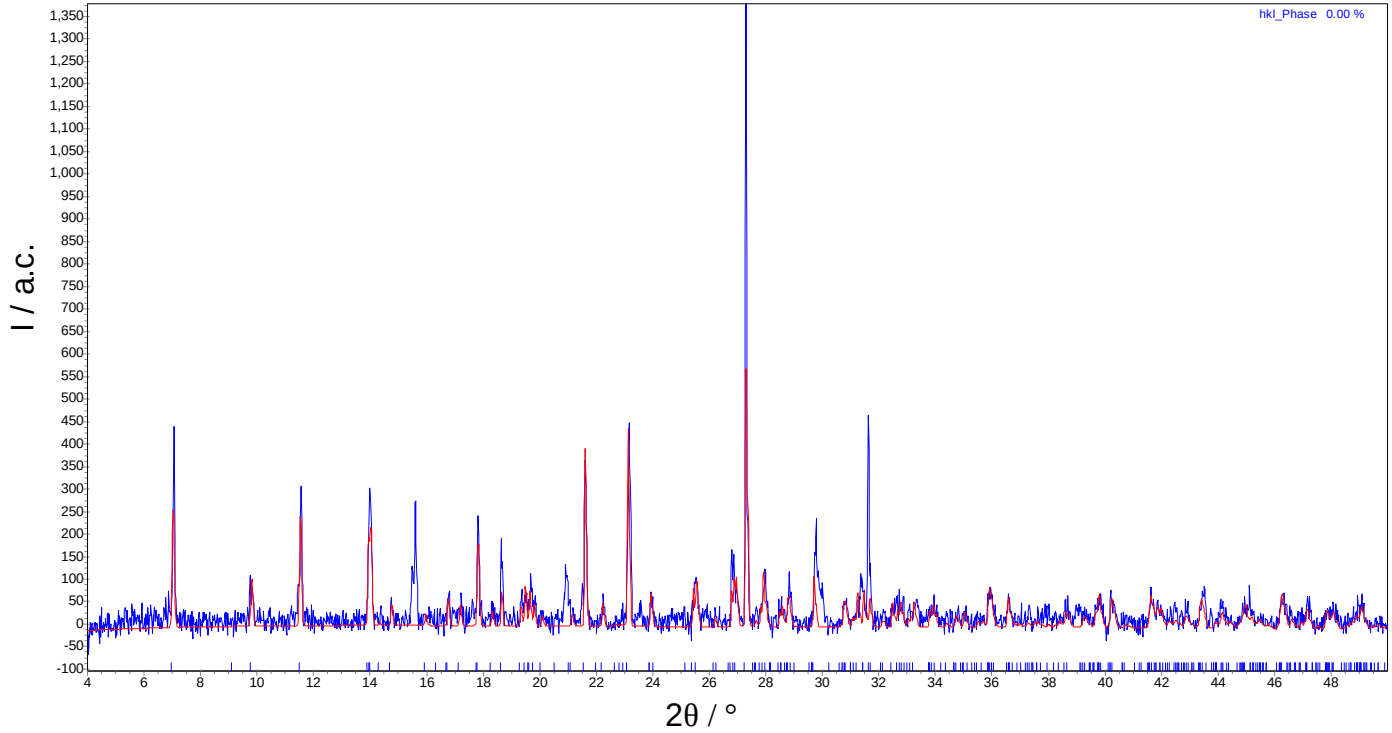

Comparison between refined (red) and observed (blue) powder X-ray diffraction data for **(15)**

Refined lattice parameters for $[Gd_2(SO_4)_6(enH)_2](enH_2)_2$ **(16)**

Lattice parameters / Å	Parameters obtained for SCXRD	Refined parameter in TOPAS
a	19.3359(6)	19.3821(15)
b	6.5175(2)	6.5432(66)
c	25.1950(8)	25.1893(30)

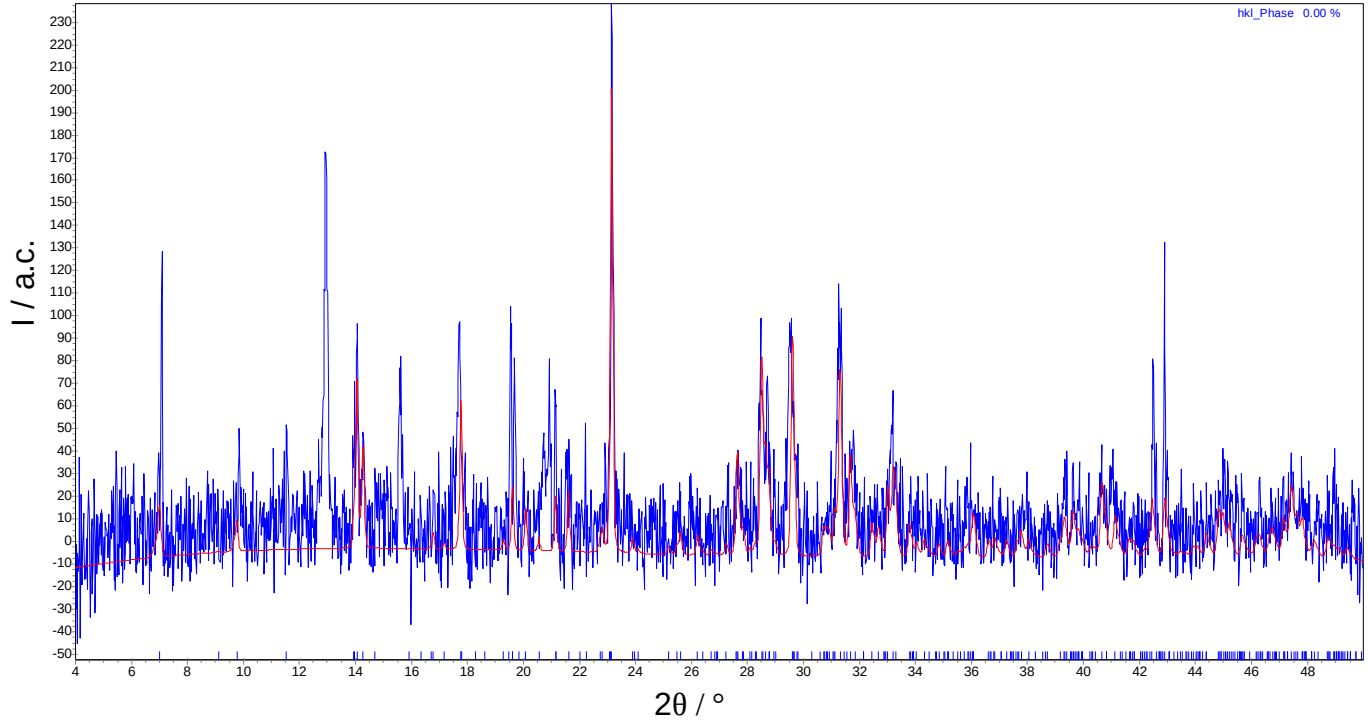

Comparison between refined (red) and observed (blue) powder X-ray diffraction data for **(16)**

Refined lattice parameters for $[Er_2(SO_4)_6(H_2O)_2](enH_2)_3$ **(17)**

Lattice parameters / Å	Parameters obtained for SCXRD	Refined parameter in TOPAS
a	9.6427(4)	9.6651(8)
b	19.9307(9)	19.9933(21)
c	30.3349(13)	30.4162(30)

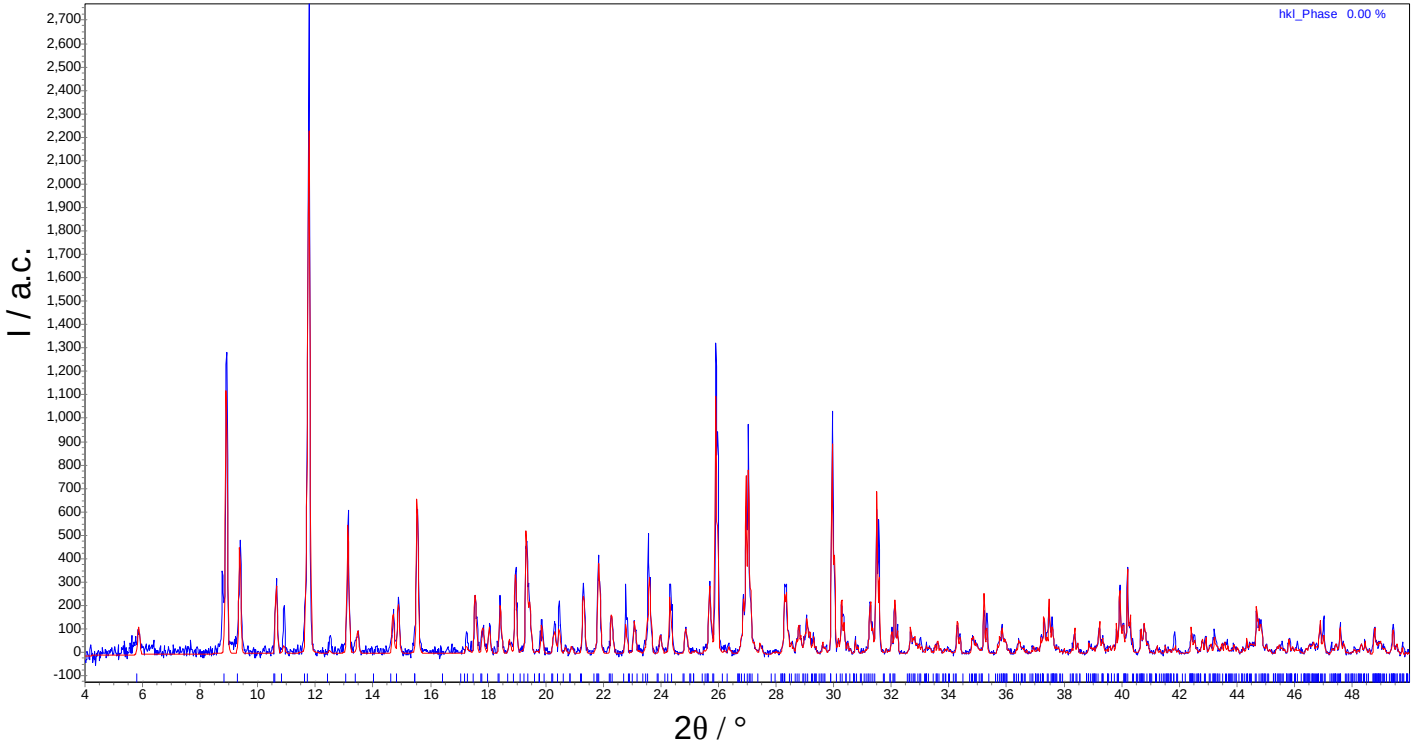

Comparison between refined (red) and observed (blue) powder X-ray diffraction data for **(17)**

Refined lattice parameters for $[Dy_2(SO_4)_6(H_2O)_2](enH_2)_3$ **(18)**

Lattice parameters / Å	Parameters obtained for SCXRD	Refined parameter in TOPAS
a	9.6396(5)	9.6724(11)
b	19.9399(12)	20.0305(20)
c	30.4327(17)	30.5007(45)

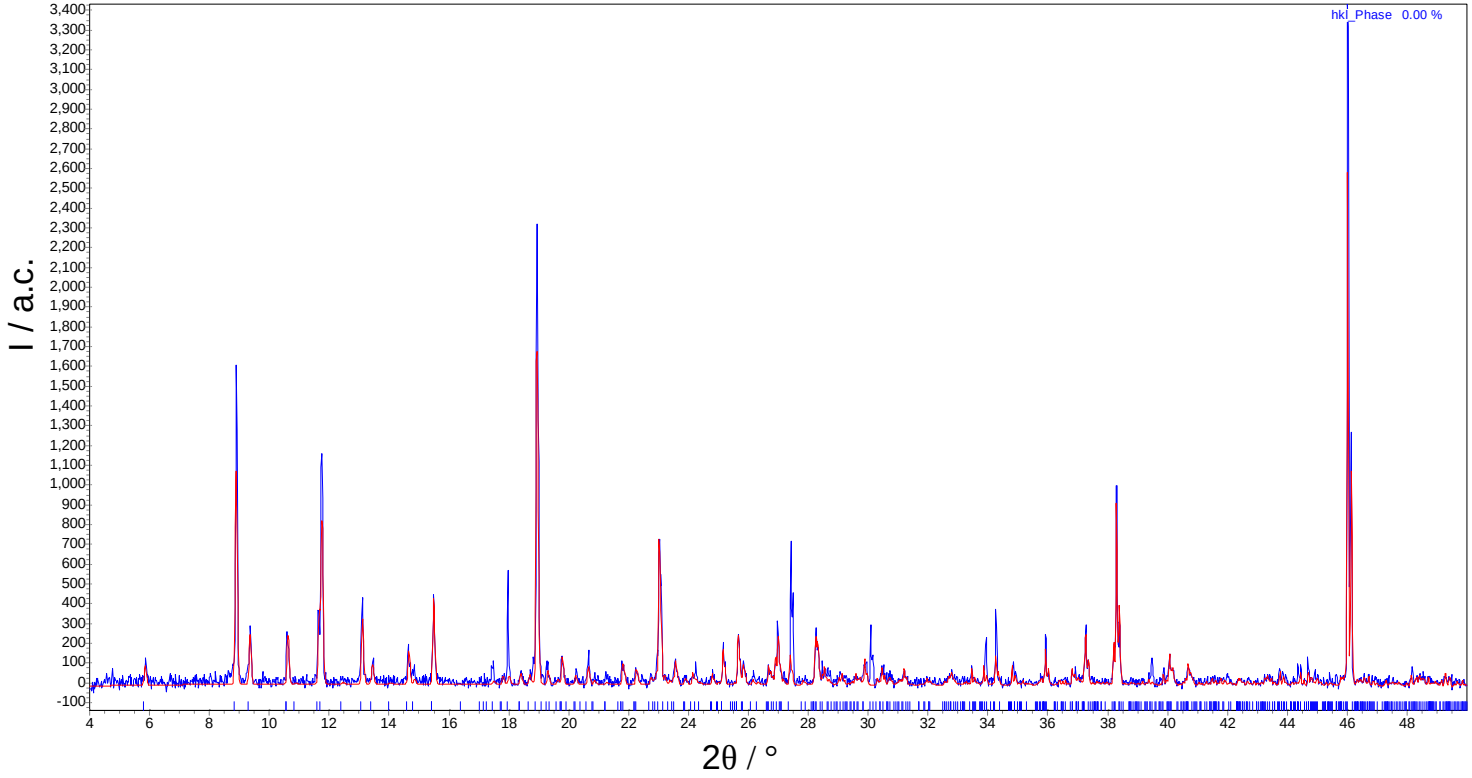

Comparison between refined (red) and observed (blue) powder X-ray diffraction data for **(18)**

Refined lattice parameters for $[Dy(SO_4)_2](enH_2)_{0.5}$ **(19)**

Lattice parameters / Å	Parameters obtained for SCXRD	Refined parameter in TOPAS
a	5.3542(2)	5.3628(20)
b	7.1078(3)	7.1185(28)
c	9.6853(3)	9.7064(29)
α	87.078(2)	87.033(19)
β	83.5850(10)	83.698(22)
γ	80.1310(10)	80.084(19)

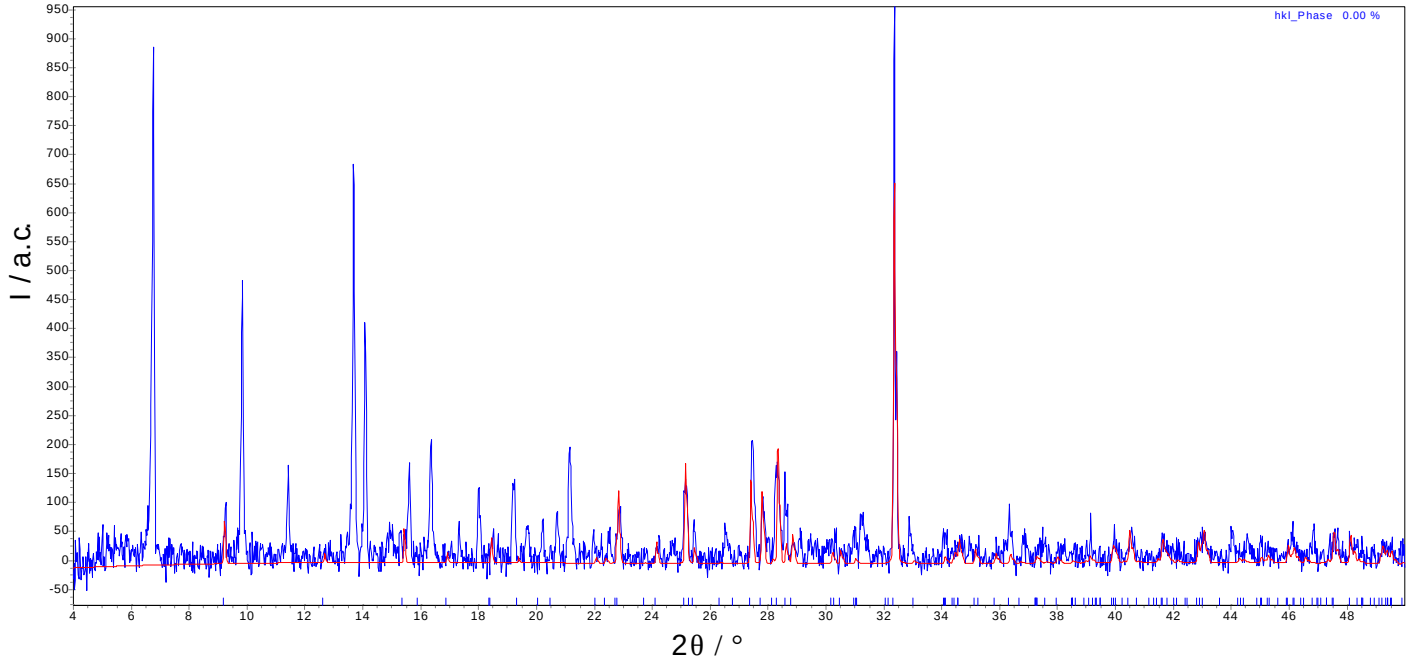

Comparison between refined (red) and observed (blue) powder X-ray diffraction data for **(19)**

Refined lattice parameters for $[Sm_4(SO_4)_{10}(H_2O)_4](pipH_2)_4$ **(20)**

Lattice parameters / Å	Parameters obtained for SCXRD	Refined parameter in TOPAS
a	19.7936(7)	19.787(24)
b	19.3266(7)	19.273(31)
c	13.2525(5)	13.257(13)
β	92.316(2)	92.355(64)

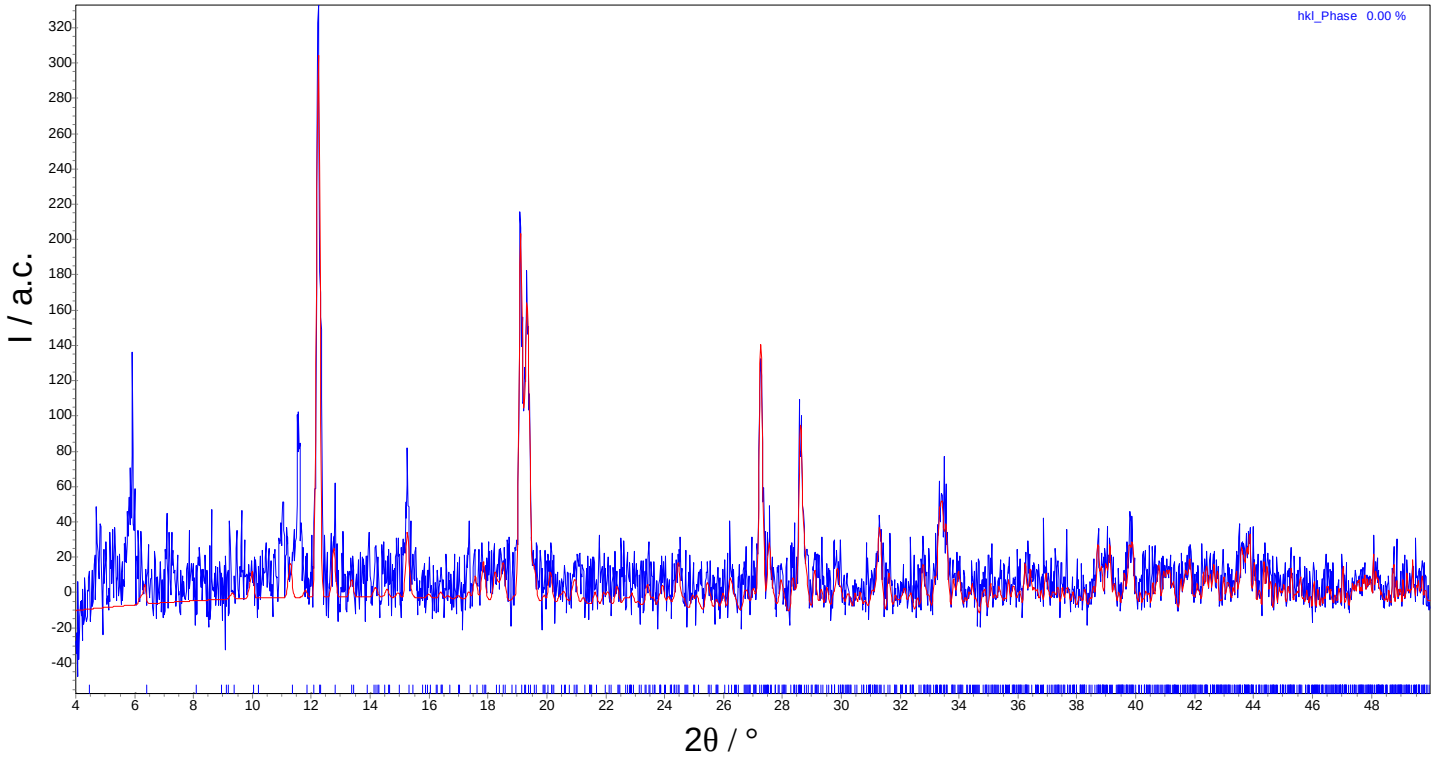

Comparison between refined (red) and observed (blue) powder X-ray diffraction data for **(20)**

REFERENCES

[1]M. G. Kanatzidis ,K. R. Poeppelmeier, *Progress in solid state chemistry*, **36**, 1 (2007).
[2]F. J. Disalvo, *Pure Appl. Chem.*, **72**, 1799 (2000).
[3]M. O'Keeffe, M. Eddaoudi, H. Li, T. Reineke ,O. M. Yagui, *J. Solid State Chem.*, **152**, 3 (2000).
[4]T. Siegrist, C. Zandbergen, J. J. Krajewski ,J. W. F. Peck, *Nature*, **367**, 254 (1994).
[5]J. L. Sarrao, L. A. Morales, J. D. Thompson, B. L. Scott, J. R. Stewart ,F. Wastin, *Nature*, **420**, 293 (2002).
[6]T. Park, F. Ronning, H. Q. Yuan, M. B. Salamon, M. Movshovich ,J. L. Serrao, *Nature*, **440**, 65 (2006).
[7]J. R. Salvador, D. Bilc, S. D. Mahanti ,M. G. Kanatzidis, *Angew. Chem. Int. Ed.*, **42**, 1929 (2003).
[8]M. G. Kanatzidis, R. Pottgen ,W. Jeitschko, *Angew. Chem. Int. Ed.*, **44**, 6996 (2005).
[9]A. J. Karkamkar ,M. G. Kanatzidis, *J. Am. Chem. Soc.*, **128**, 6002 (2006).
[10]B. M. Leonard, N. S. P. Bhuvanesh ,R. E. Schaak, *J. Am. Chem. Soc.*, **127**, 7326 (2005).
[11]A. Stein, S. W. Keller ,T. E. Mallouk, *Science*, **259**, 1558 (1993).
[12]T. L. Hennigan, D. C. MacQuarrie, P. Losier, R. D. Rogers ,M. J. Zaworotko, *Angew. Chem. Int. Ed.*, **36**, 972 (1997).
[13]B.Chen, M. Eddaoudi, S. T. Hyde, M. O'Keeffe ,O. M. Yagui, *Science*, **291**, 1021 (2001).
[14]O. M. Yagui, Z. Sun, D. A. Richardson ,T. L. Groy, *J. Am. Chem. Soc.*, **116**, 807 (1994).
[15]N. Zheng, X. Bu ,P. Feng, *Nature*, **426**, 428 (2003).
[16]N. Zheng, X. Bu, H. Vu ,P. Feng, *Angew. Chem. Int. Ed.*, **44**, 5299 (2005).
[17]A. Corma, *Chem. Rev.*, **97**, 2373 (1997).
[18]W. S. Sheldrick ,M. Wachhold, *Coord Chem. Rev.*, **176**, 211 (1998).
[19]A. K. Cheetham, G. Ferey ,T. Loiseau, *Angew. Chem. In. Ed.*, **38**, 3268 (1999).
[20]C. N. R. Rao, S. Natarajan ,R. Vaidhyanathan, *Angew. Chem. Int. Ed.*, **43**, 1466 (2004).
[21]S. Natarajan ,S. Mandal, *Angew. Chem. Int. Ed.*, **47**, 4798 (2008).
[22]E. R. Cooper, C. D. Andrews, P. S. Wheatley, P. B. Webb, P. Wormald ,R. E. Morris, *Nature*, **430**, 1012 (2004).
[23]E. R. Parnham ,R. E. Morris, *J. Am. Chem. Soc.*, **128**, 2204 (2006).
[24]C. Y. Sep, S. F. Lee ,K. H. Lii, *Inorg. Chem.*, **45**, 1891 (2006).
[25]M. E. Davis ,R. F. Lobo, *Chem. Mater.*, **4**, 756 (1992).
[26]R. E. Morris ,S. J. Weigel, *Chem. Soc. Rev.*, **26**, 309 (1997).
[27]R. M. Barrer, *J. Chem. Soc.*, 127 (1948).
[28]R. M. Milton, *US-Pat. 2882434* (1959).
[29]S. L. Lawton, D. H. Olson, W. M. Meier ,G. T. Kokotailo, *Nature*, **272**, 437 (1978).
[30]A. Taubert, *Angew. Chem. Int. Ed.*, **43**, 5380 (2004).
[31]A. Taubert, P. Steiner ,A. Mantion, *J. Phys. Chem. B.*, **109**, 15542 (2005).
[32]S. T. Wilson, B. M. Lok, C. A. Mesina, T. R. Cannan ,E. D. Flanigen, *J. Am. Chem. Soc.*, **104**, 1146 (1982).
[33]J. Yu ,R. Xu, *Chem. Soc. Rev.*, **35**, 593 (2006).
[34]J. Rocha ,M. W. Anderson, *Eur. J. Inorg. Chem.*, 801 (2000).
[35]W. Schnick ,J. Lucke, *Angew. Chem. Int. Ed.*, **31**, 213 (1992).
[36]J. D. Martin ,K. B. Greenwood, *Angew. Chem. Int. Ed.*, **36**, 2072 (1997).

[37]P. Feng, X. Bu ,N. Zheng, *Acc. Chem. Res.*, **38**, 293 (2005).
[38]C. N. Rao, J. N. Behera ,M. Dan, *Chem. Soc. Rev.*, **35**, 375 (2006).
[39]M. Eddaoudi, J. Kim, N. Rosi, D. Vodak, J. Wachter, M. O'Keefe ,O. M. Yaghi, *Science*, **295**, 469 (2002).
[40]N. L. Rosi, J. Eckert, M. Eddaoudi, D. T. Vodak, J. Kim, M. O'Keefe ,O. M. Yaghi, *Science*, **300**, 1127 (2003).
[41]O. M. Yagui ,H. Li, *J. Am. Chem. Soc.*, **118**, 295 (1996).
[42]K. S. Min ,M. S. Suh, *J. Am. Chem. Soc.*, **122**, 6834 (2000).
[43]A. Kamiyama, T. Noguchi, T. Kajiwara ,T. Ito, *Angew. Chem. Int. Ed.*, **39**, 3130 (2000).
[44]M. Fujita, Y. J. Kwon, S. Washizu ,K. Ogura, *J. Am. Chem. Soc.*, **116**, 1151 (1994).
[45]T. Sawaki ,Y. Aoyama, *J. Am. Chem. Soc.*, **121**, 4793 (1999).
[46]K. Uemura, S. Kitagawa, M. Kondo, K. Fukui, R. Kitaura, H. C. Chang ,T. Mizutani, *Chem. Eur. J.*, **8**, 3586 (2002).
[47]D. Maspoch, D. Ruiz-Molina ,J. Veciana, *Chem Soc. Rev.*, **36**, 770 (2007).
[48]W. M. Meier, D. H. Olsen ,C. Baerlocher, *Atlas of Zeolite Structure Types*, Elsevier, London (1996).
[49]R. J. Francis ,A. J. Jacobson, *Angew. Chem.*, **113**, 2963 (2001).
[50]X. Wang, L. Liu ,A. J. Jacobson, *J. Am. Chem. Soc.*, **124**, 7812 (2002).
[51]S. M. Kuznicki, K. A. Thrush, F. M. Allen, S. M. Levine, M. M. Hamil, D. T. Hayhurst ,M. Mansor, *Synth. Microporous Mater.*, **1**, 427 (1992).
[52]X. Wang ,A. J. Jacobson, *Chem. Commun.*, 973 (1999).
[53]A. I. Bortun, L. N. Bortun ,A. Clearfield, *Chem. Mater.*, **9**, 1854 (1997).
[54]R. J. Francis ,A. J. Jacobson, *Angew. Chem. Int. Ed.*, **40**, 2879 (2001).
[55]J. B. Parise, *Inorg. Chem.*, **24**, 4312 (1985).
[56]G. Ferey, *J. Fluorine Chem.*, **72**, 187 (1995).
[57]A. M. Chippindale ,A. R. Cowley, *Microporous Mesoporous Mater.*, **21**, 271 (1998).
[58]A. M. Chippindale ,A. D. Law, *J. Solid State Chem.*, **142**, 236 (1999).
[59]M. Iwamoto, H. Furukawa, Y. Mine, F. Uemura, S. L. Mikuriya ,S. Kagawa, *J. Chem. Soc., Chem. Commun.*, 1272 (1986).
[60]S. L. Brock, N. G. Duan, Z. R. Tian, O. Giraldo, H. Zhou ,S. L. Suib, *Chem. Mater.*, **10**, 2619 (1998).
[61]A. M. Chippindale ,A. R. Cowley, *J. Solid State Chem.*, **159**, 59 (2001).
[62]A. R. Cowley, R. H. Jones, S. J. Teat ,A. M. Chippindale, *Microporous Mesoporous Mater.*, **51**, 51 (2002).
[63]D. R. Corbin, J. F. Whitney, W. C. Fultz, G. D. Stucky, M. M. Eddy ,A. K. Cheetham, *Inorg. Chem.*, **25**, 2279 (1986).
[64]A. Choudhury ,S. Natarajan, *Int. J. Inorg. Mater.*, **2**, 217 (2000).
[65]S. Mandal, S. K. Pati, M. A. Green, S. L. Wang ,S. Natarajan, *Z. Anorg. Allg. Chem.*, **629**, 2549 (2003).
[66]P. Feng, X. Bu ,G. D. Stucky, *J. Solid State Chem.*, **129**, 328 (1997).
[67]J. R. D. DeBord, R. C. Haushalter ,J. Zubieta, *J. Solid State Chem.*, **125**, 270 (1996).
[68]S. Neeraj, M. L. Noy ,A. K. Cheetham, *Solid State Sci.*, **4**, 397 (2002).
[69]J. Escobal, J. L. Mesa, J. L. Pizarro, L. Lezama, R. Olazcuaga ,T. Rojo, *J. Mater. Chem.*, **9**, 2691 (1999).
[70]E. Alda, B. Bazan, J. L. Mesa, J. L. Pizarra, M. I. Arriortua ,T. Rojo, *J. Solid State Chem.*, **173**, 101 (2003).
[71]S. H. Jhung, J. S. Chang, S. E. Park, P. M. Foster, G. Ferey ,A. K. Cheetham, *Chem. Mater.*, **16**, 1394 (2004).

[72]S. H. Jhung, J. W. Yoon, J. S. Hwang, A. K. Cheetham ,J. S. Chang, *Chem. Mater.*, **17**, 4455 (2005).
[73]A. Dakhlaoui, S. Ammar ,L. S. Smiri, *Mater. Res. Bull.*, **40**, 1270 (2005).
[74]Z. Bircsak, A. K. May ,W. T. A. Harrison, *J. Solid State Chem.*, **142**, 168 (1999).
[75]R. K. Chiang, *J. Solid State Chem.*, **153**, 180 (2000).
[76]S. Neeraj, T. Loiseau, C. N. R. Rao ,A. K. Cheetham, *Solid State Sci.*, **6**, 1169 (2004).
[77]G. Z. Liu, S. T. Zheng ,G. Y. Yang, *Inorg. Chem.*, **46**, 231 (2007).
[78]R. A. Ramik, B. D. Sturman, P. J. Dunn ,A. S. Povernnykh, *Can. Mineral.*, **18**, 185 (1980).
[79]L.Liu, X. Wang, R. Bontchev, K. Ross ,A. J. Jacobson, *J. Mater. Chem.*, **9**, 1585 (1999).
[80]S. Mahesh, M. A. Green ,S. Natarajan, *J. Solid State Chem.*, **165**, 334 (2002).
[81]Y. Guo, Z. Shi, J. Yu, J. Wang, Y. Liu, N. Bai ,W. Pang, *Chem. Mater.*, **13**, 203 (2001).
[82]S. Mandal, S. Natarajan, J. M. Greneche, M. Riou-Cavellec ,G. Ferey, *Chem. Mater.*, **14**, 3751 (2002).
[83]J. Escobal, J. L. Pizarro, J. L. Mesa, L.Lezama, R. Olazcuaga, M. I. Arriortua ,T. Rojo, *Chem. Mater.*, **12**, 376 (2000).
[84]P. B. Moore, *J. Am. Mineral.*, **55**, 135 (1970).
[85]P. B. Moore ,J. Shen, *Nature*, **306**, 356 (1983).
[86]A. D. Bond, A. M. Chippindale, A. R. Cowley, J. E. Readman ,A. V. Powell, *Zeolites*, **19**, 326 (1997).
[87]N. Guillou, Q. Gao, M. Nogues, R. E. Morris, M. Hervieu, G. Ferey ,A. K. Cheetham, *C.R. Acad. Sci. Ser. IIc*, 387 (1999).
[88]J. S. Chang, S. E. Park, Q. Gao, G. Ferey ,A. K. Cheetham, *Chem. Commun.*, 859 (2001).
[89]L. Duan, M. Yuan, E. Wang, Y. Li, Y. Lu ,C. Hu, *J. Mol. Struct.*, **654**, 95 (2003).
[90]V. Soghomonian, R. C. Haushalter, J. Zubieta ,C. J. O'Connor, *Inorg. Chem.*, **35**, 2826 (1996).
[91]J. S. Chen, R. H. Jones, S. Natarajan, M. B. Hursthouse ,J. M. Thomas, *Angew. Chem. Int. Ed.*, **33**, 639 (1994).
[92]S. Natarajan, S. Neeraj, A. Choudhury ,C. N. R. Rao, *Inorg. Chem.*, **39**, 1426 (2000).
[93]W. K. Chang, R. K. Chiang, Y. C. Jiang, S. L. Wang, S. F. Lee ,K. H. Lii, *Inorg. Chem.*, **43**, 2564 (2004).
[94]Y. L. Lai, R. K. Chiang, K. H. Lii ,S. L. Wang, *Chem. Mater.*, **20**, 523 (2008).
[95]D. J. Price, A. K. Powell ,P. T. Wood, *J. Chem. Soc. Trans.*, 200 (2000).
[96]M. Eddaoudi, J. Kim, N. Rosi, D. Vorak, J. B. Wachter, M. O'Keefe ,O. M. Yagui, *Science*, **295**, 469 (2002).
[97]S. R. Batten, B. F. Hoskins, B. Moubaraki, K. S. Murray ,R. Robson, *Chem. Commun.*, 1095 (2000).
[98]G. Dong, Z. Biang-Guang, D. C. Ying, P. Ke-Liang ,M. Qing-Jin, *Chem. Soc. Dalton Trans.*, 3783 (2002).
[99]Y. Laget, C. Hornick ,M. Drillon, *J. Mater. Chem.*, **9**, 169 (1999).
[100]S. Yamanaka, T. Sako, K. Seki ,M. Hattori, *Solid State Ionics*, **53**, 527 (1992).
[101]J. Legendziewicz, M. Borzechowka, G. Oczko ,G. Meyer, *New J. Chem.*, **24**, 53 (2000).
[102]I. Kutlu, G. Meyer, G. Oczko ,J. Legendziewicz, *Eur. J. Solid State Inorg.*, **34**, 231 (1997).
[103]R. Vaidhyanathan, S. Natarajan ,C. N. R. Rao, *Inorg. Chem.*, **41**, 5226 (2002).
[104]P. M. Forster ,A. K. Cheetham, *Chem. Mater.*, **14**, 17 (2002).

[105]N. L. Rosi, M. Eddaoudi, J. Kim, M. O'Keefe ,O. M. Yagui, *CrystEngComm.*, **4**, 401 (2002).
[106]M. Eddaoudi, J. Kim, M. O'Keefe ,O. M. Yagui, *J. Am. Chem. Soc.*, **124**, 376 (2002).
[107]N. Guillou, S. Patre, C. Livage ,G. Ferey, *Chem. Commun.*, 2358 (2002).
[108]C. Livage, C. Egger, M. Nogues ,G. Ferey, *J. Mater. Chem.*, **8**, 2743 (1998).
[109]F. Serpaggi ,G. Ferey, *J. Mater. Chem.*, **8**, 2737 (1998).
[110]S. Decurtins, H. W. Schamalle, P. Schneuwly, L. M. Zheng, J. Ensling ,A. Hauser, *Inorg. Chem.*, **34**, 5501 (1995).
[111]H. K. Fun, S. S. S. Raj, X. Fang, L. M. Zheng ,X. Q. Xin, *Acta Cryst.*, **C55**, 903 (1999).
[112]D. Deguenon, G. Bernardinelli, J. P. Tuchagues ,P. Castan, *Inorg. Chem.*, **29**, 3031 (1990).
[113]B. Modec, J. V. Brencic, D. Dolenc ,J. Zubieta, *J. Chem. Soc., Dalton Trans.*, 4582 (2002).
[114]H. Tamaki, Z. J. Zhong, N. Matsumoto, S. Kida, M. Koikawa, N. Achiwa, Y. Hashimoto ,H. Okawa, *J. Am. Chem. Soc.*, **114**, 6974 (1992).
[115]E. Coronado, M. Clemente-Leon, J. R. Galan-Mascaros, C. Gomenez-Saiz, C. J. Gomez-Garcia ,E. Martinez-Ferrero, *J. Chem. Soc., Dalton Trans.*, 3955 (2000).
[116]E. Coronado, J. R. Galan-Mascaros, C. J. Gomez-Garcia ,J. M. Martinez-Agudo, *Adv. Mater.*, **11**, 558 (1999).
[117]W. W. Wendlandt, T. D. George ,G. R. Horton, *J. Inorg. Nucl. Chem.*, **273**, 273 (1961).
[118]I. L. Jenkins, F. H. Moore ,M. J. Waterman, *J. Inorg. Nucl. Chem.*, **27**, 77 (1965).
[119]I. A. Kahwa, F. R. Fronczek ,J. Selbin, *Inorg. Chim. Acta*, **82**, 167 (1984).
[120]I. A. Kahwa ,J. Selbin, *J. Therm. Anal.*, **28**, 359 (1983).
[121]T. Bataille ,D. Louer, *Acta Cryst.*, **B56**, 998 (2000).
[122]P. Klauss, J. P. Sutter, S. Golhen, L. Quahab ,O. Khan, *Inorg. Chem.*, **39**, 1626 (2000).
[123]D. Trollet, S. Romero, A. Mosset ,J. C. Trombe, *C. R. Acad. Sci. Paris Ser. IIb*, **325**, 663 (1997).
[124]S. Romero, A. Mosset ,J. C. Trombe, *Eur. J. Solid State Inorg. Chem.*, **34**, 209 (1997).
[125]T. Bataille, M. Louer, J. P. Auffredic ,D. Louer, *J. Solid State Chem.*, **150**, 81 (2000).
[126]T. Bataille, J. P. Auffredic ,D. Louer, *J. Mater. Chem.*, **10**, 1707 (2000).
[127]A. E. Bradley, J. E. Hatter, M. Nieuwenhuyzen, W. R. Pitner, K. R. Seddon ,R. C. Thied, *Inorg. Chem.*, **41**, 1692 (2002).
[128]R. Vaidhyanathan, S. Natarajan ,C. N. R. Rao, *Chem. Mater.*, **13**, 185 (2001).
[129]R. Vaidhyanathan, S. Natarajan ,C. N. R. Rao, *Inorg. Chem.*, **41**, 4496 (2002).
[130]Z. A. D. Lethbridge, A. D. Hillier, R. Cywinski ,P. Lightfoot, *J. Chem. Soc., Dalton Trans.*, 1595 (2000).
[131]A. Choudhury, S. Natarajan ,C. N. R. Rao, *Chem. Eur. J.*, **6**, 1168 (2000).
[132]P.Smith-Verdier ,S. Garcia-Blanco, *Z. Kristallogr.*, **151**, 175 (1980).
[133]A. Wittmann, *Fortschr. Miner.*, **43**, 230 (1966).
[134]R. J. Francis ,A. J. Jacobson, *Chem. Mater.*, **13**, 4676 (2001).
[135]M. A. Monge, E. Gutierrez-Puebla, C. Cascales ,J. A. Campa, *Chem. Mater.*, **12**, 1926 (2000).
[136]H. Li, M. Eddaoudi, J. Plevert, M. O'Keefe ,O. M. Yagui, *J. Am. Chem. Soc.*, **122**, 12409 (2000).
[137]B. Bazan, J. L. Mesa, J. L. Pizarro, A. T. Aguayo, M. I. Arriortua ,T. Rojo, *Chem. Commun.*, 622 (2003).

[138]B. Bazan, J. L. Mesa, J. L. Pizarro, J. Rodríguez-Fernandez, J. Sanchez-Marcos, A.Roig, E. Molins, M. I. Arriortua ,T. Rojo, *Chem. Mater.*, **16**, 5249 (2004).
[139]W. T. A. Harrison, M. L. F. Phillips, J. Stanchfield ,T. M. Nenoff, *Angew. Chem. Int. Ed.*, **39**, 3808 (2000).
[140]A. Choudhury, D. Udayakumar ,C. N. R. Rao, *Angew. Chem. Int. Ed.*, **41**, 158 (2002).
[141]D. Udayakumar ,C. N. R. Rao, *J. Mater. Chem.*, **13**, 1635 (2003).
[142]F. Millange, C. Serre, T. Cabourdin, J. Marrot ,G. Ferey, *Solid State Sci.*, **6**, 229 (2004).
[143]I. Pasha, A. Choudhury ,C. N. R. Rao, *Solid State Sci.*, **5**, 257 (2003).
[144]Z. Dai, Z. Shi, G. Li, X. Chen, X. Lu, Y. Xu ,S. Feng, *J. Solid State Chem.*, **172**, 205 (2003).
[145]Z. Dai, X. Chen, Z. Shi, D. Zhang, G. Li ,S. Feng, *Inorg. Chem.*, **42**, 908 (2003).
[146]M. L. Feng, J. G. Mao ,J. L. Song, *J. Solid State Chem.*, **177**, 3529 (2004).
[147]D. Udayakumar, M. Dan ,C. N. R. Rao, *Eur. J. Inorg. Chem.*, 1733 (2004).
[148]J. N. Behera, A. A. Ayi ,C. N. R. Rao, *Chem. Commun.*, 968 (2004).
[149]T. A. Sullens, P. M. Almond, J. A. Byrd, J. V. Beitz, T. H. Bray ,T. E. Albretch-Schmidt, *J. Solid State Chem.*, **179**, 1192 (2006).
[150]A. Choudhury, J. Krishnamoorthy ,C. N. R. Rao, *Chem Commun.*, 2610 (2001).
[151]G. Paul, A. Choudhury ,C. N. R. Rao, *J. Chem. Soc., Dalton Trans.*, 3859 (2002).
[152]M. I. Khan, S. Cevik ,R. J. Doedens, *Inorg. Chim. Acta*, **292**, 112 (1999).
[153]H. Y. Guo, Z. H. Li, X. Y. Li, C. Y. Zhang ,R. J. Wang, *Chin. J. Chem.*, **21**, 466 (2003).
[154]J. N. Behera ,C. N. R. Rao, *Angew. Chem. Int. Ed.*, **631**, 3030 (2005).
[155]F. C. Hawthrone, S. V. Krivovichev ,P. C. Burns, *Rev. Mineral. Geochem.*, **40**, 1 (2002).
[156]G. Paul, A. Choudhury, R. Natarajan ,C. N. R. Rao, *Inorg. Chem.*, **42**, 2004 (2003).
[157]X. C. Sun, G. P. Zhou, X. F. Zheng ,Y. Xu, *Acta Cryst.*, **E63**, m1388 (2007).
[158]T. Loiseau, F. Serpaggi ,G. Ferey, *Chem. Commun.*, 1093 (1997).
[159]A. Choudhury, S. Natarajan ,C. N. R. Rao, *J. Chem. Soc., Dalton Trans.*, 2595 (2000).
[160]U. Kolitsch, *Acta Cryst.*, **C60**, i3 (2004).
[161]Y. Fu, Z. Xu, J. Ren, H. Wu ,R. Yuan, *Inorg. Chem.*, **45**, 8452 (2006).
[162]R. A. Ramik, B. D. Sturman, P. J. Dunn ,A. S. Poverennukh, *Can. Mineral.*, **18**, 185 (1980).
[163]G. Paul, A. Choudhury ,C. N. R. Rao, *Chem. Mater.*, **15**, 1174 (2003).
[164]L. Fafani, A. Nunzi ,P. F. Zanazzi, *J. Am. Mineral.*, **56**, 751 (1971).
[165]F. C. Hawthrone, *Tschemarks Mineral. Petrogr. Mitt.*, **31**, 121 (1983).
[166]S. Ekambaran ,S. Sevov, *Inorg. Chem.*, **39**, 2405 (2000).
[167]R. C. Haushalter, Z. W. Wang, L. M. Meyer, S. S. Dhingra, M. E. Thompson ,J. Zubieta, *J. Chem. Mater.*, **6**, 1463 (1994).
[168]L. Fanfani, A. Nunzi, P. F. Zanazzi ,A. R. Zanzari, *J. Am. Mineral.*, **58**, 314 (1973).
[169]J. R. Gutnick, E. A. Muller, A. N. Sarjeant ,A. J. Norquist, *Inorg. Chem.*, **43**, 6528 (2004).
[170]S. Chakrabarti ,S. Natarajan, *Angew. Chem. Int. Ed.*, **41**, 1224 (2002).
[171]A. Choudhury, S. Neeraj, S. Natarajan ,C. N. R. Rao, *J. Mater. Chem.*, **11**, 1537 (2001).
[172]P. M. Thomas, A. J. Norquist, M. B. Doran ,D. O'Hare, *J. Mater. Chem.*, **13**, 88 (2002).
[173]A. J. Norquist, P. M. Thomas, M. B. Doran ,D. O'Hare, *Chem. Mater.*, **14**, 5179 (2002).

[174]A. J. Norquist, M. B. Doran, P. M. Thomas ,D. O'Hare, *Dalton Trans.*, 1168 (2003).
[175]I. Bull, L. A. Villaescusa, S. J. Teat, M. A. Camblor, P. A. Wright, P. Lightfoot ,R. E. Morris, *J. Am. Chem. Soc.*, **122**, 7128 (2000).
[176]M. B. Doran, A. J. Norquist ,D. O'Hare, *Inorg. Chem.*, **42**, 6989 (2003).
[177]C. L. Stuart, M. B. Doran, A. J. Norquist ,D. O'Hare, *Acta Cryst.*, **E59**, m446 (2003).
[178]M. B. Doran, B. E. Cockbain, A. J. Norquist ,D. O'Hare, *Dalton Trans.*, 3810 (2004).
[179]V. V. Tabachenko, V. N. Serezhkin, L. B. Serezhkina ,L. M. Kovka, *Koord. Khim.*, **5**, 1563 (1979).
[180]*Solid State Protonic Conductors: For fuel Cells and Sensors*, 3rd European Workshop, Odense University, Odense, Denmark 191 (1985).
[181]M. B. Doran, B. E. Cockbain ,D. O'Hare, *Dalton Trans.*, 1774 (2005).
[182]Y. Xing, Y. Liu, Z. Shi, H. Meng ,W. Pang, *J. Solid State Chem.*, **174**, 381 (2003).
[183]X. Wang, L. Liu ,A. Jacobson, *J. Solid State Chem.*, **147**, 641 (1999).
[184]P. R. Slater, C. Greaves, M. Slaski ,C. M. Muirhead, *Phisica C*, **208**, 193 (1993).
[185]C. N. R. Rao, S. Neeraj ,S. Natarajan, *J. Am. Chem. Soc.*, **122**, 2810 (2000).
[186]M. Cavellec, D. Riou ,G. Ferey, *J. Solid State Chem.*, **112**, 441 (1994).
[187]G. Paul, A. Choudhury, E. V. Sampathakumaran ,C. N. R. Rao, *Angew. Chem. Int. Ed.*, **41**, 1224 (2002).
[188]J. N. Behera, K. V. Gopalkrishnan ,C. N. R. Rao, *Inorg. Chem.*, **43**, 2636 (2004).
[189]F. C. Hawthrone, S. V. Krivovichev ,P. C. Burns, *Rev. Miner. Geochem.*, **40**, 55 (2000).
[190]M. S. Wickleder, *Chem. Rev.*, **102**, 2011 (2002).
[191]M. Dan, J. N. Behera ,C. N. R. Rao, *J. Mater. Chem.*, **14**, 1257 (2004).
[192]Y. Xing, Z. Shi, G. Li ,W. Pang, *Dalton Trans.*, 940 (2003).
[193]T. Bataille ,D. Louer, *J. Mater. Chem.*, **12**, 3487 (2002).
[194]S. Govindarajan, K. C. Patil, H. Manohar ,P. E. Werner, *J. Chem. Soc., Dalton Trans.*, 119 (1986).
[195]D. Wang, R. Yu, Y. Xu, S. Feng, R. Xu, N. Kumada, N. Kinomura, Y. Matsumura ,M. Takano, *Chem. Lett.*, 1120 (2002).
[196]M. H. Xin, Y. Wang, G. S. Zhu, J. Y. Sun, Q. R. Fang, M. Xue, G. Tian ,S. L. Qiu, *Chem. J. Chin. Universities*, **28**, 1227 (2007).
[197]B. M. Casari ,V. Langer, *Eur. J. Inorg. Chem.*, 3514 (2007).
[198]A. J. Norquist, M. B. Doran ,D. O'Hare, *Inorg. Chem.*, **44**, 3837 (2005).
[199]J. N. Behera ,C. N. R. Rao, *Z. Anorg. Allg. Chem.*, **631**, 3030 (2005).
[200]Z. F. Tian, L. Wang, T. Y. Song, Y. Wang, L. L. Huang, L. R. Zhang ,S. H. Shi, *J. Solid State Chem.*, **181**, 842 (2008).
[201]J. B. Goodenough, *Phys. Chem. Solids*, **6**, 287 (1958).
[202]J. B. Goodenough, *Magnetism and Chemical Bond*, Wiley, New York (1963).
[203]J. Kanamori, *Phys. Chem. Solids*, **10**, 87 (1959).
[204]S. K. Pati, S. Ramasesha ,D. Sen, *Magnetism: Molecules to Materials IV*, (Ed.: J.S. Miller, M. Drillon), Wiley-VCH, Weinheim (2002).
[205]P. Day, *Molecules into Materials: Case Study in Materials Chemistry-Mixed Valency, Magnetism and Superconductivity*, World Scientific, Singapore (2007).
[206]A. P. Ramirez, *Handbook on Magnetic Materials*, Vol. 13 (Ed.: K.J.H. Busch), Elsevier, Amsterdam (2001).
[207]P. Schiffer, *Con. Mat. Phys.*, **18**, 21 (1996).
[208]D. Dai ,M.-H. Whangbo, *J. Chem. Phys.*, **121**, 672 (2004).
[209]F.Nori, E. Gagliano ,S. Bacci, *Phys.Rev. Lett.*, **68**, 240 (1992).

[210]T. Hasegawa, M. Inui, K. Hondou, Y. Fujiwara, T. Kato ,K. Iio, *J. Alloys Compd.*, **364**, 199 (2004).
[211]N. Oba, C. Michioka, M. Kato, K. Yoshimura ,K. Miau, *J. Phys.Chem. Solids*, **66**, 1438 (2005).
[212]F. Ladieu, F. Bert, V. Dupuis, E. Vincent ,J. Hammann, *J. Phys.:Condens. Matter*, **16**, 5735 (2004).
[213]N. Rogado, M. K. Haas, G. Lawes, D. A. Huse, A. P. Ramirez ,R. J. Cava, *J. Phys.: Condens. Matter*, **15**, 907 (2003).
[214]A. M. Todea, A. Merca, H. Bogge, J. Slageren, M. Dressel, L. Hengelhardt, M. Luban, T. Glaser, M. Henry ,A. Muller, *Angew. Chem. Int. Ed.*, **119**, 6218 (2007).
[215]J. E. Greedan, *J. Mater. Chem.*, **11**, 37 (2001).
[216]C. N. R. Rao, E. V. Sampathkumaran, R. Nagarajan, G. Paul, J. N. Behera ,A. Choudhury, *Chem. Mater.*, **16**, 1441 (2004).
[217]S. K. Pati ,C. N. R. Rao, *Chem. Commun.*, 4683 (2008).
[218]A. P. Ramirez, *Annu. Rev. Mater. Sci.*, **24**, 453 (1994).
[219]J. E. Dutrizac ,S. Kaiman, *Can. Mineral.*, **14**, 151 (1976).
[220]G. Paul, A. Choudhury, E. V. Sampathkumaran ,C. N. R. Rao, *Angew. Chem. Int. Ed.*, **41**, 4297 (2002).
[221]G. Paul, A. Choudhury ,C. N. R. Rao, *Chem. Commun.*, 1904 (2002).
[222]A. S. Wills ,A. Harrison, *J. Chem. Soc., Faraday Trans.*, **92 (12)**, 2161 (1996).
[223]E. A. Earle, A. P. Ramirez ,R. J. Cava, *Physica B*, **262**, 199 (1999).
[224]A. S. Wills, A. Harrison, C. Ritter ,R. I. Smith, *Phys. Rev. B.*, **61**, 6156 (2000).
[225]J. N. Behera ,C. N. R. Rao, *Inorg. Chem.*, **45**, 9475 (2006).
[226]J. N. Behera ,C. N. R. Rao, *J. Am. Chem. Soc.*, **128**, 9334 (2006).
[227]J. N. Behera, G. Paul, A. Choudhury ,C. N. R. Rao, *Chem. Commun.*, 456 (2004).
[228]J. N. Behera ,C. N. R. Rao, *Dalton Trans.*, 669 (2007).
[229]A. Rujiwatra, C. J. Kepert, J. B. Claridge, M. J. Rosseinsky, H. Kumagai ,M. Kurmoo, *J. Am. Chem. Soc.*, **123**, 10584 (2001).
[230]J. N. Behera ,C. N. R. Rao, *Can. J. Chem.*, **83**, 668 (2005).
[231]A. Rujiwatra, C. J. Kepert ,M. J. Rosseinsky, *Chem. Commun.*, 2307 (1999).
[232]B. Salah, S. Vilminot, G. Andre, M. Richard-Plouet, F. Bouree-Vigneron, T. Mhiri ,M. Kurmoo, *Chem. Eur. J.*, **10**, 2048 (2004).
[233]S. Vilminot, M. Richard-Plouet, G. Andre, D. Swierczynski, F. Bouernee-Vigneron ,M. Kurmoo, *Inorg. Chem.*, **42**, 6859 (2003).
[234]M. S. Salah, S. Vilminot, G. Andre, F. Bouree-Vigneron, M. Richard-Plouet, T. Mhiri ,M. Kurmoo, *Chem. Mater.*, **17**, 2612 (2005).
[235]S. Lauchan, T. J. Prior, S. Meansiri ,A. Rujiwatra, *J. Inorg. Organomet. Polym. Mater.*, **18**, 352 (2008).
[236]N. Lah, I. K. Cigic ,I. Leban, *Inorg. Chem. Commun.*, **6**, 1441 (2003).
[237]C. Liu, Y. Yin, X. Shi, D. Zhang ,M. Hu, *Inorg. Chem. Commun.*, **10**, 37 (2007).
[238]I. Bull, P. S. Wheatley, P. Lightfoot, R. E. Morris, E. Sastre ,P. A. Wright, *Chem. Commun.*, 1180 (2000).
[239]Y. Fu, Z. Xu ,J. Ren, *J. Mol. Struct.*, **788**, 190 (2006).
[240]C. D. Wu ,Z. Y. Liu, *J. Solid State Chem.*, **179**, 3500 (2006).
[241]Z. He, E. Q. Gao, Z. M. Wang, C. H. Yan ,M. Kurmoo, *Inorg. Chem.*, **44**, 862 (2005).
[242]H. Akkari, P.Benard-Rocherulle, H. Merazig, T. Roisnel ,J. Rocherulle, *Solid State Sci.*, **8**, 704 (2006).
[243]J. Yang, N. Lu, G. Zhang, L. Cheng ,S. H. Gou, *Polyhedron*, **27**, 2119 (2008).

[244]Y. P. Yuan, R. Y. Wang, D. Y. Kong, J. G. Mao ,A. Clearfield, *J. Solid State Chem.*, **178**, 2030 (2005).
[245]M. Doran, A. J. Norquist ,D. O'Hare, *Chem. Commun.*, 2946 (2002).
[246]R. E. Wilson, S. Skanthakumar, K. E. Knope, C. L. Cahill ,L. Soderholm, *Inorg. Chem.*, **47**, 9321 (2008).
[247]J. Y. Kim, A. J. Norquist ,D. O'Hare, *J. Am. Chem. Soc.*, **125**, 7707 (2003).
[248]K. M. Ok, J. Sung, G. Hu, R. M. J. Jacobs ,D. O'Hare, *J. Am. Chem. Soc.*, **130**, 3762 (2008).
[249]P. Walden, *Bull. Acad. Imper. Sci.*, 1800 (1914).
[250]F. H. Hurdley, *US Patent 2*, **446**, 331 (1948).
[251]T. Welton, *Chem. Rev.*, **99**, 2071 (1999).
[252]H. L. Jones ,R. A. Osteryoung, *Adv. Molten Salt Chem.*, **3**, 121 (1975).
[253]R. M. Pagni, *Adv. Molten Salt Chem.*, **6**, 211 (1987).
[254]R. R. Deshmukh, R. Rajagopal ,K. V. Srinivasan, *Chem. Commun.*, 1544 (2001).
[255]J. Dupont, G. S. Fonseca, A. P. Umpierre, P.F.P.Fichtner ,S. R. Texeira, *J. Am. Chem. Soc.*, **124**, 4228 (2002).
[256]F. Endres ,S. Z. Abedin, *Chem. Commun.*, **8**, 892 (2002).
[257]M. Antonietti, D. Kuang, B. Smarsly ,Y. Zhou, *Angew. Chem. Int. Ed.*, **43**, 4988 (2004).
[258]A. Elaiwi, S. B. Hitchcock, K. R. Seddon, N. Srinivasan, Y. M. Tan, T. Welton ,J. A. Zora, *J. Chem. Soc., Dalton Trans.*, **21**, 3467 (1995).
[259]A. Mele, C. D. Tran ,S. H. D. Lacerda, *Angew. Chem. Int. Ed.*, **42**, 4364 (2003).
[260]V. Tambyrajah, A. P. Abbott, D. L. Davies, R. K. Rasheed ,G. Capper, *Canadian Intellectual Property 2 423 803*, (2002).
[261]A. P. Abbott, G. Capper, D. L. Davies ,R. Rasheed, *Inorg. Chem.*, **43**, 3447 (2004).
[262]Y. P. Xu, Z. J. Tian, S. J. Wang, Y. Hu, L. Wang, B. C. Wang, Y. C. Ma, L. Hou, J. Y. Yu ,L. W. Lin, *Angew. Chem. Int. Ed.*, **45**, 3965 (2006).
[263]E. R. Parnham ,R. E. Morris, *Accounts Chem. Res.*, **40**, 1005 (2007).
[264]E. R. Parnham ,R. E. Morris, *J. Mater. Chem.*, **16**, 3682 (2006).
[265]E. R. Parnham ,R. E. Morris, *Chem. Mater.*, **18**, 4882 (2006).
[266]E. R. Parnham, *PhD Thesis, University of St Andrews, St Andrews, UK*, Chapter 10 (2006).
[267]L. Vidal, C. Pray ,J. Patarin, *Microporous Mesoporous Mater.*, **39**, 113 (2000).
[268]L. Lakiss, A. Simon-Masseron, V. Gramlich ,J. Patarin, *Solid State Sci.*, **7**, 141 (2005).
[269]E. R. Parnham, E. A. Drylie, P. S. Wheatley, A. M. Z. Slawin ,R. E. Morris, *Angew. Chem. Int. Ed.*, **45**, 4962 (2006).
[270]E. A. Drylie, D. S. Wragg, E. R. Parnham, P. S. Wheatley, A. M. Z. Slawin, J. E. Warren ,R. E. Morris, *Angew. Chem. Int. Ed.*, **46**, 7839 (2007).
[271]H. Z. Xing, J. Y. Li, W. F. Yan, P. Cheng, Z. Jin, J. H. Yu, S. Dai ,R. R. Xu, *Chem. Mater.*, **20**, 4179 (2008).
[272]K. Jin, X. Huang, L. Pang, J. Li, A. Appel ,S. Wherland, *Chem. Commun.*, 2872 (2002).
[273]D. N. Dybstsev, H. Chun ,K. Kim, *Chem. Commun.*, 1594 (2004).
[274]Y. Y. Qin, J. Zhang, Z. J. Li, L. Zhang, X. Y. Cao ,Y. G. Yao, *Chem. Commun.*, 2532 (2008).
[275]J. H. Liao, P. C. Wu ,W. C. Huang, *Cryst. Growth Des.*, **6**, 1062 (2006).
[276]Z. Lin, D. S. Wragg ,R. E. Morris, *Chem. Commun.*, 2021 (2006).
[277]L. Xu, E. Y. Choi ,Y. U. Kwon, *Inorg. Chem.*, **46**, 10670 (2007).

[278]J. H. Liao, P. C. Wu ,Y. H. Bai, *Inorg. Chem. Commun.*, **8**, 390 (2005).
[279]C.P.Tsao, C. Y. Sheu, N. Nguyen ,K. H. Lii, *Inorg. Chem.*, **45**, 6361 (2006).
[280]C. Y. Sheu, S. F. Lee ,K. H. Lii, *Inorg. Chem.*, **45**, 1891 (2006).
[281]M. F. Tang, Y. H. Liu, P. C. Chang, Y. C. Liao, H. M. Kao ,K. H. Lii, *Dalton Trans.*, 4523 (2007).
[282]D. E. Akporiaye, I. M. Dahl, A. Karlsson ,R. Wendelbo, *Angew. Chem. Int. Ed.*, **37**, 609 (1998).
[283]Y. Song, J. Yu, Y. Li, M. Zhang ,R. Xu, *Eur. J. Inorg. Chem.*, **18**, 3718 (2004).
[284]W. Krauss ,G. Nolze, *Powder Cell for Windows, Version 2.4.*, Berlin, Germany (2002).
[285]D. A. Fletcher, R. F. McMeeking ,D. J. Perkin, *J. Chem. Inf. Comput. Sci.*, **36**, 746 (1996).
[286]EVA, 0, 0, 3., Bruker AXS (1996-2007).
[287]P. M. Library, Version 9.0.1.33. (2007).
[288]*TOPAS V.3. General profile and structure analysis software for powder diffraction data*, Bruker AXS, Karlsruhe, Germany (2005).
[289]*Apex-2 Software, Bruker-AXS, Madison*, Wisconsin, USA (2004).
[290]G. M. Sheldrick, *SADABS*, University of Göttingen, Germany (1996).
[291]A. Altamore, G. Cascarazo, G. Giaacovazzo, A. Guangliardi, M. Burla, G. Polidori ,M. Camalli, *J. Appl. Cryst.*, **A27**, 435 (1994).
[292]D. J. Watkin, C. K. Prout, J. R. Carruthers ,P. W. Betteridge, *CRYSTALS, Issue 10*, Chemical Crystallography Laboratory, University of Oxford, UK (1996).
[293]D. Watkin, *Acta Cryst.*, **A50**, 411 (1994).
[294](Heriot-Watt University, Analytical and Technical Services).
[295]J. M. Du, Z. M. Liu, Z. H. Li, B. X. Hon, Y. Huang ,J. L. Zhang, *Microporous Mesoporous Mater.*, **83**, 145 (2005).
[296]X. M. Zhang, Z. M. Hao ,S. W. Ng, *Acta Cryst.*, **E61**, i82 (2005).
[297]G. Will, *Acta Cryst.*, **19**, 854 (1965).
[298]D. Samaras ,G. Coing-Boyat, *B. Soc. Fr. Mineral. Cr.*, **93**, 190 (1970).
[299]V. G. Gatton ,J. Zemann, *Z.Anorg.Allg. Chem.*, **293**, 233 (1958).
[300]T. Hikita, M. Kitabatake ,T. Ikeda., *J. Phys. Soc. Jpn.*, **49**, 1421 (1980).
[301]H. F. McMurdie, M. C. Morris ,J. Degroot, *J. Res. Nat. Bur. Std. A*, **75**, 435 (1971).
[302]J. Liebertz, *J.Cyst. Growth*, **6**, 109 (1969).
[303]K. Nassau ,J. W. Siever, *J. Cryst. Growth*, **42**, 588 (1977).
[304]A. Hidalgo-Lopez ,S. Veintemillas-Verdaguer, *J. Cryst. Growth*, **178**, 559 (1997).
[305]H. Iwanaga, M. Fujii, T. Hikita, M. Tanimoto ,S. Takeuchi, *J. Cryst. Growth*, **206**, 93 (1999).
[306]T. Hikita, S. Sato, H. Sekiguchi ,T. Ikeda, *J. Phys. Soc. Jpn.*, **42**, 1656 (1977).
[307]I. V. Ogorodnyk, I. V. Zatovsky, N. S. Slobodyanik, V. N. Baumer ,O. Shishkin, *J. Solid State Chem.*, **179**, 3461 (2006).
[308]R. V. Shpanchenko, O. A. Lapshina, E. V. Antipov, J. Hadermann, E. E. Kaul ,C. Geibel, *Mater. Res. Bull.*, **40**, 1569 (2005).
[309]B. Gossner ,I. Koch, *Z. Kristallogr.*, **80**, 455 (1931).
[310]A. Zemann ,J. Zemann, *Acta Cryst.*, **10**, 409 (1957).
[311]T. Hikita, H. Sekiguchi ,T. Ikeda, *J. Phys. Soc. Jpn.*, **43**, 1327 (1977).
[312]F. Jona ,R. Pepinsky, *Phys. Rev.*, **103**, 1126 (1956).
[313]B. Brezina ,M. Glogarova, *Phys. Status Solidi A*, **11**, K39 (1972).
[314]D. Speer ,E. Salje, *Phys. Chem. Miner.*, **13**, 17 (1986).
[315]C. Moriyoshi ,K. Itoh, *J. Phys. Soc. Jpn.*, **65**, 3082 (1996).

[316]J. I. Artman, *PhD. dissertation*, Brigham Young University (1990).
[317]E. B. Brackett, T. E. Brackett ,R. L. Sass, *J. Phys. Chem.*, **67**, 2132 (1963).
[318]W. R. Busing, *T. Am. Cryst. Assoc.*, **6**, 57 (1970).
[319]W. H. Zacheriasen, *Skifter utigitt av det Norske Videnskaps-Akademi i Oslo 1: Matematisk-Naturvidenskapelin klasse*, **1**, (1928).
[320]M. Y. Colby ,J. S. l. Coste, *Z. Kristallogr. Kristallgeom. Kristallphys. Kristallchem*, **90**, 1 (1935).
[321]B. Frit, B. Holmberg ,J. Galy, *Acta Cryst.* , **B26**, 16 (1970).
[322]B. Frit, B. Tanguy ,P. Hagenmuller, *B. Soc. Chim. Fr.*, **1**, 234 (1967).
[323]B. Frit ,M. M. Chbany, *J. Inorg. Nucl. Chem.*, **31**, 2685 (1969).
[324]P. Vaqueiro, D. P. Darlow, A. V. Powell ,A. M. Chippindale, *Solid State Ionics*, **172**, 601 (2004).
[325]A. Puls, M. Schaefer, C. Näther, W. Bensch, A. V. Powell, S. Boissière ,A. M. Chippindale, *J Solid State Chem.*, **178**, 1171 (2005).
[326]L. G. Sillen ,R. Petterson, *Ark. Mineral. Och. Geol.*, **13**, 1 (1945).
[327]G. Giuseppetti ,C. Tadini, *Tschermaks Min. Petr. Mitt.*, **21**, 101 (1974).
[328]B. Aurivillius, *Acta Chem. Scand. A*, **37**, 159 (1983).
[329]U. Leufer ,E. Tillmanns, *Tschermaks Min. Petr. Mitt.*, **27**, 261 (1980).
[330]N. W. Alcock, *Acta Cryst.*, **B29**, 498 (1973).
[331]I. Oftedal, *Z. Kristallogr.*, **72**, 239 (1929).
[332]G. Donnay ,J. D. H. Donnay, *J. Am. Mineral.*, **38**, 932 (1953).
[333]P. Held, *Acta Cryst.*, **E59**, m197 (2003).
[334]P. Leyva-Bailen, A. V. Powell ,P. Vaqueiro, *Acta Cryst.*, **E63**, m2643 (2007).
[335]Y. L. Fur, J. Coing-Bayet ,G. Bassi, *C.R. Seances Acad. Sci., Ser C.*, **269**, 632 (1966).
[336]S. Chaabouni, S. Kamoun, A. Daoud ,T. Jonini, *Acta Cryst.*, **C52**, 505 (1996).
[337]W. M. Baur, *Acta Cryst.*, **17**, 1167 (1964).
[338]M. Fleck, L. Botany ,E. Tillmans, *Solid State Sci.*, **6**, 469 (2004).
[339]G. Kreiner ,H. Jacobs, *J. Alloys Compd.*, **183**, 345 (1992).
[340]E. Dubler ,H. R. Oswald, *Helvetica Chimica Acta*, **54**, 1621 (1971).
[341]W. Rekik, H. Naili, T. Bataille, T. Roisnel ,T. Mhiri, *Inorg. Chim. Acta*, **359**, 3954 (2006).
[342]S. Yahyaoui, W. Rekik, H. Naili, T. Mhiri ,T. Bataille, *J. Solid State Chem.*, **180**, 3560 (2007).
[343]V. Zima ,K. H. Lii, *J. Chem. Soc., Dalton Trans.*, 1409 (1998).
[344]R. F. Giese ,G. Penna, *J. Am. Mineral.*, **68**, 255 (1983).
[345]P. Suesse, *Z. Kristallogr.*, **127**, 261 (1968).
[346]A. F. Orchand, *Magnetochemistry*, Oxford University Press Inc., New York, 113 (2003).
[347]J. S. Haynes, A. Kostikas, J. R. Sams, A. Simopoulos ,R. C. Thompson, *Inorg. Chem.*, **26**, 2360 (1987).
[348]D. W. Smith, *J. Chem. Soc. A*, 1708 (1969).
[349]M. Dan, G. Cottereau ,C. N. R. Rao, *Solid State Sci.*, **7**, 437 (2005).
[350]J. C. Trombe ,J. Jaud, *J. Chem. Cryst.*, **33**, 19 (2003).
[351]P. C. Junk, C. J. Kepert, B. W. Skelton ,A. H. White, *Aus. J. Chem.*, **52**, 601 (1999).
[352]J. C. Barnes, *Acta Cryst.*, **C51**, 2466 (1995).
[353]M. Tsvirko, S. Meshkova, G. Kiriiak ,V. Gorodnyuk, *J. Physics: Conference Series*, **79**, 012007 (2007).
[354]J. Li, C. Zhang, Q. Tang, J. Hao, Y. Zhang, Q. Su ,S. Wang, *J. Rare Earth*, **26**, 203 (2006).

[355]H. Icbudak, P. Naumov, M. Ristova ,G. Jovanovski, *J. Mol. Str.*, **606**, 77 (2002).
[356]K. A. Thiakou, V. Nastopoulos, A. Terzis, C. P. Paptopoulou ,S. P. Perlepes, *Polyhedron*, **25**, 539 (2006).
[357]N. S. Hussain, V. Aruna ,S. Buddhudu, *Mater. Res. Bull.*, **35**, 703 (2000).
[358]P. C. Punk, C. J. Kepert, B. W. Skelton ,A. H. White, *Aust. J. Chem.*, **52**, 601 (1999).
[359]D. Y. Wei ,Y. Q. Zheng, *Z. Kristallogr.*, **218**, 23 (2003).
[360]R. Wolf ,R. Hoppe, *Z. Anorg. Allg. Chem.*, **529**, 61 (1985).
[361]E. G. Sherry, *J. Solid State Chem.*, **19**, 271 (1976).
[362]R. C. Brown ,N. J. Clark, *J. Inorg. Nucl. Chem.*, **36**, 2507 (1974).
[363]I. Hartenbach ,T. Schleid, *Z. Anorg. Allg. Chem.*, **628**, 2171 (2002).
[364]H. U. Hummel, E. Fischer, T. Fischer, P. Joerg ,G. Pezzei, *Z. Anorg. Allg. Chem.*, **619**, 805 (1993).
[365]H. Jacobs ,U. Fink, *Z. Anorg. Allg. Chem.*, **438**, 151 (1978).
[366]W. Klemm ,G. Winkelmann, *Z. Anorg. Allg. Chem.*, **288**, 87 (1956).
[367]N. V. Padberezskaya ,S. V. Boriso, *Z. Structur. Khim.*, **17**, 186 (1976).
[368]K. A. Gschneider ,L. Eyring, *Handbook on the Physics and Chemistry of the Rare-Earths*, North Holland eds., vol.21 (1995).
[369]T. Y. Song, M. B. Hursthouse, J. S. Chen, R. R. Xu ,J. M. Thomas, *Adv. Mater.*, **6**, 679 (1994).
[370]R. K. Chiang, C. C. Huang ,C. R. Lin, *J. Solid State Chem.*, **156**, 242 (2001).
[371]K. A. G. Jr ,L. Eyring, *Handbook of the Physics and Chemistry of the Rare Earths*, North Holland, vol. 1-vol. 21 (1978-1995).
[372]J. P. Costes, J. M. Clemente-Juan, F. Dahan, F. Nicodeme ,M. Verelst, *Angew. Chem. Int. Ed.*, **41**, 223 (2002).
[373]J. C. Munoz, A. M. Atria, R. Baggio, M. T. Garland, O. Pena ,C. Orrego, *Inorg. Chim. Acta*, **358**, 4027 (2005).